

UNIVERSITÉ DU QUÉBEC À CHICOUTIMI

**THÈSE PRÉSENTÉE À
L'UNIVERSITÉ DU QUÉBEC À CHICOUTIMI
COMME EXIGENCE PARTIELLE
DU DOCTORAT EN INGÉNIERIE**

**PAR
GUILLERMO HERNÁN GARZA ELIZONDO**

**EFFET DE L'AJOUT DE Ni, Mn, Zr et Sc SUR LA
PERFORMANCE DES ALLIAGES Al-Si-Cu-Mg**

AVRIL 2016

UNIVERSITÉ DU QUÉBEC À CHICOUTIMI

**THESIS PRESENTED TO THE
UNIVERSITY OF QUEBEC AT CHICOUTIMI
IN PARTIAL FULFILLMENT OF THE
REQUIREMENT FOR THE DEGREE OF
DOCTOR OF PHILOSOPHY IN ENGINEERING**

**BY
GUILLERMO HERNÁN GARZA ELIZONDO**

**EFFECT OF Ni, Mn, Zr AND Sc ADDITIONS ON THE
PERFORMANCE OF Al-Si-Cu-Mg ALLOYS**

APRIL 2016

*Dedicated to my parents, my wife Stephanie,
and to my daughters Maya and Ana Rosa.*

RÉSUMÉ

Les alliages d'aluminium-silicium ont montré de nombreux avantages dans divers domaines de l'ingénierie. Ils ont prouvé être adaptés à l'industrie automobile, marine et aérospatiale pour lesquelles, avec des procédés de fusion et de traitements thermiques adaptés, la fabrication de différentes pièces est possible. Le développement des alliages d'aluminium et l'optimisation des techniques de coulées ont permis d'améliorer les propriétés des alliages et leur intégration fonctionnelle. Ceci permet aux alliages d'aluminium de satisfaire les critères actuels du marché. Bien que l'industrie automobile soit concentrée sur la réduction de la consommation d'essence, le développement ces dernières années des moteurs de haute puissance, à injection direct ainsi qu'à diesel, a entraîné un impact marqué sur la performance des matériaux servant à la fabrication des pistons, ceci due à l'augmentation de la pression de combustion et de la température des pistons. La réduction de poids dans les composants clés des moteurs ainsi qu'une température de service plus haute permettraient des opérations encore plus efficaces.

Alors que les pièces coulées d'aluminium-silicium sont généralement limitées à des conditions de services inférieurs à 230°C, les conditions d'opérations des composants automobiles sont souvent à plus haute température. Améliorer les propriétés mécaniques de haute température demande une compréhension des facteurs reliés à une baisse de la résistance des alliages lors de l'augmentation de la température. L'ajout d'éléments de transition de Ni, Zr et Sc pour améliorer la résistance aux hautes températures des alliages d'aluminium est basé sur la production de précipité de Al_3Ni , Al_3Zr , ou Al_3Sc de type $L1_2$ cohérent et semi-cohérent, lesquels supportent mieux le vieillissement à haute température, ceci due à une meilleure stabilité à ces mêmes températures en comparaison avec les précipités de Al_2Cu et Mg_2Si qui sont généralement présents dans les alliages d'aluminium.

Cette étude a été réalisée dans le but d'évaluer les effets des ajouts de Ni (à fort ou faible taux), Mn, Zr et Sc, individuellement ou combinés avec d'autres additifs, sur les microstructures et les propriétés de traction, à température ambiante et à haute température, de l'alliage 354 (Al-9wt%Si-1.8wt%Cu-0.5wt%Mg) pour un temps de vieillissement plus ou moins long. Les échantillons de traction ont été testés dans des conditions «as-cast», et en utilisant diverses températures de traitement thermique et différents temps de vieillissement. Des diagrammes d'indice de qualité ont été utilisés comme outil d'évaluation pour choisir les conditions optimums devant être appliquées pour obtenir des propriétés de traction supérieures et la meilleure qualité possible pour les alliages 354. Neuf alliages 354 ont été préparés comprenant a) les alliages de l'étape I – alliage 354 de base (G1) et quatre autres (alliages G2 à G5) contenant des ajouts de Ni (faible taux) et de Zr, pour être testé à température ambiante et à haute température et b) les alliages de l'étape II contenant l'alliage de base (G1) et cinq autres (alliages G6 à G10) contenant Ni (fort taux), Mn, Sc, et Zr ajoutés individuellement ou combinés et un alliage (G7) ne contenant pas de cuivre, testé à température ambiante.

Une analyse des données obtenues à partir des études microstructurale et thermique ainsi que des essais de traction montrent que le comportement mécanique des alliages 354 est fortement influencé par la température et le temps pendant lequel elle est maintenue avant l'essai. L'influence d'ajout mineur de Ni et Zr à ces alliages sur leur performance à haute température est contrôlée par leurs propriétés T6 à température ambiante. L'ajout de 0.2wt% Ni et 0.2wt% Zr (alliage G4) améliore considérablement les propriétés de traction T6 en comparaison au «as-cast». L'ajout de 0.4wt% Ni + 0.4wt% Zr (alliage G5) à l'alliage 354 n'est pas suffisant pour résister au ramollissement à 300°C/100h. L'ajout de 0.4wt% Ni à l'alliage 354 (alliages G2 et G5) amène une diminution des propriétés de traction. Cette diminution peut être attribuée à une réaction Ni-Cu qui interférerait avec la formation du précipité, renforçant Al₂Cu, et affecterait le processus de durcissement par le vieillissement. La phase L1₂ Al₃(Zr,Ti), la phase massive «block-like» (Al,Si)₂(Zr,Ti), et la phase aciculaire (Al,Si)₃(Zr,Ti) sont les principales caractéristiques observées dans la microstructure des alliages G3, G4 et G5 contenant 0.2-0.4wt% d'ajout de Zr. La présence de la phase Q-Al₅Cu₂Mg₈Si₆ et de la phase Al₃Ni est observée dans les échantillons traités à 300°C et après plus de 10h de vieillissement. Maintenir pour un temps donné les échantillons de traction de l'alliage G1 traité thermiquement avec la méthode T6 entraîne une augmentation marquée de la densité de particules précipitées, la majorité des particules restant de forme sphérique. De plus, vieillir l'alliage mis en solution à 190°C durant deux heures augmente la densité d'Al₂Cu précipité. Augmenter la durée du temps de maintien, avant la déformation, à 100h permet de changer la morphologie du précipité Al₂Cu en fines plaquettes distribuées selon deux directions perpendiculaires.

Dans les alliages de l'étape II, les principales réactions sont détectées durant la solidification de l'alliage 354 soit: la formation de réseau dendritique de α -Al, suivi de la précipitation de des phases eutectique Al-Si et post-eutectique β -Al₅FeSi; Mg₂Si; la transformation de la phase β en π -Al₈Mg₃FeSi₆; et finalement, la précipitation des phases Al₂Cu et Q-Al₅Mg₈Cu₂Si₆. Avec un ajout de 2wt% Ni, la formation des phases Al₉FeNi et Al₃CuNi est observée. Dans l'alliage 354 de base, les principales phases sont restreintes aux phases intermétalliques de Cu, Mg et Fe. Les caractéristiques de la particule Si et le volume de fractions intermétalliques sont influencés par la vitesse de refroidissement et le taux de Mg, alors que l'ajout de Fe et/ou Mn à une faible influence (alliage G9). Dans l'alliage G8 et G9, Fe, Mn, et Ni interagissent pour former de nouvelles phases intermétalliques; une augmentation de la quantité de Fe entraîne la formation de particules «sludge» de forme polyédrique et étoilée en plus des phases α -Fe et β -Al₅FeSi, augmentant le volume de la fraction intermétallique formée; la présence de particules «sludge» dures dans les dendrites α -Al molles améliore les propriétés de l'alliage. Le deuxième espace du bras dendritique (SDAS) n'est pas très différent dans les divers alliages étudiés. La moyenne SDAS des échantillons de traction « as-cast » des six alliages est d'environ 18 μ m.

Le traitement en solution des alliages de l'étape II (à 500°C/8h) permet la dissolution presque complète de la phase Al₂Cu; la dissolution partielle de la phase β -Al₅FeSi, et un fort degré de décomposition de la phase π en phase β ; les particules Q-Al₅Mg₈Cu₂Si₆, α -Fe et «sludge» restent insoluble. Zr et Sc réagissent uniquement avec Ti,

Si et Al pour former les phases $ZrSi$, $(Al,Si)_2(Zr,Ti)$, $(Al,Si)_3(Zr,Ti)$, $Si(Ti,Zr)$, Al_3Zr , et $Si(Sc,Zr)$. Les phases intermétalliques riche en Zr apparaissent sous deux formes différentes: (a) la phase $(Al,Si)_2(Zr,Ti)$ en forme de bloc qui contient plus de silicium, et la phase aciculaire $(Al,Si)_3(Zr,Ti)$ contenant plus d'aluminium. Les effets bénéfiques des ajouts de Zr, Sc et Ti se voit à l'affinement de la taille des grains α -Al et à la transformation de leurs morphologie dendritique en non dendritique, ce qui réduit la taille des particules Al_2Cu et α -Fe. Les phases intermétalliques contenant Zr semblent être affinées et distribuées de manière plus uniforme dans la matrice en présence de Sc.

Dans les alliages de l'étape II (G6 à G10), le traitement thermique améliore les propriétés de traction et la qualité de tous les alliages. La présence de Ni et Zr dans l'alliage G7 (sans Cu) et de Sc et Zr dans l'alliage G10 améliore ces alliages puisqu'ils montrent les meilleures valeurs Q et YS. Concernant l'ajout de Cu et Mg dans l'alliage 354, l'indice de qualité de l'alliage coulé est contrôlé par le taux d'augmentation de la résistance et de la réduction de la ductilité. Le vieillissement des alliages 354 coulés produit un large éventail de propriétés de traction dépendamment des températures et temps de vieillissement. Des pics multiples de vieillissement sont observés le long des courbes de durcissement par le vieillissement des alliages G6 à G10. Ces pics sont reliés à la séquence de précipitation qui a lieu dans chaque alliage. Dépendamment des propriétés de tension requises, des conditions de vieillissement appropriées peuvent être recommandées, basé sur le meilleur compromis entre la résistance, la qualité et le temps de vieillissement impliqués dans le procédé.

La meilleure combinaison de propriétés est atteinte après un vieillissement à $190^\circ C/h$ pour tous les alliages étudiés à l'exception de l'alliage G9 qui montre une meilleure combinaison à $190^\circ C/4h$. Ces conditions peuvent donc être considérées comme le traitement T6 le plus approprié pour ces alliages. Un vieillissement à $190^\circ C$ est une méthode intéressante pour ce système d'alliage en particulier puisqu'elle amène une économie significative par la réduction du temps de vieillissement requis pour atteindre le pic de résistance. Les diagrammes d'indice de qualité développés durant ce projet facilitent l'interprétation des propriétés de traction de l'alliage 354, permettant un outil d'évaluation pour une prédiction précise de l'influence des paramètres métallurgiques étudiés pour ces alliages. Basé sur les diagrammes d'indice de qualité développés, il est possible de faire une sélection rigoureuse des paramètres les plus appropriés devant être appliqués aux alliages 354 et d'obtenir le meilleur compromis entre la résistance et la qualité de l'alliage.

ABSTRACT

Aluminum-silicon casting alloys have shown great promise in several fields of engineering and have proved highly suitable for use in automotive, marine, and aerospace applications where, through appropriate molten metal processing and suitable heat treatments, the manufacturing of diverse parts is made possible. Developments in aluminum alloys and optimization of casting techniques have led to improved material properties and functional integration which enable aluminum castings to satisfy current market requirements. Although the automotive industry is focused on reducing fuel consumption, the development of diesel and direct fuel injection gasoline engines with high specific powers in recent years have resulted in a marked performance impact on piston materials due to increased combustion pressure and piston temperatures. Reductions in the weight of key engine components together with higher service temperatures would allow for more efficient operation.

While aluminum-silicon cast components are generally limited to service conditions of no more than 230°C, operating conditions in automotive components often result in much higher temperatures. Improving the high temperature mechanical properties requires an understanding of the factors which are related principally to a decrease in the strength of the alloy with increasing temperature. The use of transition element additions of Ni, Zr and Sc to increase high temperature strength in aluminum alloys is based on the production of coherent or semi-coherent $L1_2$ type precipitates of Al_3Ni , Al_3Zr , or Al_3Sc , which are better able to support overaging at higher temperatures due to their stability at higher temperatures, compared to the Al_2Cu and Mg_2Si precipitates normally present in cast aluminum alloys.

The present study was carried out to investigate the effects of Ni (high and low), Mn, Zr, and Sc additions, individually or in combination with other additives, on the microstructure and tensile properties of 354 casting alloy (Al-9wt%Si-1.8wt%Cu-0.5wt%Mg) at ambient and at high temperatures (155°C and 300°C) using different holding times at testing temperature. Tensile tests were carried out in the as-cast, solution heat-treated, and aged conditions using different aging temperatures and times. Quality charts were used as an evaluation tool for selecting the optimum conditions to achieve superior tensile properties and optimum quality in 354-type alloys. Nine alloys were prepared using the 354 alloy, comprising a) Stage I alloys – base 354 alloy (G1) and four others (alloys G2 to G5) containing Ni (low) and Zr additions, for testing at room and at high temperature, and b) Stage II alloys comprising the base alloy (G1) and five others (alloys G6 to G10) containing Ni (high), Mn, Sc, Zr, added individually or in combination, and one alloy (G7) containing no copper, which were tested at room temperature.

An analysis of the data obtained from microstructural and thermal analyses and tensile tests shows that the tensile behavior of 354-type cast alloys is strongly influenced by

the testing temperature and the holding time at temperature prior to testing. The influence of minor additions of Ni and Zr to these alloys on their high temperature performance is controlled by their T6-properties at room temperature. Addition of 0.2wt% Ni and 0.2wt% Zr (alloy G4) improves the T6-tensile properties considerably, compared to the as-cast condition. Addition of 0.4wt% Ni + 0.4wt% Zr (alloy G5) is not sufficient to resist softening at 300°C/100h. Addition of 0.4wt% Ni to alloy 354 (G2 and G5 alloys) leads to a decrease in the tensile properties, attributed to a Ni–Cu reaction that interferes with the formation of Al₂Cu strengthening precipitates and affects the age hardening process. The L1₂ Al₃(Zr,Ti) phase, the block-like (Al,Si)₂(Zr,Ti) phase, and the needle-like (Al,Si)₃(Zr,Ti) phase are the main features observed in the microstructure of alloys G3, G4 and G5 containing 0.2-0.4wt% Zr additions. The presence of *Q*-Al₅Cu₂Mg₈Si₆ phase and Al₃Ni phase is observed in samples tested at 300°C after 10 h holding. Holding the tensile samples of T6-treated G1 alloy resulted in a marked increase in the density of precipitated particles, most of the particles maintaining a spherical shape. Also, aging the solutionized alloy at 190°C for 2 h resulted in an increase in the density of the precipitated Al₂Cu. Increasing the holding time prior to deformation to 100 h resulted in the change in the morphology of the Al₂Cu precipitates into thin platelets distributed in two perpendicular directions.

In the Stage II alloys, the main reactions are detected during the solidification of the 354 alloys: formation of the α -Al dendritic network, followed by precipitation of the Al-Si eutectic and post-eutectic β -Al₅FeSi; Mg₂Si phase; transformation of the β -phase into π -Al₈Mg₃FeSi₆ phase; and finally precipitation of Al₂Cu and *Q*-Al₅Mg₈Cu₂Si₆ phases. With 2wt% Ni addition, the formation of Al₉FeNi and Al₃CuNi phases is observed. In the base 354 alloy, the main phases are restricted to Cu-, Mg-, and Fe-rich intermetallic phases. The Si particle characteristics and volume fraction of intermetallics are influenced by the cooling rate and Mg level, while addition of Fe and/or Mn also has a slight influence (alloy G9). In alloys G8 and G9, Fe, Mn and Ni interact to form new intermetallic phases; an increase in Fe content leads to the formation of polyhedral/star-like sludge particles in addition to the α -Fe script and β -Al₅FeSi phases, increasing the volume fraction of intermetallics formed; the presence of the hard sludge particles within the soft α -Al dendrites improves the alloy properties. The secondary dendrite arm spacing (SDAS) does not differ much among the alloys studied. The average SDAS of the as-cast tensile samples of the six alloys was found to be ~18 μ m.

Solution treatment of Stage II alloys (at 500°C/8h) results in almost complete dissolution of the Al₂Cu phase; partial dissolution of the β -Al₅FeSi phase, and a high degree of decomposition of the π -phase into β -phase; the *Q*-Al₅Mg₈Cu₂Si₆, α -Fe and sludge particles remain insoluble. Zirconium and Sc react only with Ti, Si and Al to form ZrSi, (Al,Si)₂(Zr,Ti), (Al,Si)₃(Zr,Ti), Si(Ti,Zr), Al₃Zr, and Si(Sc,Zr) phases. The Zr-rich intermetallics appear in two different forms: (a) the block-like (Al,Si)₂(Zr,Ti) phase which contains a higher level of Si, and the needle-like (Al,Si)₃(Zr,Ti) phase containing a higher level of aluminum. The beneficial effects of Zr, Sc and Ti additions appear in the refining of the α -Al grain size and transforming its morphology from dendritic to non-dendritic

type, which reduces the size of the Al_2Cu and $\alpha\text{-Fe}$ particles. The Zr-containing intermetallics appear to be refined and more uniformly distributed in the matrix in the presence of Sc.

Among the Stage II alloys (G6 to G10), solution heat treatment improves the tensile properties and alloy quality of all alloys. The presence of Ni and Zr in G7 alloy (with no Cu), and Sc and Zr in G10 alloy provides further improvement as these alloys show the best Q and YS values. With respect to the addition of Cu and Mg in 354 type alloys, the quality index of the alloy castings is controlled by the net amount by which the strength is increased and the ductility is reduced. Aging treatment of 354-type alloy castings produces a wide range of tensile properties based on the aging temperatures and times applied. Multiple aging peaks are observed in the age-hardening curves of alloys G6 to G10, related to the precipitation sequence which occurs in each alloy. Depending on the required tensile properties, suitable aging conditions may be recommended based on the best possible compromise between strength, quality, and aging time involved in the process.

The best combination of properties is achieved after aging at $190^\circ\text{C}/2\text{h}$ for all alloys studied, with an exception of alloy G9 that showed the best combination at $190^\circ\text{C}/4\text{h}$. These conditions may therefore be considered as the appropriate T6 treatment for these alloys. Aging at 190°C introduces a technologically useful strategy for this particular alloy system as it provides a significant economic benefit in the form of a noticeable reduction in the aging time required to reach peak strength. The quality charts developed in the course of this study facilitate the interpretation of the tensile properties of 354 alloys, providing a logical evaluation tool for an accurate prediction of the influence of the various metallurgical parameters investigated on the alloys. Based on the quality charts developed, it is possible to make a rigorous selection as to the most suitable parameters to be applied to 354 type alloys so as to obtain the best possible cost-effective compromise between alloy strength and quality.

ACKNOWLEDGEMENTS

Firstly, I would like to express my sincere thanks to my supervisors, Professors F.H. Samuel and A.M. Samuel, Research Professors at Université du Québec à Chicoutimi, for motivating me to complete my Ph.D degree and for the hard work during the different stages of my studies at UQAC. Without their continuous guidance and support it would have not been possible to do so. My sincere gratitude to Professor Saleh A. Alkahtani, Vice rector of Development and Quality and Development, Prince Sattam bin Abdulaziz University, AlKharj, Saudi Arabia, for his support and advice throughout the years.

I would also like to thank the committee members, Dr. S. Valtierra, Dr. H. Doty, and Dr. M. Moustafa, for their time and effort to read this thesis and for providing me helpful suggestions in improving the quality of my thesis.

Financial support in the form of scholarships received from the Natural Sciences and Engineering Research Council of Canada (NSERC), from General Motors Powertrain Group (U.S.A), and from Corporativo Nemark (Mexico) is gratefully acknowledged.

It is a great pleasure to have the opportunity of conveying my thanks to all those who were involved, directly or indirectly, in making this work a success. Thanks to Ms Amal Samuel for enhancing the quality of the illustrations used in this thesis.

Finally, but most importantly, I would not reach this height in my life without the unconditional love and support of my family, especially my parents. My deepest gratitude goes to my wife Stephanie and to my daughters Maya and Ana Rosa, for their patience and encouragements without which this thesis could not have been completed successfully.

PUBLICATIONS

Journal Papers

1. G.H. Garza-Elizondo, H.R. Ammar, A.M. Samuel, S. Valtierra and F.H. Samuel, "Effect of Ni, Mn, Sc, and Zr addition on the tensile properties of 354-type alloys," *(submitted to International Journal of Metalcasting)*.
2. G.H. Garza-Elizondo, H.R. Ammar, A.M. Samuel, S. Valtierra and F.H. Samuel, "Effect of alloying elements on the performance of 354-type alloys: Quality index charts and analytical analysis," *(submitted to Advances in Materials Science and Engineering)*.
3. G.H. Garza-Elizondo, A.M. Samuel, S. Valtierra and F.H. Samuel, "Hardening Precipitates in 354-type alloys: role of minor additives," *(submitted to Advances in Materials Science and Engineering)*.
4. G.H. Garza-Elizondo, A.M. Samuel, S. Valtierra and F.H. Samuel, "Phase precipitation in transition metals containing 354-type alloys," *(submitted to International Journal of Materials Research)*.
5. G.H. Garza-Elizondo, A.M. Samuel, S. Alqahtany and F.H. Samuel, "Effect of Minor Additions on the High Temperature Performance of 354 Alloys," *Advances in Material Sciences and Applications (AMSA)*, 2014.
6. J. Hernandez-Sandoval, G.H. Garza-Elizondo, A.M. Samuel, S. Valtierra and F.H. Samuel, "The ambient and high temperature deformation behavior of Al-Si-Cu-Mg alloy with minor Ti, Zr, Ni additions," *Materials and Design* 58 p. 89-101, January 2014.

Other Articles

7. M.F. Ibrahim, G.H. Garza-Elizondo, A.M. Samuel and F.H. Samuel, "Optimizing the Heat Treatment of High Strength 7075-Type Wrought Alloys: A Metallographic Study," *International Journal of Metalcasting*, April 2016.
8. A.M. Samuel, G.H. Garza-Elizondo, H.W. Doty and F.H. Samuel, "Role of modification and melt thermal treatment processes on the microstructure and tensile properties of Al-Si Alloys," *Materials and Design*, p. 99-108, August 2015.

Conferences and Presentations

9. M.F. Ibrahim, G.H. Garza-Elizondo, A.M. Samuel and F.H. Samuel, “Optimizing the Heat Treatment of High Strength 7075-Type Wrought Alloys: A Metallographic Study,” American Foundry Society (AFS), Publication and Presentation, April 2015.
10. G.H. Garza-Elizondo, A.M. Samuel, S. Alqahtany and F.H. Samuel, “Role of Ni and Zr in Preserving the Strength of 354 Aluminum Alloy at High Temperature,” The Minerals, Metals and Materials Society (TMS), Publication and Presentation, February 2014.
11. G.H. Garza-Elizondo, A.M. Samuel, S. Alqahtany and F.H. Samuel, “Development of New Aluminum-Based Alloy for High Temperature Performance,” REGAL (*Poster*), October 2013.
12. G.H. Garza-Elizondo, A.M. Samuel, S. Alqahtany and F.H. Samuel, “Role of Ni and Zr on 354 Aluminum Alloy at High Temperature,” REGAL (*Poster*), November 2012.

TABLE OF CONTENTS

RÉSUMÉ	i
ABSTRACT	iv
ACKNOWLEDGEMENTS	vii
PUBLICATIONS	viii
TABLE OF CONTENTS	x
LIST OF FIGURES	xiv
LIST OF TABLES	xxv
CHAPTER 1 DEFINING THE PROBLEM	1
1.1 INTRODUCTION.....	2
1.2 OBJECTIVES	6
1.3 THESIS LAYOUT	8
CHAPTER 2 LITERATURE SURVEY	9
2.1 INTRODUCTION.....	10
2.2 ALUMINUM-SILICON CASTING ALLOYS	12
2.2.1 354 – Al-Si-Cu-Mg ALLOY SYSTEM.....	16
2.2.2 MELT TREATMENT OF EUTECTIC Al-Si ALLOYS.....	19
2.2.3 CHEMICAL MODIFICATION IN EUTECTIC Al-Si ALLOYS	20
2.2.4 CHEMICAL GRAIN REFINEMENT IN EUTECTIC Al-Si ALLOYS.....	23
2.2.5 INFLUENCE OF HEAT TREATMENT IN Al-Si ALLOYS	25
2.2.6 SOLUTION HEAT TREATING.....	26
2.2.7 QUENCHING	29
2.2.8 AGE HARDENING.....	31
2.3 ROLE OF COPPER (Cu) AND MAGNESIUM (Mg) IN Al-Si ALLOYS	37
2.4 ROLE OF IRON (Fe) AND MANGANESE (Mn) IN Al-Si ALLOYS	42

2.5	EFFECTS OF CERTAINS ALLOYING ELEMENTS	47
2.5.1	EFFECTS OF ZIRCONIUM (Zr)	48
2.5.2	EFFECTS OF NICKEL (Ni)	51
2.5.3	EFFECTS OF SCANDIUM (Sc)	54
2.6	MECHANICAL PROPERTIES OF Al-Si ALLOYS	57
2.6.1	TENSILE TESTING.....	58
2.7	EFFECTS OF TEMPERATURE ON CAST ALUMINUM ALLOYS	61
2.8	FRACTURE BEHAVIOUR	65
2.9	QUALITY OF CAST ALUMINUM ALLOYS	71
2.9.1	QUALITY INDEX Q (AFTER DROUZY <i>et al.</i>)	72
	CHAPTER 3 EXPERIMENTAL PROCEDURES	75
3.1	INTRODUCTION.....	76
3.2	CLASSIFICATION OF ALLOYS	78
3.3	MELTING AND CASTING PROCEDURES	78
3.4	HEAT TREATMENT	82
3.5	MECHANICAL TESTING	85
3.5.1	TENSILE TESTING AT ELEVATED TEMPERATURE.....	85
3.5.2	TENSILE TESTING AT ROOM TEMPERATURE	87
3.6	CHARACTERIZATION OF THE MICROSTRUCTURE	88
3.6.1	THERMAL ANALYSIS.....	88
3.6.2	OPTICAL MICROSTRUCTURE	91
3.6.3	SCANNING ELECTRON MICROSCOPY AND ELECTRON PROBLE MICROANALYSIS.....	94
	CHAPTER 4 Stage I Alloys – Room and High Temperature Testing MICROSTRUCTURE AND TENSILE PROPERTIES	97
4.1	INTRODUCTION.....	98
4.2	MICROSTRUCTURE OF TENSILE TEST SAMPLES.....	99

4.3	EVALUATION OF TENSILE PROPERTIES IN AS-CAST AND T6 CONDITIONS	108
4.4	EVALUATION OF TENSILE PROPERTIES AT HIGH TEMPERATURE	113
4.5	COMPARISON BETWEEN AMBIENT AND HIGH TEMPERATURE TESTING RESULTS	117
4.6	FRACTOGRAPHY.....	120
4.6.1	SEM ANALYSIS OF FRACTURE SURFACES	120
4.6.2	MICROSTRUCTURAL ANALYSIS OF FRACTURE PROFILE	135
4.7	HARDENING PRECIPITATES.....	143
4.8	CONCLUSIONS.....	160
CHAPTER 5 Stage II Alloys – Room Temperature Testing		
MICROSTRUCTURE AND MECHANICAL PROPERTIES PART I		
MICROSTRUCTURE CHARACTERIZATION.....		
5.1	INTRODUCTION.....	165
5.2	LOW COOLING RATE – THERMAL ANALYSIS	166
5.2.1	SILICON PARTICLE CHARACTERISTICS AND VOLUME FRACTION	167
5.2.2	THERMAL ANALYSIS: BASE ALLOY G1	173
5.2.3	THERMAL ANALYSIS: ALLOY G6 (2wt% Ni + 0.25wt% Zr)	182
5.2.4	THERMAL ANALYSIS: ALLOY G7 (2wt% Ni + 0.25wt% Zr, no Cu)	187
5.2.5	THERMAL ANALYSIS: ALLOY G8 (0.75wt% Mn + 0.25wt% Zr)	191
5.2.6	THERMAL ANALYSIS: ALLOY G9 (2wt% Ni + 0.75wt% Mn + 0.25wt% Zr)	197
5.2.7	THERMAL ANALYSIS: ALLOY G10 (0.15wt% Sc + 0.25wt% Zr)	202
5.3	HIGH COOLING RATE – TENSILE TEST SAMPLES	209
5.3.1	SILICON PARTICLE CHARACTERISTICS AND VOLUME FRACTION OF INTERMETALLICS	210
5.3.2	CHARACTERISTICS OF INTERMETALLIC PHASES	225
5.3.2.1	AS-CAST AND SOLUTION HEAT-TREATED CONDITIONS	226
5.4	CONCLUSIONS.....	232

CHAPTER 5 Stage II Alloys – Room Temperature Testing	
MICROSTRUCTURE AND MECHANICAL PROPERTIES PART II	
TENSILE PROPERTIES	236
5.5 INTRODUCTION.....	237
5.6 AS-CAST AND SOLUTION HEAT-TREATED CONDITIONS.....	238
5.7 INFLUENCE OF AGING PARAMETERS.....	247
5.7.1 AGING BEHAVIOR OF BASE ALLOY G1	248
5.7.2 AGING BEHAVIOR OF ALLOY G6 (2wt% Ni + 0.25wt% Zr).....	256
5.7.3 AGING BEHAVIOR OF ALLOY G7 (2wt% Ni + 0.25wt% Zr, no Cu)	262
5.7.4 AGING BEHAVIOR OF ALLOY G8 (0.75wt% Mn + 0.25wt% Zr)	268
5.7.5 AGING BEHAVIOR OF ALLOY G9 (2wt% Ni + 0.75wt% Mn + 0.25wt% Zr)	275
5.7.6 AGING BEHAVIOR OF ALLOY G10 (0.15wt% Sc + 0.25wt% Zr).....	283
5.7.7 QUALITY INDEX CHARTS: COMPARISON BETWEEN AGING BEHAVIORS OF ALLOY G1, AND ALLOYS G6 THROUGH G10	289
5.8 STATISTICAL ANALYSIS	295
5.9 CONCLUSIONS.....	301
RECOMMENDATIONS FOR FUTURE WORK.....	305
REFERENCES.....	307

LIST OF FIGURES

Chapter 2

- Figure 2.1 The growing trend of fifty years of uninterrupted aluminum alloys for North American manufactured light vehicles.²⁴⁻²⁶ 11
- Figure 2.2 Al-Si casting alloys: (a) Al-Si phase diagram; (b) microstructure of hypoeutectic alloy; (c) microstructure of eutectic alloy; and (d) microstructure of hypereutectic alloy.³⁷ 15
- Figure 2.3 Schematic diagram showing behavior of the Si particle during solution heat treatment in the case of: (a) non-modified, and (b) modified Al-Si alloys.⁶⁹ 22
- Figure 2.4 Comparison of the silicon morphology in: (a) unmodified and (b) Sr-modified (300 ppm Sr), hypoeutectic aluminum-silicon alloys.⁶¹ 22
- Figure 2.5 Portion of the Al-Ti phase diagram and a schematic representation of the nucleation of α -Al through the peritectic reaction in the Al-Ti system.⁷⁵ 25
- Figure 2.6 Diagram showing the three steps of heat treatment for precipitation hardening. 27
- Figure 2.7 Diagram representing precipitation stages with aging time.¹⁰² 32
- Figure 2.8 Schematic diagram showing: (a) a non-coherent precipitate that is not related to the crystal structure of the surrounding matrix, (b) a coherent precipitate that is related to the structure of the surrounding matrix.^{104,105} 33
- Figure 2.9 Schematic diagrams showing the Orowan process of dislocation: (a) bowing between precipitates, then (b) by-passing the particles by leaving a dislocation loop surrounding each one.¹⁹ 34
- Figure 2.10 Effects of Mg-content on tensile properties and quality index of Al-7%Si alloy castings.^{78, 131} 41
- Figure 2.11 Quality chart illustrating the influence of the content of Cu and other elements (Mg, Si, Fe, and Mn) and cooling rate, as indicated by arrows, on the strength and quality index of Al-Si-Cu-Mg alloys. The numbers 1 through 21 located in the chart represent various alloy compositions.¹³² 42
- Figure 2.12 Length measurements of iron phase particles: (a) β -Al₅FeSi platelets in A356 alloys with different Fe levels; (b) α -Al₈Fe₂Si script particles in A356 alloys with different Fe and Cr levels.¹³⁸ 44
- Figure 2.13 Average surface fraction and areas below the intermetallic peaks as they vary with the iron concentrations in the melt.¹⁴⁶ 46

Figure 2.14 Tensile properties and quality index values of 356 alloys as a function of aging time at 155°C and iron content. ^{74, 131, 147}	47
Figure 2.15 Al rich corner of the Al-Zr binary phase diagram (adapted from Murray ¹⁶¹) with metastable Al ₃ Zr (L1 ₂) solvus calculated by Liu <i>et al.</i> ^{162, 163}	51
Figure 2.16 Al-Ni binary phase diagram. ¹⁶⁶	53
Figure 2.17 Al-Sc binary phase diagram. ¹⁷⁷	55
Figure 2.18 A schematic diagram of the aluminum-rich end of the Al-Sc phase diagram, showing a eutectic reaction at 0.55wt% Sc. ¹⁸⁰	56
Figure 2.19 Characteristics of the engineering stress-strain curve.	60
Figure 2.20 Schematic diagram showing precipitation of (a) a coherent particle and (b) a non-coherent particle in relation to the surrounding Al matrix. ¹¹	62
Figure 2.21 (a) L1 ₂ , (b) D0 ₂₂ , and (c) D0 ₂₃ structures. ¹⁶³	63
Figure 2.22 Stress-strain curves for permanent-mold A356-T6 castings at various temperatures (exposure time = 1hr). ^{19, 192}	65
Figure 2.23 Schematic showing classification of the type of fracture at different test temperatures for the study of an A356 alloy (SCU = sand cast, unmodified; SCM = sand cast, modified; PM = permanent mold). ¹⁹²	69
Figure 2.24 Example of the quality chart proposed by Drouzy <i>et al.</i> ¹³⁰ with <i>iso-Q</i> and <i>iso-YS</i> lines generated using Equations 1 and 2.	74

Chapter 3

Figure 3.1 Electrical resistance furnace.	79
Figure 3.2 Graphite degassing impeller.	80
Figure 3.3 ASTM B-108 permanent mold used for casting tensile test bars.	81
Figure 3.4 Dimensions of the tensile test bar (in mm).	81
Figure 3.5 Lindberg Blue M electric furnace.	84
Figure 3.6 Instron Universal mechanical testing machine with chamber for high temperature testing.	86
Figure 3.7 MTS Mechanical Testing machine used for room temperature testing.	87
Figure 3.8 Schematic drawing showing the graphite mold used for thermal analysis.	90
Figure 3.9 Thermal analysis set-up.	90
Figure 3.10 Diagram showing the sectioned area of tensile-tested samples prepared for microstructure analysis using optical microscopy.	92

Figure 3.11 (L) Struers LaboPress-3 and (R) TegraForce-5 machines, for mounting and polishing samples for metallography.	93
Figure 3.12 Clemex Vision PE optical microscope and image-analysis system used in the current study.	93
Figure 3.13 JEOL 840A scanning electron microscope used in this study.	95
Figure 3.14 Hitachi-SU-8000 field emission scanning electron microscope used in the current study.	95
Figure 3.15 JEOL JXA-8900L WD/ED combined microanalyzer (EPMA) system used in the current study.	96

Chapter 4 - Stage I Alloys

Figure 4.1 Optical micrographs of a tensile test specimen of the base alloy G1 showing the as-cast microstructure at (a) low (200X) magnification, and (b) high (500X) magnification.	102
Figure 4.2 Optical micrographs of a tensile test specimen of alloy G2 (G1 + 0.4wt% Ni) showing the as-cast microstructure at (a) low (200X) magnification, and (b) high (500X) magnification.	103
Figure 4.3 Optical micrographs of a tensile test specimen of alloy G5 (G1 + 0.4wt% Ni + 0.4wt% Zr) showing the as-cast microstructure at (a) low (200X) magnification, and (b) high (500X) magnification.	104
Figure 4.4 Optical micrographs of a T6 heat-treated tensile test specimen of the base alloy G1 showing the microstructure at (a) low (200X) magnification, and (b) high (500X) magnification.	105
Figure 4.5 Optical micrographs of a T6 heat-treated tensile test specimen of alloy G2 (G1 + 0.4wt% Ni) showing the microstructure at (a) low (200X) magnification, and (b) high (500X) magnification.	106
Figure 4.6 Optical micrographs of a T6 heat-treated tensile test specimen of alloy G5 (G1 + 0.4wt% Ni + 0.4wt% Zr) showing the microstructure at (a) low (200X) magnification, and (b) high (500X) magnification.	107
Figure 4.7 Average values of ultimate tensile strength (UTS), yield strength (YS), and percentage elongation to fracture (%El) obtained from Stage I alloys (G1 to G5) in the as-cast and T6-treated condition for different aging times at 190°C aging temperature (Testing was done at room temperature).	110
Figure 4.8 Average values of ultimate tensile strength (UTS), yield strength (YS), and percentage elongation (%El) obtained for the Stage I alloys (G1 to G5) tested at high temperature under different conditions.	116

- Figure 4.9 Average values of ultimate tensile strength (UTS), yield strength (YS), and percentage elongation (%El) for the Stage I alloys (G1 to G5) tested under different conditions at room and at high temperature. 119
- Figure 4.10 SEM images of the fracture surface of as-cast G1 alloy: (a) SE image showing a well-defined dimple structure, (b) BSE image showing presence of bright particles, and (c) EDS spectrum of the circled area in (b) showing the particles to be Q - $Al_5Cu_2Mg_8Si_6$ phase. 122
- Figure 4.11 SEM images of T6-treated G1 alloy: (a) SE image showing coarser dimples, (b) BSE image showing presence of broken Si particles, (c) high magnification image of cluster of broken particles in circled area in (b), and (d) corresponding EDS spectrum showing these particles to be mainly π - $Al_8FeMg_3Si_6$ phase. ... 123
- Figure 4.12 SEM images of fracture surface of G1 alloy tested at 300°C/100 h condition: (a) SE image showing very coarse and deep dimples, (b) BSE image showing presence of broken intermetallic particles, and (c) EDS spectrum of circled particle in (b) corresponding to Q - $Al_5Cu_2Mg_8Si_6$ phase. 125
- Figure 4.13 SEM images of fracture surface of as-cast G2 alloy: (a) SE image showing a fine dimple structure, (b) BSE image showing a large Chinese-script particle attached to a massive particle, and (c) EDS spectrum corresponding to the circled area in (b) revealing presence of Al_9NiFe and Al_3CuNi phases. 126
- Figure 4.14 SEM images of fracture surface of T6-treated G2 alloy: (a) SE image showing a mixture of elongated and rounded dimples, (b) BSE image showing several intermetallic particles within the dimples, and (c) EDS spectrum of circled area in (b) revealing the particles to be a mix of Al_9NiFe and Al_3CuNi phases. 127
- Figure 4.15 SEM images of fracture surface of G2 alloy tested at 300°C/100 h: (a) SE image showing large dimples with deformation lines on their surfaces, (b) BSE image showing the deformation lines more clearly, and (c) EDS spectrum of the circled area in (b) indicating the presence of eutectic Si phase particles. 128
- Figure 4.16 SEM images of fracture surface of as-cast G5 alloy: (a) SE image showing some long Si particles, (b) BSE image showing a bright fractured particle, and (c) EDS spectrum of the circled area in (b) showing the particle to be $Al_3(Ti, Zr)$ phase. 130
- Figure 4.17 SEM images of T6-treated G5 alloy: (a) SE image showing a uniform dimple structure, (b) BSE image showing grey plates of varying intensity, and (c, d) EDS spectra corresponding to the red and blue circled areas in (b) corresponding to a mixture of Al_9NiFe , Al_3CuNi , and $Al_3(Ti,Zr)$ phases. 131
- Figure 4.18 SEM images of fracture surface of G5 alloy tested at 300°C/100 h: (a) SE image showing dimple structure, (b) BSE image showing ultra-fine precipitates (white circled area) and coarse particles (red circled area), and (c) EDS spectrum showing these particles to be a mix of π - $Al_8FeMg_3Si_6$, Al_9NiFe ,

Al ₃ CuNi phases	132
Figure 4.19 Optical micrographs showing the longitudinal sections of tensile-tested samples of alloy G1 in (a) as-cast, (b) T6 heat-treated, and (c) 300°C/100 h tested conditions. (L: Low magnification micrographs; R; high magnification micrographs).	139
Figure 4.20 Optical micrographs showing the longitudinal sections of tensile-tested samples of alloy G2 in (a) as-cast, (b) T6 heat-treated, and (c) 300°C/100 h tested conditions. (L: Low magnification micrographs; R; high magnification micrographs).	140
Figure 4.21 Optical micrographs showing the longitudinal sections of tensile-tested samples of alloy G5 in (a) as-cast, (b) T6 heat-treated, and (c) 300°C/100 h tested conditions. (L: Low magnification micrographs; R; high magnification micrographs).	141
Figure 4.22 Model for the fracture mechanism of modified Al-Si alloys. ⁶⁵	142
Figure 4.23 Precipitation of ultra-fine particles in as-quenched G1 base alloy.	145
Figure 4.24(a) Backscattered electron image showing the co-existence of Q -Al ₅ Mg ₈ Si ₆ Cu ₂ phase and Fe-based intermetallics in the as-quenched G1 alloy, (b-d) images showing distribution of Fe, Cu and Mg elements in (a).	146
Figure 4.25 EDS spectrum corresponding to the medium-gray phase in Figure 4.24(a). ..	147
Figure 4.26 Precipitation observed in G1 base alloy in the T6-treated condition.	147
Figure 4.27(a) Precipitation in T6-treated G1 base alloy deformed at 155°C after holding for 10 h, (b) enlarged image of circled area in (a).	148
Figure 4.28(a) Precipitation in T6-treated tensile G1 base alloy sample deformed at 155°C after holding for 100 h, (b) high magnification BSE image of (a) showing the presence of two perpendicular precipitate families – see white arrows.	150
Figure 4.29 Backscattered electron images of T6-treated G1 base alloy tensile sample held for 10 h at 300°C prior to deformation (a) general view, (b) high magnification image, (c) EDS spectra obtained from different particles showing strong reflections of Al and Cu elements, corresponding to Al ₂ Cu.	151
Figure 4.30(a) Backscattered electron image of G5 alloy following solution treatment/quenching, (b) EDS spectrum corresponding to the circled area in (a) revealing presence of Al ₆ Cu ₃ Ni phase, and (c) EDS spectrum obtained from the arrowed area in (a) corresponding to Al ₉ FeNi phase.	152
Figure 4.31(a) BSE image of T6-treated tensile sample of G5 alloy held at 300°C/10 h prior to deformation, (b) EDS spectrum obtained from the bright particles arrowed in (a), reveals that these particles are mainly Al ₃ Ni phase.	154

- Figure 4.32(a) High magnification image of insoluble phases observed in G5 alloy, (b) EDS spectra corresponding to different areas in (a), indicate the presence of Q - $Al_5Mg_8Si_6Cu_2$ phase and Al_3Ni phase. Note the presence of precipitate free zones (marked PFZ) in (a). 155
- Figure 4.33(a) Backscattered electron image of the fine precipitates observed in the T6-treated tensile sample of G5 alloy shown in Figure 4.31(a) and (b) EDS spectra corresponding to different particles in (a), displaying strong peaks of Al and Cu elements. 156
- Figure 4.34(a) Backscattered electron (BSE) image, (b) BSE image showing no precipitate free zones (PFZ) around the pre-existing phases, (c) secondary electron image obtained from tensile sample of G5 alloy held at 300°C/100 h prior to deformation, (d) EDS spectra corresponding to (c) revealing presence of Al_2Cu , and (e) high magnification image of (a). 159

Chapter 5 - Stage II Alloys - Part I

- Figure 5.1 Optical microstructure showing the incomplete transformation of Si particles at low cooling rate in Sr-modified: (a) G1 base alloy, (b) G8 alloy (0.75wt% Mn + 0.25wt% Zr), and (c) G10 alloy (0.15wt% Sc + 0.25wt% Zr). 171
- Figure 5.2 Temperature-time plot and first derivative obtained from the thermal analysis of base alloy G1. 175
- Figure 5.3 (a) Optical microstructure (200X) and (b) backscattered electron image of the G1 alloy sample obtained from the thermal analysis casting (cooling rate 0.35°C/s), showing different phases in the alloy. 177
- Figure 5.4 Backscattered electron image showing some of the phases observed in base alloy G1. 178
- Figure 5.5 EDS spectra corresponding to Al_2Cu , β - Al_5FeSi , π - $Al_8Mg_3FeSi_6$, and Q - $Al_5Mg_8Cu_2Si_6$ phases observed in Figure 5.4. 179
- Figure 5.6 Temperature-time plot and first derivative from the thermal analysis of alloy G6 (containing 2wt% Ni + 0.25wt% Zr). 183
- Figure 5.7 (a) Optical microstructure at 200X magnification, and (b) backscattered image of the G6 (2wt% Ni + 0.25wt% Zr) alloy sample, obtained from the thermal analysis casting (cooling rate 0.35°C/s), showing different phases present in the alloy. 184
- Figure 5.8 (a) Backscattered electron image of G6 alloy (2wt% Ni + 0.25wt% Zr), showing the different intermetallic phases observed, and (b) through (e) corresponding X-ray images of Fe, Mg, Ni and Zr, respectively. 185
- Figure 5.9 EDS spectrum corresponding to $AlSiNiZrFe$ phase observed in Figure 5.8(a). 186

Figure 5.10 Temperature-time plot and first derivative from the thermal analysis of alloy G7 (containing 2wt% Ni + 0.25wt% Zr, but no Cu).	188
Figure 5.11 (a) Optical microstructure at 200X magnification and (b) backscattered electron image of the G7 (2wt% Ni + 0.25wt% Zr, but no Cu) alloy sample, obtained from the thermal analysis casting (cooling rate 0.35°C/s), showing the different phases present in the alloy.	189
Figure 5.12 (a) High-magnification backscattered electron image of alloy G7, showing different phases; (b) and (c) corresponding X-ray images of Si and Zr.	190
Figure 5.13 Temperature-time plot and first derivative from the thermal analysis of alloy G8 (containing 0.75wt% Mn + 0.25wt% Zr).	192
Figure 5.14 (a) Optical microstructure at 200X magnification and (b) backscattered electron image of the G8 (0.75wt% Mn + 0.25wt% Zr) alloy sample, obtained from the thermal analysis casting (cooling rate 0.35°C/s), showing different phases present in the alloy.	194
Figure 5.15 (a) Backscattered electron image of the G8 alloy (0.75wt% Mn + 0.25wt% Zr) sample showing the $(Al,Si)_3(Zr,Ti)$ phase; (b) through (e) corresponding X-ray images of Al, Si, Ti, and Zr.	195
Figure 5.16 EDS spectrum corresponding to $(Al,Si)_3(Zr,Ti)$ phase observed in Figure 5.15(a).	196
Figure 5.17 Temperature-time plot and first derivative from the thermal analysis of alloy G9 (containing 2wt% Ni + 0.75wt% Mn + 0.25wt% Zr).	198
Figure 5.18 (a) Optical microstructure at 200X magnification and (b) backscattered electron image of the G9 (2wt% Ni + 0.75wt% Mn + 0.25wt% Zr) alloy sample, obtained from the thermal analysis casting (cooling rate 0.35°C/s), showing the different phases present in the alloy.	199
Figure 5.19 (a) High-magnification backscattered electron image of the G9 alloy sample, showing Al_3CuNi and Ni-rich Al_3Ni phase; (b) and (c) corresponding X-ray images of Cu and Ni.	200
Figure 5.20 EDS spectra corresponding to (a) Al_3CuNi and (b) $(Al,Si)_2(Ti,Zr)$ phases listed in Table 5.9. See also Figure 5.19(a).	201
Figure 5.21 Temperature-time plot and first derivative from the thermal analysis of alloy G10 (containing 0.15wt% Sc + 0.25wt% Zr).	203
Figure 5.22 (a) Optical microstructure at 200X magnification and (b) backscattered image of the G10 (0.15wt% Sc + 0.25wt% Zr) alloy sample, obtained from the thermal analysis casting (cooling rate 0.35°C/s), showing the different phases present in the alloy.	204

Figure 5.23 Backscattered electron image and corresponding X-ray images of Al, Sc, Si, Ti and Zr showing the distribution of these elements in (a) AlSiScTiZr, and (b) Si(ScZrTi) phase particles in G10 alloy sample.	207
Figure 5.24 EDS spectra corresponding to (a) (Al,Si) ₂ (Zr,Ti) and (b) Si(Sc,Zr) phases observed in Figure 5.23(a) and Figure 5.23(b).	208
Figure 5.25 Optical micrographs at 500X showing the effect of solution heat treatment at 500°C on Si morphology in G1 base alloy for (a) 0 h and (b) 8 h solution treatment times.	214
Figure 5.26 Optical micrographs at 500X showing the effect of solution heat treatment at 500°C on Si morphology in alloy G6 (containing 2wt% Ni + 0.25wt% Zr) for (a) 0 h and (b) 8 h solution treatment times.	215
Figure 5.27 Optical micrographs at 500X showing the effect of solution heat treatment at 540°C on Si morphology in alloy G7 (containing 2wt% Ni + 0.25wt% Zr, but no Cu) for (a) 0 h and (b) 8 h solution treatment times.	216
Figure 5.28 Optical micrographs at 500X showing the effect of solution heat treatment at 500°C on Si morphology in alloy G8 (containing 0.75wt% Mn + 0.25wt% Zr) for (a) 0 h and (b) 8 h solution treatment times.	217
Figure 5.29 Optical micrographs at 500X showing the effect of solution heat treatment at 500°C on Si morphology in alloy G9 (containing 2wt% Ni + 0.75wt% Mn + 0.25wt% Zr) for (a) 0 h and (b) 8 h solution treatment times.	218
Figure 5.30 Optical micrographs at 500X showing the effect of solution heat treatment at 500°C on Si morphology in alloy G10 (containing 0.15wt% Sc + 0.25wt% Zr) for (a) 0 h and (b) 8 h solution treatment times.	219
Figure 5.31 Model of granulation of unmodified eutectic Si during heat treatment. (a) transport of Si with the cooperation of Al begins; (b) transport continues after fragmentation; and (c) eutectic Si becomes spheroidized. ²⁶⁶	221
Figure 5.32 Backscattered electron images of G1 base alloy samples: (a) as-cast, and (b) after solution heat treatment.	230
Figure 5.33 Backscattered electron images of G6 (2wt% Ni + 0.25wt% Zr) alloy samples: (a) as-cast, and (b) after solution heat treatment.	230
Figure 5.34 Backscattered electron images of G7 (2wt% Ni + 0.25wt% Zr, no Cu) alloy samples: (a) as-cast, and (b) after solution heat treatment.	230
Figure 5.35 Backscattered electron images of G8 (0.75wt% Mn + 0.25wt% Zr) alloy samples: (a) as-cast, and (b) after solution heat treatment.	231
Figure 5.36 Backscattered electron images of G9 (2wt% Ni + 0.75wt% Mn + 0.25wt% Zr) alloy samples: (a) as-cast, and (b) after solution heat treatment.	231

Figure 5.37 Backscattered electron images of G10 (0.15wt% Sc + 0.25wt% Zr) alloy samples: (a) as-cast, and (b) after solution heat treatment. 231

Chapter 5 - Stage II Alloys - Part II

Figure 5.38 Variation in ultimate tensile strength (MPa), yield strength (MPa), and percent elongation to fracture (%El) for as-cast and solution heat-treated samples. ... 242

Figure 5.39 Quality chart generated using Equations 1 and 2, showing the influence of different additions on the tensile properties and the quality indices (Q) of test bars in the as-cast (blue) and solution heat-treated (red) conditions..... 245

Figure 5.40 Variation in UTS (MPa), YS (MPa), and %El observed in base alloy G1 as a function of aging conditions. 250

Figure 5.41 Quality chart generated using Equations 1 and 2 showing the tensile properties and the quality indices (Q) of G1 base alloy test bars in the as-cast, solution heat-treated, and aged conditions (five aging temperatures used and aging times of 2, 10, and 100 hours)..... 254

Figure 5.42 Variation in UTS (MPa), YS (MPa), and %El observed in alloy G6 (2wt% Ni + 0.25wt% Zr) as a function of aging conditions..... 257

Figure 5.43 Quality chart generated using Equations 1 and 2 showing the tensile properties and the quality indices (Q) of G6 (2wt% Ni + 0.25wt% Zr) alloy test bars in the as-cast, solution heat-treated, and aged conditions (at the five aging temperatures used and aging times of 2, 10, and 100 hours)..... 259

Figure 5.44 Yield strength-color contour charts for the base alloy G1 and alloy G6 (2wt% Ni + 0.25wt% Zr), comparing the effect of aging conditions..... 261

Figure 5.45 Variation in UTS (MPa), YS (MPa), and %El observed in alloy G7 (2wt% Ni + 0.25wt% Zr, no Cu) as a function of aging conditions. 263

Figure 5.46 Quality chart generated using Equations 1 and 2 showing the tensile properties and the quality indices (Q) of G7 (2wt% Ni + 0.25wt% Zr, no Cu) alloy test bars in the as-cast, solution heat-treated, and aged conditions (at the five aging temperatures used and aging times of 2, 10, and 100 hours)..... 265

Figure 5.47 Yield strength-color contour charts for alloys G1, G6 (2wt% Ni + 0.25wt% Zr), and G7 (2wt% Ni + 0.25wt% Zr, no Cu) comparing the effect of aging conditions..... 268

Figure 5.48 Variation in UTS (MPa), YS (MPa), and %El observed in alloy G8 (0.75wt% Mn + 0.25wt% Zr) as a function of aging conditions. 270

Figure 5.49 Quality chart generated using Equations 1 and 2 showing the tensile properties and the quality indices (Q) of G8 (0.75wt% Mn + 0.25wt% Zr) alloy test bars in

the as-cast, solution heat-treated, and aged conditions (at the five aging temperatures used and aging times of 2, 10, and 100 hours).....	273
Figure 5.50 Yield strength-color contour charts for the base alloy G1 and alloy G8 (0.75wt% Mn + 0.25wt% Zr), comparing the effect of aging conditions.	274
Figure 5.51 Variation in UTS (MPa), YS (MPa), and %El observed in alloy G9 (2wt% Ni + 0.75wt% Mn + 0.25wt% Zr) as a function of aging conditions.....	276
Figure 5.52 Quality chart generated using Equations 1 and 2 showing the tensile properties and the quality indices (Q) of G9 alloy test bars in the as-cast, solution heat-treated and aged conditions (at the five aging temperatures used and aging times of 2, 10, and 100 hours).	279
Figure 5.53 Yield strength-color contour charts for alloys (a) G1; (b) G6; (c) G8; and (d) G9 comparing the effect of aging conditions.	282
Figure 5.54 Variation in UTS (MPa), YS (MPa), and %El observed in alloy G10 (0.15wt% Sc + 0.25wt% Zr) as a function of aging conditions.....	284
Figure 5.55 Quality chart generated using Equations 1 and 2 showing the tensile properties and the quality indices (Q) of G10 (0.15wt% Sc + 0.25wt% Zr) alloy test bars in the as-cast, solution heat-treated and aged conditions (at the five aging temperatures used and aging times of 2, 10, and 100 hours).....	286
Figure 5.56 Yield strength-color contour charts for the base alloy G1 and alloy G10, comparing the effect of aging conditions.	288
Figure 5.57 Quality chart generated using Equations 1 and 2 to compare the strength and quality of the alloys studied, after aging treatment at 155°C for aging times of 2, 10, and 100 hours.	293
Figure 5.58 Quality chart generated using Equations 1 and 2 to compare the strength and quality of the alloys studied, after aging treatment at 190°C for aging times of 2, 10, and 100 hours.	293
Figure 5.59 Quality chart generated using Equations 1 and 2 to compare the strength and quality of the alloys studied, after aging treatment at 240°C for aging times of 2, 10, and 100 hours.	294
Figure 5.60 Quality chart generated using Equations 1 and 2 to compare the strength and quality of the alloys studied, after aging treatment at 300°C for aging times of 2, 10, and 100 hours.	294
Figure 5.61 Quality chart generated using Equations 1 and 2 to compare the strength and quality of the alloys studied, after aging treatment at 350°C for aging times of 2, 10, and 100 hours.	295
Figure 5.62 Comparison of tensile properties of G6, G7, G8, G9, G10 alloys relative to those of G1 alloy: (a) UTS, (b) YS, and (c) %El at 155°C and 350°C.	299

Figure 5.63 UTS vs. %El relationship for heat-treated 354 alloys, depicting the peak-, under-, and over-aged regions within the heat treatment conditions used in this study. 300

LIST OF TABLES

Chapter 2

Table 2.1	Composition of common aluminum-silicon casting alloys ¹⁶	13
Table 2.2	Casting characteristics of aluminum-silicon alloys ¹⁶	14
Table 2.3	Chemical composition limits of 354-type casting alloys ^{28, 31, 47}	17
Table 2.4	Minimum mechanical properties for casting alloy 354-T6 at room temperature ¹⁹	17
Table 2.5	Summary of elevated-temperature fracture behavior ¹⁹²	67

Chapter 3

Table 3.1	Chemical composition of the 354 alloys used in this study (wt%)	82
Table 3.2	Conditions used for high temperature tensile testing for Stage I alloys with low Ni content	83
Table 3.3	Conditions used for room temperature tensile testing for Stage II alloys with high Ni content.....	84

Chapter 4 - Stage I Alloys

Table 4.1	Volume fraction (%) of undissolved phases observed in the matrix of as-cast alloys G1 through G5 used for this research ¹⁹	99
-----------	---	----

Chapter 5 - Stage II Alloys - Part I

Table 5.1	Chemical composition of the alloys used in in this part of the study (wt%)... ..	168
Table 5.2	Silicon particle measurements for the alloys studied using a graphite mold ..	169
Table 5.3	Volume fraction of undissolved phases observed in the matrix of alloys G1, and G6 through G10 used for this part of the study	171
Table 5.4	Proposed main reactions occurring during solidification of alloys G1, G6 through G10 ^{19, 30, 36, 126, 261}	174
Table 5.5	WDS analysis of phases observed in base alloy G1	178
Table 5.6	WDS analysis of phases observed in alloy G6	186
Table 5.7	WDS analysis of phases observed in alloy G7	191

Table 5.8	WDS analysis of phases observed in alloy G8	196
Table 5.9	WDS analysis of phases observed in alloy G9	202
Table 5.10	WDS analysis of phases observed in alloy G10	208

Chapter 5 - Stage II Alloys - Part II

Table 5.11	Silicon particle characteristics for alloy G1 and G6 through G10.....	213
Table 5.12	Volume fraction of undissolved phases observed in the matrix of alloys G1, and G6 through G10 in the as-cast (AC) and solution heat-treated (SHT) conditions	223
Table 5.13	Average SDAS measured for the alloys G1 and G6 through G10 (samples were obtained from the tensile test bars samples)	225
Table 5.14	Mean values of UTS, YS, %El obtained for alloy studied in the as-cast and solution heat-treated conditions, Q values obtained with Equation 1	241
Table 5.15	Mean values of UTS, YS, %El obtained for base alloy G1 subjected to different heat treatment conditions, Q values obtained with Equation 1	253
Table 5.16	Age-Hardening Behavior of Al-Si-Cu-Mg alloys ²³⁷	291

CHAPTER 1

DEFINING THE PROBLEM

CHAPTER 1

DEFINING THE PROBLEM

1.1 INTRODUCTION

Aluminum-Silicon (Al-Si) casting alloys are characterized by their high strength-to-weight ratio and excellent ductility, and show great promise for several fields of engineering applications thus making them suitable for automotive, marine, and aerospace applications where, by means of the smelting of the metal and the carrying out of suitable heat treatments, the manufacturing of cylinder heads, engine blocks, pistons, intake manifolds, and other parts is made possible.¹⁻³ Al-Si alloys are heat-treatable, *i.e.* their mechanical properties may be improved considerably following an appropriate heat treatment comprising solution heat treatment, quenching, and natural or artificial aging. Developments in aluminum alloys and optimization of casting techniques have led to improved material properties and functional integration which enable aluminum castings to satisfy the new market requirements and have allowed replacing, in many cases, engine components made from heavy cast iron alloys.⁴

In recent years, the development of diesel and direct fuel injection gasoline engines with high specific powers have resulted in a marked performance impact on piston materials due to increased combustion pressure and piston temperatures.⁵ The automotive industry, based on the continued usage of traditional fuels such as oil or gasoline, is focused on reducing fuel consumption; consequently, lower emission may be achieved either by significantly improving the efficiency of the car engine or by bringing about a sizeable reduction in total car weight. Recent work on mass decompounding for internal combustion (IC) vehicles has quantified how additional secondary mass reductions can further increase fuel economy.⁶⁻⁸ Reductions in the weight of key engine components together with higher service temperatures seems to allow for more efficient operation than hitherto. Reducing the mass of a vehicle by 10% can increase fuel economy by up to 8%.⁹

The 354-type Al-Si-Cu-Mg (Al-9wt%Si-1.8wt%Cu-0.5wt%Mg) hypoeutectic casting alloys displaying superior strength-to-weight ratio (which leads to reducing fuel consumption and improving mechanical performance) and hardness values after the application of suitable heat treatment procedures as a result of the presence of hardening elements, namely, copper, magnesium and silicon. The high 9% Si-content of 354 alloys enhances castability, reduces shrinkage and improves both strength and ductility.

Aluminum-silicon cast components are generally limited to service conditions of no more than 230°C.^{10, 11} For certain automotive components, however, operating conditions can vary over a wide range of temperatures and stress conditions, with temperatures going much higher than 230°C.¹² Improving the high temperature mechanical properties in an

aluminum alloy requires an understanding of the factors which are related principally to a decrease in the strength of the metal with increasing temperature.

Magnesium (Mg) and/or copper (Cu) are the most common strengthening elements added to Al-Si casting alloys, for the purposes of improving the strength and hardness of these alloys, specifically, after applying the appropriate heat treatments.¹³⁻¹⁸ The use of nickel (Ni) and zirconium (Zr) as additions to increase high temperature strength in aluminum alloys is based on the production of the precipitates L1₂-type Al₃Zr or Al₃Ni, which are better able to support overaging at higher temperatures than the precipitates normally present in cast aluminum alloys, namely Al₂Cu and Mg₂Si.^{19, 20} Manganese (Mn) is a common alloying addition, and has a very limited solubility in aluminum. It is used to neutralize the effect of iron (Fe) and to modify the morphology and type of intermetallic phases formed. Small amounts of Mn play a positive role in combining with Fe to form the Chinese-script α -Fe intermetallic phase instead of the platelet-like β -Fe phase, which is detrimental to the mechanical properties of the alloy.

Transition elements are usually added to aluminum wrought alloys and a number of aluminum casting alloys in order to alter their microstructure and thus improve their mechanical properties.^{21, 22} Scandium (Sc) in aluminum alloys acts as an effective grain refiner and increases the recrystallization temperature, the corrosion resistance, and weldability, as well as reduces the hot cracking susceptibility of the alloys. The presence of fine coherent L1₂-type precipitates of Al₃Sc inhibits the migration of dislocations and increases the recovery temperature by stabilizing the substructure. The presence of other

coherent and semi-coherent $L1_2$ -type precipitates or dispersoids as Al_3Ni and Al_3Zr which are essentially inert in the matrix, similarly affects the strength of the material directly because they act as hard pinning points in the matrix, inhibiting dislocation motion. The main advantage of the formation of such precipitates is their stability at elevated temperatures; because of the low solubility of these finely dispersed second phase particles, these alloys can resist over aging and growth, thereby preserving their mechanical properties to a greater extent.^{19, 20}

An extensive study was carried out to investigate the effects of Ni, Mn, Zr, and Sc additions individually or in combination with other additives, on the microstructure and tensile properties at ambient and high temperature of 354-type alloy. Quality charts were used as an evaluation tool for selecting the optimum conditions to be applied in practice in order to develop superior tensile properties and optimum quality in 354 casting alloys. The right alloy quality in engineering applications involves reaching a suitable compromise between numerous factors so as to present the least possible risk and maximum performance combined with cost efficiency. Alloy composition, solidification rate, and heat treatment procedures are all parameters which closely affect alloy quality since they also influence the tensile properties of the casting. In the present study, the tensile test data at room temperature will be presented in the form of quality charts, which provide an accurate tool for evaluating the tensile properties and the quality of the 354-type castings under the various metallurgical conditions applied to these castings.

1.2 OBJECTIVES

The principal aim of the present research study was to investigate the effects of Ni (low and high contents), Mn, Zr and Sc additions on the strength of cast aluminum alloy 354 (Al-9wt%Si-1.8wt%Cu-0.5wt%Mg) at room and at high temperature, for different holding times. The effects of individual and combined additions of these elements on the mechanical properties, microstructural features, as well possible interactive effects were also investigated. The main objectives of the study therefore covered:

1. Investigating the influence of the following metallurgical variables on the tensile properties and the quality index values of 354 alloys:
 - i. Nickel (Ni) content;
 - ii. Manganese (Mn) content;
 - iii. Zirconium (Zr) content;
 - iv. Scandium (Sc) content;
 - v. Solidification rate;
 - vi. Heat treatment condition:
 - Solution heat treatment; and
 - Aging temperatures and times.
2. Examining the microstructural features of the alloys used to acquire a better understanding of (a) the phases and intermetallics present in the structure, (b) the fracture surface of tested samples, and (c) the precipitates formed, and their identifying characteristics and evolution during controlled exposure at different temperatures and times.

3. Correlating the room and high-temperature mechanical properties with the microstructural features of the corresponding alloy samples, to determine the strengthening parameters involved.
4. Analyzing the alloy quality obtained under various conditions by using suitable proposed quality indices, in order to recommend the optimum metallurgical conditions for improving the properties of 354-type casting alloys used in specific applications.

In order to implement the above mentioned objectives, nine melts were prepared from the 354-base alloy composition used in this study. These nine alloys were divided into two stages. Accordingly, Stage I alloys comprised the 354-base alloy and four other alloy compositions containing additions of Ni (low content) and Zr, which were tested at room temperature (as-cast and T6-treated conditions) and at high temperature (155°C and 300°C).

Stage II alloys involved the 354 base alloy and four alloys containing Ni, Mn, Sc, Zr, added individually or in combination, and one alloy containing no copper. Testing of these alloys was carried out at room temperature using the alloys in the as-cast, solution heat-treated, and aged conditions employing different aging temperatures and times.

1.3 THESIS LAYOUT

The research associated with this thesis is presented in five chapters. Chapter 1 of the thesis defines the motivation for undertaking this study and its objectives. Chapter 2 provides a detailed overview of the literature pertaining to the main aspects of the study. Experimental procedures and testing methods are given in Chapter 3. Analysis and discussion of experimental data results confirmed by Quality Index analysis are provided in Chapters 4 and 5, with a section on conclusions at the end of each chapter. Finally, recommendations for future work and references are provided at the end of the thesis.

CHAPTER 2
LITERATURE SURVEY

CHAPTER 2

LITERATURE SURVEY

2.1 INTRODUCTION

The use of aluminum and its alloys has increased significantly over the past several years in numerous applications, successfully replacing iron and steel. Furthermore, aluminum alloys become highly resistant after undergoing heat treatment, and are easy to cast. The principal areas in which aluminum has increased in importance are the automotive and aerospace industries, where by means of the smelting of the metal and the carrying out of suitable heat treatments, the manufacturing of cylinder heads, engine blocks, pistons, intake manifolds, and other parts is made possible.¹⁻³ In recent years, the development of diesel and direct fuel injection gasoline engines with high specific powers have resulted in a marked performance impact on piston materials due to increased combustion pressure and piston temperatures.^{10, 11} The reduction in fuel consumption is considered to be not only a decisive economical factor but also a significant environmental advantage obtainable via the associated reduction in the production of exhaust gases.²³⁻²⁵

With the intention of reducing vehicle weight in the automotive industry, several iron-based components are in the process of being replaced with lightweight parts made of aluminum-based alloys since the density of aluminum is one-third that of steel.^{17, 18} The proposed assets of using aluminum in auto body parts may be listed as: 10% fuel economy improvement, as safe as steel, improved vehicle performance, cost-effective vs. other fuel saving technologies, lower life-cycle CO₂ than steel, and compatibility with existing stamping assets. Figure 2.1 indicates the growing trend (sheet and extrusions for body and closures) over a 50-year period, of incorporating aluminum alloys in the automotive industry, where for the year 2015, aluminum shares 400 lbs. per vehicle, an amount which is expected to increase up to 547 lbs. for 2025.^{17, 24-26}

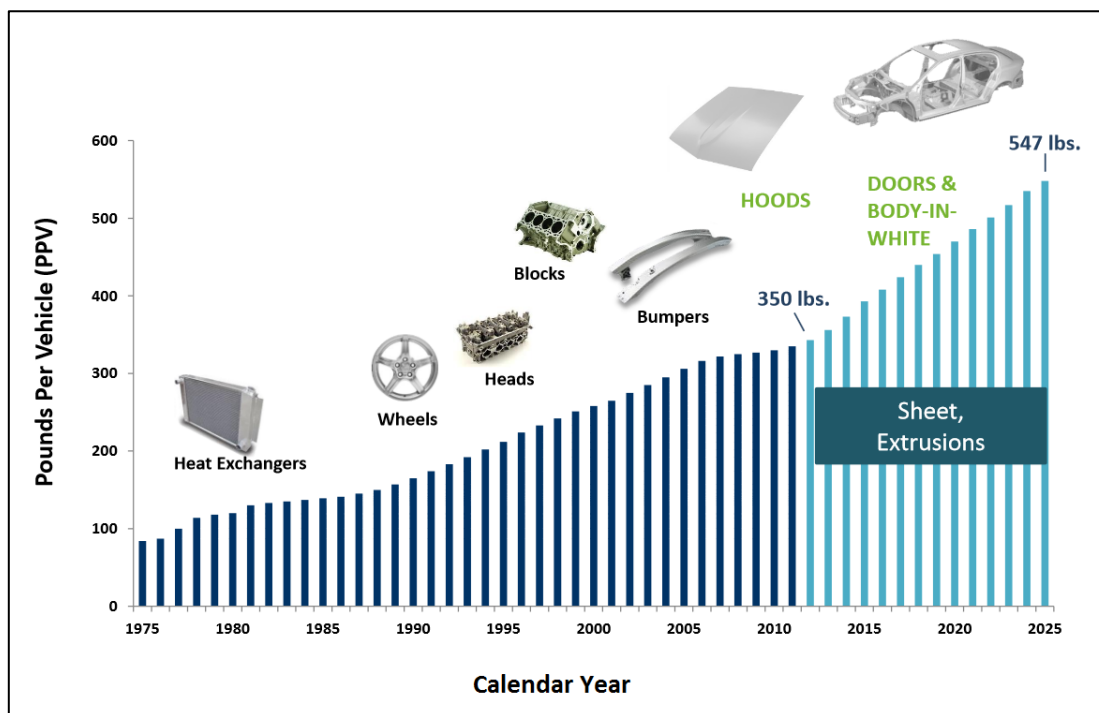


Figure 2.1 The growing trend of fifty years of uninterrupted aluminum alloys for North American manufactured light vehicles.²⁴⁻²⁶

The properties of aluminum casting alloys can be improved through the appropriate control of several metallurgical factors involved in the production of these castings. Pure aluminum has low tensile strength but can easily be alloyed with other elements, for example, copper, zinc, magnesium, manganese, and silicon (*i.e.* duralumin), to make aluminum alloys which are the materials mostly used in industry. Only a few of them are used as major alloying elements in commercial aluminum-based alloys; others are used as supplements to alloying additions for the improvement of alloy properties and characteristics. The effects of these alloying additives on the properties of aluminum depend on the individual elements and the specific amounts added, as well as on their interaction with aluminum and with each other. While these additions are primarily used for strengthening, other elements are used to obtain specific microstructural characteristics which may include a finer grain size, higher critical recrystallization temperatures, or else to block the harmful effects of certain impurities. The alloying elements in aluminum alloys may be present in the form of solid solution, dispersoids, precipitates within the grain, or intermetallic compounds at the grain boundaries.

2.2 ALUMINUM-SILICON CASTING ALLOYS

Aluminum alloys with silicon as the main alloying element are the most important category of alloys used in the casting process, where the use of silicon in aluminum offers excellent properties such as castability, good weldability, good thermal conductivity, excellent corrosion resistance and good retention of physical and mechanical properties at elevated temperatures.¹⁶ The addition of silicon as a dominant alloying element produces

castings with physical and mechanical properties which are of great pertinence to industrial requirements. Aluminum-silicon (Al-Si) alloys experience an increase in mechanical resistance with the addition of copper, magnesium or nickel and by applying adequate heat treatments. These characteristics of Al-Si castings are the main reason for their acknowledged versatility in several fields of industrial application where Al-Si cast parts form as much as 85-90% of the total of cast aluminum pieces produced.^{17, 28-35} Table 2.1 summarizes the most common aluminum casting alloys and their principal elements.¹⁶ The relative casting characteristics achieved through these compositions are listed in Table 2.2.¹⁶

Table 2.1 Composition of common aluminum-silicon casting alloys¹⁶

Alloy	Elements (wt.%)						
	Method	Si	Cu	Mg	Fe	Zn	Others
319.0	S,P	6.0	3.5	<0.1	<1.0	<1.0	-
332.0	P	9.5	3.0	1.0	1.2	1.0	-
355.0	S,P	5.0	1.25	0.5	<0.06	<0.35	-
A356.0	S,P	7.0	<0.2	0.35	<0.2	<0.1	-
A357.0	S,P	7.0	<0.2	0.55	<0.2	<0.1	0.05 Be
380.0	D	8.5	3.5	<0.1	<1.3	<3.0	-
383.0	D	10.0	2.5	0.1	1.3	3.0	0.15Sn
384.0	D	11.0	2.0	<0.3	<1.3	<3.0	-
390.0	D	17.0	4.5	0.55	<1.3	<0.1	0.35 Sn
413.0	D	12.0	<0.1	<0.1	<2.0	-	<0.10 Mg
443.0	S,P	5.25	<0.3	<0.05	<0.8	<0.5	-

- (a) Remainder: Aluminum and other impurities
 (b) S: Sand casting; P: Permanent mold casting;
 D: High pressure die casting

Table 2.2 Casting characteristics of aluminum-silicon alloys ¹⁶

Alloy	Casting method	Resistance to tearing	Pressure tightness	Fluidity tendency	Shrinkage
319.0	S,P	2	2	2	2
332.0	P	1	2	1	2
355.0	S,P	1	1	1	1
A356.0	S,P	1	1	1	1
A357.0	S,P	1	1	1	1
380.0	D	2	2	2	-
390.0	D	2	2	2	-
413.0	D	1	1	1	-
443.0	P	1	1	2	1

Ratings: 1, best; 5, worst.

Commercial alloys of this type represent the full range of compositions, including hypoeutectic (5-10% Si), eutectic (11-13% Si) and hypereutectic (14-20% Si), as shown in Figure 2.2(a). Thus, in accordance with the level of silicon present, the microstructural features of each group differ from one another. Consequently, the mechanical properties of these groups of alloys/castings are directly related to the specific features of the microstructure in each case. The main feature of Al-Si casting alloys is that a eutectic is formed between aluminum and silicon at a Si content of 11.5-12%.

In hypoeutectic alloys, the α -Al precipitates in the form of a dendritic network, followed by the precipitation of eutectic Al-Si in the interdendritic regions, as will be observed in Figure 2.2(b). In the case of eutectic alloys, the entire cast structure consists mainly of an Al-Si eutectic structure, as may be seen in Figure 2.2(c). Hypereutectic alloys are characterized by the precipitation of primary silicon cuboids followed by the solidification of the eutectic structure, as shown in Figure 2.2(d).^{36, 37} Hypoeutectic and

eutectic Al-Si casting alloys are the types most commonly used in industrial applications,³⁸ whereas hypereutectic alloys are used principally for high wear resistance applications.³⁹⁻⁴³

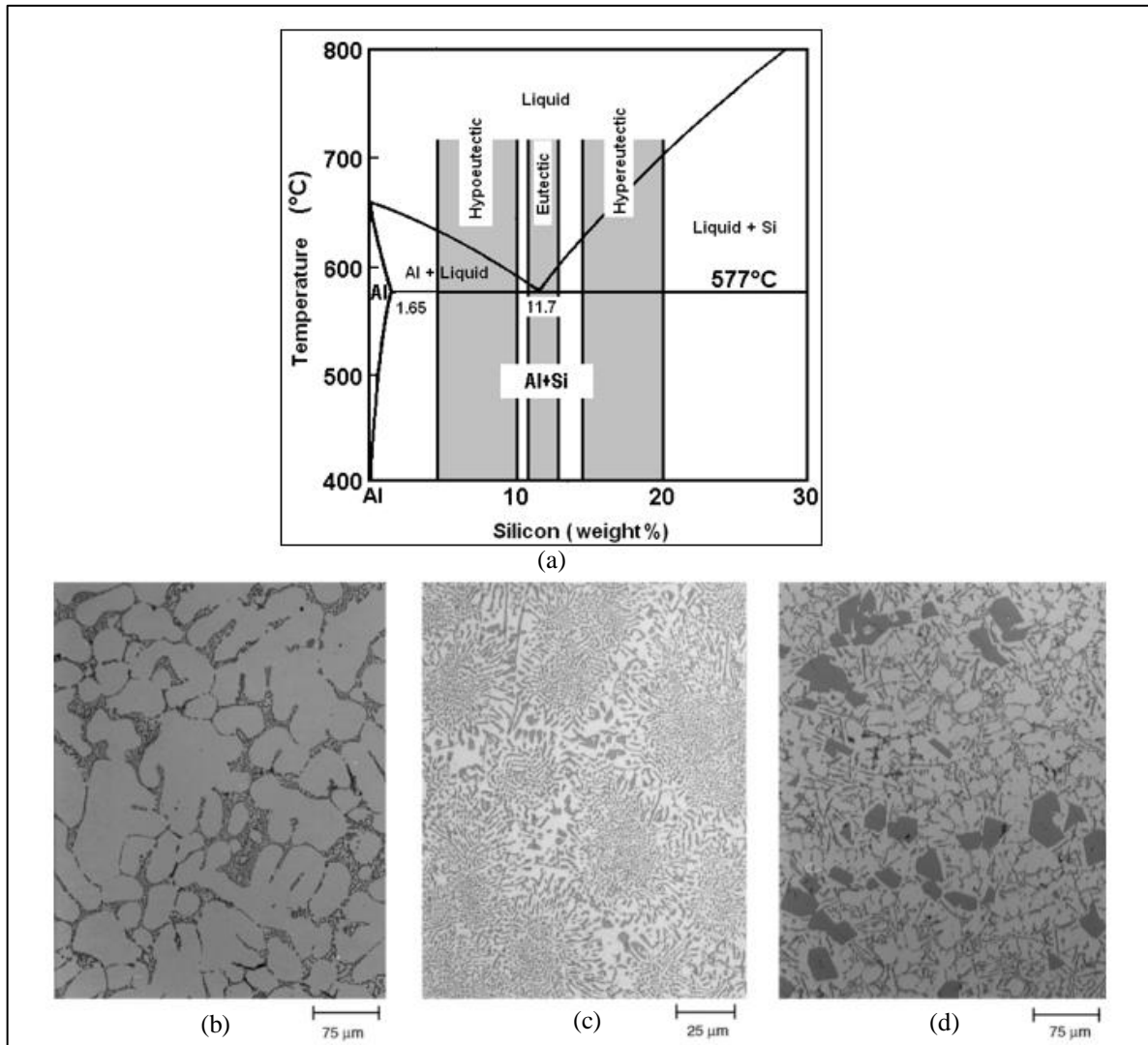


Figure 2.2 Al-Si casting alloys: (a) Al-Si phase diagram; (b) microstructure of hypoeutectic alloy; (c) microstructure of eutectic alloy; and (d) microstructure of hypereutectic alloy.³⁷

With regard to this type of alloy, it is necessary to control a series of parameters which have a direct effect on alloy properties. As mentioned before, these variables are related to the microstructure and depend as much on the alloy composition as on the casting process used. These include: (a) dendrite arm spacing (DAS), (b) level of modification of eutectic silicon, (c) grain size, and (d) gas porosity and shrinkage.

2.2.1 354 – Al-Si-Cu-Mg ALLOY SYSTEM

From Figure 2.2, it may be seen that the solidification process of Al-Si hypoeutectic alloys includes the formation of the α -Al dendritic network and the Al-Si eutectic reaction to produce the Al-Si eutectic.³² Aluminum-silicon alloys containing copper and magnesium such as the permanent mold-cast 354-type alloys show a greater response to heat treatment as a result of the presence of both Mg and Cu. Within Al-Si alloys, Al-Si-Mg, Al-Si-Cu, and Al-Si-Cu-Mg are the three major alloy systems in the 3xx series, of which A356, A319, and B319 are typical examples. The main function of Mg and Cu is to form the Mg_2Si and Al_2Cu hardening precipitates.

Addition of Cu leads to a slight increase in alloy fluidity, and a depression in the Si eutectic temperature of $\sim 1.8^\circ C$ for every 1wt% Cu added. Also, a number of the mechanical properties, including YS and UTS, obviously benefit from the addition of Cu as an alloying element.¹⁴ The presence of magnesium improves strain hardenability, while also enhancing the material strength by solid solution.⁴⁴ At $\sim 548^\circ C$, the amount of Cu in solid solution in Al is known to be about 5.7%; this value decreases with decreasing temperatures, reaching 0.1-0.2% at $250^\circ C$.³⁰ Copper forms an intermetallic phase with Al

which precipitates during solidification either as block-like CuAl_2 or in its eutectic form as $(\text{Al} + \text{CuAl}_2)$. In the 319 alloys, the copper intermetallic phase precipitates in both of these forms.⁴⁵ At the same time, because of the presence of certain impurity elements such as Fe and Mn, intermetallic phases also precipitate during solidification.

Al-Si-Cu-Mg alloy types display excellent strength and hardness values although at some sacrifice to ductility and corrosion resistance. While the properties in the as-cast condition are acceptable for certain applications, the alloys are typically heat-treated for optimal properties. These alloys may then be used for a wide range of applications, including engine cooling fans, crankcases, high speed rotating parts (*e.g.* fans and impellers), structural aerospace components, air compressor pistons, fuel pumps, compressor cases, timing gears, rocker arms, machine parts, and so forth.^{31, 47} Table 2.3 shows the chemical composition limits of this alloy while Table 2.4 list its tensile properties at room temperature.

Table 2.3 Chemical composition limits of 354-type casting alloys^{28, 31, 47}

Alloy	Elements (wt%)								
	Si	Cu	Mg	Fe	Mn	Zn	Ti	Others	Al
354	8.6-9.5	1.6-2	0.4-0.6	0.2 max	0.1 max	0.1 max	0.2 max	0.15	Bal.

Table 2.4 Minimum mechanical properties for casting alloy 354-T6 at room temperature¹⁹

UTS (MPa)	Tensile YS (MPa)	Elongation (%)	Compressive YS (MPa)
296	227	2	227

The mechanical properties of Al-Si casting alloys are related directly to various metallurgical parameters involved in production procedures. The quality of Al-Si castings may be expressed in terms of their mechanical properties, via a concept known as “quality index.” Several quality indices have been proposed in the literature with the intention of evaluating the quality of Al-Si castings as a function of their mechanical properties.

Another important group of alloys in the Al-Si system are Al-Si-Mg alloys, such as the 356 alloy, which are hardened by Mg_2Si precipitation. Magnesium is the basis for strength and hardness development in heat-treated Al-Si alloys. In the heat-treated condition, the hardening phase Mg_2Si has a solubility limit corresponding to approximately 0.7% Mg.^{48, 49} At room temperature, quantities of magnesium exceeding 0.3% Mg will be present as Mg_2Si . An increase of magnesium, within the alloy range, results in increased strength at the expense of ductility and has a beneficial effect on corrosion resistance. With regard to these alloys, iron is considered an impurity originating in the process of mining aluminum from the ore. It often appears in the form of AlFeSi intermetallics at the grain boundaries, causing a severe loss of ductility in the alloy; strength may also be noticeably affected. As a result, the iron-content is kept significantly low in premium quality alloys which are used for aircraft and aerospace castings requiring high-grade quality and properties. Copper decreases the sensitivity of the alloy to quench rates but increases the strain-hardening effect as well as the strength in the T6 temper. Additions of manganese, chromium, and zirconium inhibit recrystallization during solution treatment. Manganese increases creep and fatigue resistance, converts the crystallization of needle-like intermetallic phases to cubic or globular forms, such as Chinese-script, which have less

harmful characteristics. This type of morphology improves tensile strength and ductility.^{31,}

50, 51

2.2.2 MELT TREATMENT OF EUTECTIC Al-Si ALLOYS

Melt treatments such as eutectic modification and grain refinement are frequently applied to Al-Si alloys which goes far to explain why the effects of these processes on the microstructure and mechanical properties of Al-Si alloys have attracted so much attention. The microstructure, and hence the mechanical properties of the Al-Si alloys as well, are likely to be affected by the type of melt treatment applied in that they can be classified as either physical or chemical. A physical melt treatment may be interpreted as the application of rapid cooling rates, thereby transforming the microstructure into a fine eutectic structure, small dendritic arm spacing, and reduced grain size.¹⁹ When a melt is rapidly cooled (chilled), the rate of heat extraction can greatly exceed the rate of heat generated by the freezing process (latent heat of solidification). As a result, the liquid undercools when its temperature falls below the liquidus temperature. If this undercooling is sufficient, the full range of heterogeneous nucleants present in the liquid can become active. This multiple nucleation results in a fine eutectic microstructure.³²

2.2.3 CHEMICAL MODIFICATION IN EUTECTIC Al-Si ALLOYS

The morphology of eutectic silicon, that is to say, particle size and shape, plays an important role in determining the mechanical properties of Si-containing aluminum cast alloys. The silicon particles appear in the form of coarse acicular plates, and they therefore act as internal stress raisers leading to a lowering in the mechanical properties particularly ductility and impact strength.^{52, 53} Changing this morphology, with its deleterious aspect, into a finer and more interconnected fibrous one is known as eutectic modification.^{32, 54-56} Modification of the eutectic silicon phase was discovered about 95 years ago in 1921, when Aladar Pacz found that Al-Si alloy containing between 5% and 15% silicon could be modified by sodium fluoride to yield an improvement in ductility and machinability.^{57, 58} The modified alloy since then has been established commercially.

Chemical modification is the most commonly applied method of modification which produces a fine fibrous silicon structure through the addition of trace levels of certain modifying elements, such as strontium, sodium, and antimony.^{34, 49, 54, 59-61} In North America, it is mainly either sodium or strontium which is used to modify the Al-Si eutectic; strontium is usually introduced directly into the melt in the form of an Al-10 wt% Sr master alloy.^{32, 62, 63}

The amount of Sr necessary to achieve a specific degree of modification depends on the Si level, on the cooling rate, and on the concentration of other minor alloying elements. This modification of Si morphology reduces the stress-raising capacity of the silicon particles and significantly improves the mechanical properties. Hafiz *et al.*⁶⁴ reported that,

for steel mold-cast Al-Si alloys, the UTS improved from 177.2 MPa for the non-modified alloy to 225.6 MPa for the modified one using 240 ppm Sr. In addition, percent elongation increased dramatically from 8.03% in the non-modified state, to 18.2% with 120 ppm, and to 22.2% at a strontium level of 240 ppm. Fat-Halla⁶⁵ also reported that the addition of 200 ppm Sr to Al-13%Si type alloys increase the percentage elongation and the ultimate tensile strength values without significantly changing the yield strength. Kulunk and Zuliani⁶⁶ also studied the effect of strontium on the 380 high-pressure die casting alloy. They showed that the reduction in both size and number of iron intermetallic phase particles through the addition of strontium would lead to an increase in the tolerance of these alloys to higher iron concentrations without altering the mechanical properties.

Unfortunately, eutectic modification has also been associated with undesirable changes in porosity characteristics. Modification causes a redistribution of the porosity, which is sometimes accompanied by an increase in porosity levels. It has been observed that the redistribution of porosity is a fundamental characteristic of modification, whereas the effects of modification on the amount of porosity may depend on the casting design and the casting conditions.^{54, 67, 68} Figure 2.3 shows the effect of modifiers on Si particles. Typical examples of the microstructure of unmodified, Sr-modified alloys are shown in Figure 2.4.

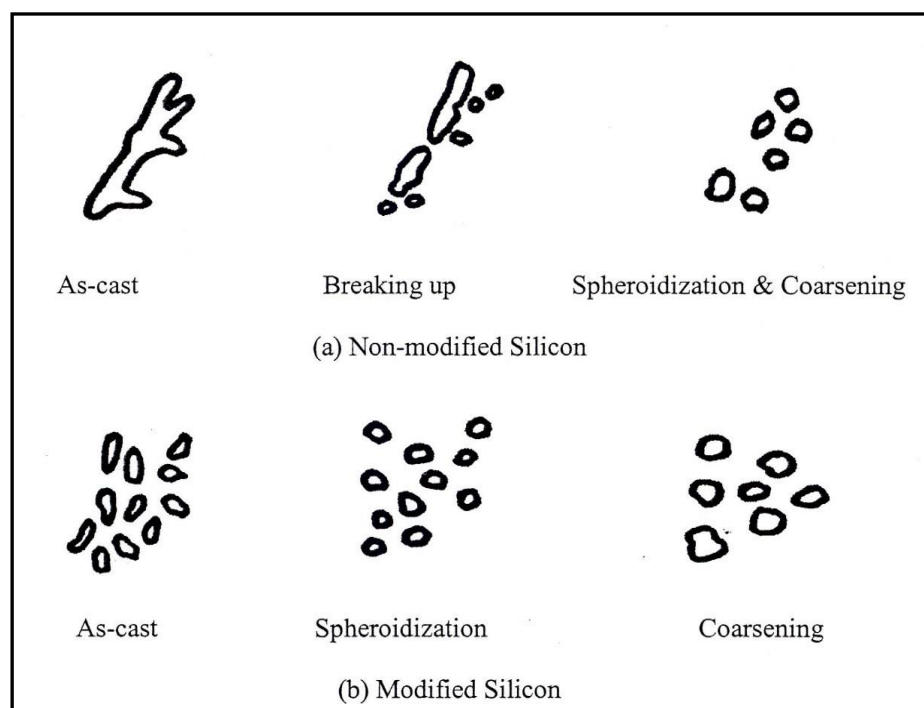


Figure 2.3 Schematic diagram showing behavior of the Si particle during solution heat treatment in the case of: (a) non-modified, and (b) modified Al-Si alloys.⁶⁹

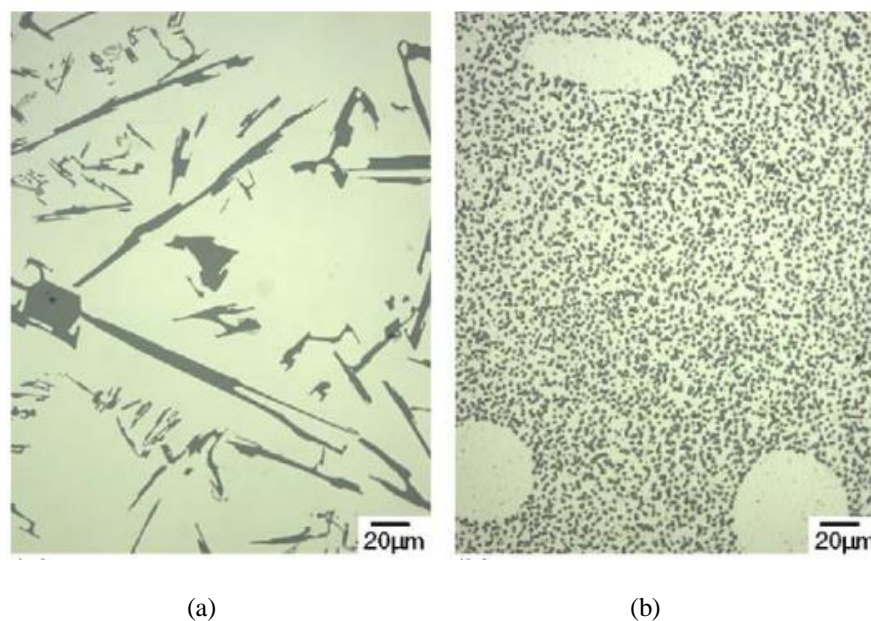


Figure 2.4 Comparison of the silicon morphology in: (a) unmodified and (b) Sr-modified (300 ppm Sr), hypoeutectic aluminum-silicon alloys.⁶¹

Of significant importance to the foundryman in choice of modifier for Al-Si alloys are such characteristics as: (i) ease of handling (reactivity with air, water, and so forth); (ii) ease of dissolution (temperature/time requirements); (iii) recovery (loss of modifier due to evaporation, reactions); and (iv) fading (time before losses become significant). In most applications, strontium is the recommended choice as a eutectic modifier. The ability to use strontium in master alloy form is a significant advantage over sodium for two reasons:

1. The problem of reactivity with air and water is eliminated (in master alloys containing less than 45%Sr).
2. Using master alloys allows the foundryman to weigh out larger quantities of modifier, especially when preparing smaller quantities of melt, as opposed to the case of pure sodium, for instance, thereby making the process easier and allowing accuracy in modifier content.

2.2.4 CHEMICAL GRAIN REFINEMENT IN EUTECTIC Al-Si ALLOYS

The quality of aluminum cast alloys can be improved by grain refining which reduces the size of the primary α -Al grains which would otherwise solidify with a coarse, columnar grain structure. Chemical refining is advantageous to mechanical properties, particularly those which are sensitive to hot-tearing and porosity.^{17, 19} As is the case with modification, grain refinement can be achieved by rapid solidification and/or chemical additives. In most cases, it is not possible to remove the heat content rapidly. Medium to large size castings cannot be significantly refined by means of chilling, and therefore other forms of grain refinement are required.¹⁹

Chemical grain refinement involves the addition of special substrates to act as nucleating agents or to react with other elements in the melt thereby forming solid nucleant particles. A fine grain size is promoted by the presence of an enhanced number of nuclei, with solidification proceeding at minimal undercooling. The best grain refiner is that which possesses the same crystal structure as α -Al and which can be effective in small quantities without harming the melt properties. Generally speaking, Al-Ti, Al-B and Al-Ti-B master alloys are efficient grain refiners for cast aluminum alloys.⁷⁰⁻⁷³

The grain refining power of Al-5%Ti-1%B master alloy appears to be less than that of Al-3%B and Al-3%Ti-3%B master alloys, however, in Al-Si alloys containing high levels of Si. This occurrence may be attributed to the formation of titanium silicide over the surface of TiAl_3 particles in the melt which poisons the nucleating action of the latter reacting with the liquid phase upon cooling to below 665°C according to the peritectic reaction shown in Figure 2.5.^{19, 54, 74, 75}

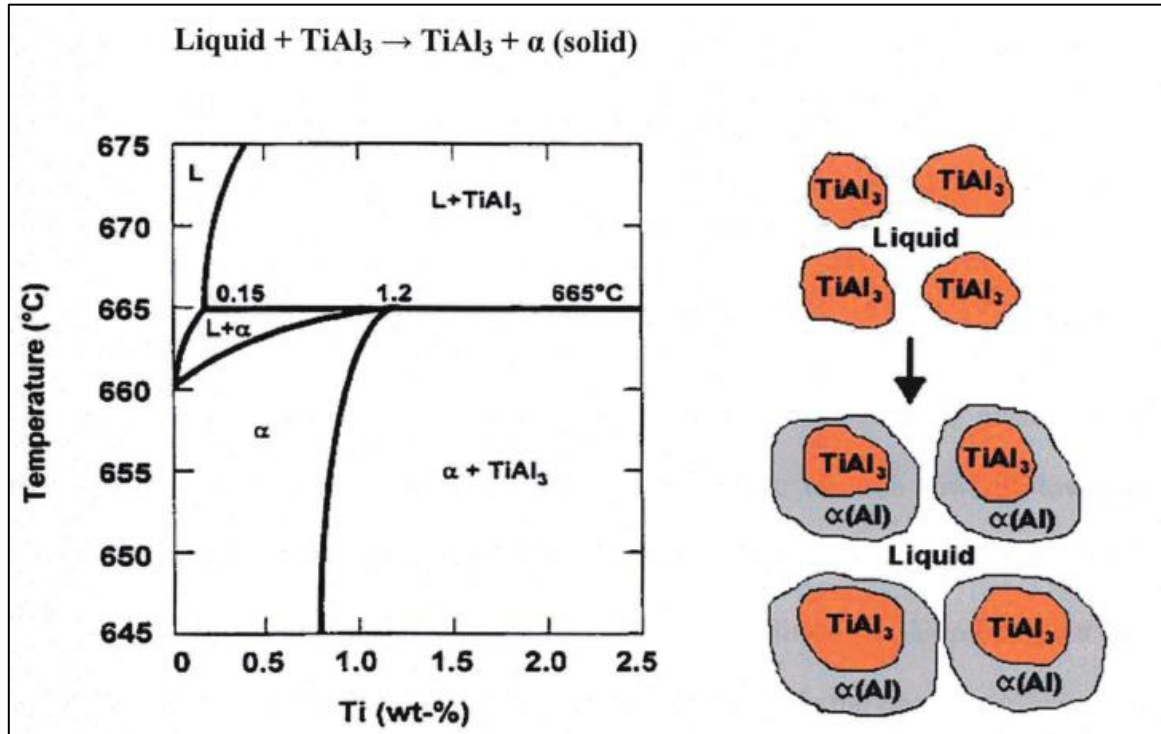


Figure 2.5 Portion of the Al-Ti phase diagram and a schematic representation of the nucleation of α -Al through the peritectic reaction in the Al-Ti system.⁷⁵

2.2.5 INFLUENCE OF HEAT TREATMENT IN Al-Si ALLOYS

There are two ways to increase the mechanical strength of aluminum alloys once they are in solid form: mechanical work and heat treatment. Both methods may be applied to alloys prepared for mechanical work (*viz.* wrought Al alloys), although the response to hardening by heat treatment will depend on the individual alloying elements present in each alloy. With regard to casting alloys, however, the sole means is heat treatment.^{76, 77} The process for increasing the mechanical strength of Al-Si alloys through heat treatment consists of three stages:

- Solution heat treatment at a relatively high temperature, to dissolve the alloying elements;
- Quenching, to obtain a supersaturated solid solution of solute atoms; and
- Aging, to form precipitates from the supersaturated solid solution, either at room temperature or at an elevated temperature.

The T6 heat treatment is commonly used to increase the strength of cast Al-Si components containing Cu and/or Mg.^{47, 78-80} This treatment consists of solution treating at a high temperature to dissolve large intermetallic particles and homogenize the alloying elements, quenching at a high cooling rate to retain a high concentration of vacancies and solute in solid solution, and artificial aging at a lower temperature to form fine precipitates. Alloy composition, aging temperature and thermal history (solution treatment, quench, natural aging) are the main parameters influencing the age hardening response.

2.2.6 SOLUTION HEAT TREATING

Solution heat treatment is the first step of the precipitation hardening process in which the solute atoms are dissolved to form a single phase in solid solution.^{19, 20} It comprises heating the alloy to a suitable temperature, maintaining this temperature long enough to allow the constituents to become supersaturated in solid solution, and then cooling rapidly enough to allow the excess solute to precipitate. The purpose of solution heat treatment is to put the maximum amount of hardening solutes such as Cu and Mg into solid solution in the aluminum matrix. The treatment must be applied for a sufficient length of time to obtain a homogeneous supersaturated structure, followed by the application of

quenching, with the aim of maintaining the supersaturated structure at ambient temperature. Figure 2.6 shows the major steps of the heat treatment which are normally used to improve the mechanical properties of aluminum.

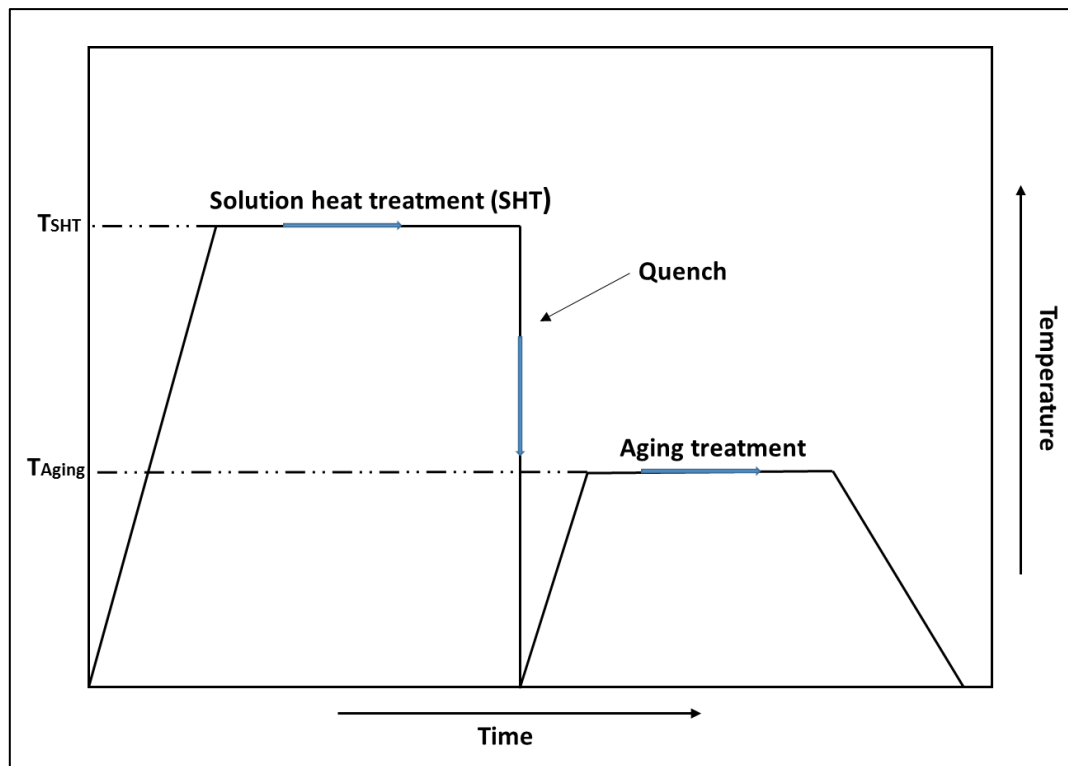


Figure 2.6 Diagram showing the three steps of heat treatment for precipitation hardening.

Solution heat treatment of Al-Si-Cu-Mg alloys fulfils three roles: homogenization of the as-cast structure, dissolution of certain intermetallic phases such as Al_2Cu and Mg_2Si , and changing the morphology of eutectic silicon.^{81, 82} The dissolution of these elements will cause precipitation hardening during the artificial aging treatment, or even in some cases, during natural aging. In order to reach the supersaturated solid solution condition, the temperature should be maintained at a sufficiently high level, at which the solution and

diffusion conditions are optimum. A number of investigators⁸³⁻⁸⁵ made an attempt to solve the problem of incipient melting during solution heat treatment and they concluded that this type of melting can be avoided by applying three techniques. The first of these involves maintaining the solution temperature at 495°C or below, while the second technique requires applying a two-stage solution heat treatment, where the first solution stage is usually applied in the form of a conventional solution treatment such as 495°C/8h which is normally used in order to dissolve the considerable amount of Al₂Cu already present; then the second stage may proceed at higher temperatures so as to maximize the amount of Al₂Cu particles dissolved in the absence of incipient melting. The third technique is implemented through the addition of Be since it has been found that Be raises the eutectic temperature of the Al₂Cu phase, thus the solution temperature can also be raised without any melting of the Al₂Cu.

Studies by Gauthier *et al.*^{82, 86} on the solution heat treatment of 319 alloy over a temperature range of 480°C to 540°C, for solution times of up to 24 hours, showed that the best combination of tensile strength and ductility was obtained when the as-cast material was solution heat-treated at 515°C for 8 to 16 hours, followed by quenching in warm water at 60°C. A higher solution temperature was seen to result in the partial melting of the copper phase, the formation of a structure less form of the phase and related porosity upon quenching, with a consequent deterioration in the tensile properties. Ouellet *et al.*⁸⁷ reported that solution treatment at 500°C for 8 to 10 hours appeared to be the best solution heat treatment recommended for high Mg-containing 319 alloys.

Solution heat treatment can also be used to dissolve and alter the harmful β -iron Al_5FeSi phase which displays a platelet-like morphology that leads to deterioration in the mechanical properties and an increase in the shrinkage porosity. It was concluded from a number of articles written by Crepeau,⁸⁸ Samuel and coworkers,^{89, 90} and Mbuya and Odera⁹¹ that, in order to investigate the effects of solution heat treatment on iron intermetallics, a solution temperature below 500°C (*i.e.* equilibrium heat treatment) cannot dissolve the β -iron phase. The dissolution of the phases accelerated as the solution temperature increases. The process of the dissolution of β -iron platelets starts with their necking, then segmentation, and finally spheroidization to smaller particles which are easier to dissolve.

The cooling rate during casting is an important factor which must be taken into consideration during the solution heat treatment stage. Castings solidified at lower cooling rates need to undergo longer solution heat treatment time spans than those obtained at higher cooling rates to achieve good strength and ductility.⁹²

2.2.7 QUENCHING

Quenching is the critical stage in the heat treatment process following solution heat treatment. Its main objective is to retain the solute atoms in solid solution through rapid cooling to a temperature often close to ambient.⁷⁷ In the previous stage, however, not only is a supersaturated solid solution desired, but an attempt is also made to preserve a certain density of vacancies favoring diffusion at low temperatures, which will be required during the aging stage. If the quench rate is sufficiently high, solute is retained in solid solution

and the high number of vacancies is also retained. On the other hand, if the cooling is too slow, particles precipitate heterogeneously at grain boundaries or defects, which results in a reduction in supersaturation of the solute and thereby a lower maximum yield strength after aging.

Quenching of aluminum castings is often done in warm or hot water (65-80°C), brine solution or polymer solution to reduce quenching stresses in complex castings.^{77, 93-95} It has been reported that the water temperature affects the properties of cast aluminum alloy A356 subjected to T6 heat treatment once the water exceeds 60-70°C, with UTS and YS being significantly more sensitive than ductility.⁹⁶ Garcia-Celis *et al.*⁹⁷ found that the aging behavior of heat-treatable cast aluminum alloys depends on the quenching rate. Hot water quenching is recommended for Al-Si cast alloys since it minimizes quenching stresses and distortion.

During quenching, the solute atoms that precipitate either on grain boundaries, dispersoids, or other particles, as well as the vacancies that migrate to disordered regions, are irretrievably lost for practical purposes or fail to contribute to the subsequent strengthening. To prevent this type of precipitation which can be detrimental to mechanical properties or to corrosion resistance, two requirements must be met.²⁸ The first is that the solid solution formed during solution heat treatment must be quenched rapidly enough to produce a supersaturated solution at room temperature, the optimum condition for precipitation hardening.²⁸ This lapse of time should be short enough to prevent the temperature from reaching the critical range where precipitation accelerates. The second

requirement is to apply a heat extraction rate which is high enough to curtail the period of time during which the temperature crosses the critical range, thereby causing the precipitation to be practically negligible or even zero.⁷⁷ This last requirement may be met by applying a cold water process for the extraction of heat, in view of the fact that this is one of the most commonly used means to obtain cooling. It should be kept in mind, however, that such an abrupt form of cooling can, in some cases, generate problems of distortion and residual cracks. It is necessary to use a lower heat extraction rate to allow the type of cooling which will create a balance between the residual stresses generated and the distortions and precipitation mentioned above. Once these precautions have been taken, it becomes possible to obtain an acceptable dimensional stability and the mechanical properties required with the final heat treatment.⁹⁸

2.2.8 AGE HARDENING

Aging, the final stage of the heat treatment process, is an important technique for strengthening aluminum alloys, and involves strengthening the alloys by coherent precipitates which are capable of being sheared by dislocations.^{49, 99} It consists of maintaining the alloy at a certain temperature for a sufficient period of time to permit the solute atoms to precipitate in the form of finely dispersed metastable phases. By controlling the aging time and temperature, a wide variety of mechanical properties may be obtained; tensile strength can be increased, residual stresses can be reduced, and the microstructure can be stabilized. The precipitation process can occur at room temperature or may be accelerated by artificial aging at a temperature ranging from 90° to 260°C. In some alloys,

the room temperature is suitable enough to promote the precipitation over the course of a few days, a phenomenon known as natural aging. Aging can thus take place at room temperature (natural aging) or at an elevated temperature (150°C - 200°C). The idea of aging is to obtain a uniform distribution of small precipitates, which gives high strength to the alloy.^{100, 101} In other alloys, however, a longer time may be needed, so that it becomes necessary to promote precipitation by using higher temperatures. This is known as artificial aging or precipitation treatment.⁷⁷ The stages in this type of precipitation are shown as a function of aging time in Figure 2.7.

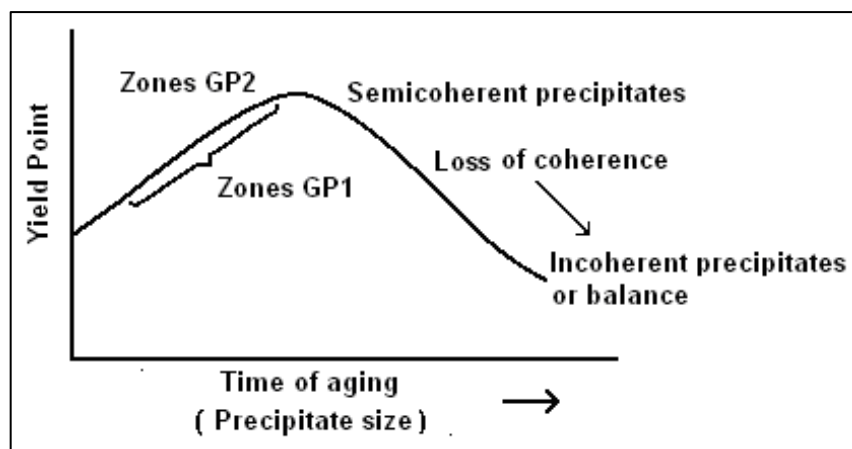


Figure 2.7 Diagram representing precipitation stages with aging time.¹⁰²

Precipitation occurs in the sequential appearance of metastable phases which differ in size and other parameters with respect to the matrix (Figure 2.7). Guinier-Preston (GP) zones may be classified as either GP1 or GP2 zones according to the order and area in which they fall. The main difference between them is that GP2 zones are larger in size. In fact, GP zones are not a single phase which differs from the matrix, but rather they are made up of regions consisting of a rich concentration of solute atoms. The temperatures

required to effectuate the aging process vary for each alloy, and are determined by the solvus line of the metastable phases. Each metastable phase formed during aging has its own solvus line, below which the phase can be formed and above which it is dissolved. It is necessary for the aging temperature to be below the solvus line of the GP zones.^{77, 103}

The difference between a coherent precipitate and non-coherent precipitate is principally the matching present in the interface between matrix and precipitates, as shown in Figure 2.8, where the coherent precipitate has a continuous relationship with the matrix in its crystal structure and its atomic arrangement.^{104, 105}

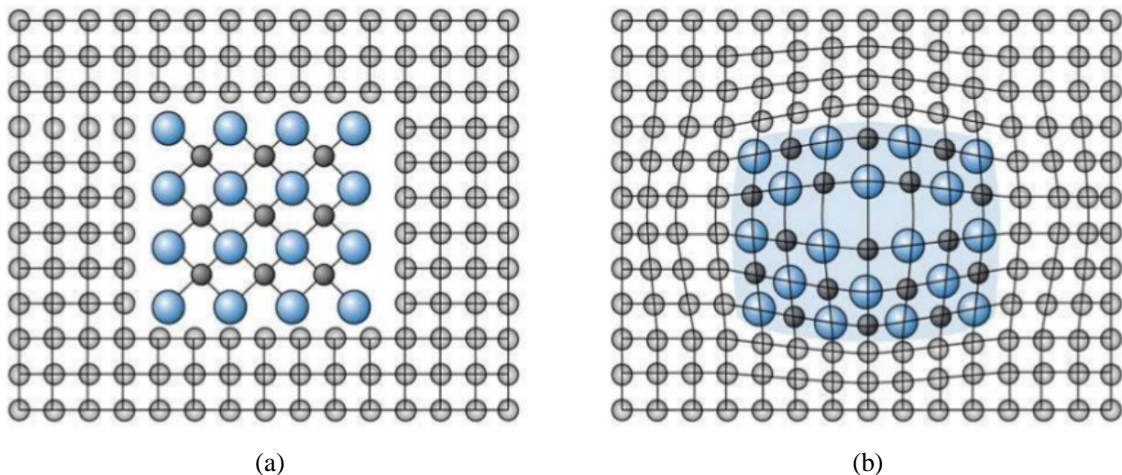


Figure 2.8 Schematic diagram showing: (a) a non-coherent precipitate that is not related to the crystal structure of the surrounding matrix, (b) a coherent precipitate that is related to the structure of the surrounding matrix.^{104, 105}

The strength mechanisms resulting from age hardening process can be explained by two basic concepts which depend on the interaction between the moving dislocations and the precipitated phases as well as the number and size of the precipitating particles.^{19, 49, 112,}

²⁴⁶ An increased number, or high volume fraction, of GP zones in the matrix increases the

distortion and thus also the stress required to move dislocations, since a single GP zone on its own has only a minimal effect on impeding dislocation gliding. The strengthening effect increases as the size of the precipitates increases, as long as the dislocations continue to cut through the precipitates. This stage is regarded as the peak aging condition, *i.e.* where the highest strength is achieved. As aging progresses, these particles grow, thereby increasing coherency strains, until the interfacial bond is exceeded and coherency disappears. As precipitates grow and become more widely spaced, they can be readily bypassed by dislocations forming loops around them, a phenomenon known as the Orowan mechanism for dispersion hardening, and causing the strengthening to decrease, as shown in Figure 2.9.^{19, 49, 112, 246} This stage is called overaging, which may occur by treatment at a higher temperature and/or longer time than used for a T6 temper, as in case of a T7 temper which is applied at 240°C.²⁴⁶ Hard particles provide maximum hardening levels for the age-hardened alloys while soft phases provide lower strength values. The strengthening effect which results from hard particles depends on the volume fraction and size of these precipitates. The level of hardening obtained also depend on the inter-particle spacing.

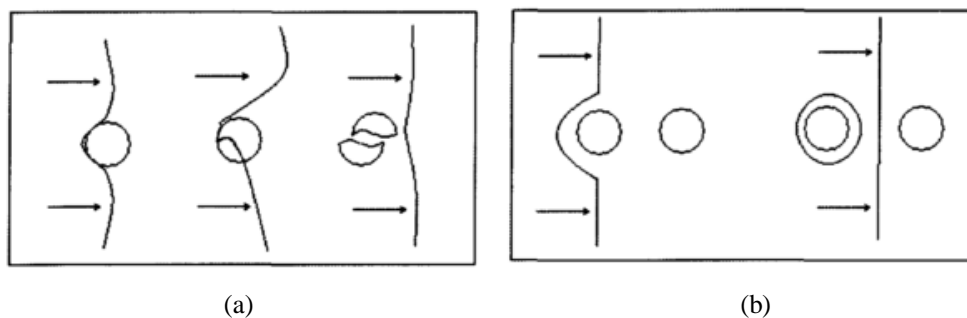


Figure 2.9 Schematic diagrams showing the Orowan process of dislocation: (a) bowing between precipitates, then (b) by-passing the particles by leaving a dislocation loop surrounding each one.¹⁹

The aging treatment of an aluminum alloy containing copper as the alloying element results in the formation of various forms of Al-Cu-containing precipitates. The precipitation sequence of an Al-Cu alloy during the aging process has been proposed as follows:¹⁰⁶⁻¹⁰⁸



The coherent and semi-coherent phases, θ'' and θ' respectively, contribute to increasing the strengthening of the alloys. On the other hand, the incoherent equilibrium precipitate θ (Al_2Cu) results in diminishing the hardening level of the alloys because of the loss of coherency between the stable phases and the metal matrix. With regard to an aluminum alloy containing Cu and Mg as the hardening elements, the aging treatment results in the formation of a range of precipitates. The generally accepted sequence of precipitation in Al-Cu-Mg alloys is:^{109, 110} θ - Al_2Cu precipitate and its precursors, along with other hardening phases/precipitates such as the S - Al_2CuMg phase and its precursors, which are observed to form during the aging treatment of an aluminum alloy containing Cu and Mg. The formation of the S -phases during aging treatment occurs via the following precipitation sequence:^{106, 111-115}



Starting by the decomposition of the supersaturated solid solution (SSS) followed firstly by the formation of GPB (Guinier-Preston-Bagaryatsky) zones, and then by the precipitation of the coherent S'' , the semi-coherent S' , and finally the incoherent equilibrium S (Al_2CuMg) phase. The coherent S'' and the semi-coherent S' precipitates are the main source of hardening in aluminum alloys containing Cu and Mg and they are also

responsible for increasing the strengthening level of this type of alloy, whereas overaging conditions result in the precipitation of the incoherent equilibrium S phase. Moreover, there is another phase containing Si which may form in the Al-Cu-Mg-Si system, called the Q phase or quaternary $\text{Al}_4\text{Mg}_8\text{Cu}_2\text{Si}_6$ phase which can form upon solidification or during aging.¹¹⁶⁻¹¹⁹ This Q phase can also coexist with Al_2Cu , Mg_2Si , and Si depending on the ratio between Cu, Mg, and Si. One of the suggested mechanisms for the formation of the Q phase is that the Cu atoms dissolve in the β'' which then evolves either to β (Mg_2Si) or to the Q phase, based on the chemical composition of the alloy and precipitation status.^{120, 121}

The Mg/Si ratio, the Cu/Mg ratio, as well as the Cu and Si contents are all principal controlling factors which determine the main precipitation-hardening phases in Al-Cu-Mg-Si alloys. The strengthening mechanism results from an age-hardening treatment which depends on the interaction between the moving dislocations and the precipitated phases.^{17,}
¹²² Throughout the aging process, the precipitates present increase in size with aging time. This affects the properties of the alloy. Initially, there is an increase in tensile strength and hardness up to a maximum value (peak strength achieved with T6 treatment); this may be ascribed to an optimum distribution of precipitates as well as their size and the presence of coherent and semi-coherent precipitates. After reaching this maximum value, the tensile strength and hardness begin to decrease. This phenomenon is known as over-aging or stabilization (T7 treatment, which produces alloy softening), and appears to be the result of the formation of incoherent precipitates or an equilibrium phase.

2.3 ROLE OF COPPER (Cu) AND MAGNESIUM (Mg) IN Al-Si ALLOYS

Hardening elements are added to Al-Si castings for the purpose of increasing their strength and hardness values. It is possible to further optimize the beneficial outcome of the addition of these strengthening elements by applying adequate heat treatment procedures. As mentioned previously, copper (Cu) and magnesium (Mg) are the most common hardening elements added to Al-Si alloys to increase their strength and hardenability, and have been used extensively in such alloys to improve the mechanical properties.

The addition of copper to Al-Si alloys leads to the formation of the copper intermetallic phase, which increases the alloy strength both at room and at high temperatures. This intermetallic phase is present in three forms: (i) eutectic-like Al-Al₂Cu, (ii) block-like Al₂Cu, and (iii) *Q*-Al₅Mg₈Cu₂Si₆ phases. The block-like Al₂Cu phase is much harder to dissolve in the aluminum matrix, and thus the benefits of having Cu as a strengthening agent during heat treatment are diminished.

The mechanism of Al₂Cu precipitation has been proposed by Samuel *et al.*¹²³ as follows. During the first stages of solidification, the formation of the α -Al dendritic network is associated with the segregation of Si and Cu in the melt ahead of the progressing dendrite interfaces. When the solidification temperature approaches the eutectic temperature, the Si particles precipitate ultimately, leading to a local concentration of Cu in the remaining areas.

The presence of Mg leads to an increase in the yield strength and tensile strength, as well as impact toughness, although it tends to decrease ductility noticeably. The presence of Mg also leads to a reduction in the eutectic temperature pertaining to the Cu-containing phases as a result of the precipitation of the $Q\text{-Al}_5\text{Mg}_8\text{Cu}_2\text{Si}_6$ intermetallic phase; this would indicate that the addition of Mg curtails the maximum solutionizing temperature. When the Mg content is less than 0.6%, Mg has a tendency to refine the eutectic Si particles. The addition of Mg also leads to segregation of the Cu phase in areas away from the eutectic Si regions. This segregation leads to the formation of the block-like Al_2Cu , as well as to that of the $Q\text{-Al}_5\text{Mg}_8\text{Cu}_2\text{Si}_6$ intermetallic phase which forms out of the Al_2Cu phase along its edges during the last stage of solidification.

The addition of Mg can bring about the segregation of the Al_2Cu phase, causing it to become more difficult to dissolve during solution heat treatment. An addition of up to 0.5% Mg leads to a significant increase in the volume fraction of the Cu-containing phase, showing a clear tendency to segregate towards localized areas, ultimately leading to the formation of the block-like Al_2Cu phase, rather than to one displaying a fine eutectic-like form.¹²⁴ It is important to avoid segregation of the copper phases in order to prevent incipient melting and to ensure that the alloy properties and casting remain sound. Silicon alone contributes very little to the strength of aluminum casting alloys, yet provides a very effective level of strengthening when combined with magnesium to form Mg_2Si . The Mg_2Si phase is soluble in the alloy to a limit of $\sim 0.7\%$ Mg, and provides the precipitation strengthening basis for heat-treatable alloys.^{125, 126}

During the T6 heat treatment process, the solution treatment stage ensures that soluble elements such as Mg and Cu become supersaturated in solid solution; this is followed by cooling (*i.e.*, quenching) which is rapid enough to prevent the excess solute from precipitating. In the case of 319 alloys, the solution temperature must be as close as possible to the Cu-eutectic temperature, although this temperature should, at the same time, be limited to a safe level below the maximum so as to avoid overheating and partial melting of the Al_2Cu phase.

Narayanan *et al.*¹²⁷ found that increasing the Mg content depresses the Si-eutectic temperature; this is one of the reasons why it was more difficult to crystallize the $\alpha\text{-Al}_8\text{Fe}_2\text{Si}$ phase in high-Mg alloys even at a high melt superheat temperature of 900°C. This effect was also reported by Awano and Shimizu,¹²⁸ who found that it is more difficult to force the $\beta\text{-Al}_5\text{FeSi}$ phase start temperature to below the Si-eutectic temperature in high-Mg alloys by using either a high melt super heating temperature, a high cooling rate, or both. In addition, the plate length and volume fraction of the $\beta\text{-Al}_5\text{FeSi}$ phase increased with Mg content due to the increase in the growth time of the primary $\beta\text{-Al}_5\text{FeSi}$ phase.¹²⁷ In contrast, Samuel *et al.*¹²⁹ found that the addition of Mg to 319 type alloys transformed a large proportion of the $\beta\text{-Al}_5\text{FeSi}$ needles into the $\pi\text{-Al}_8\text{Mg}_3\text{FeSi}_6$ compacted Chinese-script phase.

The effects of Mg-content on the quality index and the mechanical properties of Al-Si casting alloys were examined in a number of studies. Drouzy *et al.*¹³⁰ reported that increasing the Mg content from 0.25% to 0.44% in a sand cast Al-7Si-Mg alloy results in

increasing the strength of the alloy without any appreciable change being observed in its quality index. A further study investigated the influence of Mg-content in the range of 0.06% to 0.44%.^{78, 131} It was observed that increasing Mg-levels in the range mentioned results in increasing the strength and raising the quality index of the alloys, as may be observed in Figure 2.10. The improved quality of the casting, in this case, is related to the fact that the amount by which alloy ductility is decreased as a result of adding Mg is less than the amount by which the strength is increased; thus, the overall effect of increasing Mg from 0.06% to 0.44% is an increase in the quality index.^{78, 131}

Caceres *et al.*¹³² studied the influence of the content of Cu and other elements, such as Mg, Si, Fe and Mn, as well as of the cooling rate on the mechanical properties and quality index of T6-tempered Al-Si-Cu-Mg casting alloys. They concluded that the overall effect of the strengthening elements Cu and Mg is to lower the quality index values of the alloys, as may be seen in the quality chart shown in Figure 2.11. The loss in quality in this case is directly related to the decreased ductility as a result of the cracking of second phase particles occurring in the strengthened alloys. It was also observed that the degree by which the quality index is affected upon by the addition of copper depends not only on the Cu content itself but also on the presence of other elements existing with the copper such as Mg, Si, and Fe, as may be seen from Figure 2.11.

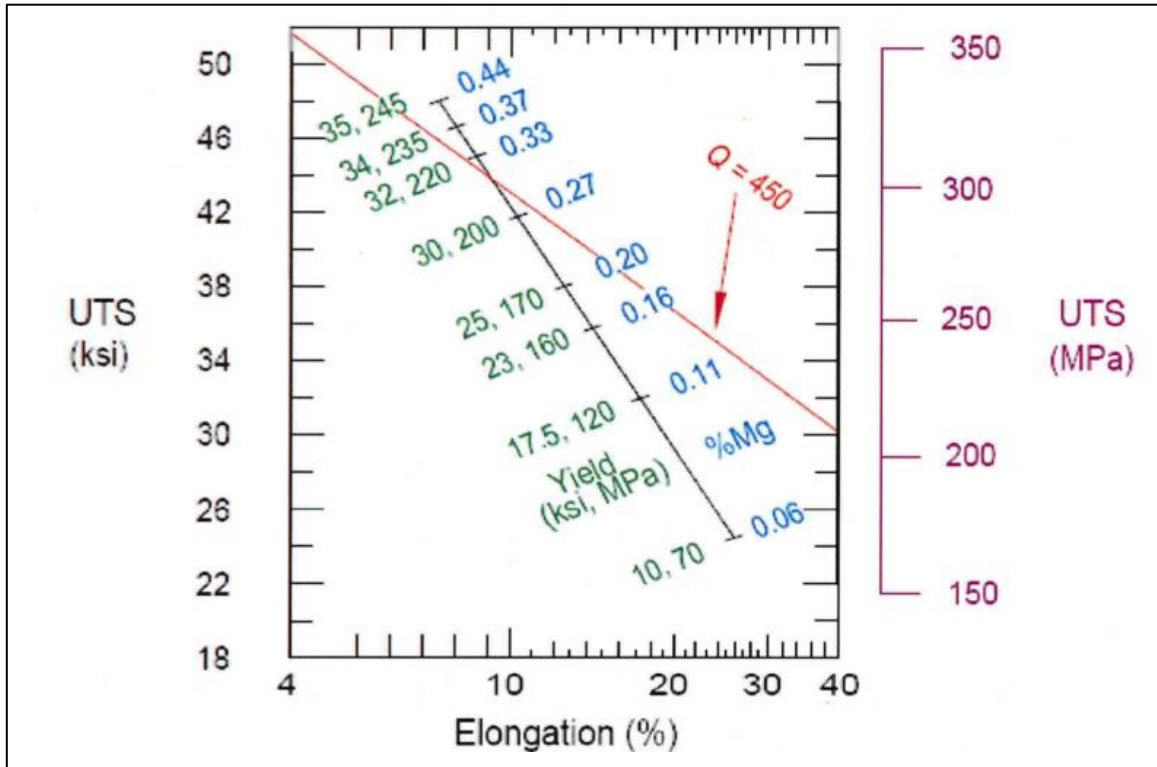


Figure 2.10 Effects of Mg-content on tensile properties and quality index of Al-7%Si alloy castings.^{78, 131}

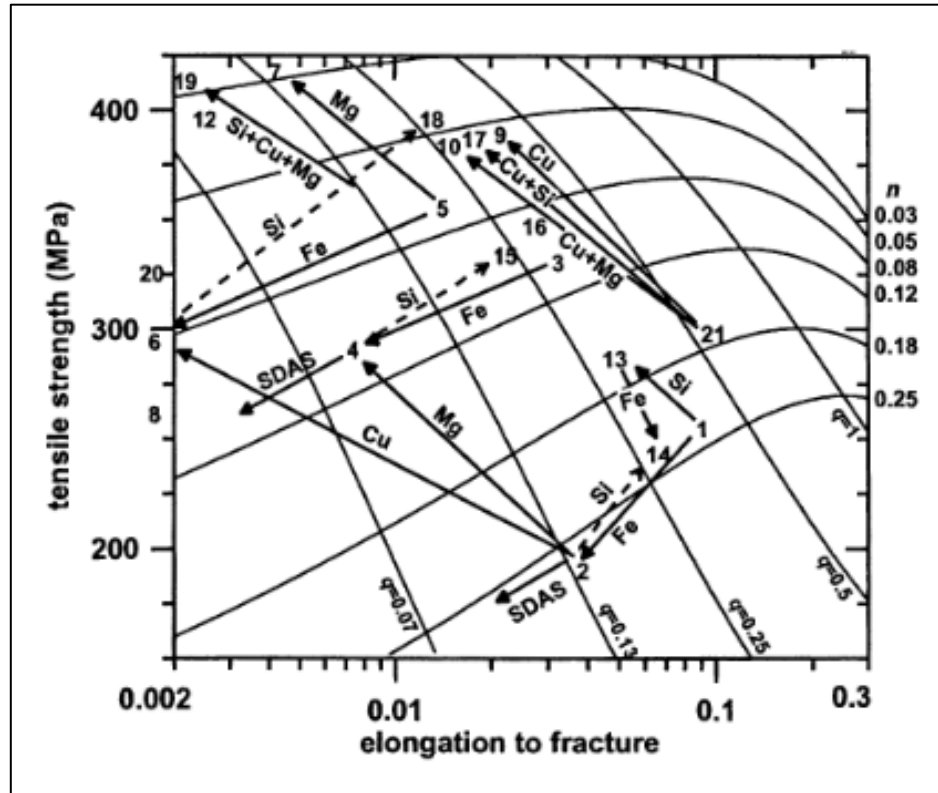


Figure 2.11 Quality chart illustrating the influence of the content of Cu and other elements (Mg, Si, Fe, and Mn) and cooling rate, as indicated by arrows, on the strength and quality index of Al-Si-Cu-Mg alloys. The numbers 1 through 21 located in the chart represent various alloy compositions.¹³²

2.4 ROLE OF IRON (Fe) AND MANGANESE (Mn) IN Al-Si ALLOYS

Iron is one of the most common impurities normally present in Al-Si cast alloys; this impurity is present in alloys made from commercially pure base material.^{88, 133}

Commercial unalloyed aluminum and aluminum-base alloys contain a considerable amount of iron and silicon as impurities or alloying additions. As the solid solubility of iron in aluminum is less than 0.05wt% at 655°C, nearly all the iron in aluminum alloys forms second-phase particles. Iron and silicon have partition coefficients less than unity, and accordingly segregate to the liquid between the α -Al dendrite arms during the course of

solidification. Therefore, when considering the non-equilibrium lever-rule assumption,⁷⁶ primary particles of binary Al-Fe and ternary Al-Fe-Si phases, and even silicon, can form during casting of an aluminum-rich alloy. The chemical composition and local cooling rate are the controlling factors that determine which phases will form and their particle size.¹³³⁻¹³⁶ The detrimental influence of iron on the mechanical properties of aluminum casting alloys, specifically on ductility and fracture toughness, is directly related to the volume fraction, size and morphology of the iron-containing phases formed in the metal matrix.^{88, 91, 137}

In general, the length of the β -Al₅FeSi platelets increases with increase in the iron content and decrease in the cooling rate.^{138, 139} Gustafsson *et al.*¹³⁸ investigated the microstructure of cast aluminum Al-7%Si-0.3%Mg (or A356) alloys as a function of Fe and Cr contents and the solidification rate. They observed that the length of both β -Al₅FeSi platelets and the arms of the α -Al₈Fe₂Si script phase increase with increasing iron content and decreasing solidification rate, as shown in Figure 2.12, where the cooling rate is indicated in terms of the dendrite arm spacing (DAS). As the iron level of the alloy increases, the number of β -Al₅FeSi platelets (or needles as they appear in optical micrographs) does not increase appreciably, but their size does. Thus, when the iron content is above 0.7wt%, the β -Al₅FeSi compound tends to crystallize in the form of extremely large particles, *i.e.*, in primary crystal form.¹⁴⁰

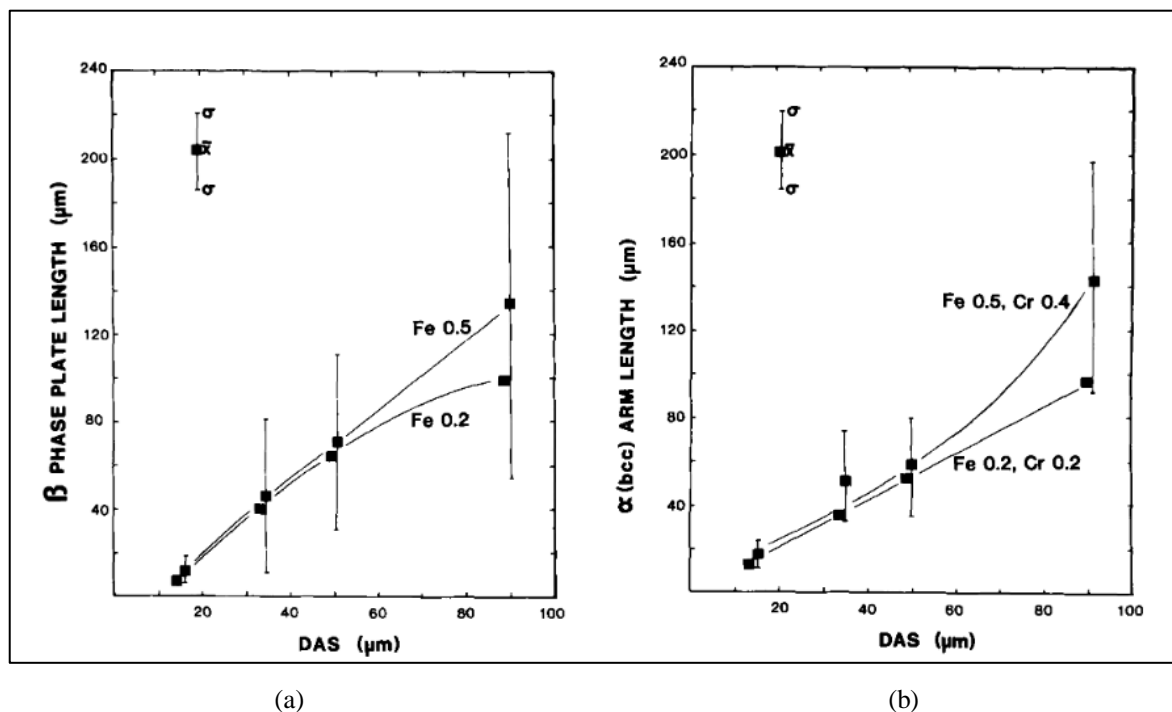


Figure 2.12 Length measurements of iron phase particles: (a) β - Al_5FeSi platelets in A356 alloys with different Fe levels; (b) α - $\text{Al}_8\text{Fe}_2\text{Si}$ script particles in A356 alloys with different Fe and Cr levels.¹³⁸

Iron and manganese are usually present as impurity elements. Manganese is the most common alloying additive which is used to neutralize the effects of iron as well as to modify the morphology and type of the intermetallic phases formed.^{141, 142} This element is capable of changing the morphology of the iron-rich phase from platelets to a more compact form or to globules, thereby improving tensile strength, elongation, and ductility.^{141, 143, 144} In the presence of Mn, the Fe-compounds crystallize in three distinctly different morphologies, namely: (i) needle-like (β - Al_5FeSi phase), (ii) Chinese-script (α - $\text{Al}_8\text{Fe}_2\text{Si}$ phase), and (iii) a star-like or polyhedral morphology (primary α - $\text{Al}_8\text{Fe}_2\text{Si}$ phase), depending on the Fe/Mn weight ratio and the cooling rate. At low cooling rates, Fe-compounds appear in the primary α - $\text{Al}_8\text{Fe}_2\text{Si}$ form, whereas at high cooling rates, both α -

script and β -Al₅FeSi phases crystallize. In the absence of Mn, the Fe-compounds crystallize only in the β -Al₅FeSi form, which is stable at cooling rates less than 20°C/s. When the melt is superheated to a high temperature and solidified under high cooling rates, the Fe-compounds crystallize in the metastable form of the α -Al₅FeSi phase.¹²⁷

The ratio of Mn to Fe necessary to compensate for the negative effects of Fe-intermetallics has not yet been established. The ASTM B108-95 (standard specification for Al permanent mold casting) and ASTM B26-95 (standard specification for Al-alloy sand castings) standards set the maximum Fe level in Al-alloys from very low, *e.g.*, 0.15% in alloy 201.0 to very high, *e.g.*, 1.5% in alloy 222.0, while in other alloys such as 355 and 356, the Fe content is allowed to reach 0.6% or more, with the comment that if Fe exceeds 0.45wt%, the Mn content shall not be less than half of the Fe content.¹⁴⁵ In order to obtain the Fe-compounds in the Chinese-script form and to avoid the needle-like and polyhedron crystal morphologies, a certain critical ratio of Fe:Mn is required and this ratio depends on the cooling rate as mentioned above.

In relation to the investigation of a new *in situ* thermal analysis probe for use in aluminum alloy melts, Musmar¹⁴⁶ studied the temperature of formation of the β -iron Al₅FeSi phase in 356 alloy melts, using Fe levels ranging from 0.93 to 1.56 wt%. He found that the higher the concentration of iron in the melt, the higher the temperature at which the β -iron phase was formed. From the first derivative curves and using a time zone range of 2s before and 2s after the inflection point corresponding to the formation of the iron phase, the beginning and end of the phase formation were determined from the corresponding second

derivative curves. The areas below the iron intermetallic peaks on the first derivative curves were calculated as representing the amount of the iron phase formed. The average surface fraction of the β -Al₅FeSi was also determined from metallographic samples obtained from the solidified materials, using electron probe microanalysis (EPMA). The two results are shown in **Error! Reference source not found.** As may be seen, there is a direct correlation between the iron content and the amount of β -Al₅FeSi phase formed.

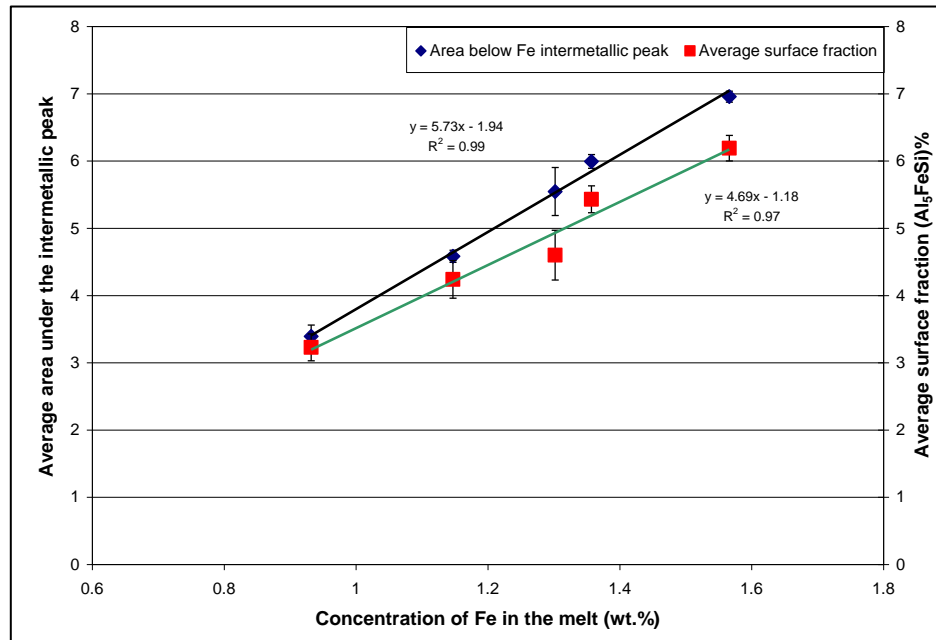


Figure 2.13 Average surface fraction and areas below the intermetallic peaks as they vary with the iron concentrations in the melt.¹⁴⁶

Another study^{74, 131, 147} investigated the influence of iron-level on the quality index of 356 casting alloys aged at 155°C for various lengths of time. The results of this study are shown in Figure 2.14 where it may be observed that increasing the iron content reduces the tensile properties and quality index values of 356 castings for the various aging times

applied. It was concluded that the alloys incorporating the best quality could be obtained by minimizing their iron content.

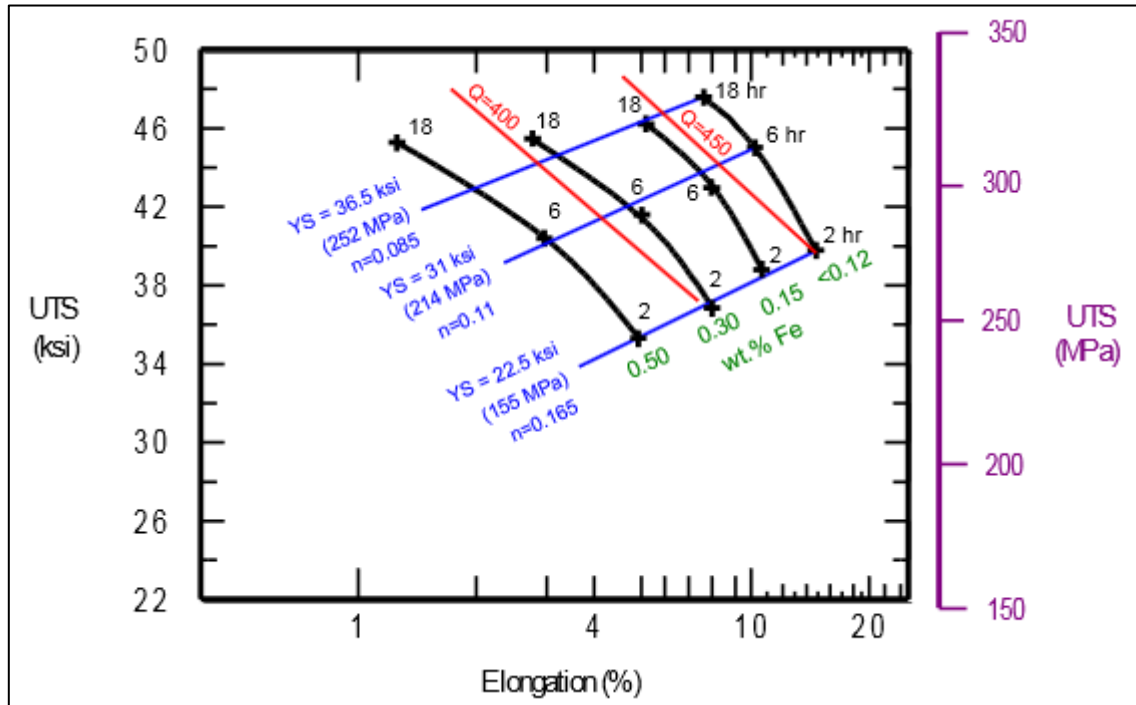


Figure 2.14 Tensile properties and quality index values of 356 alloys as a function of aging time at 155°C and iron content.^{74, 131, 147}

2.5 EFFECTS OF CERTAINS ALLOYING ELEMENTS

As mentioned previously, the addition of alloying elements is used in combination with heat treatment to improve the mechanical properties of aluminum cast alloys. The influence of the alloying elements used in this research, specifically manganese, nickel, zirconium and scandium, on heat treatment characteristics, and hence on the mechanical properties, of aluminum alloys is reviewed below.

2.5.1 EFFECTS OF ZIRCONIUM (Zr)

Zirconium is one of the transition elements which is used in a wide selection of aluminum alloys in order to control the microstructure and mechanical properties.^{30, 54, 92, 148} Minor additions of zirconium are often made to high strength wrought aluminum alloys for the purpose of regulating grain structure and inhibiting recrystallization during heat treatment, which occurs as a result of the obstructive action of coherent particles with dislocations.¹⁴⁹ According to Seperband *et al.*,¹⁵⁰ it would be necessary to obtain a microstructure containing thermally stable and coarsening-resistant dispersoids in order to improve mechanical properties at high temperatures in aluminum alloys. These dispersoids or particles will be resistant to coarsening if the energy of their interface with the matrix is low, and if the diffusivity and solubility of the rate-controlling element are both minimal.

Zirconium has the smallest diffusion flux in aluminum of all the transition metals,¹⁵¹ and its addition in the range of 0.1 to 0.3% to aluminum base alloys results in the formation of fine coherent L1₂-ordered trialuminide (Al₃Zr) dispersoids/precipitates,^{54, 152, 153} which precipitate out during the initial solution heat treatment in the form of metastable L1₂-Al₃Zr particles, as shown in Figure 2.8. These coherent particles are observably stable upon heating and they resist coarsening because of the low solubility and diffusivity of Zr in the Al matrix and also because of the low interface energy of the particles with the matrix.¹⁵⁴ As a result, these dispersoids effectively inhibit recovery and recrystallization during heat treatment due to their obstructive action, thereby causing an increase in hardness and strength properties.^{12, 155}

The Al_3Zr particles are resistant to dissolution and coarsening; they can also control the evolution of the grain and subgrain structure, thereby making it possible to increase strength and ductility in the precipitation-hardened T6 condition or during subsequent processing operations, such as the hot rolling of wrought alloys.¹² The effectiveness of the dispersoids will depend on their size, spacing, and distribution. In direct-chill cast alloys, the alloying elements are highly segregated following solidification. The Al_3Zr particles precipitate from this segregated structure, leading to an inhomogeneous distribution of the dispersoids which is not optimal for inhibiting recrystallization.^{156, 157} Proof stress, tensile strength, and the elongation to failure are all improved by the addition of Zr to cast aluminum alloys. It should be noted that in this case, there is an additive strengthening effect combined with the strengthening produced by the aging process. Such improvements in strength and ductility enhance the quality index of the material.¹⁵⁰

Minor additions of Zr to A319 aluminum casting alloys improve the hardness of the material in both the as-solutionized and age-hardened conditions provided that the alloy is solutionized for sufficiently long times. This is believed to be a direct result of the precipitation of the Al_3Zr phase, which not only induces an increase in the hardness of the alloy, but also increases the wear resistance of the material to an appreciable extent and has a very slow kinetic of precipitation.^{150, 151} The same study showed that the aging curve of the Zr-containing A319 alloy exhibits almost constant behaviour after peak hardness has been attained thereby confirming the resistance of the Al_3Zr dispersoids to coarsening. Yin *et al.*¹⁵⁸ found that the simultaneous addition of 0.1%Zr and 0.2%Sc to Al-5%Mg alloy increases the strength by 150 MPa, while the ductility remains at a high level. These

authors attributed the increment in strength mainly to grain-refinement strengthening, to $\text{Al}_3(\text{Zr,Sc})$ dispersive strengthening, and to substructure strengthening.

Forbord *et al.*¹⁵⁹ and Jia and Hu¹⁶⁰ reported that these tiny precipitates of Al_3Zr , or dispersoids, strengthen the matrix through a process of pinning and the prevention of dislocation motion; additionally these precipitates succeeded in pinning the grain boundary and slowing the recrystallization kinetics. Also, due to the low solubility and diffusion coefficient of zirconium trialuminide (Al_3Zr), this phase stabilises the alloy microstructure at high temperatures.

According to the binary Al-Zr phase diagram shown in Figure 2.15, dispersoid precipitation can only be thermodynamically possible if the Zr concentration is higher than 0.08 at.% at temperatures approaching 500°C. Precipitation will thus occur at the dendrite cores with Zr concentrations of more than 0.15 at.% and will continue until the concentration is reduced to 0.08 at.%, which is the minimum required limit for precipitation at or near 500°C.

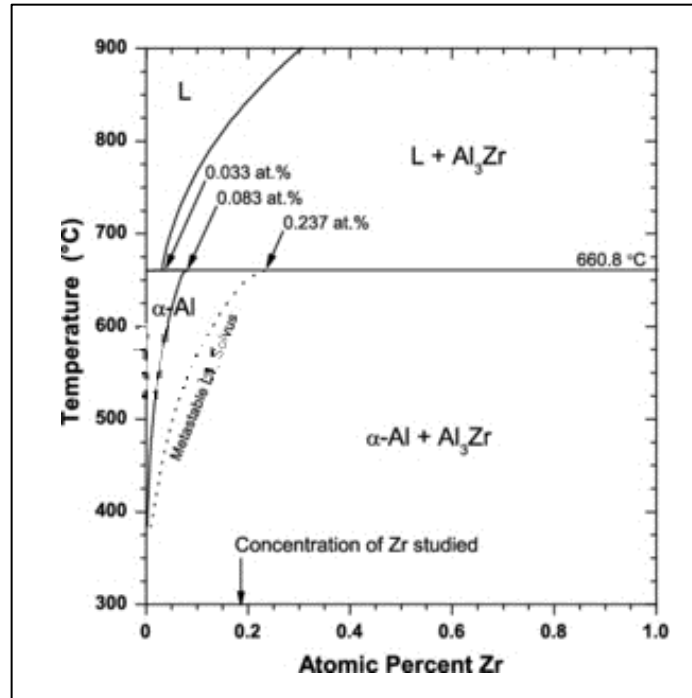


Figure 2.15 Al rich corner of the Al-Zr binary phase diagram (adapted from Murray¹⁶¹) with metastable Al₃Zr (L₂) solvus calculated by Liu *et al.*^{162, 163}

2.5.2 EFFECTS OF NICKEL (Ni)

Modern Ni-based superalloys are able to sustain stresses of the order of 150 MPa for thousands of hours, operating at temperatures ca. $0.75 T_m$ (T_m being the absolute melting temperature).¹⁶³ Aluminum acts as a solid solution hardener in nickel. Lattice expansion associated with atomic diameter oversize can be related to the hardening observed in nickel base alloys using additions of Al. The precipitation of γ' , Ni₃Al, in a high nickel matrix provides significant strengthening to nickel base alloys. This unique intermetallic phase has a face-centered cubic structure similar to that of the matrix, and a lattice constant with a mismatch of 1% or less with the γ matrix. In nickel base alloys, the volume percent of γ' precipitated is also of significance since high temperature strength increases with the

amount of the phase present. In order to retard coarsening, the alloy designer can add elements with a view to increasing the volume percent of γ' which has a face-centered cubic structure with an ordered $L1_2$ form.¹⁶⁴

The solid solubility of nickel in aluminum cannot exceed 0.04wt%. If this amount is exceeded, then it is present as an insoluble intermetallic, usually in combination with iron. Nickel content of up to 2wt% increases the strength of high-purity aluminum but reduces its ductility. Binary Al-Ni alloys are no longer in use, but nickel is added to Al-Cu and Al-Si alloys to improve both hardness and strength parameters at elevated temperatures as well as to reduce the coefficient of thermal expansion.¹⁶⁵ In a number of studies^{149, 150} on Al-Si casting alloys, it was shown that Ni contents of less than 2% do not affect the mechanical properties, whereas nickel variations of up to 2-3% affect only the specific gravity from among the usual physical properties. Nickel is present largely as a relatively massive acicular dispersion of Al_3Ni and the amount of this compound has been shown to increase with increasing nickel content. Effective strengthening would thus necessitate a much finer dispersion of Al_3Ni or a much higher volume fraction of the coarse compound, leading to the view that much larger amounts of nickel would be necessary for any useful improvement in strength. With regard to aluminum casting alloys, a high percentage of Ni seems not to be practical, mainly because it would increase the cost of the alloy. Figure 2.16 depicts the Al-Ni binary phase diagram.¹⁶⁶

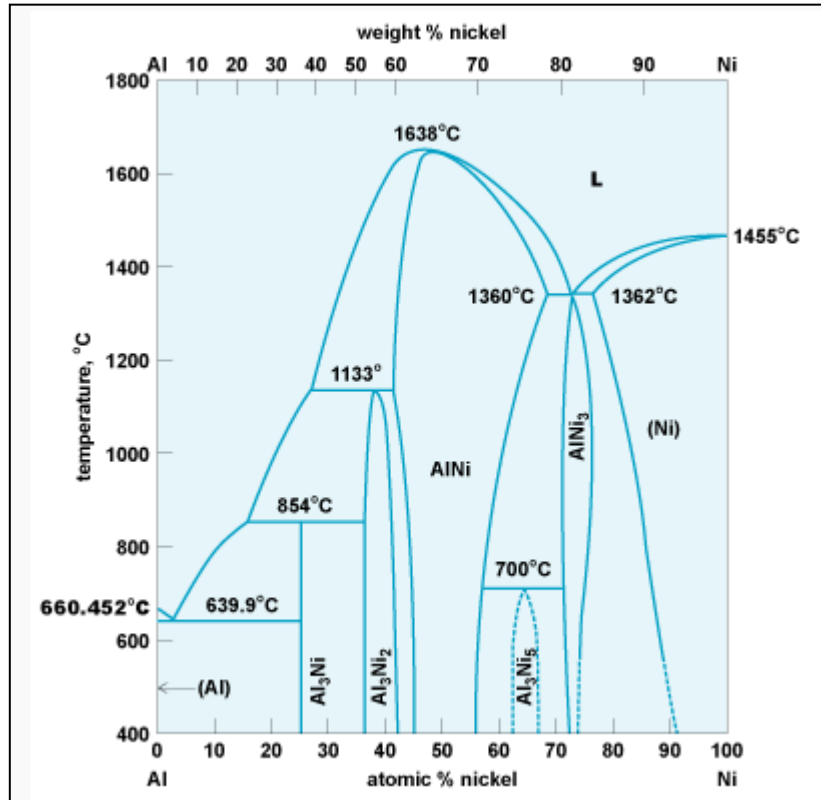


Figure 2.16 Al-Ni binary phase diagram.¹⁶⁶

Based on the behavior of nickel-base superalloys, which resist degradation of mechanical properties up to approximately 75% of their absolute melting temperature, it is conceivable that aluminum-based alloys could be similarly developed which would be useful up to 400°C. As is true for γ' in the nickel-base systems, a high-temperature aluminum alloy must contain a large volume fraction of a suitable dispersed phase, which must be thermodynamically stable at the intended service temperature.¹⁶³

The capacity of nickel for improving the strength of wrought aluminum alloys at high temperature has already been established; nickel is thus used in combination with copper to enhance high temperature properties.¹⁶⁷

Asghar *et al.*¹⁶⁸ reported that the elevated temperature strength up to 400°C of cast aluminum alloys is slightly improved by adding 0.6-1.96wt% of Ni. It was shown that the addition of 1.2wt% of Ni and 0.7wt% of Fe to an Al-Si alloy results in the formation of ~8 vol.% of Fe and Ni aluminides.¹⁶⁹ These phases have a higher strength and Young's modulus than the α -Al, especially at high temperature.¹⁷⁰

2.5.3 EFFECTS OF SCANDIUM (Sc)

Scandium is a transition element added to aluminum alloys to alter their microstructure and mechanical properties. The decomposition of a supersaturated solid solution of Al(Sc) produces elastically hard and coherent Al₃Sc precipitates with a high number density.¹⁷¹⁻¹⁷³ The Al₃Sc precipitates are characterized by their observable stability at high temperature (1320C° ± 7°C).¹⁷⁴ The use of scandium in aluminum alloys has shown that it is an effective grain refiner and increases the recrystallization temperature, as well as the corrosion resistance and weldability, and reduces the hot cracking susceptibility of aluminum alloys. Scandium forms a stable L1₂-phase (*i.e.*, Al₃Sc) with the matrix which is coherent.

The presence of fine coherent precipitates of Al₃Sc impedes the migration of dislocations and increases the recovery temperature by stabilizing the substructure. Scandium does not form any second phase intermetallic compound with other alloying elements such as iron, magnesium, manganese, silicon and chromium.¹⁷⁵ An effective method to refine the grain size of heat-treatable alloys is micro-alloying with transition metals or rare earth metals, such as additions of Sc, Zr, and Er.¹⁷⁶ The Al-Sc binary phase

diagram is illustrated in Figure 2.17, and reveals the presence of four intermetallic phases in the diagram: Al_3Sc , Al_2Sc , AlSc , and AlSc_2 .¹⁷⁷ A eutectic reaction occurs at 659°C in the Al-rich region:

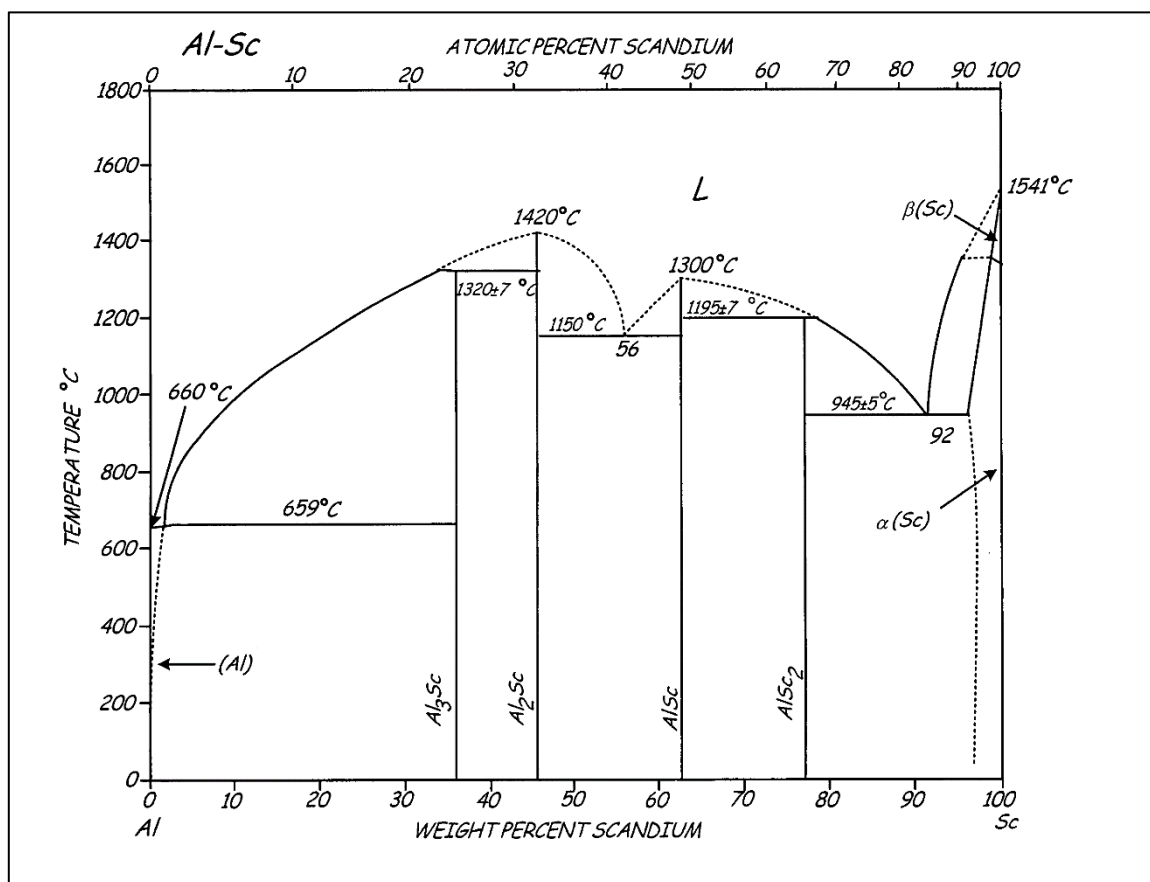


Figure 2.17 Al-Sc binary phase diagram.¹⁷⁷

Marquis *et al.*¹⁷⁴ and Zakharov¹⁷⁸ investigated the behaviour of scandium in Al-Sc alloys and they observed that, in the Al-0.5wt% Sc alloy, Al_3Sc precipitates may form below 350°C although they lose their coherency and undergo rapid coarsening above 400°C . These Al_3Sc precipitates strengthen the aluminum matrix by pinning the dislocation

lines and resisting their motion. In addition to this, these precipitates play another important role in which they prevent recrystallization almost to the solidus by Zener pinning of grain boundaries.^{174, 179}

Eskin *et al.*^{152, 179} reported that the effect of the addition of scandium on the grain size of α -Al is to refine the α -Al to a great degree through a eutectic reaction. Based on the Al-Sc phase diagram displayed in Figure 2.18, when the scandium content reaches the eutectic composition of 0.55wt% Sc, primary particles of L_{12} - Al_3Sc are formed in a peritectic reaction $L + Al_3Sc \rightarrow (Al)$ (refined) at 665°C, and they in turn act as nucleation sites for α -Al in the molten metal during solidification.^{152, 179, 180}

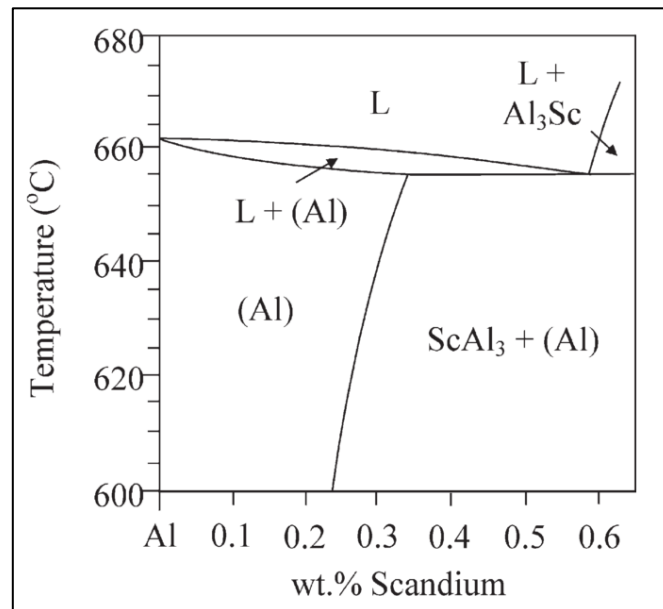


Figure 2.18 A schematic diagram of the aluminum-rich end of the Al-Sc phase diagram, showing a eutectic reaction at 0.55wt% Sc.¹⁸⁰

Similarly, Hyde *et al.*¹⁸⁰ observed that the addition of Sc below the eutectic composition of 0.55wt% has no effect on the grain size of α -Al although, as the Sc content

continues to exceed eutectic composition and reaches 0.7wt%, the α -Al is refined perfectly. The potent grain refining efficiency of $L1_2$ - Al_3Sc for α -Al may be attributed to the near identical crystal structures of Al_3Sc and α -Al as well as to the very low lattice misfit between the two phases ($\sim 1.5\%$).¹⁸¹

The Al_3Sc dissolves up to 35% Zr and forms the $Al_3(Sc_xZr_{1-x})$ intermetallic whether during solidification as primary particles with a lower misfit ($\sim 0.5\%$) with the matrix compared to the Al_3Sc phase, or through the decomposition of the solid solution into tiny dispersoid precipitates.^{182, 183} The primary particles of $Al_3(Sc_xZr_{1-x})$ have greater refining efficiency than the primary particles of $Al_3(Sc_{1-x}Ti_x)$. In the combined presence of titanium and zirconium, $Al_3(Sc_{1-x-y}Zr_xTi_y)$ may be formed.^{179, 184}

2.6 MECHANICAL PROPERTIES OF Al-Si ALLOYS

Strength, hardness, toughness, elasticity, brittleness, and ductility are mechanical properties used to determine how metals behave under load. These properties are described in terms of the types of force or stress that the metal must withstand and the manner in which they are resisted. Any improvement in mechanical properties is commonly evaluated through the tensile properties. Almost all of the steps in the processing of aluminum, from establishing a composition to heat-treatment, produce a variation in mechanical properties. The fact that tensile properties depend on several variables may go far to explain the confusion existing in connection with the properties of cast aluminum alloys. The following may be considered among the most important of the many variables which affect the mechanical properties of aluminum-silicon alloy castings:^{49, 52, 63, 128, 185, 186}

1. Alloy type and the variation of the chemical composition within the specified limits for that alloy.
2. Metal soundness, which may be affected by gas porosity, shrinkage porosity and non-metallic inclusions.
3. Metallurgical characteristics, examples of which are macro grain size and constituent distribution.
4. Solidification rate, which may be related directly to the dendrite arm spacing.
5. Heat-treatment, which brings about phase transformation in the solid state of the alloy.

These factors, in reality, are interconnected and often interdependent in a complex manner. The interdependency varies from one alloy system to another and from one casting process to another. The casting process used dictates the mechanical properties.

2.6.1 TENSILE TESTING

Tensile testing is one of the most common techniques used to measure the static mechanical properties of a metallic material. Hence, there is more data available on the tensile properties of Al-Si cast alloys and the influence of various factors such as modification and grain refinement on the former, than on any other properties. As mentioned previously, the tensile properties of cast Al-Si alloys depend on several and often interrelated variables such as the solidification rate, casting soundness, heat treatment, eutectic modification, magnesium content, etc.³² Tension tests provide information on the strength and ductility of materials under a uniaxial applied load. Standard analysis is based

on an idealized physical situation, which in general may be thought of as being represented by a long, thin sample of material in which an applied load results in an elongation along its length. There are some basic assumptions which must be considered when analyzing the data obtained from such a test: firstly, that the loading must be entirely axial, and secondly, that the deformation should take place uniformly along the length and through the cross-section of the test specimen. The data recorded from load and elongation may be normalized by either the original specimen diameter/cross-sectional area or the instantaneous specimen diameter/cross-sectional area to produce either engineering stress-strain plots or true stress-true strain plots, respectively. Typical points of interest when testing a material include: ultimate tensile strength (UTS) or peak stress; offset yield strength (YS) which represent a point just beyond the onset of permanent deformation; and the rupture (R) or fracture point where the specimen separates into pieces.⁴⁹

A stress-strain curve has two distinct regions: elastic deformation and plastic deformation. The curve shown in Figure 2.19 is typical of metallic behavior. Elastic deformation is temporary deformation, and displays full recovery when the load is removed. The elastic region of the stress-strain curve is the initial linear portion. Plastic deformation is permanent deformation. It does not recover when the load is removed, although a small elastic component may do so. The plastic region is the nonlinear portion generated once the load-strain exceeds its elastic limit. There is some difficulty in specifying precisely the point at which the stress-strain curve deviates from linearity and enters the plastic region. The convention defines yield strength as the intersection of the deformation curve with a straight-line parallel to the elastic portion and offset 0.2% on the

strain axis. The yield strength represents the stress necessary to generate this small amount of permanent deformation. The slope of the stress-strain curve in the elastic region is the modulus of elasticity, E .

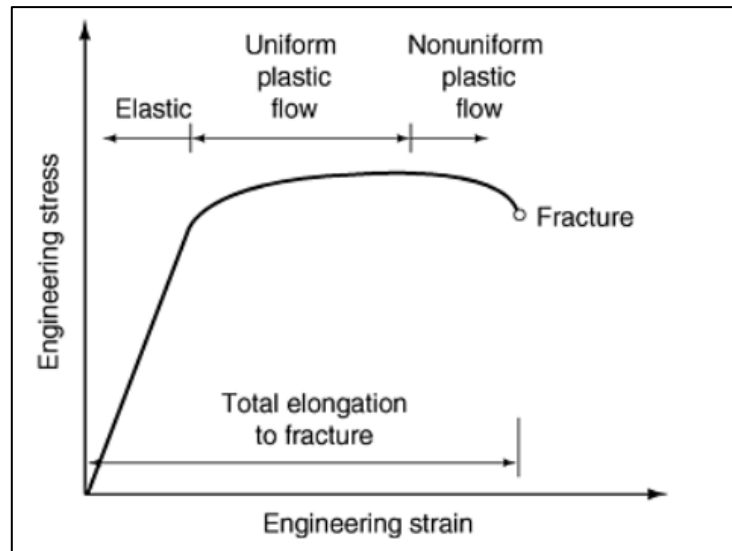


Figure 2.19 Characteristics of the engineering stress-strain curve.

Engineering stresses and strains are most frequently used in tensile tests with the objective of avoiding complications in the computation of σ and ϵ . Another indispensable objective is obtaining values which are clearly significant from an engineering point of view. The ductility of casting alloys is usually low, and changes to the casting process or changes in the chemical composition and/or heat treatment aimed at improving strength or other properties can render the material too brittle for structural applications. It is thus important to assess simultaneously what effect on material ductility and strength any changes to the microstructure would have. Hence castings are evaluated using strength-ductility diagrams known as quality index charts.¹⁸⁷

2.7 EFFECTS OF TEMPERATURE ON CAST ALUMINUM ALLOYS

In recent years, the development of diesel and direct fuel injection gasoline engines with high specific powers have resulted in a marked performance impact on piston materials due to increased combustion pressure and piston temperatures.⁵ Improved strength at elevated temperatures has been a continuing goal in aluminum alloy development for more than three decades.^{188, 189} While the applications in Al-Si casting alloys should generally be carried out at temperatures of no more than 230°C,¹⁰ for certain applications such as those required by the automotive industry, these alloys may operate over a wide range of conditions where temperatures are liable to rise much higher than 230°C.¹²

In order to improve the high temperature mechanical properties in an Al alloy, a knowledge of the different factors related to the decrease in strength with increasing temperatures is required. This behavior is linked to the change or deterioration in the principal metallurgical parameters of the specific cast aluminum alloy during its performance at higher temperatures. Al alloys are considerably more economical than existing high-temperature aerospace (*e.g.*, Ni- and Ti-based) alloys. Thus it is important to understand how the mechanical properties may be maintained at high temperatures.

To enhance the strength of Al-Si alloys, one approach is to use low cost particulate reinforcement. Lee¹⁰ reported that Al-Si alloys such as 398 alloy with a Si content in the range of 6-18wt% exhibit excellent dimensional stability, low thermal expansion, high surface hardness and wear resistant properties. The silicon gives the alloy a high elastic

modulus and low thermal coefficient of expansion, and enhances the castability of the alloy.

Such an alloy, however, has little or no practical application at elevated temperatures because the alloy lacks the coherency between the aluminum solid solution lattice and the precipitated strengthening particles.¹¹ In general, a large mismatch in lattice coherency contributes to an undesirable microstructure that cannot maintain excellent mechanical properties at elevated temperatures. Figure 2.20(a) is a diagram illustrating a coherent particle that has similar lattice parameters and crystal structure relationship with the surrounding aluminum matrix atoms, while Figure 2.20(b) illustrates a non-coherent particle having no crystal structural relationship with the aluminum atoms, so that its use is not feasible for applications at elevated temperatures.¹¹

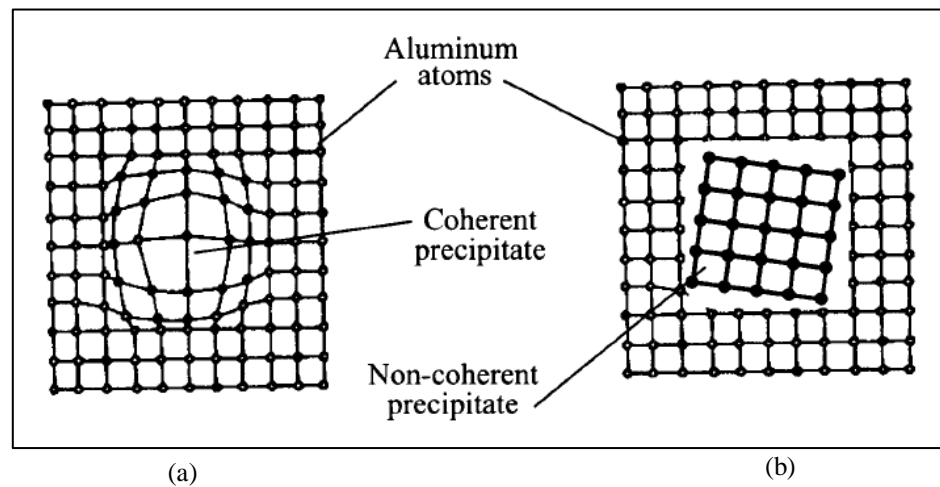


Figure 2.20 Schematic diagram showing precipitation of (a) a coherent particle and (b) a non-coherent particle in relation to the surrounding Al matrix.¹¹

To enhance the tensile strength at high temperatures, small amounts of transition elements are added to the Al-Si alloy to modify the lattice parameter of the aluminum matrix by forming compounds of the type Al_3X having $L1_2$ -type crystal structures, as shown in Figure 2.21.¹⁶³

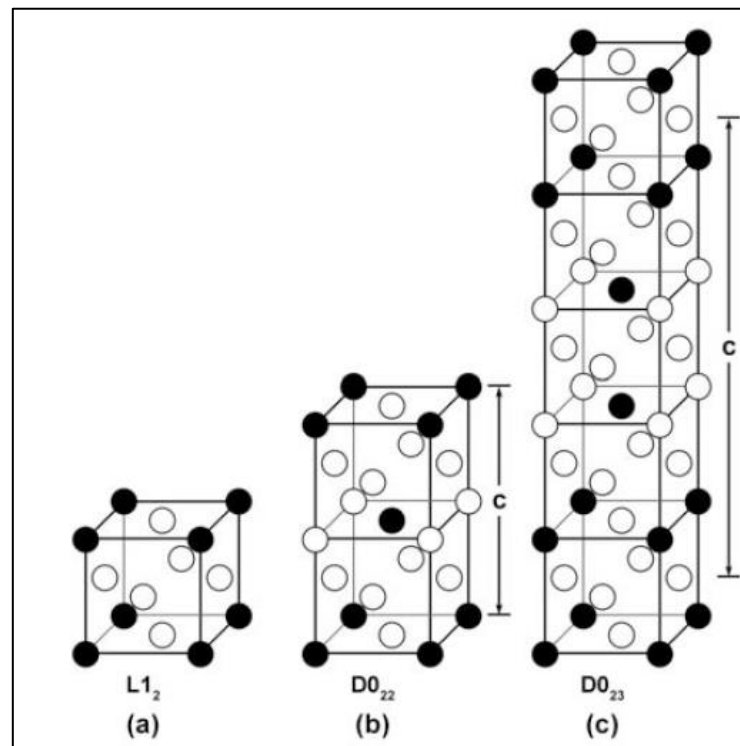


Figure 2.21 (a) $L1_2$, (b) $D0_{22}$, and (c) $D0_{23}$ structures.¹⁶³

The addition of transition elements such as Ni and Cu are considered to be an effective way to improve the high-temperature strength of cast Al-Si alloys in as-cast and solution-treated conditions by forming stable aluminides.¹⁹⁰ Copper and magnesium as alloying elements are often added to improve alloy strength at room temperature as well as at higher temperatures. At temperatures over 190°C , however, these strengthening phases which include the θ' (Al_2Cu) and S' (Al_2CuMg) phases tend to become unstable, coarsen

rapidly, and then dissolve, producing an alloy with an undesirable microstructure for high temperature applications. Apart from these phases, there are other microstructural features which contribute to strength, ductility, and durability; these include secondary dendrite arm spacing, grain size, and interdendritic Si particles.^{12, 17, 191}

If Al-Si alloys are solution heat-treated above 500°C, the eutectic Si particles are fragmented and spheroidized, converting the alloy into a particle-reinforced-like composite.¹⁶⁸ The mechanical properties of most Al-Si cast alloys are not severely affected by temperatures of up to 100°C, particularly those related to the tension test. Since most castings are used in the underaged condition, prolonged exposure to temperatures of the order of 100°C leads to additional precipitation hardening. As a result, the strength increases, and the ductility decreases slightly. At temperatures higher than 150°C, increasing temperatures and exposure times lead to an appreciable reduction in strength and an increase in ductility, as may be observed in Figure 2.22. The reduction in strength can be ascribed to overaging which may occur suddenly at temperatures close to the GP zone solvus temperature; this parameter has been measured and recorded as being of the order of 190°C.

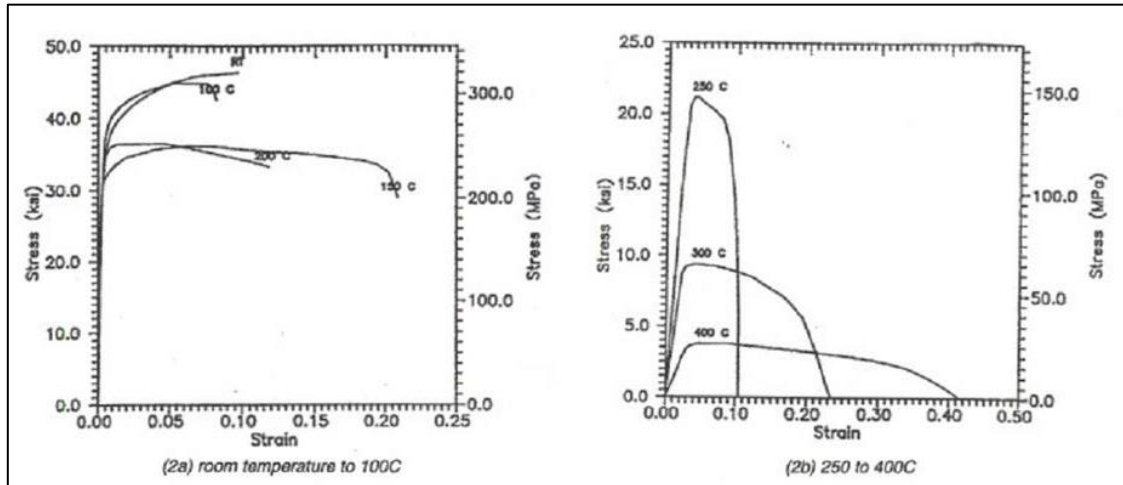


Figure 2.22 Stress-strain curves for permanent-mold A356-T6 castings at various temperatures (exposure time = 1hr).^{19, 192}

2.8 FRACTURE BEHAVIOUR

Fracture is essentially transgranular and interdendritic up to about 200°C. The fracture and debonding of silicon particles is a major aspect of damage evolution in these alloys.¹⁹³ Such fracturing or debonding, together with the formation and growth of voids around the particles and the subsequent inter-linkage of the voids, all lead to crack propagation in the interdendritic regions. The amount and the number of pores on the fracture surface of a sand casting increase with exposure to temperature and time. Furthermore, modified castings contain a significantly larger number of pores than do unmodified castings. It appears that the initial pore structure in the casting is enlarged during matrix deformation at elevated temperatures. Therefore, the pore characteristics in the casting may be a significant factor affecting elevated temperature properties.

The variation in mechanical properties resulting from exposure to high temperatures may be analyzed on the basis of the fracture behavior of cast Al-Si alloys. The fractures are classified into two categories as follows:^{191, 192, 194}

- 1) Fractures occurring at temperatures lower than $0.3 T_m$ (where T_m is the melting temperature of the alloy).
- 2) Fractures occurring at temperatures higher than $0.3 T_m$.

The fracture behavior of Al-Si alloys has been studied by several investigators, and it has been shown that fracture occurs in three stages:^{191, 192, 194}

- 1) Initiation of cracks in the Si particles;
- 2) Growth of these cracks into cavities; and
- 3) Rupture of the aluminum matrix separating the cavities.

The principal changes in the microstructural features of Al-Si alloys according to temperature are summarized in Table 2.5.¹⁹²

Table 2.5 Summary of elevated-temperature fracture behavior¹⁹²

Low Temperature ($T < 0.3T_m$)	High Temperature ($T > 0.3T_m$)
Coherent precipitates in matrix may control the strength.	Precipitates may lose coherency and strength decreases.
Dendrite arm spacing and second phase particle morphology are significant parameters.	Dendrite arm spacing and grain size are significant parameters.
Particle cracking significant.	Both particle cracking and void growth significant.
Relaxation processes not operative.	Relaxation processes become significant. Fracture postponed to higher strains
Void nucleation mainly caused by fracture of Si particles. Dislocation storage and work-hardening build up internal stresses.	Void nucleation difficult because of low stress levels due to high dislocation mobility and climb within the matrix.
Void growth difficult.	Void growth aided by dislocation slip.
Fracture is transgranular and interdendritic type.	Fracture may be intergranular if grain boundary slip occurs.

As void nucleation can occur easily, the fracture properties are regulated by the growth and coalescence of voids. When the growing voids reach a critical size, relative to their spacing, local plastic instabilities develop between voids, resulting in failure.¹⁹⁵ Under such conditions, and as shown in Figure 2.23, four types of fracture may be observed, as is shown in the case of A356 alloy castings exposed to various temperatures for short and extended periods of time.³⁶ These fracture types are differentiated as follows:¹⁹²

Type I: Low levels of plastic strain which result in a macroscopically flat surface. Below 200°C, the material fractures without extensive strain, the dislocation pile-ups are minimal, and the particles break due to fiber loading. After the Si particles fracture, the cross-sectional load-bearing area is reduced. If the specimen has exhausted its ability to strain-harden, instabilities arise in the remaining ligaments, resulting in rupture.

Type II: Intermediate degrees of plastic strain result in a sheared fracture surface. Above 200°C, Si particles exhibit random multiple cracking. At these temperatures, the samples yield at low stresses. As the stress increases, plastic flow of the matrix relieves the stresses experienced by the Si particles. With continued strain, a buildup of local stresses eventually causes the Si particles to fracture. In samples which experience large amounts of plastic deformation, cavity initiation is not determined by the magnitude of the applied stress but rather by the local state of deformation.¹⁹⁵ Fractures of this type occur by means of blocked slip and pile-up mechanisms.^{196, 197} As the plastic deformation and shearing continues, the voids eventually coalesce, and failure then occurs. Because relaxation processes are operative, the specimens exhibit significant ductility, and a slight degree of necking is observed on the fracture surface, as may be seen in Figure 2.23.

Type III: High levels of plastic strain result in a necked fracture surface. Increasing stress relief and relaxation at elevated temperatures postpone the breaking of Si particles and lead to a noticeable degree of necking. The Si particles fracture with increasing amounts of plastic strain. With continued strain, voids coalesce and lead to the fracture of the specimen. Several macroscopic coalesced voids are also observed below the fracture surface.^{191, 192}

Type IV: Extreme amounts of plastic strain result in a severe reduction of the cross-sectional area as well as lead to a large void in the center of the fracture surface. At very high temperatures, fracture of Si particles becomes difficult. Continuous stress relaxation occurs and the samples exhibit a high degree of ductility. As the specimen begins to neck, a

triaxial state of stress is produced, thereby promoting void nucleation and growth on large particles. With further strain, the voids coalesce and produce a circular flaw.^{191, 192}

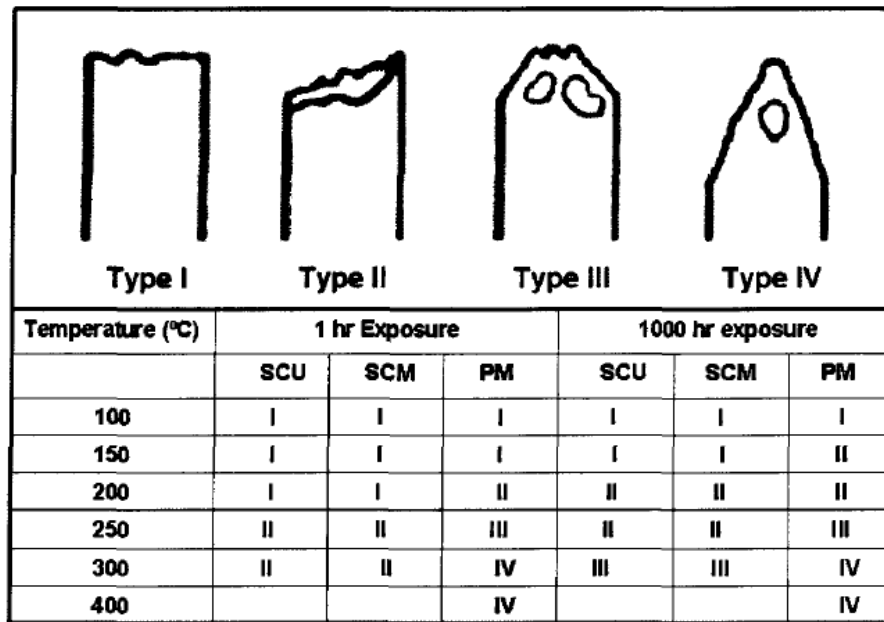


Figure 2.23 Schematic showing classification of the type of fracture at different test temperatures for the study of an A356 alloy (SCU = sand cast, unmodified; SCM = sand cast, modified; PM = permanent mold).¹⁹²

The high-temperature strength of eutectic Al-Si alloys is attributed to a transfer of load from the ductile α -Al matrix to the rigid eutectic Si, a strengthening mechanism characteristic of fiber-reinforced composites. The degree of reinforcement depends on the morphology, volume fraction and distribution of the eutectic Si particles. If Al-Si alloys are solution treated above 500°C, the eutectic Si fragments and becomes spheroidized, converting the alloy into a particle-reinforced-like composite.^{168, 191} This spheroidization of the eutectic Si limits the use of AlSi₁₂ cast alloys for high-temperature applications. The addition of transition elements such as Ni and Cu are considered to be an effective way to

improve the high-temperature strength of cast Al-Si alloys in as-cast and solution-treated conditions by forming stable aluminides.¹²

Ludtka and Laughlin¹⁹⁸ examined three 7075 (Al-Zn-Mg-Cu) alloys with different (Zn + Mg) contents and found that fracture toughness increased with decrease in the (Zn + Mg) solute content in an alloy containing 2.20wt% Mg, 5.59wt% Zn alloy (*i.e.*, a so-called low solute alloy), demonstrating the highest toughness of 102 MPa m^{1/2}. They also reported that the fracture mode of the low solute alloy was transgranular dimpled rupture, where the dimples were associated with fine Cr-dispersoids (Al₁₈Cr₂Mg₃), however, the fracture mode changed to intergranular type with increased Zn + Mg content.¹⁹⁹

The addition of Zr to binary Al-Sc alloy has been shown to increase the resistance to overaging, and TTT diagrams have shown that the addition of Zr slows down the late stages of the transformation kinetics.²⁰⁰ Bulk experiments at high temperature have shown that Zr dissolves in Al₃Sc into the Sc sublattice replacing as much as 50% or even 75% Sc. The addition of scandium has been shown to increase the strength while maintaining the ductility of Al-Mg alloys.²⁰¹⁻²⁰³ Additions of scandium and zirconium to Al-Mg alloys synergistically promote strengthening and result in higher strengths than either Sc or Zr additions alone would produce.^{158, 201} In wrought Al-Mg-Sc alloys with Zr additions, strengthening occurs primarily by development of coherent Al₃Sc and Al₃Zr dispersoids. Additional strengthening is achieved by grain refinement, as the dispersoids inhibit recrystallization during working.¹⁵⁸

At low temperatures, strengthening due to second phase particles is governed by the dislocations either cutting through or looping around the particles.²⁰⁴⁻²⁰⁶ The former process occurs predominantly for small coherent particles, and the latter for incoherent particles and large coherent particles. At higher temperatures, dislocation climb introduces other bypass mechanisms, which are classified as either local or general climb.²⁰⁶⁻²⁰⁸ Local climb refers to the situation in which the dislocation remains in the glide plane, except at the particle where it is confined to the particle-matrix interface, giving rise to a sharp bend in the dislocation line. The nature of the climb process influences the resistance associated with the particle, with the resistance being, in general, higher for local climb when the particles are coherent. For incoherent particles, the dislocations undergo local climb and then detachment.^{151, 205, 209}

2.9 QUALITY OF CAST ALUMINUM ALLOYS

The quality of aluminum casting alloys is considered a key factor in selecting an alloy for a particular engineering application. Deciding upon the right alloy quality thus involves reaching a suitable compromise between numerous factors so as to achieve maximum performance with the least possible risk, combined with cost efficiency.

The quality of an alloy may be understood as a combination of tensile strength and ductility values which meet the design prerequisites for using it in a certain application. Alloy composition, solidification rate, heat treatment procedures, casting defects, and such microstructural features as grain size and intermetallic phases are all parameters which closely affect alloy quality since they also influence the mechanical properties of the

casting. In the design of aeronautical structures, the fracture toughness of materials is also taken into account.²¹⁰⁻²¹³

The quality of an aluminum alloy may be defined using a numerical value, Q , called the Quality Index. Drouzy *et al.*¹³⁰ first proposed this concept in 1980 where they defined the quality index Q for A356 and A357 casting alloys, based on their tensile test data of Al-7wt%Si-Mg alloys containing different Mg contents and subjected to different heat treatments. The concept was subsequently developed by other researchers in different forms, to evaluate the mechanical properties of other series of cast aluminum alloys used in automotive and aerospace applications.

2.9.1 QUALITY INDEX Q (AFTER DROUZY *et al.*)

The first proposed quality index was introduced by Drouzy *et al.*¹³⁰ in 1980 to facilitate the assessment of the effects of changes in chemical composition, solidification conditions, and heat treatment on the quality of Al-7wt%Si-Mg cast aluminum alloys A356 and A357. These authors put forward the hypothesis that alloy quality may be expressed by a numerical index. They defined the quality index, Q , using the following expression:

$$Q = UTS + d \log (\%El) \quad [1]$$

where the quality index Q is in MPa units; UTS refers to the ultimate tensile strength in MPa; $\%El$ refers to the elongation to fracture in percent; and d is a material constant. The value of d is equal to 150 for Al-7wt%Si-Mg alloys. For the same alloy, the probable yield strength (YS) may be defined as follows:

$$YS = a UTS - b \log (\%El) + c \quad [2]$$

where the coefficients a , b , and c are alloy-dependent empirically determined parameters. For the Al-7wt%Si-Mg alloys, the coefficients a , b , and c were determined as 1, 60, and -13, respectively.

With the help of Equations [1] and [2], it is possible to plot lines of equal quality index or *iso-Q* lines and lines of equal probable yield strength or *iso-YS* lines in the form of a UTS-%El diagram or *quality chart*, as shown in Figure 2.24. Such quality charts are generated for use as a simple means of evaluating, selecting, and also predicting the most appropriate metallurgical conditions which may be applied to the castings so as to obtain the best possible compromise between tensile properties and casting quality. The quality index value (Q) is intrinsically related to the level of the quality of the castings which is susceptible to improvement through adequate control of the impurity elements, casting defects, modification, solution heat treatment and solidification conditions. The probable yield strength (YS) depends mainly on the presence of hardening elements such as Mg and Cu, and also on the age-hardening conditions applied to the castings.^{17, 18}

The right selection of these factors may increase both quality index values and the probable yield strength in the directions shown in Figure 2.24. The quality chart shown in this figure provides sufficient information for each point located on this type of plot so that the appropriate metallurgical conditions may be applied to obtain the specific prerequisite properties demanded of an alloy with respect to a particular application. As may be seen in Figure 2.24, the properties which are known for each point located in the chart are the

tensile strength (UTS), yield strength (YS), percentage of elongation to fracture ($\%El$), and the quality index value (Q).

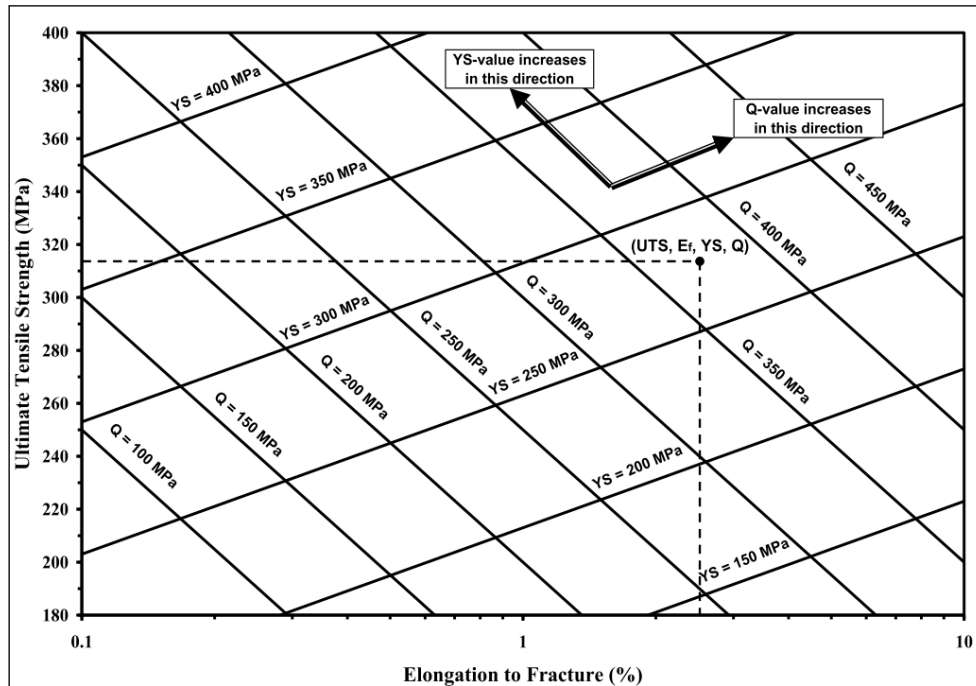


Figure 2.24 Example of the quality chart proposed by Drouzy *et al.*¹³⁰ with *iso-Q* and *iso-YS* lines generated using Equations 1 and 2.

Thus, the quality index concept is a method for evaluating the quality of a cast aluminum alloy with reference to its mechanical properties. Besides using quality charts to select the optimum alloy/conditions vis-à-vis the application, quality charts also provide the right direction to follow to improve the quality of the material.

In general, quality charts aim at providing the design engineer with a tool for selecting a material having properties which satisfy any specific application under consideration. The use of this concept for supporting material selection was reported in several studies.^{9, 17, 18, 20, 130, 210-224}

CHAPTER 3

EXPERIMENTAL PROCEDURES

CHAPTER 3

EXPERIMENTAL PROCEDURES

3.1 INTRODUCTION

This chapter will provide all the details relevant to the 354-Al-9wt%Si-1.8wt%Cu-0.5wt%Mg casting alloy with regard to general melting and casting procedures, heat treatment, the various techniques used for microstructural characterization and phase identification, namely optical microscopy, scanning electron microscopy (SEM), field-emission scanning electron microscopy (FESEM), electron probe microanalysis (EMPA) and associated EDX and WDS techniques, as well as the tensile testing method used to determine the mechanical properties.

Besides analysis of microstructures obtained from tensile test samples, further description of the microstructure involves thermal analysis, which is a method for identifying the main phase reactions related to the solidification of the alloys studied. Cooling curve experiments were carried out for each alloy melt composition prepare

using a preheated (600°C) graphite mold where, by means of a thermocouple (chromel-alumel type K) inserted through the bottom of the mold and connected to a data acquisition system, the temperature-time data could be recorded for plotting the cooling curves. Samples were sectioned from the graphite mold castings, mounted and polished for metallographic examination to identify the phases formed. The alloy codes and compositions of the various alloys which were prepared for the purpose have been collectively listed in Table 3.1.

The operations described in this study were carried out with the intention of investigating and viewing the effects of additions of nickel, manganese, zirconium, and scandium, on the mechanical properties of cast 354 aluminum alloy at different temperatures. The term “temperature” here refers to both the temperatures used for aging as applied to the samples tested at room temperature, as well as those used for conducting the mechanical testing at elevated temperatures.

The study was carried out in two parts: Stage I and Stage II, according to low and high-Ni additions made to the base 354 alloy. The alloys prepared were further divided into two groups, one containing only Ni + Zr additions, while the other included Sc and Mn additions as well. The goal of this thesis was to characterize a range of new cast aluminum alloys that are being considered for high temperature (Stage I) and ambient temperature (Stage II), diesel engine and other applications.

3.2 CLASSIFICATION OF ALLOYS

Alloys were prepared and tested in two parts (Stages) as follows, according to the Ni level *and* the temperature at which the tensile testing was carried out.

Stage I: Alloys with *low Ni* content – tested at *high* temperature

1. Alloy G1 (Alloy 354 + ~170 ppm Sr + 0.22wt% Ti);
2. Alloy G2 (Alloy G1 + 0.4wt% Ni);
3. Alloy G3 (Alloy G1 + 0.4wt% Zr);
4. Alloy G4 (Alloy G1 + 0.2wt% Ni + 0.2wt% Zr);
5. Alloy G5 (Alloy G1 + 0.4wt% Ni + 0.4wt% Zr).

Stage II: Alloys with *high Ni* content - tested at *room* temperature

1. Alloy G6 (Alloy G1 + 2wt% Ni + 0.25wt% Zr);
2. Alloy G7 (Alloy G1 + 2wt% Ni + 0.25wt% Zr) without Cu;
3. Alloy G8 (Alloy G1 + 0.75wt% Mn + 0.25wt% Zr);
4. Alloy G9 (Alloy G1 + 2wt% Ni + 0.75wt% Mn + 0.25wt% Zr);
5. Alloy G10 (Alloy G1 + 0.15wt% Sc + 0.25wt% Zr).

3.3 MELTING AND CASTING PROCEDURES

The 354 casting alloy used in this study was supplied in the form of 12.5-kg ingots. The chemical composition of the 354 base alloy (coded G1) used for this research was listed in Table 3.1 in the previous chapter. The alloy ingots were cut into smaller pieces, dried and melted in a 150-kg capacity SiC crucible, using an electrical resistance furnace,

as shown in Figure 3.1. The melting temperature was maintained at $750 \pm 5^\circ\text{C}$. All the 354 alloy melts prepared were grain-refined by adding 0.22wt% Ti in the form of rods of Al-5wt%Ti-1wt%B; they were then Sr-modified using Al-10wt% Sr master alloy, to obtain levels of 0.22wt% Ti and ~ 170 ppm Sr in the melt. Additions of Ni, Mn, Zr, and Sc were carried out using Al-20wt%Ni, Al-25wt%Mn, Al-20wt%Zr and Al-2wt%Sc master alloys, respectively. For the remaining nine alloys, the master alloys used as additives were aggregated in order to build up the programmed chemical specification. The master alloys were cut into smaller pieces, dried and then added to the base alloy melts, only instants before degassing to ensure homogeneous mixing of the additives together with the degassing. The melts were degassed for ~ 15 -20 min with a rotary graphite impeller rotating at ~ 170 rpm, using pure dry argon injected into the molten metal at a constant rate of $20.39 \text{ m}^3/\text{h}$, as shown in Figure 3.2. Following this, the melt was carefully skimmed to remove oxide layers from the surface.



Figure 3.1 Electrical resistance furnace.



Figure 3.2 Graphite degassing impeller.

The melt was poured into an ASTM B-108 permanent mold preheated at 450°C to drive out moisture, for preparing the tensile test bars, as shown in Figure 3.3. Each casting provided two test bars, with a gauge length of 70 mm and a cross-sectional diameter of 12.7 mm, as shown schematically in Figure 3.4. Three samplings for chemical analysis were also taken simultaneously at the time of the casting; this was done at the beginning, in the middle, and at the end of the casting process to ascertain the exact chemical composition of each alloy. The chemical analysis was carried out using a Spectrolab-JrCCD Spark Analyzer, which provided the actual chemical compositions of the alloys produced.

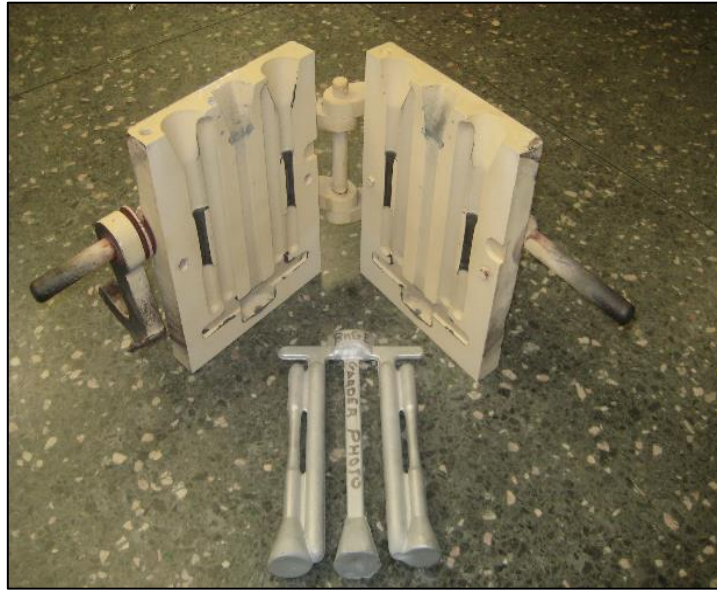


Figure 3.3 ASTM B-108 permanent mold used for casting tensile test bars.

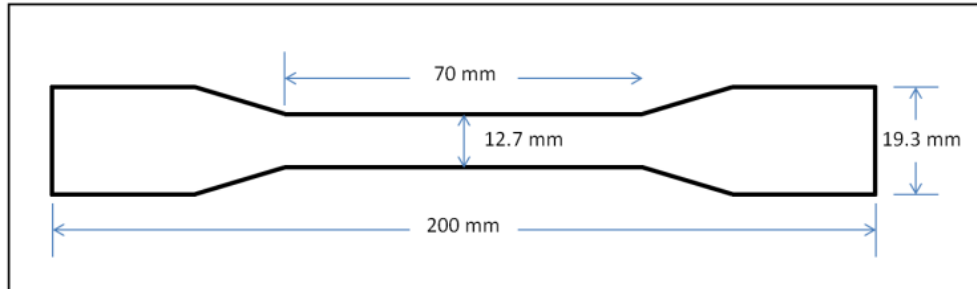


Figure 3.4 Dimensions of the tensile test bar (in mm).

Table 3.1 lists the chemical composition of the various alloys as obtained from the samplings for chemical analysis taken from the corresponding melts prepared for this study, and their corresponding codes.

Table 3.1 Chemical composition of the 354 alloys used in this study (wt%)

Alloy/Element	Si	Fe	Cu	Mn	Mg	Ti	Sr	Ni	Zr	Sc	Al
G1*	9.43	0.08	1.85	0.01	0.49	0.22	0.0150	~	~	~	Bal.
G2	9.16	0.08	1.84	0.01	0.49	0.22	0.0149	0.46	~	~	Bal.
G3	9.10	0.07	1.83	0.00	0.49	0.21	0.0145	~	0.39	~	Bal.
G4	9.01	0.08	1.85	0.00	0.45	0.21	0.0127	0.21	0.19	~	Bal.
G5	9.10	0.08	1.86	0.00	0.46	0.22	0.0122	0.40	0.39	~	Bal.
G6	8.90	0.18	1.89	0.02	0.73	0.15	0.0161	1.87	0.25	~	Bal.
G7	9.08	0.19	0.04	0.02	0.75	0.16	0.0170	1.86	0.25	~	Bal.
G8	8.92	0.18	1.88	0.75	0.74	0.15	0.0175	~	0.25	~	Bal.
G9	8.85	0.18	1.88	0.75	0.76	0.15	0.0168	1.87	0.25	~	Bal.
G10	8.95	0.19	1.87	0.03	0.75	0.15	0.0175	~	0.25	0.15	Bal.

*G1: 354 base alloy

3.4 HEAT TREATMENT

Tensile test bars of Stage I alloys G1, G2, G3, G4 and G5 were T6-heat treated which comprised solution heat treating at 505°C/8h, followed by quenching in warm water at 60°C, and then artificial aging at 190°C for aging times of 2 h, 10 h, 40 h and 100 h. The condition selected for the high temperature tensile testing was the T6-treated (190°C/2h aged), using two selected testing temperatures (155°C and 300°C) and holding times of 10 h, 40 h and 100 h at each testing temperature. The testing temperatures and holding times at room and at high temperature are listed in Table 3.2.

The Stage II alloys G6, G8, G9 and G10 were T6-heat treated using solution heat treating at 500°C/8h (maximum concentration of Cu is dissolved in the Al matrix at this temperature); and at 540°C/8h for alloy G7 (containing no Cu), followed by quenching in warm water at 60°C, and then artificial aging. The artificial aging treatment was carried out at 155°C, 190°C, 240°C, 300°C and 350°C. Time was a variable in the precipitation

hardening treatment, and ranged from 2 up to 100 hours. In all of the heat treatment stages, the soaking time did not begin to be counted until the furnace reached the desired temperature. After aging, the test bars were allowed to cool naturally at room temperature (25°C). A summary of the different conditions used for the room temperature tensile testing is presented in Table 3.3. All heat treatments were carried out in a Lindberg Blue M electrical resistance furnace, as shown in Figure 3.5.

Table 3.2 Conditions used for high temperature tensile testing for Stage I alloys with low Ni content

Room Temperature Testing				
Condition	Condition Code (room temperature)			
As-Cast	1			
T6: 505°C/8h SHT- Quenching-190°C Aging Temp.	Aging Time			
	2h	10h	40h	100h
	2	3	4	5
High Temperature Testing				
Samples used in T6 (190°C/2h aged) condition				
Temperature (°C)	Holding Time			
	10h	40h	100h	
155	6	7	8	
300	9	10	11	

Table 3.3 Conditions used for room temperature tensile testing for Stage II alloys with high Ni content

Condition	Condition Code							
As-Cast	1							
SHT	2							
Aging Temperature(°C)	Aging Time							
	2h	4h	6h	8h	10h	20h	48h	100h
155	3	4	5	6	7	8	9	10
190	11	12	13	14	15	16	17	18
240	19	20	21	22	23	24	25	26
300	27	28	29	30	31	32	33	34
350	35	36	37	38	39	40	41	42



Figure 3.5 Lindberg Blue M electric furnace.

3.5 MECHANICAL TESTING

3.5.1 TENSILE TESTING AT ELEVATED TEMPERATURE

Tensile testing for Stage I alloys was carried out at a strain rate of $4 \times 10^{-4} \text{ s}^{-1}$, using an Instron Universal Mechanical Testing Machine, as shown in Figure 3.6. The testing was carried out at room temperature (for samples in the as-cast and T6-treated conditions), and at high temperature (155°C and 300°C using holding times of 10, 40 and 100 hours at testing temperature). A data acquisition system attached to the machine provided the tensile data, namely, the ultimate tensile strength (UTS), the yield strength at 0.2% offset strain (YS), and the percentage of elongation to fracture (%El), calculated over the 25.4 mm gauge length of the test bar.

For testing of the Stage I alloys at high temperature, the samples were mounted in the testing chamber which was pre-set to the required temperature. After mounting, the sample was held at the testing temperature for 30 min before starting the test.

Five test bars were used for each alloy composition/condition studied for all room and high temperature tests carried out. The average UTS, YS and %El values obtained from each set of five tests were considered as representing the tensile properties of that alloy/condition. Thus, the tests carried out for the Stage I covered a total of 11 conditions or 55 bars per alloy, so that a total of 275 bars were tested for this part of the study.



Figure 3.6 Instron Universal mechanical testing machine with chamber for high temperature testing.

3.5.2 TENSILE TESTING AT ROOM TEMPERATURE

All samples for Stage II, whether as-cast, solution heat-treated or aged, were tested to the point of fracture using an MTS servohydraulic mechanical testing machine at a strain rate of $4 \times 10^{-4} \text{ s}^{-1}$, as shown in Figure 3.7. An extensometer, or strain gage, was used in the tests to measure the extent of deformation in the samples. Ultimate tensile strength (UTS), yield strength (YS) at 0.2% offset strain, and percentage of elongation to fracture (%El), were obtained from the data acquisition system of the machine. Five samples from each condition covered in Stage II were tested, for a total of 42 conditions or 210 bars/alloy.



Figure 3.7 MTS Mechanical Testing machine used for room temperature testing.

3.6 CHARACTERIZATION OF THE MICROSTRUCTURE

The characterization of the microstructure of the 354 alloy aims at correlating the microstructural features of these alloys with their tensile properties as well as with their quality indices. Several techniques were used in this regard for the purpose of achieving a qualitative and quantitative analysis of the microstructural constituents and features, these being intermetallic phases; hardening precipitates; and fracture surface characteristics.

3.6.1 THERMAL ANALYSIS

In order to obtain the cooling curves and to identify the main reactions and corresponding temperatures occurring during the solidification of 354 alloys, thermal analysis of Stage II (including the base alloy G1 and G6-G10) melt compositions was carried out. Ingots of the as-received commercial 354 alloy were cut into smaller pieces, cleaned, and then dried to prepare the required alloy compositions. The melting process was carried out in a cylindrical graphite crucible of 2-kg capacity, using an electrical resistance furnace; the melting temperature was maintained at 780°C, while the alloys were grain-refined by adding 0.2% Ti as Al-5%Ti-1%B master alloy in rod form and modified by adding ~170 ppm Sr in the form of an Al-10%Sr master alloy. Taking the grain-refined and modified alloy “G1” as the base alloy, addition of Ni, Zr, Mn and Sc were made in order to study the effects of these elements on the phase formation and microstructure of these alloys.

Nickel, manganese, zirconium and scandium were added to the alloys in the form of master alloys containing Al-20wt%Ni, Al-25wt%Mn, Al-20wt%Zr and Al-2wt%Sc, respectively, as was the case with the casting of the tensile samples. For the purpose of determining the reactions taking place during solidification, part of the molten metal was also poured into an 800 grams capacity graphite mold preheated to 650°C so as to obtain close-to-equilibrium solidification conditions at a cooling rate of 0.35°Cs⁻¹.

A high sensitivity Type-K (chromel-alumel) thermocouple, which has to be insulated using a double-walled ceramic tube, is attached to the centre of the graphite mold. The temperature-time data is collected using a high speed data acquisition system linked to a computer system to record the temperature-time data every 0.1 second. Figure 3.8 shows a schematic representation of the graphite mold and thermocouple, while Figure 3.9 shows the actual thermal analysis set-up that was used. From this data, the cooling curves and the corresponding first derivative curves for a number of selected alloys were plotted so as to identify the main reactions occurring during solidification with the corresponding temperatures, and the various phases which constitute the microstructure of each alloy were expected to be revealed as well.

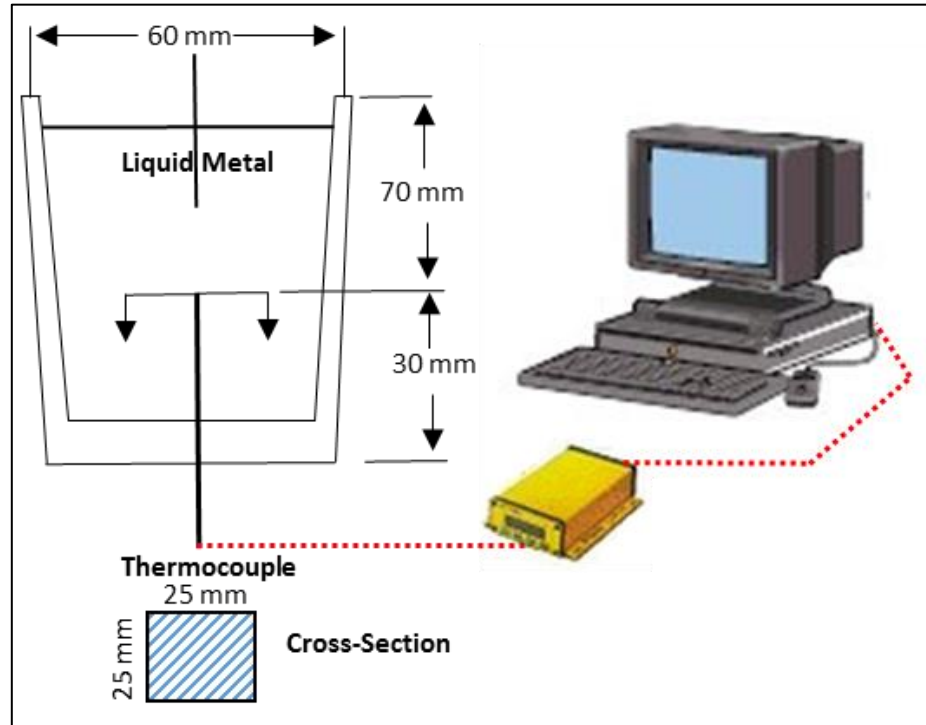


Figure 3.8 Schematic drawing showing the graphite mold used for thermal analysis.



Figure 3.9 Thermal analysis set-up.

3.6.2 OPTICAL MICROSTRUCTURE

Samples for metallography were sectioned from the tensile-tested bars of selected conditions/alloy studied, about 10 mm below the fracture surface, as shown in Figure 3.10; they were then individually mounted in bakelite, and subsequently polished to a fine finish using 1 μm diamond suspension. The study was carried out using an Olympus PMG3 optical microscope linked to a Clemex Vision PE optical microscope and image-analysis system. The samples were mounted and then subjected to grinding and polishing procedures to produce a mirror-like surface. The mounting of the samples in bakelite was carried out using a Struers LaboPress-3 machine, while the grinding and polishing procedures were carried out using a TegraForce-5 machine, as shown in Figure 3.11. The grinding procedures were applied using silicon carbide (SiC) papers in a sequence of 120 grit, 240 grit, 320 grit, 400 grit, 800 grit, and finally 1200 grit sizes; it should be noted that the word “grit” is used to represent a measure of fineness for abrasive materials and that water was used as a lubricant in this stage of sample preparation.

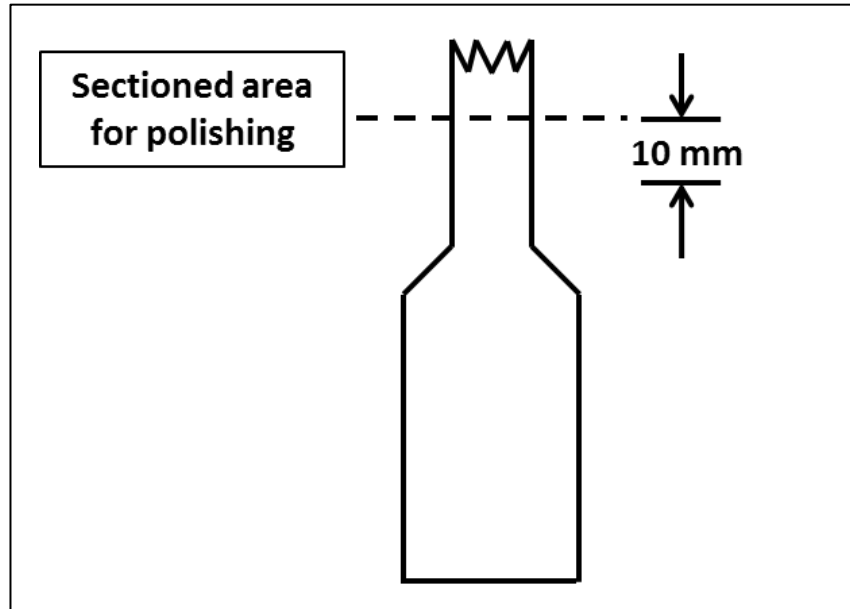


Figure 3.10 Diagram showing the sectioned area of tensile-tested samples prepared for microstructure analysis using optical microscopy.

Polishing was carried out using Struers diamond-suspension, containing a diamond particle size of 6 μm , as the first step of the polishing process followed by further polishing through the application of the same suspension containing a smaller diamond particle size of 3 μm . The lubricant used for this polishing stage is a Struers DP-lubricant. The final stage of polishing was carried out using a Mastermet colloidal silica suspension, SiO_2 having a particle size of 0.6 μm . Water was used as lubricant throughout the final polishing stage, after which the samples displayed a mirror-like surface and were ready for the microstructural examination. The microstructures of the polished sample surfaces were examined using the set-up shown in Figure 3.12.



Figure 3.11 (L) Struers LaboPress-3 and (R) TegraForce-5 machines, for mounting and polishing samples for metallography.

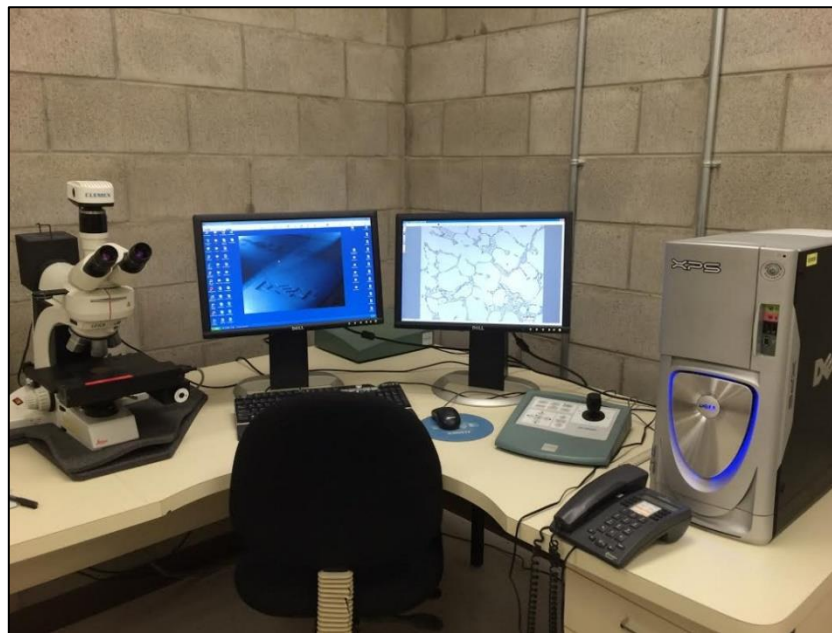


Figure 3.12 Clemex Vision PE optical microscope and image-analysis system used in the current study.

3.6.3 SCANNING ELECTRON MICROSCOPY AND ELECTRON PROBE MICROANALYSIS

Scanning electron microscopy (SEM) and field-emission scanning electron microscopy (FESEM) were used to examine the characteristics of the hardening precipitates under various heat treatment conditions for the 354 alloys investigated. The purpose of applying these techniques is mainly to investigate the distribution, size, and density of the hardening precipitates in the cast structure under the various aging temperatures and times involved.

The SEM used in the current study was a JEOL 840A scanning electron microscope (SEM) attached to an EDAX Phoenix system designed for image acquisition and energy dispersive X-ray (EDX) analysis, as shown in Figure 3.13. The SEM was operated at a voltage of 15 kV, with a maximum filament current of 3 amperes.

The field-emission scanning electron microscope (FESEM) provides clear and less electrostatically distorted high resolution images even at low voltages; it can produce images of 2.1 nm resolution at 1 kV and of 1.5 nm resolution at 15 kV. The instrument used in this study was a Hitachi-SU-8000 (FESEM), as shown in Figure 3.14, equipped with a standard secondary electron detector (SE), a backscatter electron detector (BSD) and an energy dispersive X-ray spectrometer (EDS).



Figure 3.13 JEOL 840A scanning electron microscope used in this study.



Figure 3.14 Hitachi-SU-8000 field emission scanning electron microscope used in the current study.

Identification of intermetallic phases was carried out using electron probe microanalysis (EPMA) coupled with energy dispersive X-ray (EDX) and wavelength dispersive spectroscopic (WDS) analyses, using a JEOL JXA-8900L WD/ED combined microanalyzer as shown in Figure 3.15, operating at 20 kV and 30 nA, where the electron beam size was $\sim 2 \mu\text{m}$. Mapping of certain specific areas of the polished sample surfaces was also carried out where required, to show the distribution of trace elements in the phases. The volume fraction of the intermetallic phases was quantified using the same electron probe microanalyzer and a special built-in software based on phase brightness. For each sample, 15 fields were measured at 100X magnification.



Figure 3.15 JEOL JXA-8900L WD/ED combined microanalyzer (EPMA) system used in the current study.

The fracture surface of selected tensile-tested samples were also examined using the Hitachi SU-8000 field emission scanning electron microscope, where the SE and BSD detectors and EDS facilities were employed to determine the nature of the fracture and identify the main source(s) of crack initiation and propagation in the alloy samples.

CHAPTER 4

Stage I Alloys – Room and High Temperature Testing

MICROSTRUCTURE AND TENSILE PROPERTIES

CHAPTER 4

Stage I Alloys - Room and High Temperature Testing MICROSTRUCTURE AND TENSILE PROPERTIES

4.1 INTRODUCTION

The first part of this chapter presents the results on the tensile properties of 354 casting alloys for tests carried out at ambient and at high temperature, in terms of the influence of the various metallurgical parameters described in the previous chapters. The analysis of these results will be carried out with emphasis on the two major aims of this research study: firstly, to acquire detailed information regarding the mechanical limits of alloy 354 and secondly, to obtain an understanding of the effects of the addition of nickel and/or zirconium, on the alloy, in the context of the mechanical properties obtained at room temperature (for samples in the as-cast and T6-treated conditions), and at high temperature (155°C and 300°C using holding times of 10, 40 and 100 hours at testing temperature).

The tensile properties of the castings will be examined in terms of their microstructural features and constituents observed under the above conditions for purposes

of interpreting the results. As mentioned previously, five test bars were used per alloy/condition in the tensile tests carried out for selected alloys/conditions.

4.2 MICROSTRUCTURE OF TENSILE TEST SAMPLES

As mentioned in Chapter 3, all the 354 alloy melts prepared were grain-refined and Sr-modified to obtain levels of 0.22wt% Ti and ~170 ppm Sr in the melt. Additions of Ni and Zr were carried out using Al-20wt% Ni and Al-20wt% Zr master alloys, respectively. The volume fraction of the undissolved phases in the matrix for the as-cast condition was reported in an earlier study by Hernandez-Sandoval¹⁹ who used the same set of 354 alloys in his study as those use in Stage I of the present work. For such volume fraction measurements a JEOL JX-8900 N WD/RD combined microanalyzer operating at 20 kV and 30 nA was used, and the results for as-cast samples (coded AC) of G1, G2, G3, G4 and G5 alloys are listed in Table 4.1.

Table 4.1 Volume fraction (%) of undissolved phases observed in the matrix of as-cast alloys G1 through G5 used for this research¹⁹

Alloy Condition/Vol.%	G1	G2	G3	G4	G5
AC – Average Vol.%	3.09	4.87	3.47	4.42	6.48
AC – Std. Deviation	0.32	0.60	0.35	0.65	0.31

As may be seen from Table 4.1, the volume fraction of the undissolved phases in these alloys tends to increase with the addition of Ni and Zr, alone or in combination, in comparison with the base alloy G1 (354 + ~170 ppm Sr + 0.22wt% Ti). Alloy G5 exhibits the highest volume fraction with 6.48%, and has the highest level of Ni and Zr additions, 0.4wt% each. This may be explained by the dual presence of Zr and Ni, and their

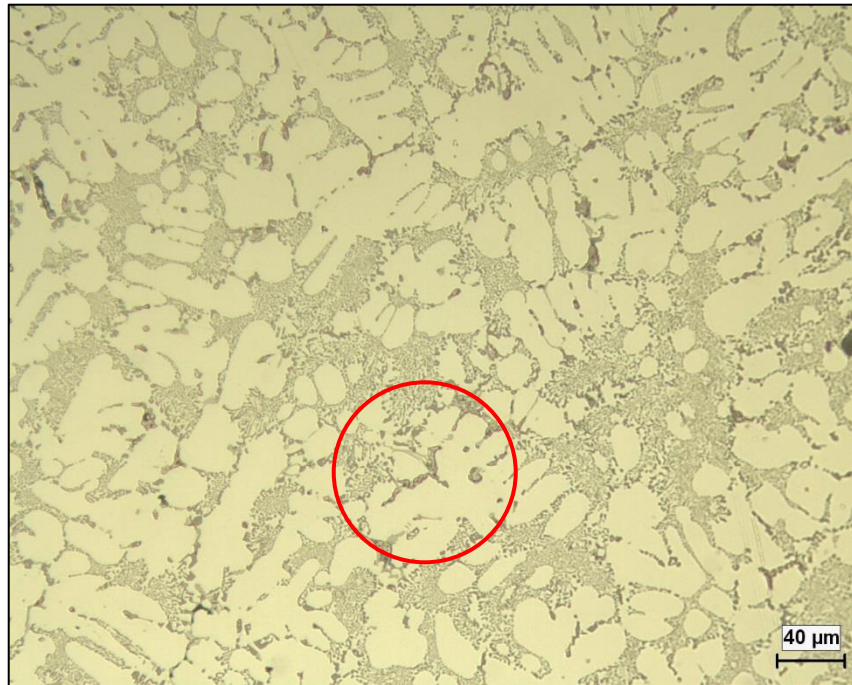
interaction with each other or with other elements present in the base alloy to form new phases and thus increase the total volume fraction of intermetallics in the alloy. Interactions between Zr, Ni and other elements to form Zr-Ni-Al-Cu, Zr-Ni-Al, and Zr-Ti-Si phases have been reported by other researchers who have studied these systems.²²⁵⁻²²⁷

A complete modification of the silicon particles in the microstructure of alloy G1, G2 and G5 in the as-cast condition may be observed in Figure 4.1 to Figure 4.3, while Figure 4.4 to Figure 4.6 show the microstructures after T6-treatment (comprising solution heat treating at 505°C/8 h, quenching in warm water at 60°C, and then artificial aging at 190°C/2 h). For each of these figures, two micrographs were taken to show (a) the general microstructure at 200X magnification, from which an area of interest (circled) containing the intermetallic phases observed in that particular alloy samples was selected and examined at a much higher magnification of 500X to view these phases clearly and to facilitate identification.

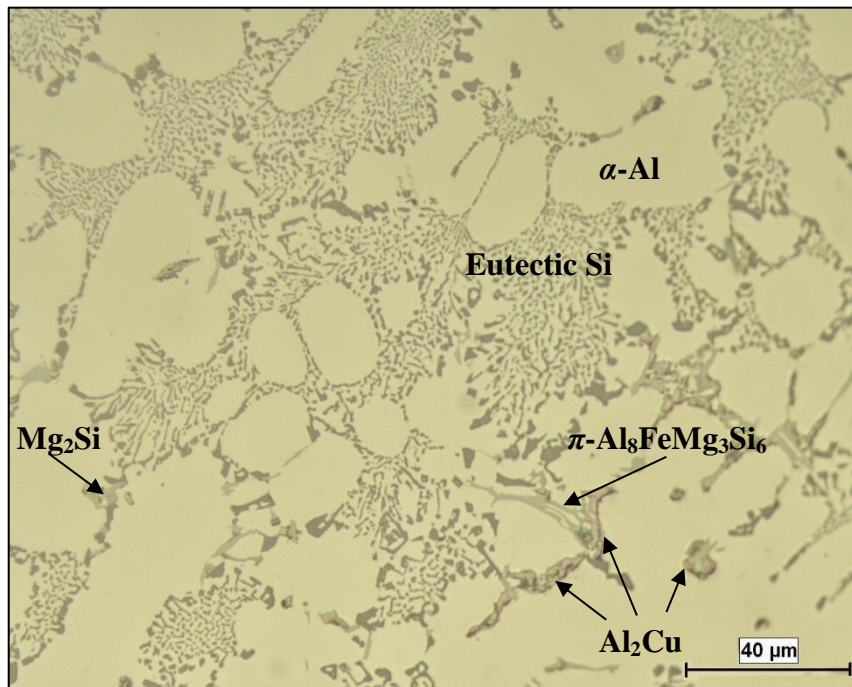
In regard to the alloys G2 and G5, the only observable difference in composition with respect to alloy G1 is the presence of Ni and Ni + Zr in the former. The optical micrographs for the three alloys in the as-cast and T6-treated condition showed expected phases such as the α -Al dendrites and eutectic silicon in the interdendritic regions, and a reduction in the amount of undissolved intermetallics in the latter case (T6 condition). Other phases such as Al-Si-Zr-Ti, reported by Hernandez-Sandoval,¹⁹ were also observed in alloys G3, G4 and G5 containing Zr.

Heat treatment results in transforming the morphology of eutectic silicon from acicular particles into fibrous ones in non-modified alloys.^{228, 229} In the case of modified alloys, where the eutectic silicon is already fibrous, increasing the solutionizing temperature and/or the solution time further improves the morphology of the silicon particles to a globular form, while aging strengthens the alloy via the formation of coherent precipitates which are capable of being sheared by dislocations. The solution heat treatment was carried out at 505°C/8 h in order to avoid risking the incipient melting of the Al₂Cu phase, followed by quenching and artificial aging at 190°C/2 h. The copper phase is seen mainly as small pockets of the block-like Al₂Cu. The Al₂Cu and Mg₂Si phases normally dissolve during solution treatment where the principal elements Cu and Mg diffuse into the metal matrix and form a supersaturated solid solution after quenching. The β -iron phase, Al₃FeSi, was not in evidence, possibly due to the relatively low Fe-content of the base alloy G1. In conjunction with the segregation of the copper phases, the presence of the β -iron phase is known to have a negative effect on the mechanical properties of Al-Si-Cu-Mg alloys.²³⁰

Among the three well-known eutectic modification methods²³¹ of (a) chemical modification through the addition of trace levels of alloying elements, (b) quench modification through high cooling rates and rapid solidification at growth rates of 400-100 $\mu\text{m/s}$, and (c) superheating modification (*viz.*, heating the melt to 850°C – 900°C, holding at the superheat temperature for 15-30 min, cooling quickly to pouring temperature (~680°C

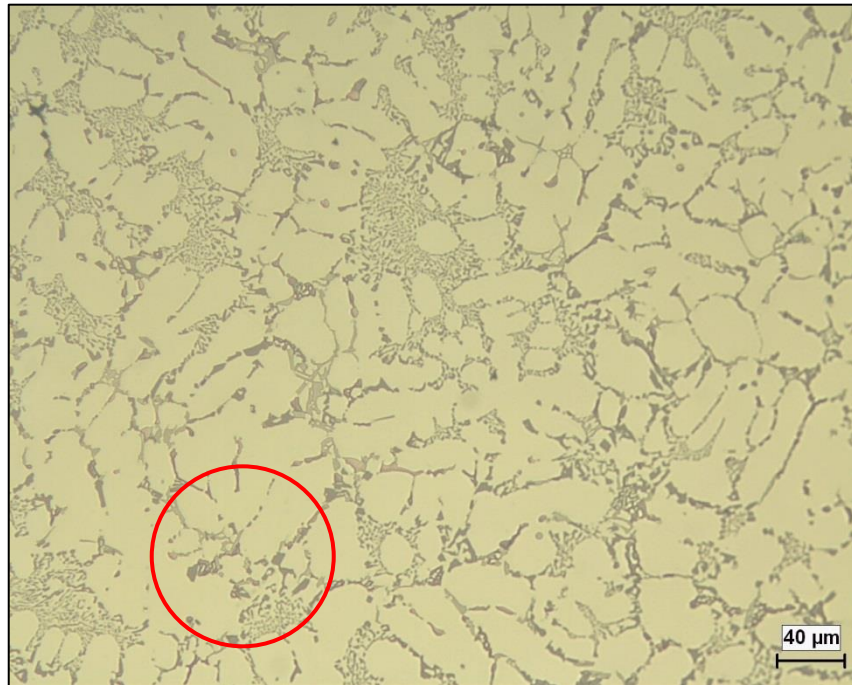


(a)

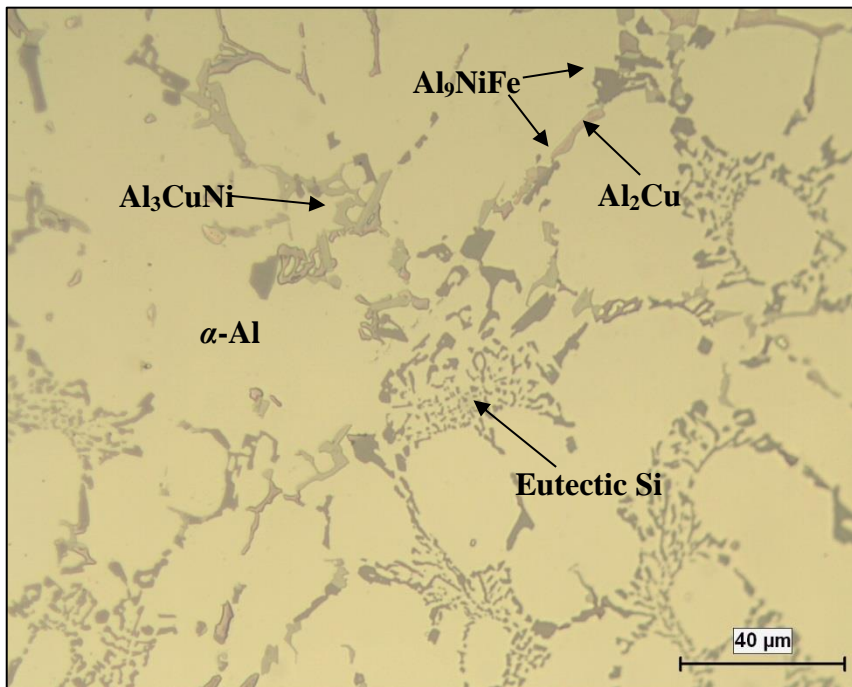


(b)

Figure 4.1 Optical micrographs of a tensile test specimen of the base alloy G1 showing the as-cast microstructure at (a) low (200X) magnification, and (b) high (500X) magnification.



(a)

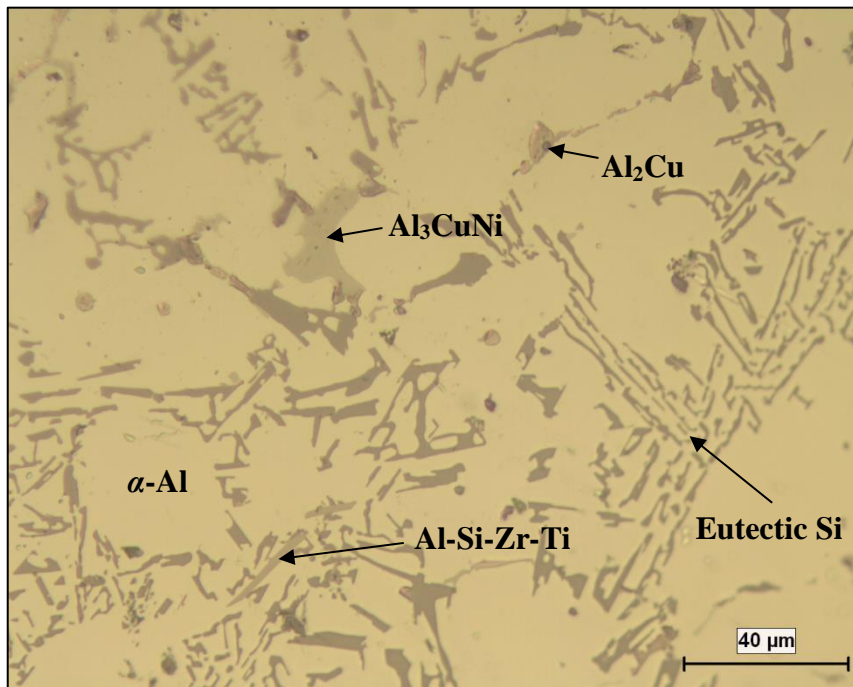


(b)

Figure 4.2 Optical micrographs of a tensile test specimen of alloy G2 (G1 + 0.4wt% Ni) showing the as-cast microstructure at (a) low (200X) magnification, and (b) high (500X) magnification.

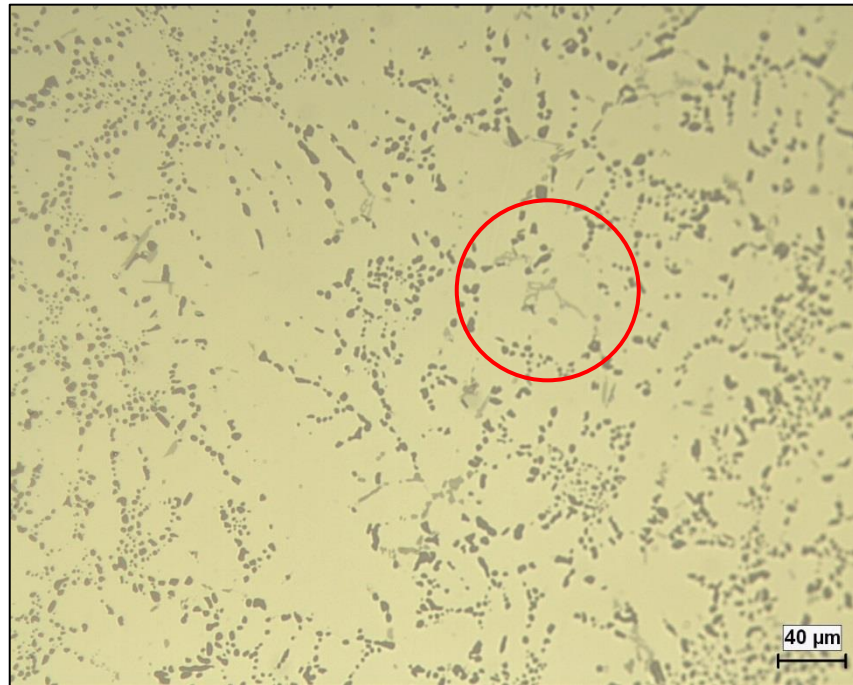


(a)

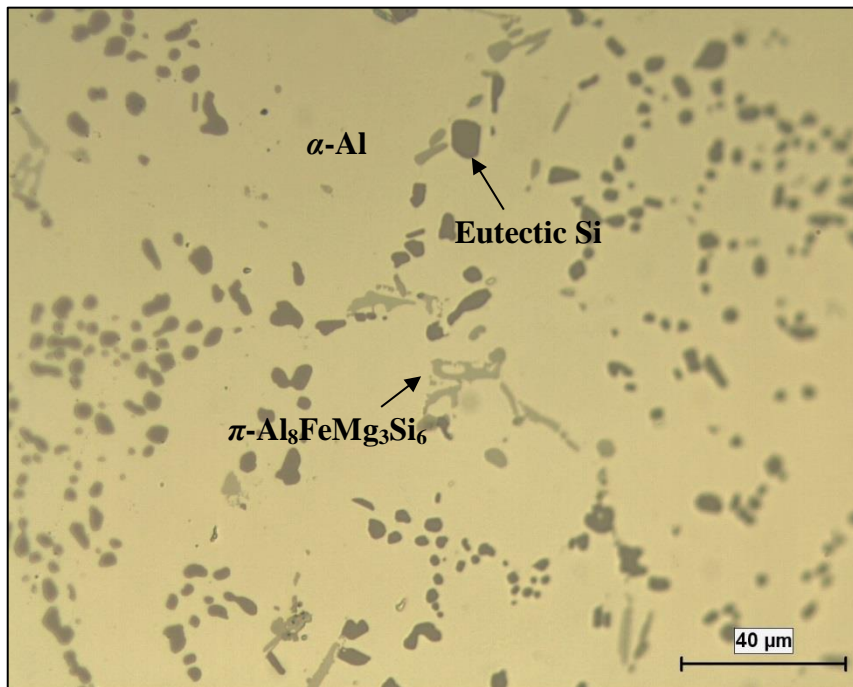


(b)

Figure 4.3 Optical micrographs of a tensile test specimen of alloy G5 (G1 + 0.4wt% Ni + 0.4wt% Zr) showing the as-cast microstructure at (a) low (200X) magnification, and (b) high (500X) magnification.



(a)

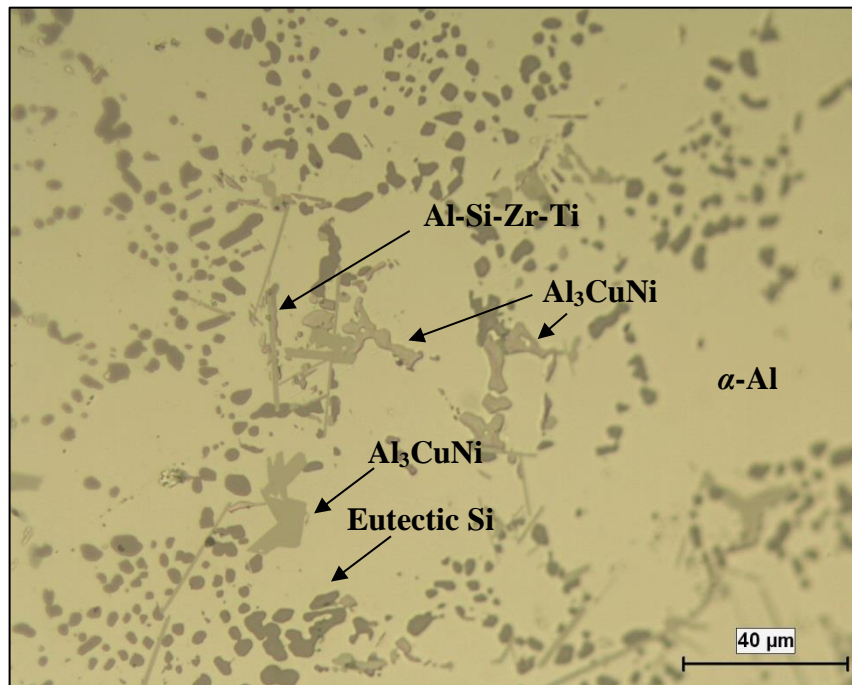


(b)

Figure 4.4 Optical micrographs of a T6 heat-treated tensile test specimen of the base alloy G1 showing the microstructure at (a) low (200X) magnification, and (b) high (500X) magnification.



(a)

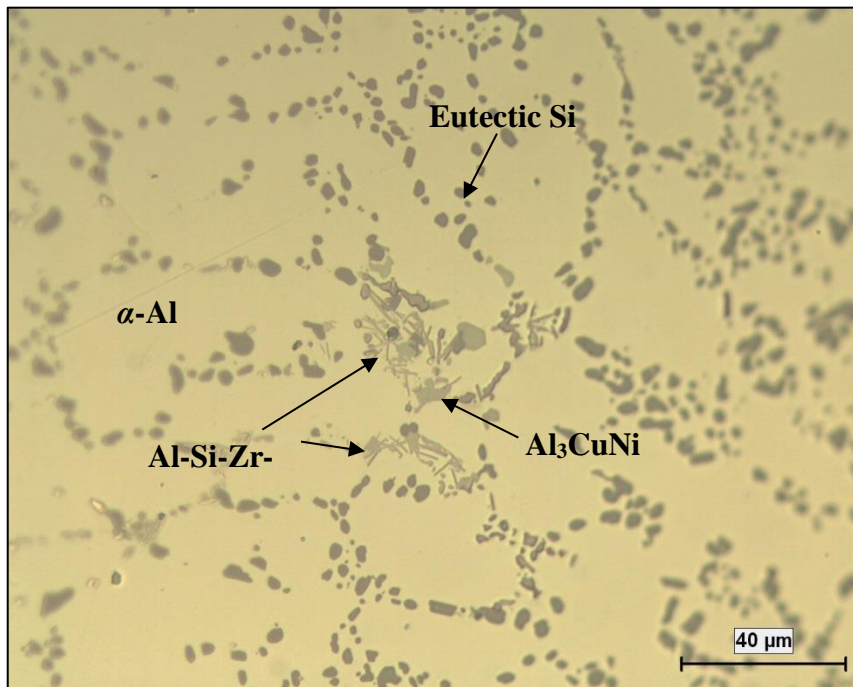


(b)

Figure 4.5 Optical micrographs of a T6 heat-treated tensile test specimen of alloy G2 (G1 + 0.4wt% Ni) showing the microstructure at (a) low (200X) magnification, and (b) high (500X) magnification.



(a)



(b)

Figure 4.6 Optical micrographs of a T6 heat-treated tensile test specimen of alloy G5 (G1 + 0.4wt% Ni + 0.4wt% Zr) showing the microstructure at (a) low (200X) magnification, and (b) high (500X) magnification.

before casting), chemical modification using Sr additions is the most popular as the resulting eutectic silicon phase is very fine and fibrous, attributing to improvement in the mechanical properties.

In this study, the alloys used were modified employing about ~170 ppm strontium. Therefore, it is expected that the microstructure even in the as-cast condition should have refined eutectic silicon particles with fine primary aluminum grains, the solidification rate of the casting process being relatively high enough to prevent a dendritic or columnar grain structure appearing in the microstructure. In addition, since the alloy contains 200 ppm Ti, the grain size is small.

4.3 EVALUATION OF TENSILE PROPERTIES IN AS-CAST AND T6 CONDITIONS

The mechanical properties of a casting are initially determined by the microstructure obtained upon solidification (as-cast condition), and may be improved thereafter by subjecting the casting to a suitable heat treatment process. By following the evolution of the microstructure during the process, the heat treatment conditions may be optimized. The most widely used thermal treatment for industrial applications is the T6-treatment.²²³

Ammar *et al.*²²³ reported that improvement in the mechanical properties of 354 and 355 alloys may be attributed to the addition of strontium, where the fine fibrous structure of the modified Si particles assists in increasing the alloy strength and ductility. In the current research, the addition of strontium to the 354 base alloy G1 and derived alloys caused significant improvement in their mechanical properties.

The T6 heat treatment used in this study consisted of solution heat treatment at 505°C for 8 h, followed by quenching in warm water (60°C) and immediate aging at 190°C for aging times of 2 h, 10 h, 40 h and 100 h. The temperature selected for the solution heat treatment might appear to be over-conservative but it was deemed necessary to avoid any risk of incipient melting of the copper phases, which could have the potential for deteriorating the mechanical properties of the alloys to a great extent. Increased strength after the treatment is normally to be observed in similar 354 alloys which use a solution heat treatment temperature of 525°C, over a 2-3 hour period, in conjunction with analogous aging treatments.²³²

All tensile testing for Stage I alloys was carried out at a strain rate of $4 \times 10^{-4} \text{ s}^{-1}$, using an Instron Universal Mechanical Testing machine, where the testing was carried out at room temperature for the as-cast and T6 heat-treated test bars of these alloys. Figure 4.7 shows the ultimate tensile strength (UTS) and yield strength (YS), as well as the percentage elongation (%El) values obtained at room temperature for the different alloys/conditions. The X-axis represents the alloy condition (as-cast and T6-treated for aging times of 10 h, 40 h and 100 h). The primary Y-axis represents the strength values (UTS and YS), while the secondary Y-axis represents the percentage elongation value obtained for each condition studied.

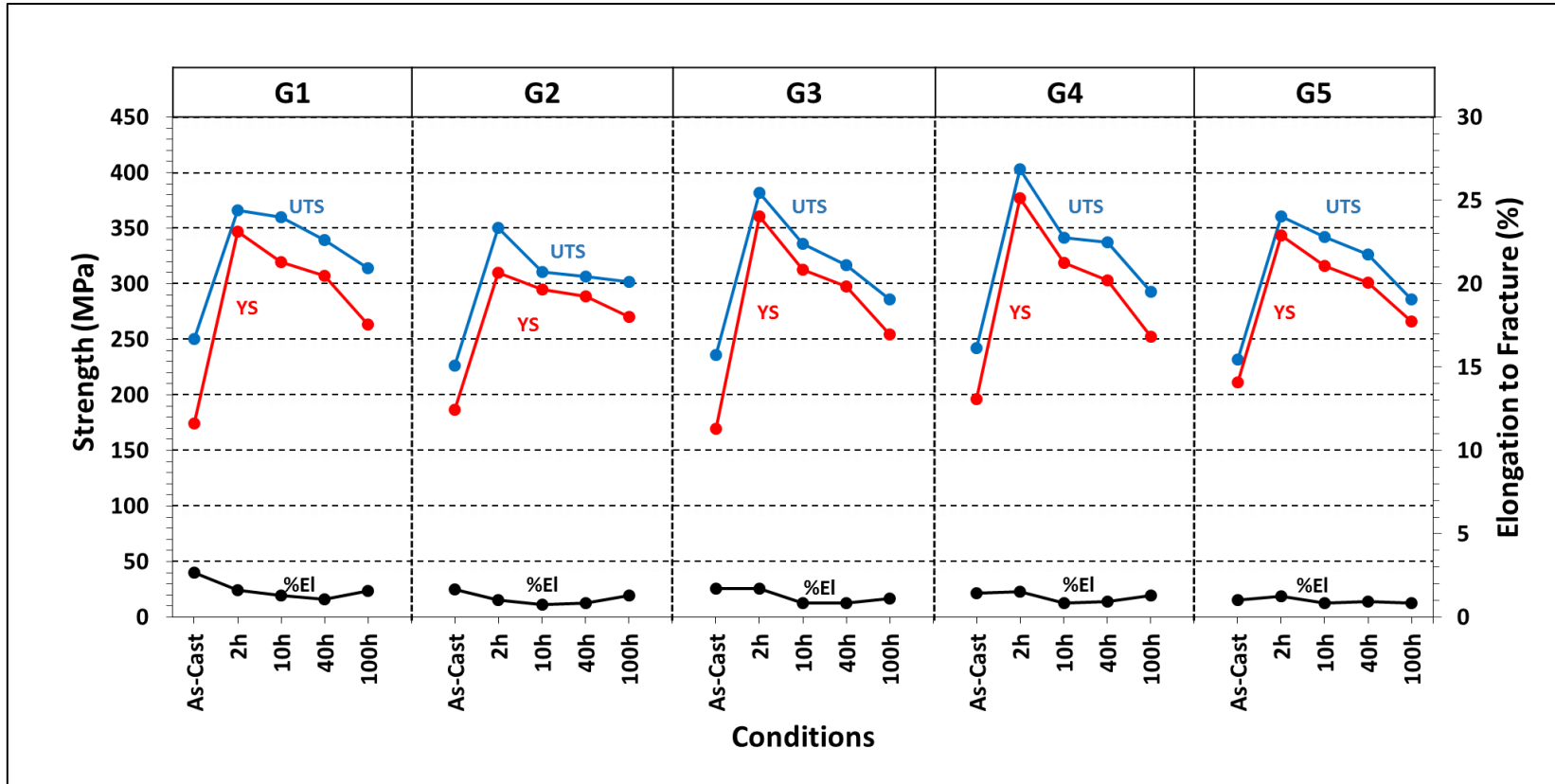


Figure 4.7 Average values of ultimate tensile strength (UTS), yield strength (YS), and percentage elongation to fracture (%El) obtained from Stage I alloys (G1 to G5) in the as-cast and T6-treated condition for different aging times at 190°C aging temperature (Testing was done at room temperature).

From Figure 4.7, it will be observed that the strength values for the as-cast alloy samples exhibit tensile strength values of 225-250 MPa, giving a difference of about 10-25 MPa between the base alloy G1 (UTS 250.03 MPa) and the remaining alloys G2 (226.34 MPa), G3 (236.16 MPa), G4 (241.87 MPa) and G5 (232.07 MPa). The solution heat treatment temperature of 505°C in combination with the aging temperature/time (190°C/2h) increases the alloy strength (UTS and YS) while maintaining more or less the same ductility as that observed in the as-cast case.

After T6 treatment, the strength values increase significantly, reaching peak strength in each case. The yield strength follows the same trend, exhibiting somewhat lower values compared to UTS. Alloy G4 (containing 0.2wt% Ni + 0.2wt% Zr) shows the maximum increase in tensile properties with a UTS of 402.93 MPa, followed by a UTS value of 381.87 MPa for alloy G3 (containing 0.4wt% Zr); alloy G5 (containing 0.4wt% Ni + 0.4wt% Zr) displays a UTS value slightly lower than that of the base alloy G1 (360.71 MPa vs. 365.97 MPa). On the other hand, G2 (containing 0.4wt% Ni) alloy displays strength values that are lower than those exhibited by the base alloy in the as-cast, T6 and other aging conditions shown in the figure.

Increase in aging time from 10 h to 100 h during T6 heat treatment continually lowers the alloy strength; the ductility is also lowered to a slight extent. Apparently, aging time is a crucial factor that has a significant effect on the alloy strength, in particular the yield strength, causing it to reduce by as much as ~100 MPa, the only exception being the G2 alloy where the decrease with aging time is much slower.

A decrease in the tensile properties of Al-Si-Cu-Mg alloys upon the addition of increasing amounts of Ni has been noted in the related literature.^{233, 234} This decrease in strength through the addition of nickel is attributed to the interaction between copper and nickel to form precipitates of Al₃CuNi in the microstructure, normally present in the alloys containing Ni, namely, G2, G4 and G5 alloys. Since copper, as well as magnesium, determine the precipitation strengthening of Al-Si-Cu-Mg alloys, the formation of the Al-Cu-Ni precipitates would thus subtract part of the copper content available for strengthening through the formation of Al₂Cu precipitates.²⁰ This is the principal reason for which a slight decrease in YS is observed with the addition of 0.4wt% Ni in G2 and G5 alloys.

The formation of Al-Cu-Ni and other precipitates will be elaborated upon in the following sections. It has also been reported²⁰ that nickel interacts with iron and copper forming the Al₉NiFe and Al₃CuNi phases; such phases would act as stress concentrators provoking instability in the flow strain, thereby reducing the ductility of the alloy. As was shown in Table 4.1, the percentage of intermetallic phases containing nickel displayed an increase in the percentage of insoluble phases from 3.08% in alloy G1 to 4.22% in alloy G2. Solution heat treatment applied to 354 alloys is considered to be a critical process because of the low melting point of the Al₂Cu phases present in the alloy. Keeping the solutionizing temperature at 505°C helped to avoid reduction in the tensile properties resulting from the incipient melting of the ternary eutectic structure α -(Al)-Si-Al₂Cu and subsequent formation of high levels of shrinkage porosity after quenching.

4.4 EVALUATION OF TENSILE PROPERTIES AT HIGH TEMPERATURE

Based on previous investigations carried out by Hernandez-Sandoval¹⁹ on 354 alloys, where it was found that the optimum metallurgical conditions for the high temperature tests (carried out on samples in the T6 (190°C/2h) condition corresponded to 155°C and 300°C testing temperatures for holding times of 10 h to 100 h, in the present study, therefore, the same two temperatures were selected for the high temperature testing of Stage I alloys, using holding times of 10, 40 and 100 hrs.

While Cu and Mg are added to improve the room and high temperature strength, the development of intermetallic phases including θ -(Al₂Cu), β -(Mg₂Si), π -(Al₈Mg₃FeSi₆), Q -Al₅Cu₂Mg₈Si₆, α -(Al₁₅(Mn,Fe)₃Si₂) and β -(Al₅FeSi) in these alloys promotes alloy strengthening, however at the expense of ductility. In this context, iron impurities are the most detrimental as they lead to the development of relatively large π -(Al₈Mg₃FeSi₆), β -(Al₅FeSi) and α -(Al₁₅(Mn,Fe)₃Si₂) brittle intermetallics, with the π - and β -iron phases being the most harmful phases in terms of mechanical integrity.^{194, 235}

Tensile tests were performed at different temperatures to acquire knowledge of the effect of the Zr and Ni additions on the high temperature mechanical performance of the 354 alloys, as shown in Figure 4.8. It is observed that alloys G1 to G5 did not show any significant change in UTS and YS at 155°C for holding times of 10, 40 and 100 hours. The amount of research studies which have been carried out on aluminum alloys with Zr additions indicates that a reduction in the grain size as well as an increase in the strength of

alloy G3 with respect to the base alloy is to be expected.¹⁴⁹⁻¹⁵¹ While the addition of 0.4wt% Zr did indeed reduce the grain size, no increase in the resistance of the alloy was observed. Therefore, at 155°C testing temperature and for holding times of up to 100 h, it could be said that, overall, the five alloys display strengths of ~300 MPa UTS, ~293 MPa YS, and a ductility of ~1.75%.

At a higher testing temperature of 300°C and for holding times up to 100 h, the morphologies of the Zr-rich and Ni-rich intermetallic phases had a harmful influence on the mechanical properties. The presence of 0.4wt% Ni + 0.4wt% Zr in alloy G5 was not sufficient to resist softening at 300°C at 100 h, so that the alloy strength decreased to 52 MPa UTS and 45 MPa YS, while the ductility increased to 23%.

At 300°C, for the proposed holding times, the alloy strength begins to decrease from ~75 MPa for the 10 h-holding time, to reach ~53 MPa after 100 h-holding time for all alloys. The YS showed the same behavior as UTS. The most important results obtained at 300°C after holding at 100 h are the high ductility values exhibited by all the alloys, with alloys G1, G2, G3, G4 and G5 showing percent elongation values of 28.4%, 27.1%, 23.2%, 27%, and 22.6%, respectively.

Alloy G4, containing 0.2wt% Ni and 0.2wt% Zr, displays greater strength than alloy G3, which contains 0.4wt% Zr, or greater even than alloy G5, which contains 0.4wt% Ni and 0.4wt% Zr. The main difference which appears upon examining the Zr-content of alloys G3, G4, and G5, involves the fact that alloy G4 is a hypo-peritectic alloy.²³⁶ According to the Al-Zr phase diagram of Figure 2.15,^{161, 162} at 0.2wt% Zr content, the

liquidus temperature is approximately 720°C. Taking into consideration the fact that the temperature of the melt was 760°C during casting, it is fairly likely that the added Zr dissolved completely. Having a completely dissolved Zr-master alloy in the melt would be the first step in obtaining alloy strengthening by means of Zr-rich precipitates. This argument is congruent with the percentage of insoluble phases observed in the matrix for the as-cast condition (presented in Table 4.1), which displays smaller values upon comparison with the alloys containing additions of Ni and/or Zr, namely alloys G3 and G5.

As was observed in the work of Knipling¹⁶³ with Al-Zr and Al-Zr-Ti alloys, Zr-rich nanoparticles precipitate during solidification forming coherent precipitates which are coarsening-resistant at temperatures in the order of 275°C - 425°C; such Zr-rich particles would improve the mechanical properties at 300°C of alloy G5 in the as-cast condition. It is possible that alloy G5 in T6 condition did not display the same properties as in the as-cast condition. This apparent contrast in behavior can be explained by the fact that the alloys in the T6 condition were submitted to a solution heat treatment at 505°C. Such temperature would change the coherency of the Zr-rich precipitates formed during the solidification of alloy G5.¹⁹

It ought to be noted here that in Figures 4.8 and 4.9, the various points representing the three tensile properties in these figures are linked together for all conditions represented on the X-axis even if they vary from room temperature to the two high temperatures at which testing was carried out.

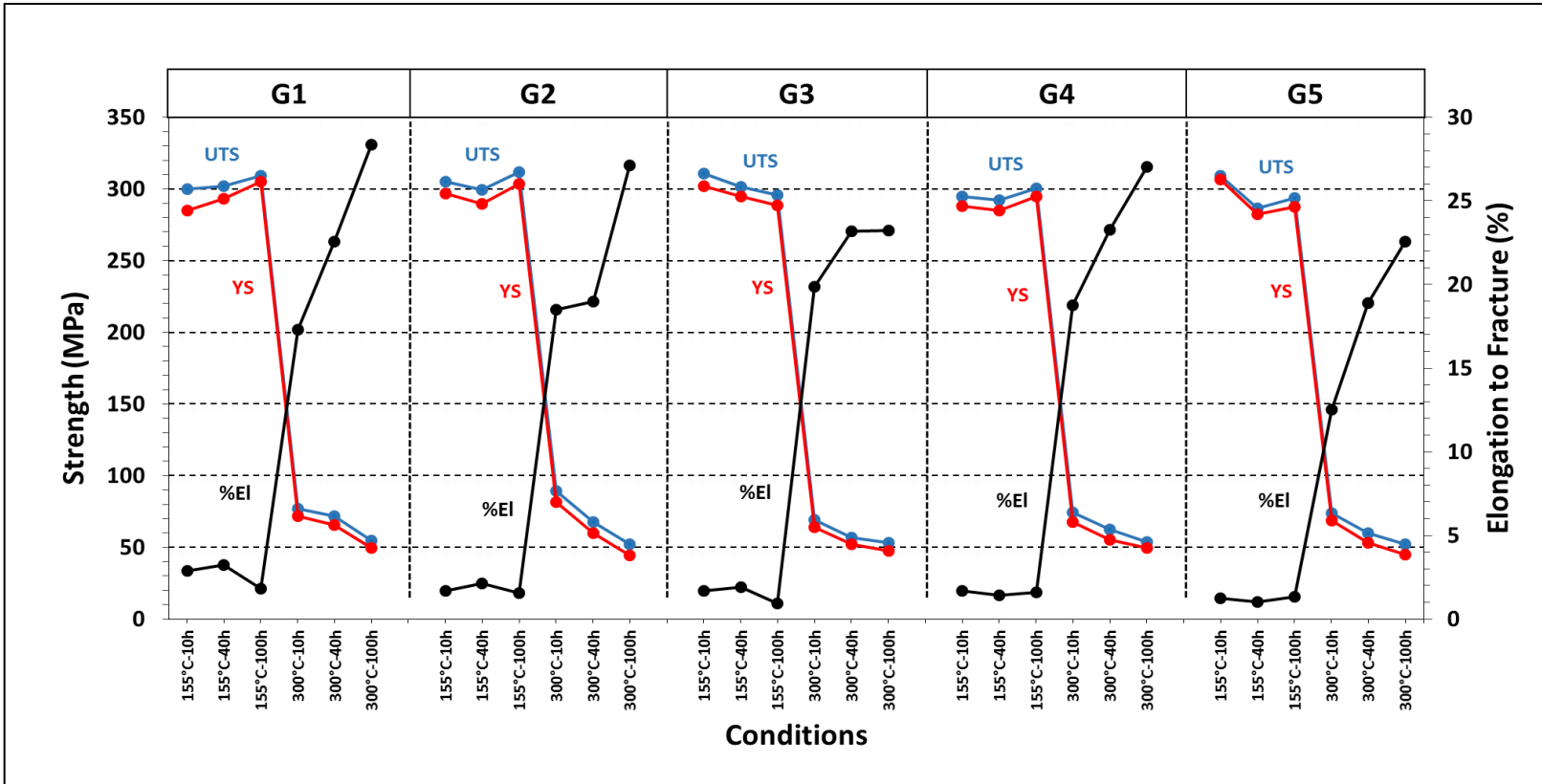


Figure 4.8 Average values of ultimate tensile strength (UTS), yield strength (YS), and percentage elongation (%El) obtained for the Stage I alloys (G1 to G5) tested at high temperature under different conditions.

4.5 COMPARISON BETWEEN AMBIENT AND HIGH TEMPERATURE TESTING RESULTS

In general, an improvement in the mechanical properties of Cu- and Mg-containing aluminum alloys is attributed to the formation of age-hardening compounds Al_2Cu and Mg_2Si , respectively, which precipitate from the solid solution during aging. The degree of strengthening depends on the copper and magnesium content, and an increase in strength due to higher levels of these elements is always accompanied by a corresponding decrease in ductility. The application of an aging treatment to these alloys causes an entire range of precipitates to form according to the temperature and time applied. Variation in chemical composition within the specific limits of the alloy, casting soundness, metallurgical characteristics (*viz.*, grain size, constituent distribution and eutectic modification), solidification rate and the type of heat treatment applied are different variables which control the mechanical properties.²³⁷ As it is possible to control grain size, constituent distribution and eutectic modification, major variations in mechanical properties then depend on/come from the ability to control shrinkage and solidification rates in the casting.

Figure 4.9 compares the tensile properties in the as-cast and T6 heat-treated conditions with those at testing temperatures of 25°C, 155°C and 300°C. The solution treatment temperature of 505°C in combination with the 190°C/2 h aging condition used in this work increased the alloy strength (UTS and YS) while maintaining more or less the same ductility as that observed in the as-cast case. After T6 treatment, alloy G4 (containing 0.2wt% Ni + 0.2wt% Zr) showed the maximum increase in tensile properties, followed by

alloy G3 (containing only 0.4wt% Zr). In the case of alloy G4 (containing 0.2wt% Ni + 0.2wt% Zr), the UTS, YS and %El values increase by ~161 MPa, ~181 MPa, and 0.10%, respectively.

As Figure 4.9 shows, increase in aging time from 10 h to 100 h during T6 heat treatment continually lowers the alloy strength; the ductility is also lowered to a slight extent. This trend continues at the 155°C and 300°C high testing temperatures, until, for the tests carried out at 300°C after 100 h-holding time, the UTS and YS values are reduced for the five alloys, whereas the ductility increases on account of alloy softening. Compared to the T6 condition, the closest tensile properties obtained are those exhibited by alloy G2 at 155°C/100 h-holding time.

Taking the five alloys into consideration, from Figure 4.9, over the three holding times, the average tensile properties for the alloys may be considered to be 300 MPa UTS, 293 MPa YS, and 1.75% elongation at 155°C, respectively. As may be noted, the presence of 0.4wt% Ni + 0.4wt% Zr (in G5 alloy) was not sufficient to resist softening at 300°C/100h, with the alloy displaying strength values of 52 MPa UTS, 45 MPa YS, and a ductility of 22.5%.

At 300°C, for the proposed holding times, the alloy strength begins to decrease from ~75 MPa for the 10 h-holding time, to reach ~53 MPa at 100 h-holding time for all alloys. The most important results obtained at 300°C after holding at 100 h are the high ductility values exhibited by all the alloys, with alloys G1, G2, G3, G4 and G5 showing percent elongation values of 28.4%, 27.1%, 23.2%, 27%, and 22.6%, respectively.

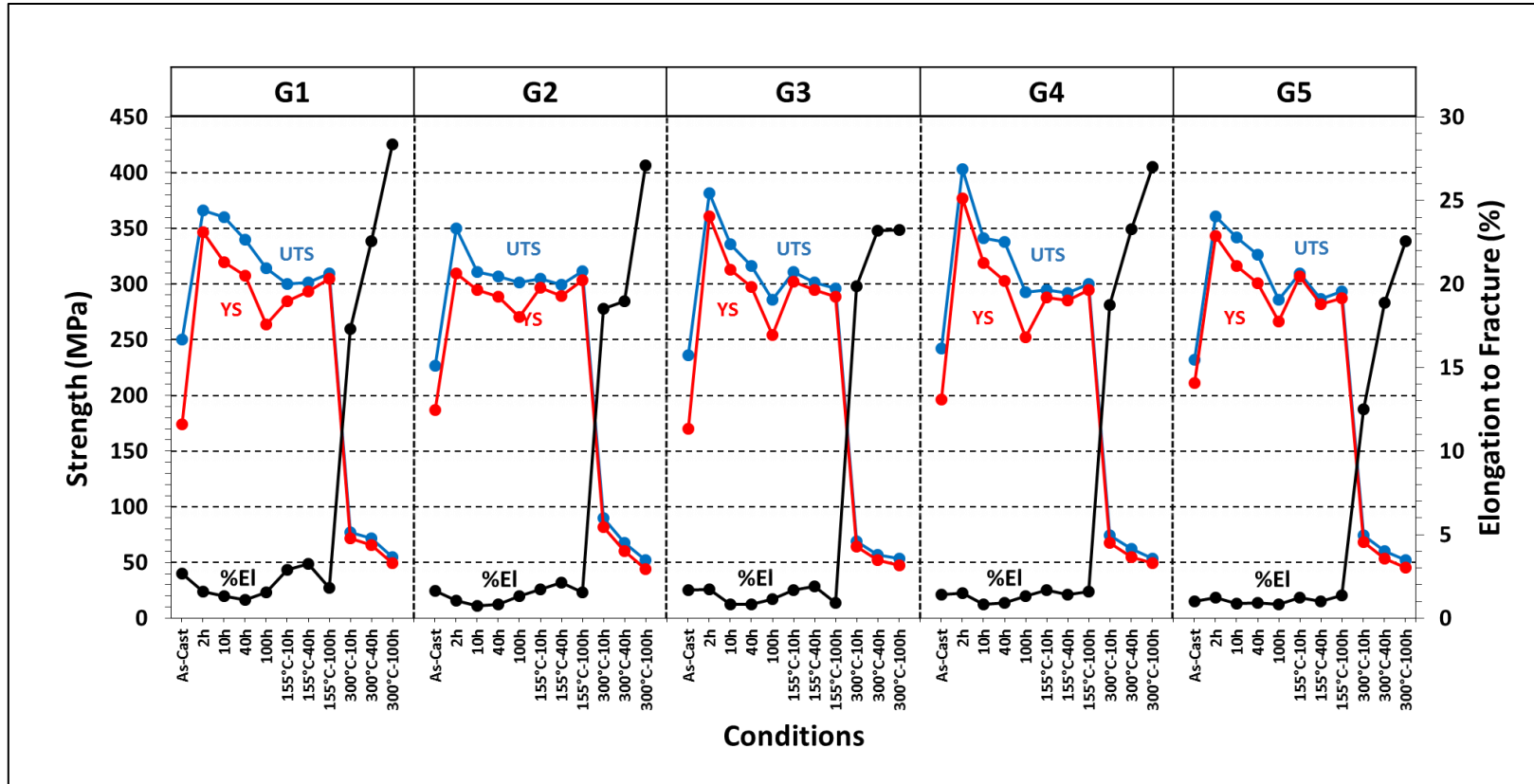


Figure 4.9 Average values of ultimate tensile strength (UTS), yield strength (YS), and percentage elongation (%EI) for the Stage I alloys (G1 to G5) tested under different conditions at room and at high temperature.

4.6 FRACTOGRAPHY

Fractography involves the detailed analysis of the fracture surface of a tested sample, so as to determine the cause of the fracture and the relationship of the fracture mode to the microstructure of the sample material itself. Examination of the fracture surface may be carried out using an optical microscope or a scanning electron microscope (SEM). A knowledge of fracture behavior is of crucial importance when upgrading material specifications and improving product design.

4.6.1 SEM ANALYSIS OF FRACTURE SURFACES

The fracture surfaces of samples of selected alloys were examined using scanning electron microscopy (SEM) in order to find the features responsible for crack initiation. Fracture surfaces of Al-Si-Cu casting alloys can be observed by means of SEM without almost any special preparation; however, it is very important that the specimens should be examined immediately after failure because of the very fast superficial oxidation of Al alloys. Fracture surfaces of tested bars of G1, G2 and G5 alloys in the as-cast and T6 heat-treated conditions (comprising solution treatment at 505°C/8 h, quenching in warm water at 60°C, artificial aging at 190°C/2 h), and those obtained from 300°C/100 h high temperature testing were examined and EDS spectra corresponding to features of interest were obtained, and are documented in Figure 4.10 through Figure 4.18. Backscattered electron (BSE) images and secondary electron (SE) images were deemed suitable for highlighting the various features observed on the fracture surfaces. Backscattered electron images provide information regarding the fracture surface morphology where the image contrast is

sensitive to the atomic mass of the material. Secondary electron images, on the other hand, provide information about the topography of the fracture surface and are not sensitive to the atomic mass of the material.²³⁸

Copper in Al-Si-Cu-Mg cast alloys is present primarily in the form of θ -Al₂Cu, Al-Al₂Cu-Si or Q -Al₅Mg₈Cu₂Si₆ phases. The average size of these Cu-phases decreases upon Sr modification.²³⁹ In the alloys examined, two types of Cu-rich intermetallic phases were observed: Al₂Cu and Al₃CuNi. With the application of T6 heat treatment, the fibrous Si particles are fragmented into smaller particles which become spheroidized during solution heat treatment at 505°C, whereas during aging these spheroidized particles grow progressively larger (coarsening). Fracture is transcrystalline ductile with fine dimple morphology. Apart from the hard microconstituents (intermetallic and Si particles) in the matrix which act as stress concentration/crack nucleation sites, the presence of casting defects such as inclusions, oxides and porosity can also lead to failure, particularly if these defects are large in size.

Figure 4.10(a) is a secondary electron (SE) image of the as-cast G1 base alloy sample, showing a fracture surface which exhibits a well-defined dimple structure throughout. The backscattered electron (BSE) image in (b) reveals the presence of bright particles (circled). The associated EDS spectrum shows the presence of Al, Cu, Mg, and Si peaks, indicating that these particles correspond to the Q -Al₅Cu₂Mg₈Si₆ phase.

The fracture surface of the T6-treated G1 alloy sample is displayed in Figure 4.11. The dimples observed in the SE image of Figure 4.11(a) are relatively coarser than those-

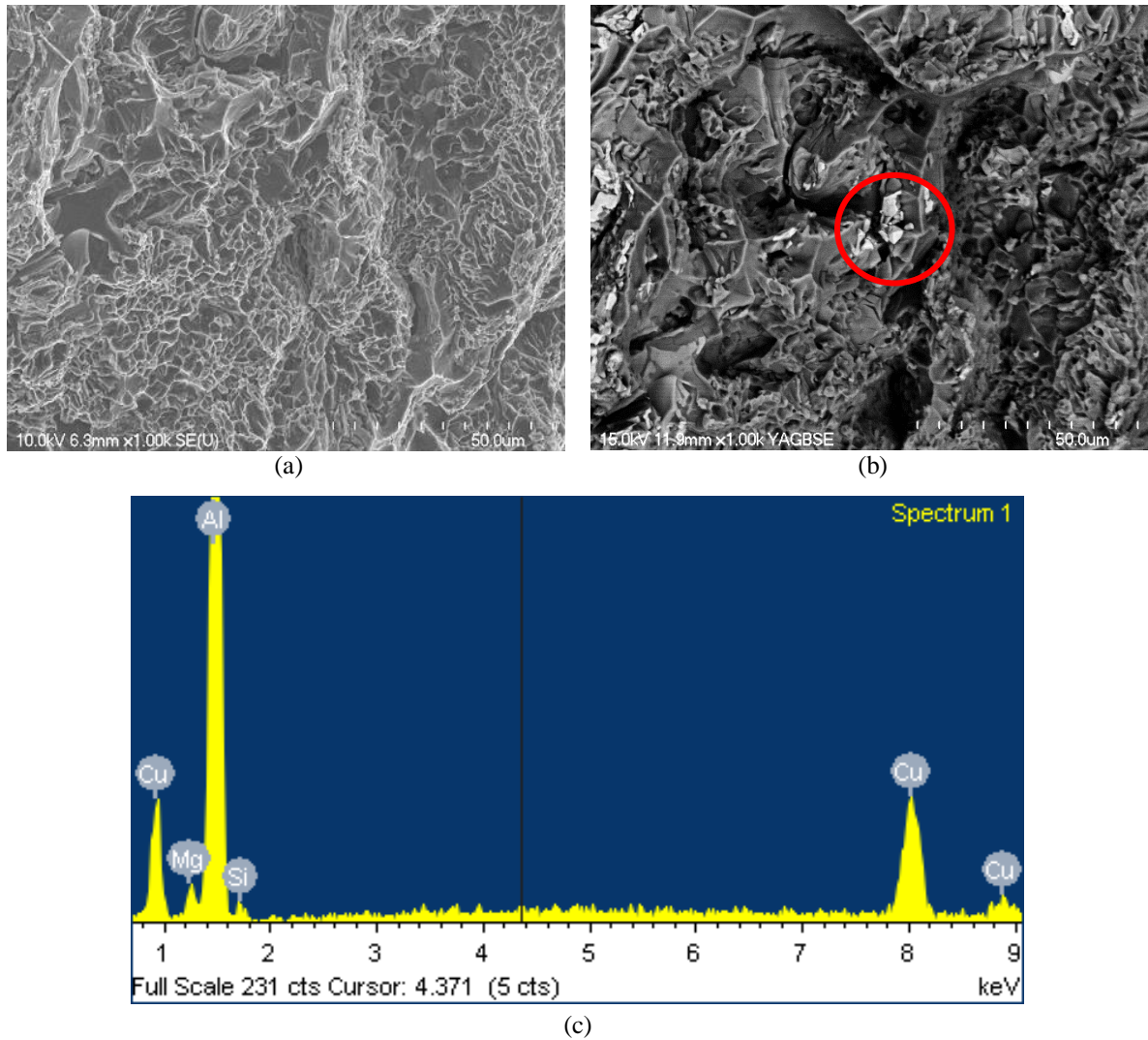


Figure 4.10 SEM images of the fracture surface of as-cast G1 alloy: (a) SE image showing a well-defined dimple structure, (b) BSE image showing presence of bright particles, and (c) EDS spectrum of the circled area in (b) showing the particles to be $Q\text{-Al}_5\text{Cu}_2\text{Mg}_8\text{Si}_6$ phase.

seen in Figure 4.10. The corresponding BSE image, Figure 4.11(b), reveals the presence of broken Si particles in the interiors of these dimples, whereas the high magnification BSE image of Figure 4.11(c) shows clearly the cluster of broken intermetallic particles observed

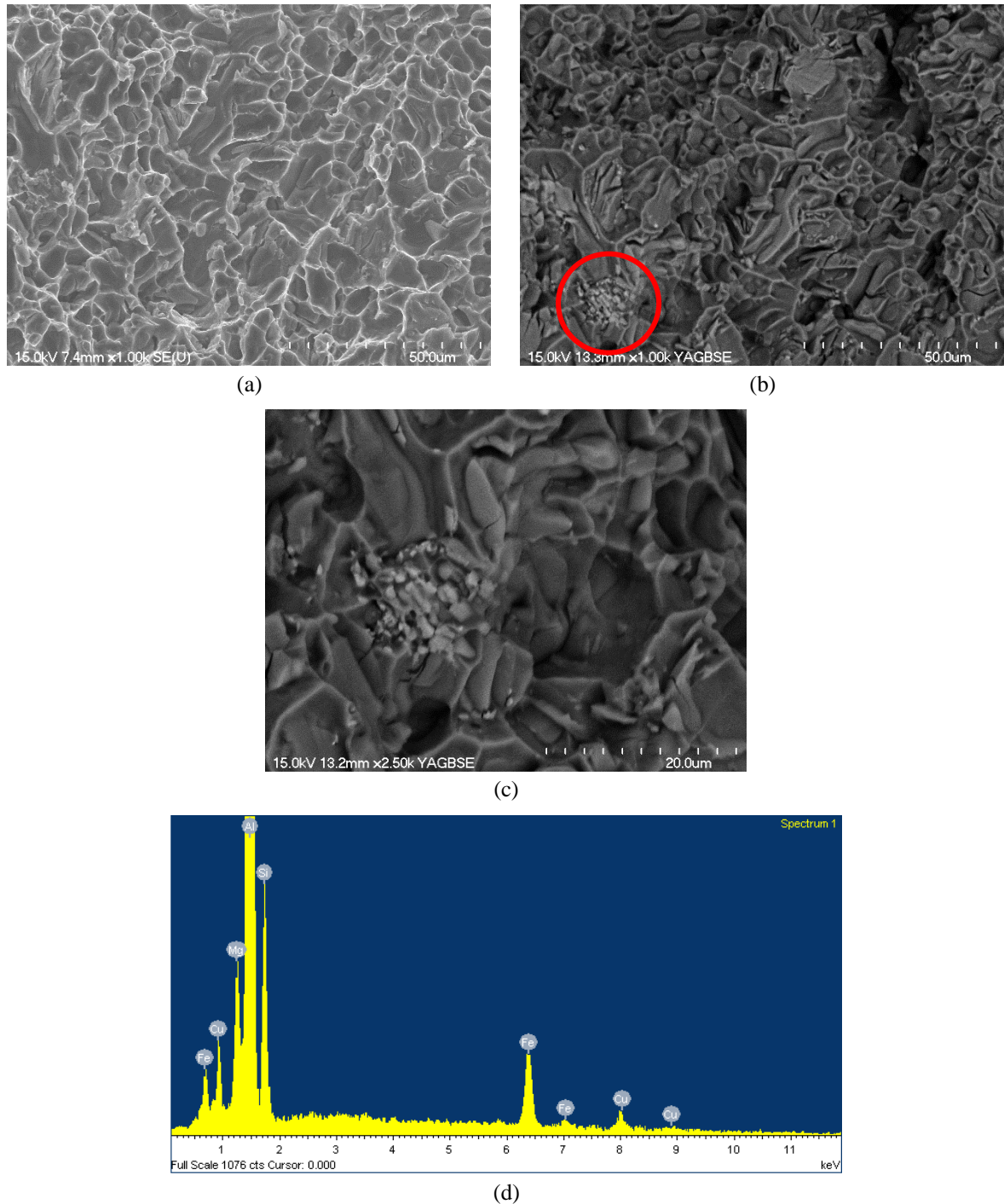


Figure 4.11 SEM images of T6-treated G1 alloy: (a) SE image showing coarser dimples, (b) BSE image showing presence of broken Si particles, (c) high magnification image of cluster of broken particles in circled area in (b), and (d) corresponding EDS spectrum showing these particles to be mainly π - $\text{Al}_8\text{FeMg}_3\text{Si}_6$ phase.

near the bottom left in (b), which were identified by EDS as corresponding mainly to the π - $\text{Al}_8\text{FeMg}_3\text{Si}_6$ phase, as shown in Figure 4.11(d).

Figure 4.12(a) shows the fracture surface of the G1 alloy sample that was tested at 300°C after 100h holding at testing temperature. The dimples observed in this case are very coarse and deep, indicating the improvement in the alloy ductility due to the softened condition of the alloy at this high temperature. The high magnification BSE image in Figure 4.12(b) reveals the presence of broken intermetallic particles in the interiors of the dimples. The particle in the circled area, for example, showed that these broken fragments corresponded to the Q - $\text{Al}_5\text{Cu}_2\text{Mg}_8\text{Si}_6$ phase, as was determined from the corresponding EDS spectrum shown in Figure 4.12(c).

Figure 4.13 depicts the fracture surface of the as-cast G2 alloy sample where the SE image in (a) reveals a fine dimple structure; the BSE image in (b) shows a Chinese script-like particle attached to a massive particle. The associated EDS spectrum shows reflections due to Al, Fe, Cu and Ni, which may be caused by the overlapping of AlNiFe and AlCuNi phases, or more precisely, Al_9NiFe and Al_3CuNi phases. It should be mentioned here that the atomic numbers of Cu and Ni are 28 and 29, respectively, which would produce the same brightness in both phases.

Figure 4.14 shows the fracture surface of G2 alloy sample in the T6 heat-treated condition. The SE image in (a) is characterized by a mixed rounded and elongated dimple structure. The BSE image of the same sample exhibits a large number of intermetallic particles within these dimples, as seen in Figure 4.14(b). Their approximate composition is

a mixture of AlCuNi and AlNiFe phases, as the EDS spectrum shown in Figure 4.14(c) indicates. It is well established that Ni has a strong affinity for, and hence tendency to react with, other transition elements; such phases would act as stress concentrators provoking instability in the flow strain, thereby reducing ductility.^{19, 20, 164}

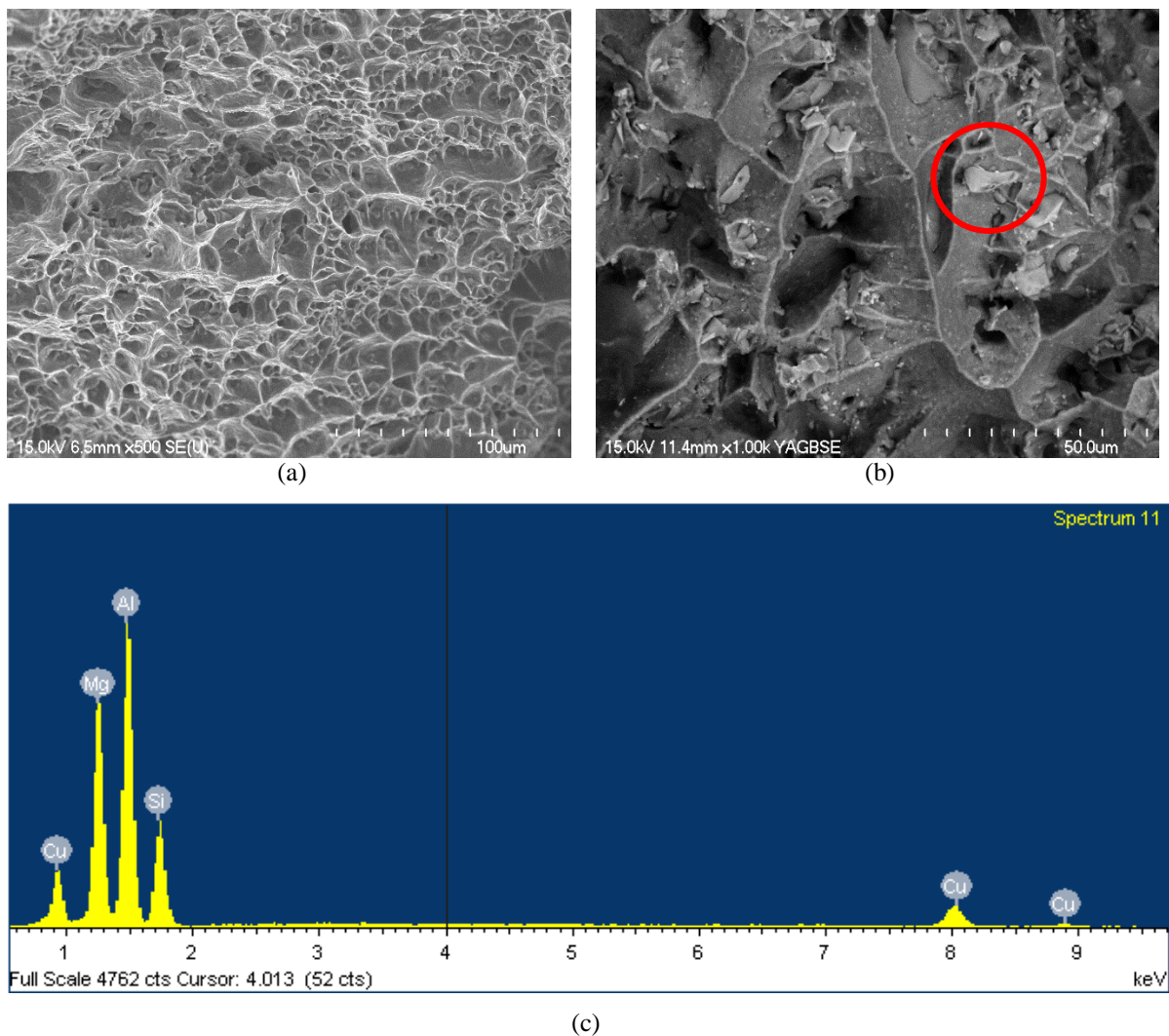


Figure 4.12 SEM images of fracture surface of G1 alloy tested at 300°C/100 h condition: (a) SE image showing very coarse and deep dimples, (b) BSE image showing presence of broken intermetallic particles, and (c) EDS spectrum of circled particle in (b) corresponding to Q -Al₅Cu₂Mg₈Si₆ phase.

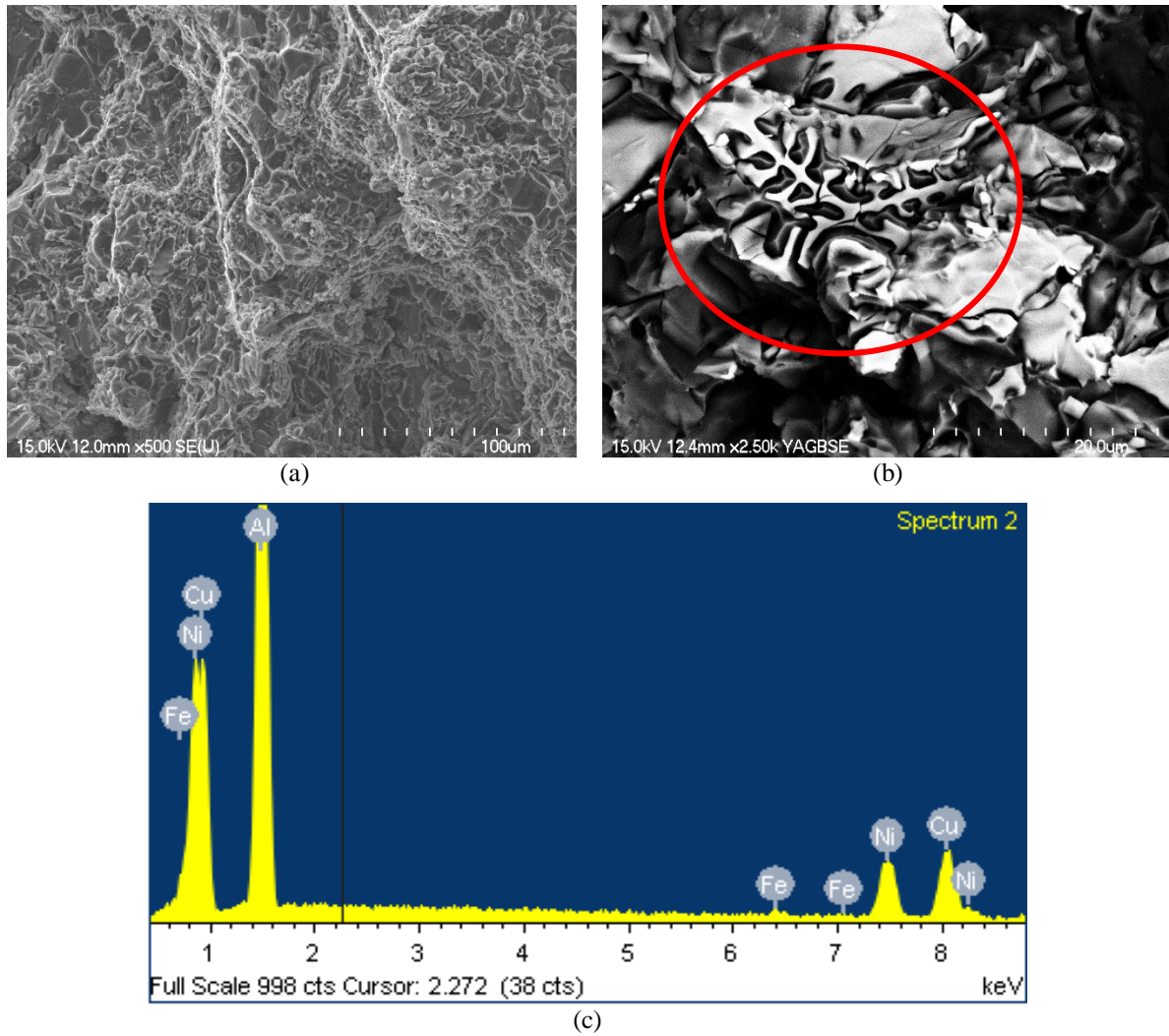


Figure 4.13 SEM images of fracture surface of as-cast G2 alloy: (a) SE image showing a fine dimple structure, (b) BSE image showing a large Chinese-script particle attached to a massive particle, and (c) EDS spectrum corresponding to the circled area in (b) revealing presence of Al_9NiFe and Al_3CuNi phases.

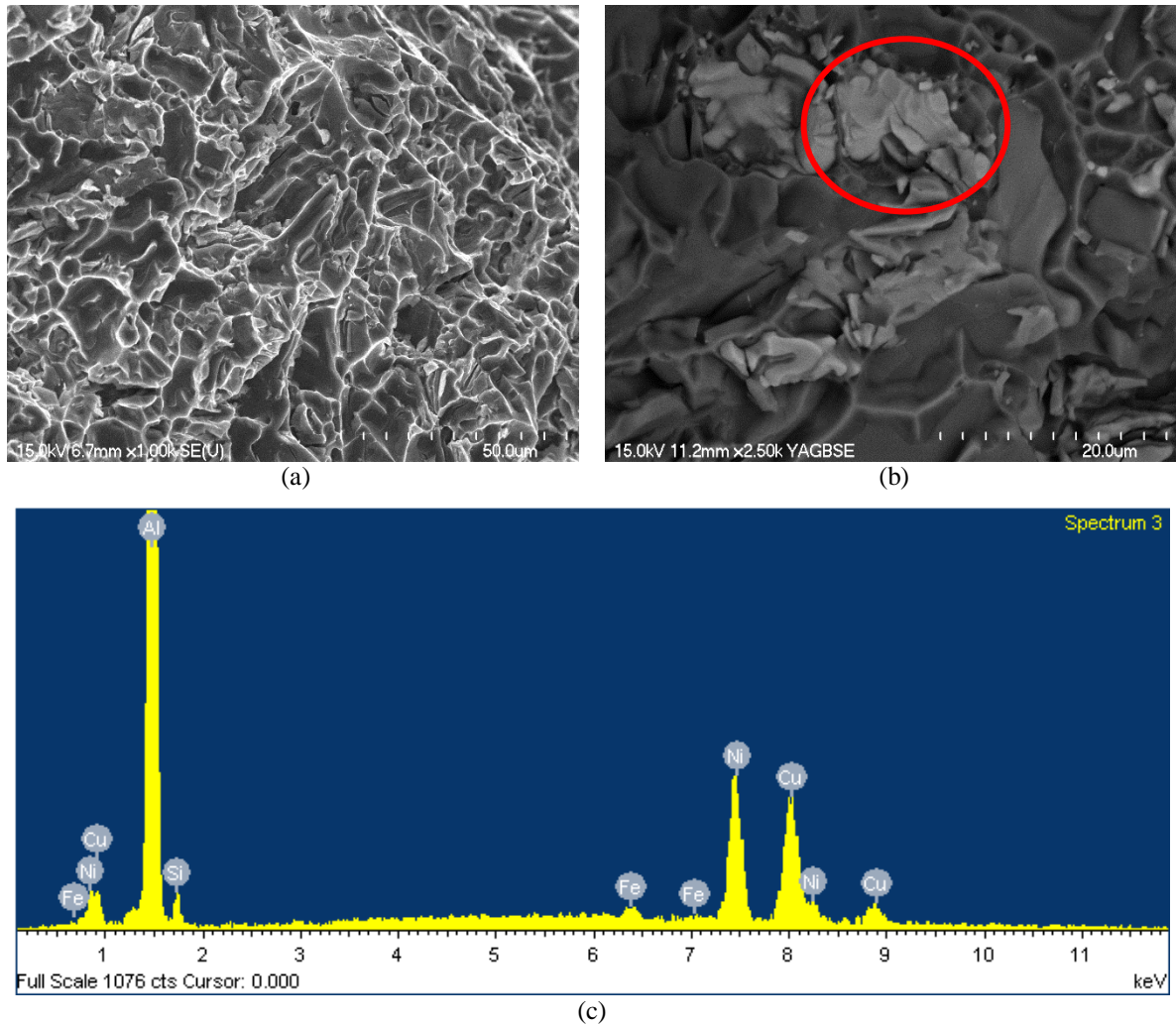


Figure 4.14 SEM images of fracture surface of T6-treated G2 alloy: (a) SE image showing a mixture of elongated and rounded dimples, (b) BSE image showing several intermetallic particles within the dimples, and (c) EDS spectrum of circled area in (b) revealing the particles to be a mix of Al_9NiFe and Al_3CuNi phases.

The SE image in Figure 4.15(a) shows the fracture surface of a G2 alloy sample after testing at the 300°C/100 h high temperature condition, and reveals the presence of large dimples with deformation lines on their surfaces, again an indication of the increase in alloy ductility. The corresponding BSE image in (b) shows the deformation lines more

clearly. Fine Si particles are also observed at the bottom of the dimples. The EDS spectrum taken from the circled area in (b) shows peaks for Al and Si. The fragmentation of the Si particles occurs during the course of plastic deformation.

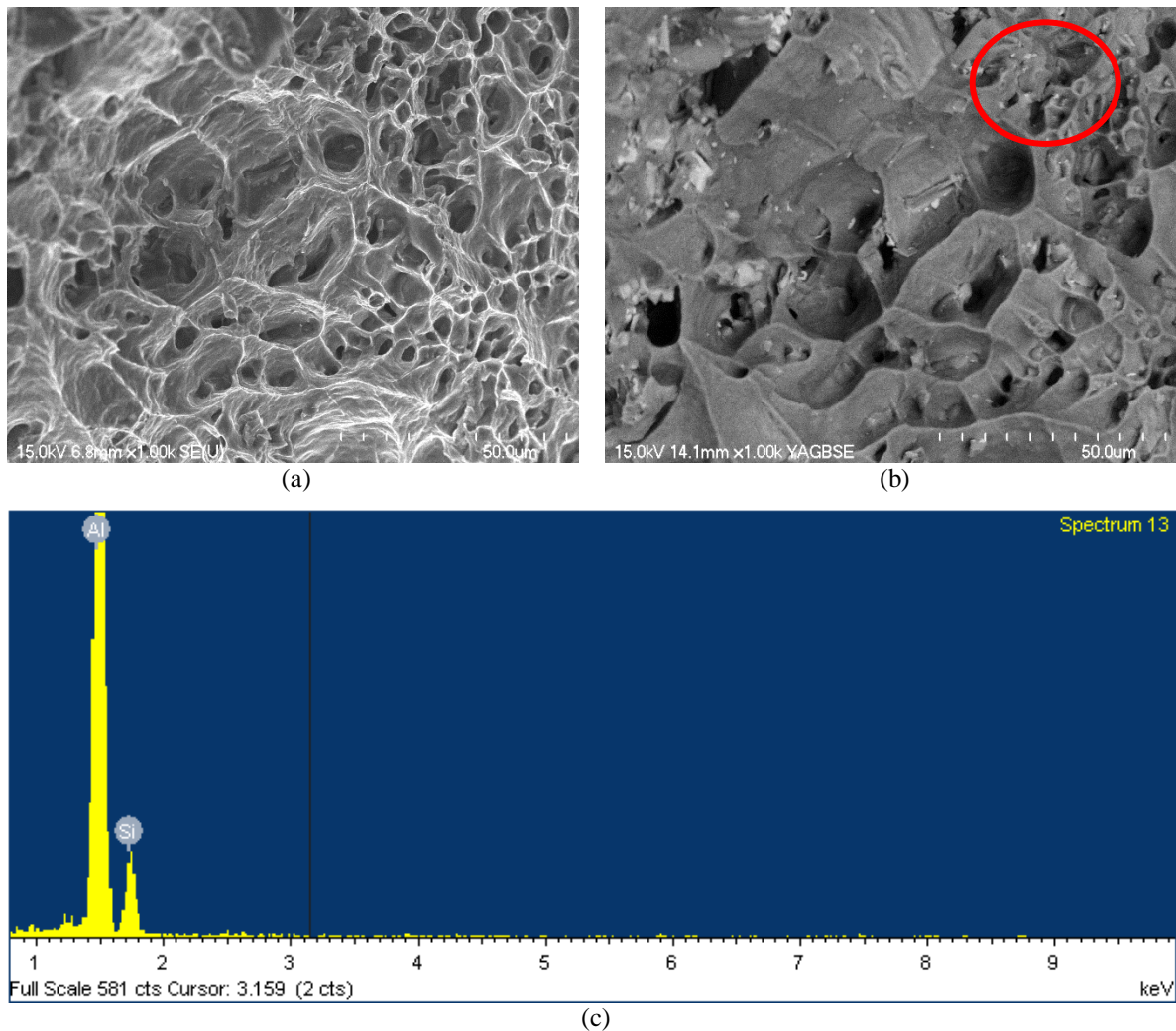


Figure 4.15 SEM images of fracture surface of G2 alloy tested at 300°C/100 h: (a) SE image showing large dimples with deformation lines on their surfaces, (b) BSE image showing the deformation lines more clearly, and (c) EDS spectrum of the circled area in (b) indicating the presence of eutectic Si phase particles.

Figure 4.16 displays the fracture surface of G5 alloy in the as-cast condition. The SE image in (a) shows the presence of some long Si particles which are the result of partial modification of the alloy. The BSE image in (b) shows a coarse bright plate-like particle, fractured into segments. The corresponding EDS spectrum shown in Figure 4.16(c) shows that these particles correspond to $\text{Al}_3(\text{Ti,Zr})$ phase.

Figure 4.17 shows the fracture surface features of the G5 alloy after T6 heat treatment. As may be observed from the SE image in (a), a uniform dimple structure replaces the one observed in the as-cast alloy. Several grey plates of varying intensity are seen in the BSE image displayed in Figure 4.17(b). EDS spectra corresponding to the red and blue circled areas in (b) revealed that these phases are a mixture of Al_9NiFe , Al_3CuNi , and $(\text{Al})_3(\text{Ti,Zr})$ phases, Figure 4.17(c) and Figure 4.17(d).

Testing the G5 alloy at $300^\circ\text{C}/100$ h resulted in a similar dimple structure as that reported for the other alloys tested under the same condition, as shown in Figure 4.18(a). The BSE image in (b) however, revealed two types of precipitates: ultra-fine ones (see white circled area) and coarse particles (red circled area). From the EDS spectrum generated from the red circled area, these particles were found to be mixed fragments of the $\pi\text{-Al}_8\text{FeMg}_3\text{Si}_6$, Al_9NiFe , and Al_3CuNi phases.

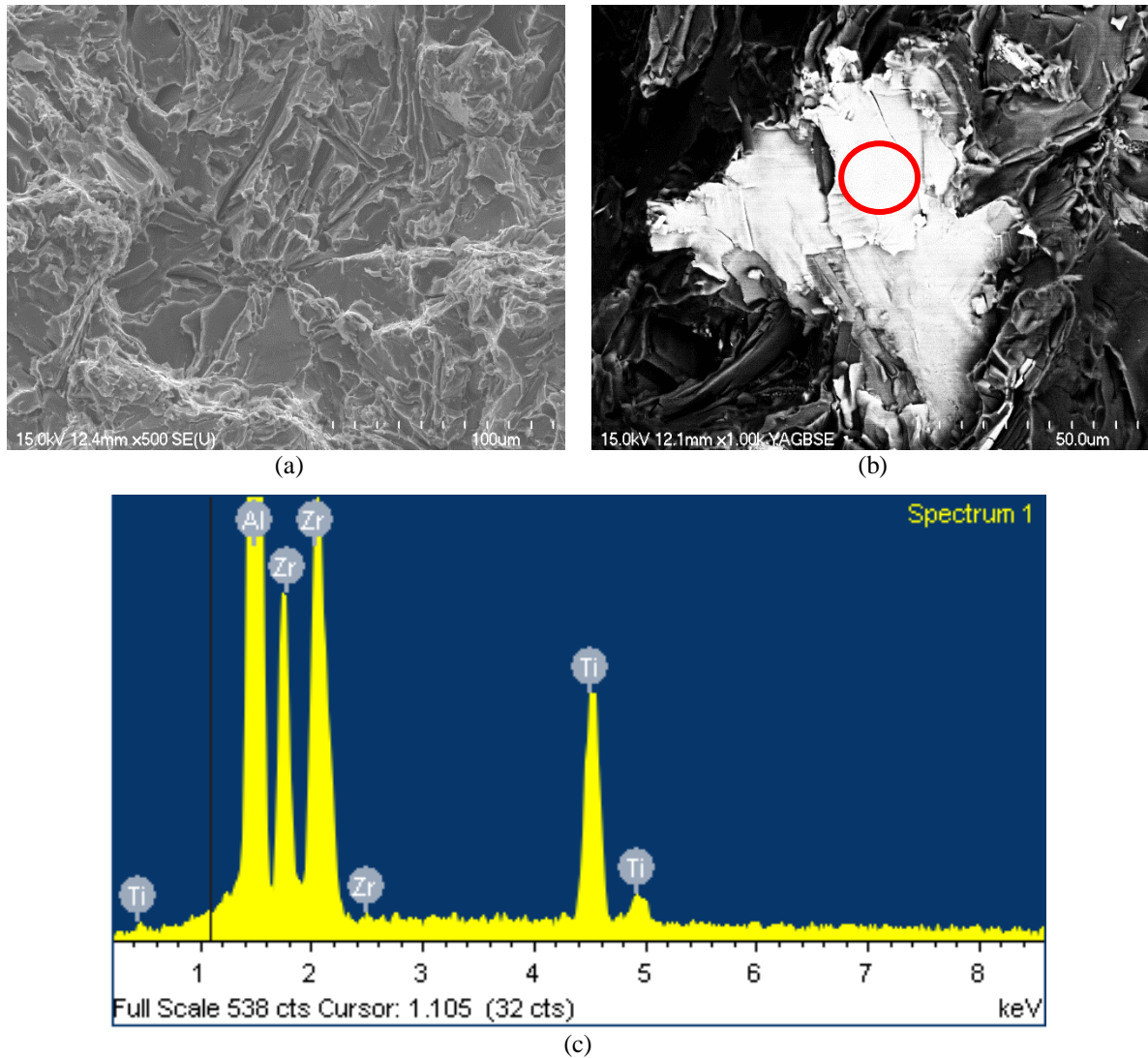


Figure 4.16 SEM images of fracture surface of as-cast G5 alloy: (a) SE image showing some long Si particles, (b) BSE image showing a bright fractured particle, and (c) EDS spectrum of the circled area in (b) showing the particle to be $\text{Al}_3(\text{Ti}, \text{Zr})$ phase.

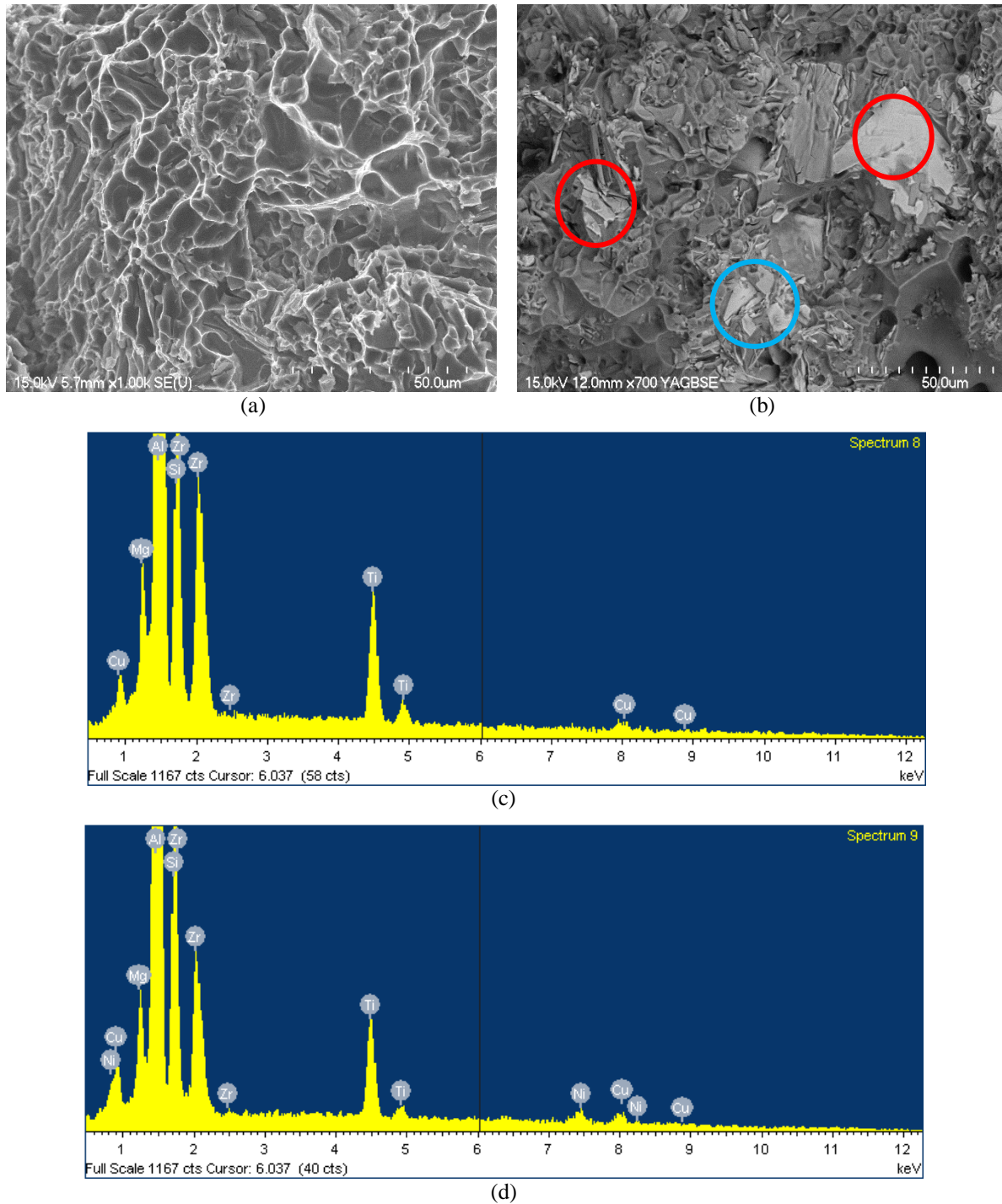


Figure 4.17 SEM images of T6-treated G5 alloy: (a) SE image showing a uniform dimple structure, (b) BSE image showing grey plates of varying intensity, and (c, d) EDS spectra corresponding to the red and blue circled areas in (b) corresponding to a mixture of Al_9NiFe , Al_3CuNi , and $\text{Al}_3(\text{Ti,Zr})$ phases.

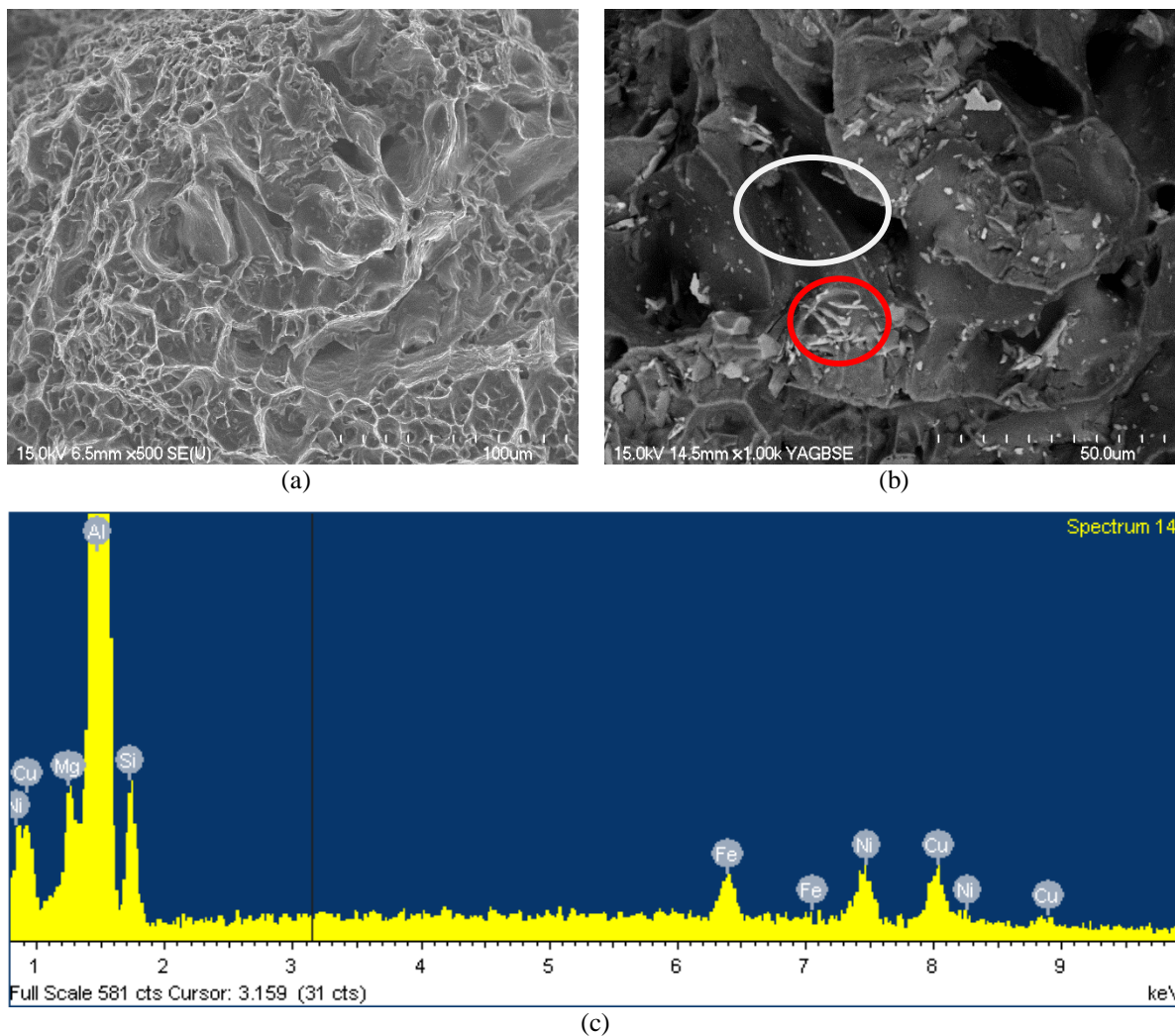


Figure 4.18 SEM images of fracture surface of G5 alloy tested at 300°C/100 h: (a) SE image showing dimple structure, (b) BSE image showing ultra-fine precipitates (white circled area) and coarse particles (red circled area), and (c) EDS spectrum showing these particles to be a mix of π -Al₈FeMg₃Si₆, A₉NiFe, Al₃CuNi phases.

As mentioned by Prasad²⁴⁰ in his study on the characterization of 354 and 388 aluminum alloys, these alloys contain a variety of elements whose solubility increases with increasing temperature. However, the decrease in solubility from high to low concentrations during solidification results in the precipitation of a number of coarse

intermetallic phases, depending on the actual concentrations of these elements in the alloy. With respect to the age hardening behavior of 354 alloys, while not much research has been carried out on 354 alloys, however, studies of alloys belonging to the Al-Cu-Mg-Si system have revealed that the precipitation is complex, and the precipitates formed can range from binary and ternary phases to more complex quaternary phases.^{241, 242} This is well evidenced in the present study, by the figures presented in this section, which show the variety of intermetallic phases present in the different 354 alloy samples investigated.

In regard to the fracture behavior, Prasad²⁴⁰ reported that for room temperature tested samples, the fracture surface was mostly rough, whereas for tests carried out at 150°C, the presence of dimples and voids in some regions indicated ductile rupture in those regions. At still higher temperatures (204°C or more), the fracture was typically ductile/dimpled in nature. Thus, with the increase in temperature, a gradual transition from brittle to ductile fracture occurred, together with an increase in the number and size of voids or cavities. Cracks were observed in the silicon particles and clusters of intermetallic phase particles inside the interior of the voids.

The $(Al, Si)_2(Zr, Ti)$ which is a Si-rich phase has a stronger Si peak while that of the block-like $(Al, Si)_3(Ti, Zr)$ phase present in the microstructures of alloys containing Zr which is a needle-like Al-rich phase shows a stronger Al peak. The copper phase is seen mainly as small pockets of the block-like Al_2Cu . This can be explained by the high percentage of magnesium, and the strontium content, causing an increase of the segregation of this phase at the limits of the α -Al dendrites. The fracture surface of the as-cast samples

exhibits ductile fracture features in general, with crack initiation mostly observed in the eutectic silicon particles, since the latter are more brittle than the matrix itself and act as preferred crack initiation sites.^{238, 244, 245} In the case of the T6-treated samples, the nature of the fracture surface appears to be relatively more brittle than that observed in the as-cast condition. The higher magnification micrographs to the right in Figure 4.19 to Figure 4.21 show the presence of many secondary cracks in the interdendritic regions indicating that the fracture starts mostly with cracks in the Si, Al₂Cu and Fe and Mg brittle intermetallic phases, rather than at their interfaces with the matrix.^{238, 244} At the high temperature condition, the fracture mode is a combination of ductile and brittle fracture, the ductile part being the α -Al matrix and the brittle part pertaining to the more brittle phases such as the eutectic Si and the Cu and Mg intermetallics. During this high temperature condition, the precipitates coarsen beyond the critical strengthening size. This coarsening has a detrimental effect on tensile strength,^{196, 246} which explains why a decrease in the strength and increase in the elongation is obtained when testing samples in this condition.

The presence of Cu-rich GP (Guinier-Preston) zones and (Cu, Mg) rich GPB (Guinier-Preston-Bagaryatsky) zones which act as precursors for θ -Al₂Cu and S -CuMgAl₂ were identified in the work of Prasad.²⁴⁰ The Al₂Cu phase starts precipitation with the formation of Guinier-Preston (GP) zones which consist of copper layers in the {100} matrix planes, then the coherent θ' phase precipitates, and finally the equilibrium Al₂Cu phase is formed. Tiny L1₂-Al₃(Zr,Ti) type precipitates are coherent to the Al matrix; have high anti-phase boundary energy and low misfit. These precipitates have extreme thermal

stability, so that, with the increase in temperature, these precipitates obtain a low coarsening rate.²⁴⁰

4.6.2 MICROSTRUCTURAL ANALYSIS OF FRACTURE PROFILE

Regardless of SEM fractography, it is also useful to examine the fracture profile on sections perpendicular to the fracture surface. Whereas the fracture surface of a tensile-tested bar is examined using an SEM, an examination of the fracture profile is carried out using an optical microscope. For this, the sample is sectioned in the longitudinal section from the tested bar, mounted in bakelite, and polished before being examined under the optical microscope. This enables examining the origin of the fracture and to determine and identify the presence of microstructural abnormalities (defects) and microconstituents (phases) beneath the fracture surface that either caused or contributed to initiation and propagation of the crack responsible for the fracture, and consequently, in the identification of the main and secondary cracks.²⁴⁷

Some examples of the longitudinal sections of the fracture profiles of samples of the G1, G2 and G5 alloys for the same three as-cast, T6-treated, and 300°C/100h tested conditions presented in the previous section are presented here in Figure 4.19 to Figure 4.21. In each case, two sets of optical micrographs are shown: one at low magnification (50X) which gives a clear picture of the fracture profile, and a corresponding high magnification micrograph (500X) which highlights the different intermetallic and other phases present in the alloys, showing how the crack propagates across the sample surface, as well as the presence of secondary and microcracks occurring in particles below the

fracture surface. In contrast, the most prominent phases observed in the low magnification micrographs are the α -Al dendrites and the eutectic silicon in the interdendritic regions.

All samples were solution heat-treated at 505°C for 8 h, subsequently quenched in warm water at 60°C, followed by artificial aging for 2 h at 190°C.

Modification has the strongest influence on the spheroidization and coarsening kinetics of Si particles in heat-treated Al-Si alloys. In the as-cast condition, the eutectic silicon particles in unmodified alloys possess an acicular form, often appearing as needle-shaped or plate-like particles, which are hard and brittle compared to the aluminum matrix. Under tensile load, the sharp tips of the needle-shaped Si particles act as stress concentration areas, which facilitate crack initiation during the early stages of tensile testing, thereby leading the sample to fracture in a brittle mode.

It will be observed from the micrographs shown in Figure 4.19 through Figure 4.21 that the formation of microcracks begins with the cracking of the brittle eutectic Si particles, or voids, in the eutectic regions. Once a large number of eutectic Si particles crack, the matrix between the microcracks becomes unstable, the microcracks begin to coalesce and form a single main crack. It should be noted here that not all of the microcracks which formed in the eutectic regions become part of the final fracture path although a majority of them do, since the presence of other intermetallic phase particles in the alloy would present discontinuities in the soft and ductile aluminum matrix.²⁴⁸ As α -Al is the softer phase and the Si phase is harder and less ductile, the resulting stresses would cause anisotropic distribution of the plastic deformation, which would be greater in the

softer phase. The local plastic constraint in the softer phase would lead to a rapid strengthening of the alloy, with dislocations piling up at the α -Al/Si particle interfaces. The critical stress at which the microcracks start to form and propagate is controlled by the properties of the microstructure and the matrix. It has also been reported that the internal stress induced in the eutectic Si particles as a result of the applied load depends on the eutectic Si particle aspect ratio and the SDAS of the matrix.¹⁶

In this regard, the addition of strontium to the unmodified alloy would have a significant effect as, by changing the coarse, acicular eutectic silicon into a fine, fibrous form, the stresses involved would be diminished, and the strength and ductility of the alloys would improve.^{32, 249} It has been noted, however, that increasing the level of Cu and Mg leads to an increase in the average length and area of the Si particles, due to the fact that both Mg and Cu react with the Si and Sr in the alloy to form $Mg_2Sr(Si,Al)$ and Al-Cu-Sr compounds, respectively.^{32, 250} This would deplete the amount of Sr available for modification of the Si particles, thereby affecting their size. High temperature treatments and/or long holding times can also alter Si particle characteristics. In recent years, both chemical and thermal modifications have been used in conjunction with each other to produce the desired properties in a casting.²⁵¹

The copper phase is seen mainly as small pockets of block-like Al_2Cu ; the relatively high percentage of magnesium and the presence of strontium lead to an increase in the tendency of this phase to segregate to the limits of the α -Al dendrites. The microstructures beneath the fracture surface of the alloy samples shown in Figure 4.19 to Figure 4.21 reveal

elongation of the dendrites in the direction of the loading axis (vertical direction). Interaction of Zr and Ni with different elements to form Al-Cu-Ni-Zr, Al-Ni-Zr and Zr-Ti-Si phases have been reported by various researchers studying these systems.^{163, 225, 232, 252}

Several studies^{232, 253, 254} mention that the spheroidization process of the eutectic silicon throughout heat treatment takes place in two stages: fragmentation or dissolution of the eutectic Si particles and the spheroidization of the fragmented parts. Controlling the microstructure during solidification is therefore very important. In Al-Si hypoeutectic alloys, nucleation and growth of the eutectic silicon have been shown to have an effect on the formation of defects such as porosity and microporosity too. These defects have an important effect on the ultimate mechanical properties of the casting alloys. Solution temperature is the most relevant parameter that can influence the kinetics of Si morphology transformation during the course of solution heat treatment. Normally, the fracture path from the micrographic aspect is mostly transgranular and the appearance of the fracture surface is more flat. The fracture of the α -Al dendritic network is ductile but in general depends on the morphology of the eutectic Si and the quantity of brittle intermetallic phases present. The fracture surface of the heat-treated alloys and those treated at high testing temperature conditions showed that coarse and deep dimples are the major feature of the fracture surface compared to the shallow dimples observed in the as-cast condition.

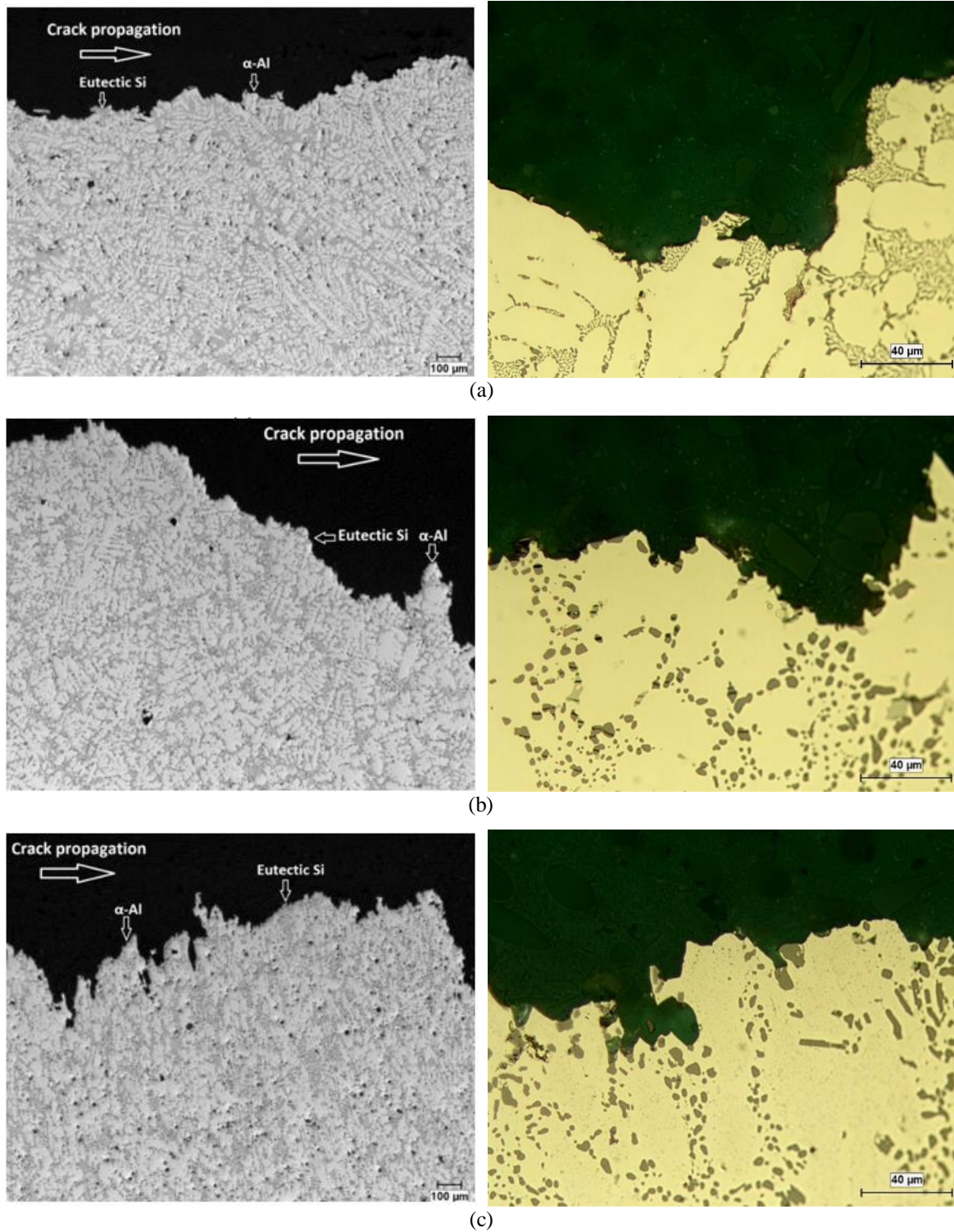


Figure 4.19 Optical micrographs showing the longitudinal sections of tensile-tested samples of alloy G1 in (a) as-cast, (b) T6 heat-treated, and (c) 300°C/100 h tested conditions. (L: Low magnification micrographs; R: high magnification micrographs).

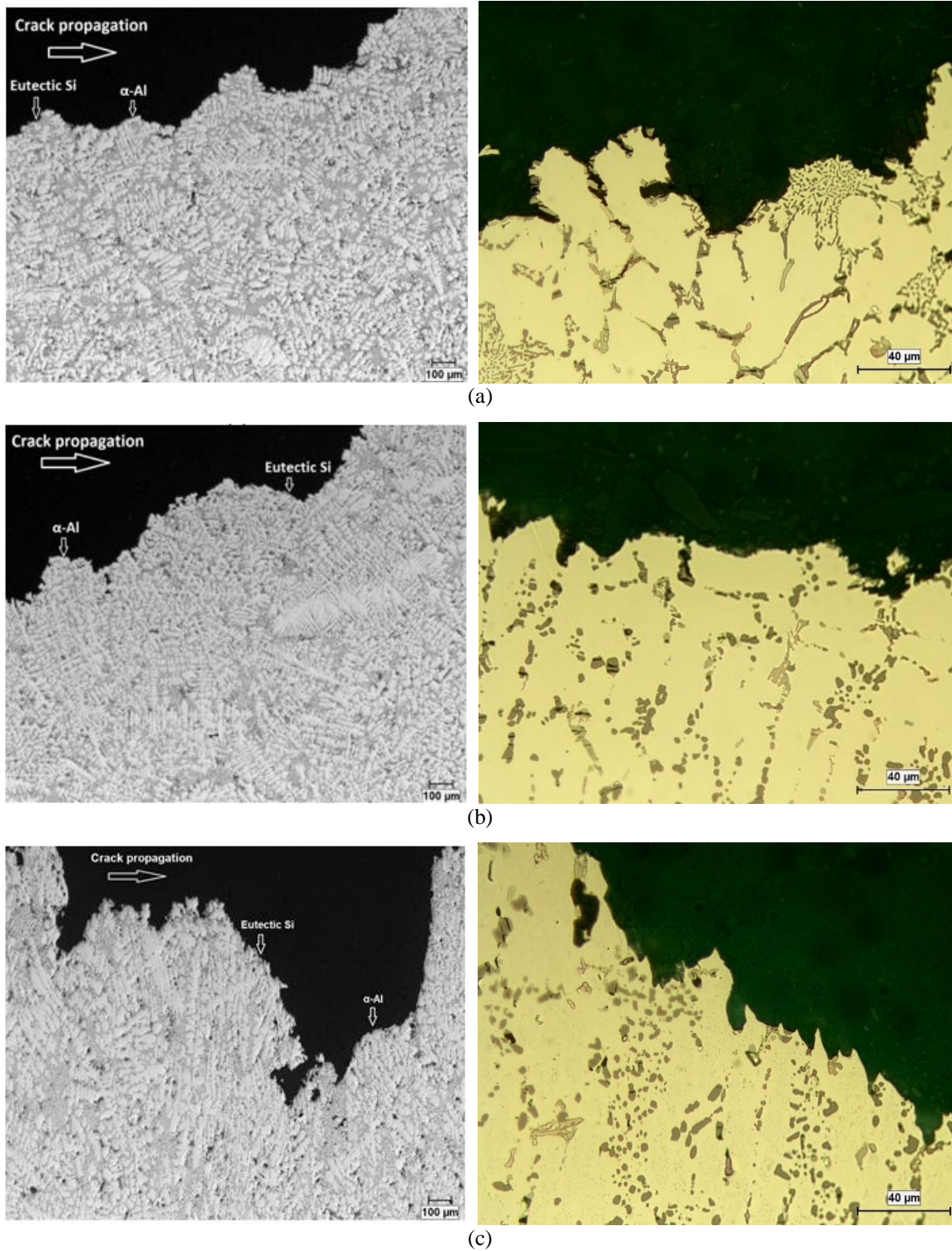


Figure 4.20 Optical micrographs showing the longitudinal sections of tensile-tested samples of alloy G2 in (a) as-cast, (b) T6 heat-treated, and (c) 300°C/100 h tested conditions. (L: Low magnification micrographs; R: high magnification micrographs).

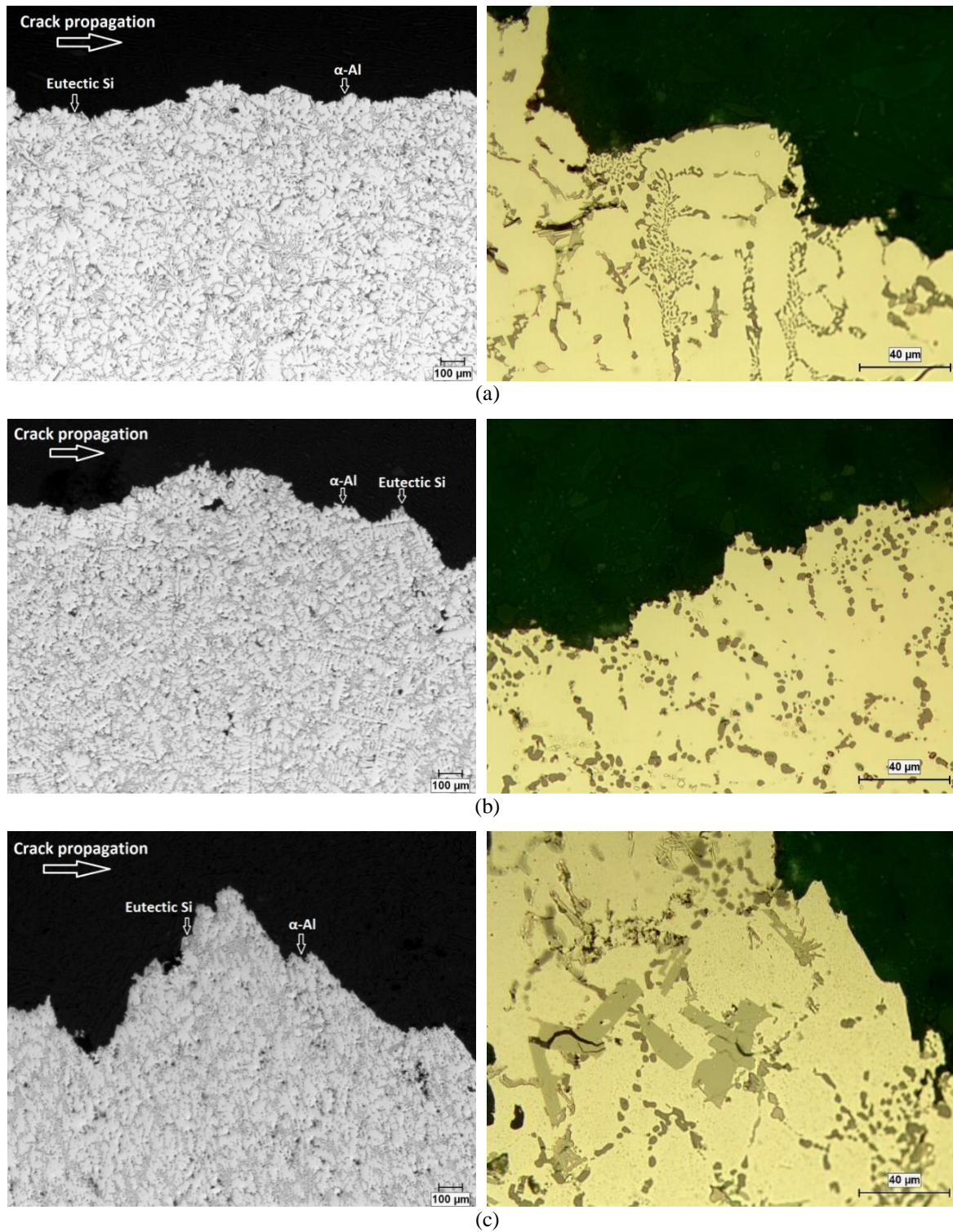


Figure 4.21 Optical micrographs showing the longitudinal sections of tensile-tested samples of alloy G5 in (a) as-cast, (b) T6 heat-treated, and (c) 300°C/100 h tested conditions. (L: Low magnification micrographs; R: high magnification micrographs).

When soft and hard phases exist in the matrix, as is the case for the 354 alloy, several factors influence the deformation behavior and fracture features: the size, morphology, density and distribution of the second phase constituents in the matrix and the strength, ductility and strain hardening behavior of the matrix in relation to these hard/second phases which, in turn, would depend on the crystallographic and other characteristics of the phases versus those of the matrix. In the case of modified Al-Si alloys, Fat-Halla⁶⁵ proposed a simple model to explain the increase in ductility with modification. Assuming that in an ideal modified Al-Si eutectic alloy where hard spherical silicon particles are uniformly distributed in the soft Al-matrix, the fracture path would continue to propagate across the Al matrix, avoiding the Si particles, so that the resulting fracture surface would exhibit a smooth appearance. A schematic diagram of the model is shown in Figure 4.22.

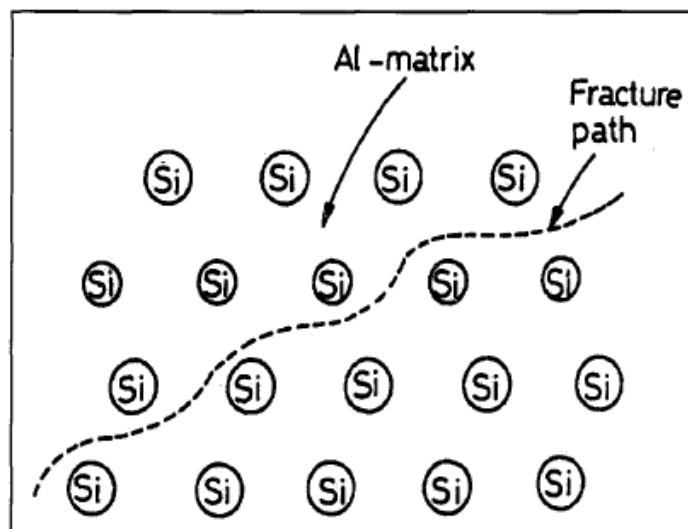


Figure 4.22 Model for the fracture mechanism of modified Al-Si alloys.⁶⁵

Further support for such a mechanism was provided by Surappara *et al.*²⁵⁵ in their study on the deformation and fracture behavior of A356 alloys. They posited that the microcracks which form in the small iron intermetallics and the Si particles in A356 alloys solidified at a high cooling rate are short and that it is difficult for them to link with each other due to the presence of a large ductile α -Al region. Consequently, the microcrack linkage would occur by ductile fracture of the α -Al between the cracks.

4.7 HARDENING PRECIPITATES

Precipitation that took place during the course of hot deformation in the 354 alloy samples studied was viewed using a Hitachi SU-8000 electron microscope. Prior to examination the surfaces of the samples were polished using ion bombardment for 20 minutes under vacuum. In a study of the ageing behavior of 319 type Al-Si-Cu-Mg alloys, Andrade²³⁷ observed that, initially, the precipitates are evenly distributed and uniformly sized. As a preferential precipitate grows, it draws atoms from the surrounding precipitates, which in turn reduces the total number of precipitates within the aluminum matrix. With fewer precipitates present, the average distance or spacing between neighboring precipitates increases, and thus it is easier for slip plane movement to occur. This is an important point, in view of the fact that the force required to cut through a precipitate is inversely proportional to the precipitate spacing. Once this critical size and precipitate spacing is reached, the tensile strength will begin to decrease.

Age-hardening of such Al-Si-Cu-Mg alloys results in the precipitation of the Q -phase and its precursors, which play an essential role in the strengthening of this specific alloy system. Similarly, in addition to the precipitation of the Q -phase ($\text{Al}_5\text{Cu}_2\text{Mg}_8\text{Si}_6$), several others, such as θ - Al_2Cu , β - Mg_2Si , S - Al_2CuMg , σ - $\text{Al}_5\text{Cu}_6\text{Mg}_2$ and their precursors, are also expected to precipitate during age-hardening treatment of 354 type Al-Si-Cu-Mg alloys; the Cu-containing precipitates such as Q -phase ($\text{Al}_5\text{Cu}_2\text{Mg}_8\text{Si}_6$) and θ - Al_2Cu are the strengthening particles obtained in the T6-tempered alloys.

The objective of applying aging treatment to casting alloys containing magnesium and silicon is to precipitate the excess Mg and Si out of the supersaturated solid solution in the form of Mg_2Si hardening phase. Dislocations are known to be potential sites for Mg_2Si precipitates which would lead to a pronounced improvement in mechanical performance following artificial aging procedures.^{96, 256} Figure 4.23 shows precipitation of θ - Al_2Cu phase particles in the as-quenched sample of the base alloy G1. (The black spots appearing in this micrograph are the result of the ion bombardment).

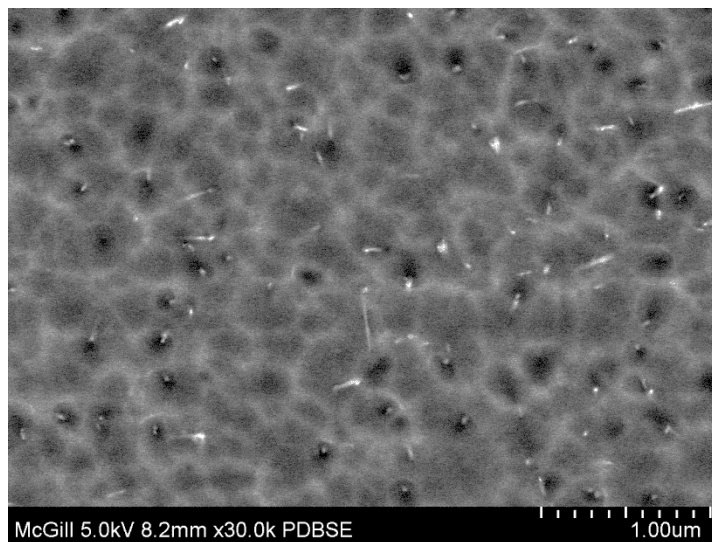


Figure 4.23 Precipitation of ultra-fine particles in as-quenched G1 base alloy.

Figure 4.24 shows clusters of undissolved Q - $\text{Al}_5\text{Mg}_8\text{Si}_6\text{Cu}_2$ phase in certain regions covered with spheroidized Fe-based intermetallics. Figure 4.25 is the EDS spectrum obtained from the medium-grey phase in Figure 4.24(a) revealing the presence of reflections due to Al, Si, Cu, and Mg.

Aging the solutionized alloy at 190°C for 2 h resulted in an increase in the density of the precipitated θ - Al_2Cu phase as displayed in Figure 4.26. It should be borne in mind that all tensile samples subjected to hot deformation were used in the T6-treated condition.

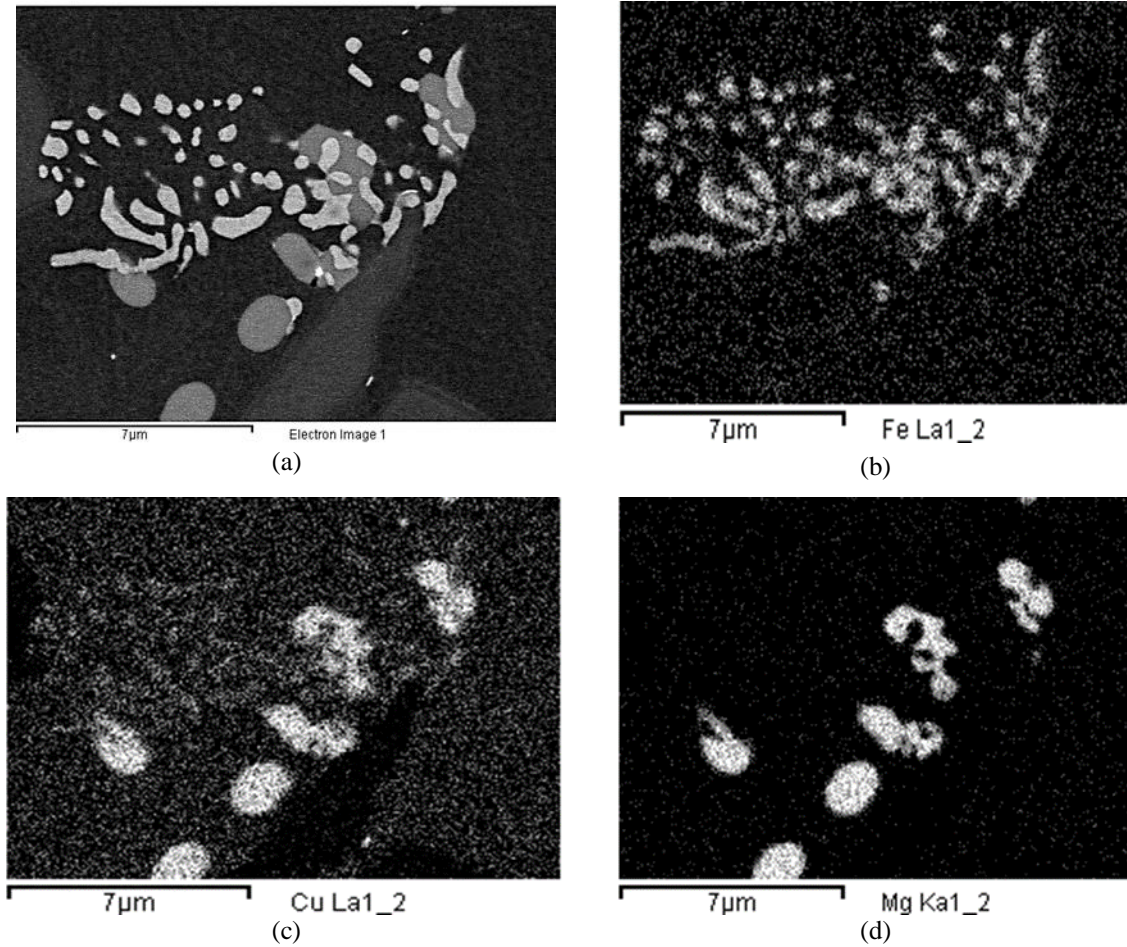


Figure 4.24 (a) Backscattered electron image showing the co-existence of Q - $\text{Al}_5\text{Mg}_8\text{Si}_6\text{Cu}_2$ phase and Fe-based intermetallics in the as-quenched G1 alloy, (b-d) images showing distribution of Fe, Cu and Mg elements in (a).

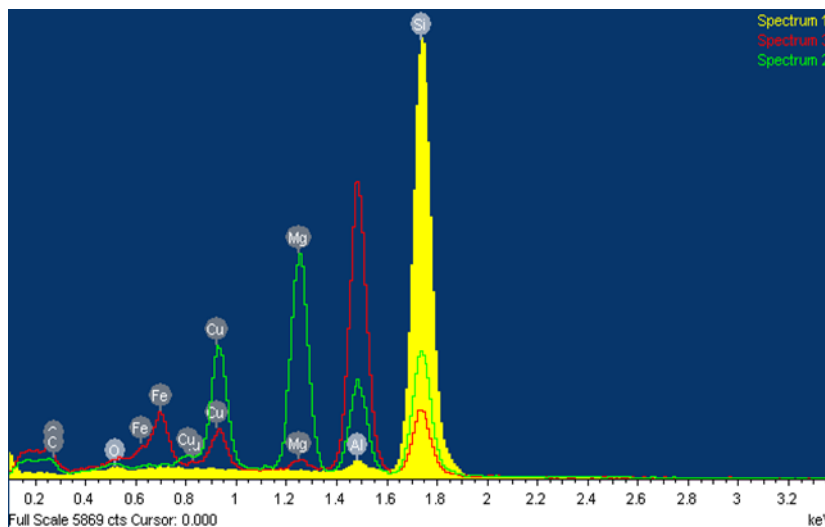


Figure 4.25 EDS spectrum corresponding to the medium-gray phase in Figure 4.24(a).

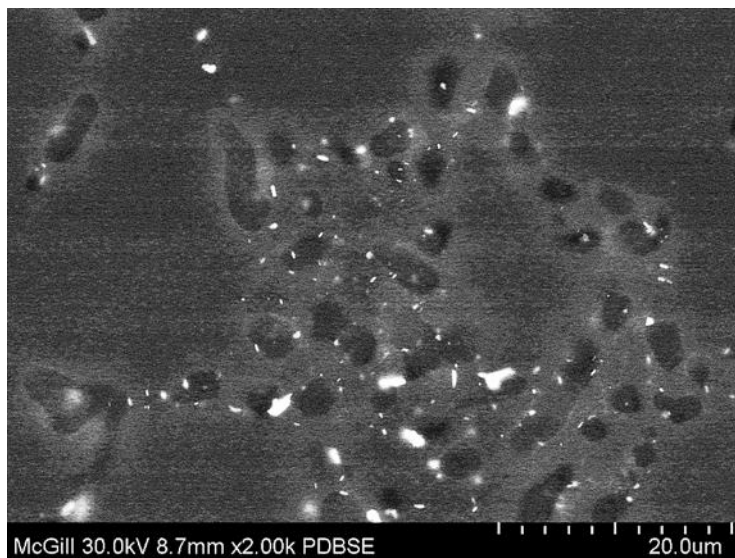


Figure 4.26 Precipitation observed in G1 base alloy in the T6-treated condition.

Holding the T6-treated tensile sample of G1 alloy at 155°C testing temperature for 10 h resulted in a marked increase in the density of precipitated particles, as shown in Figure 4.27(a). As the higher magnification image of the encircled area shown in Figure 4.27(b) reveals, most of the particles maintain their spherical shape.

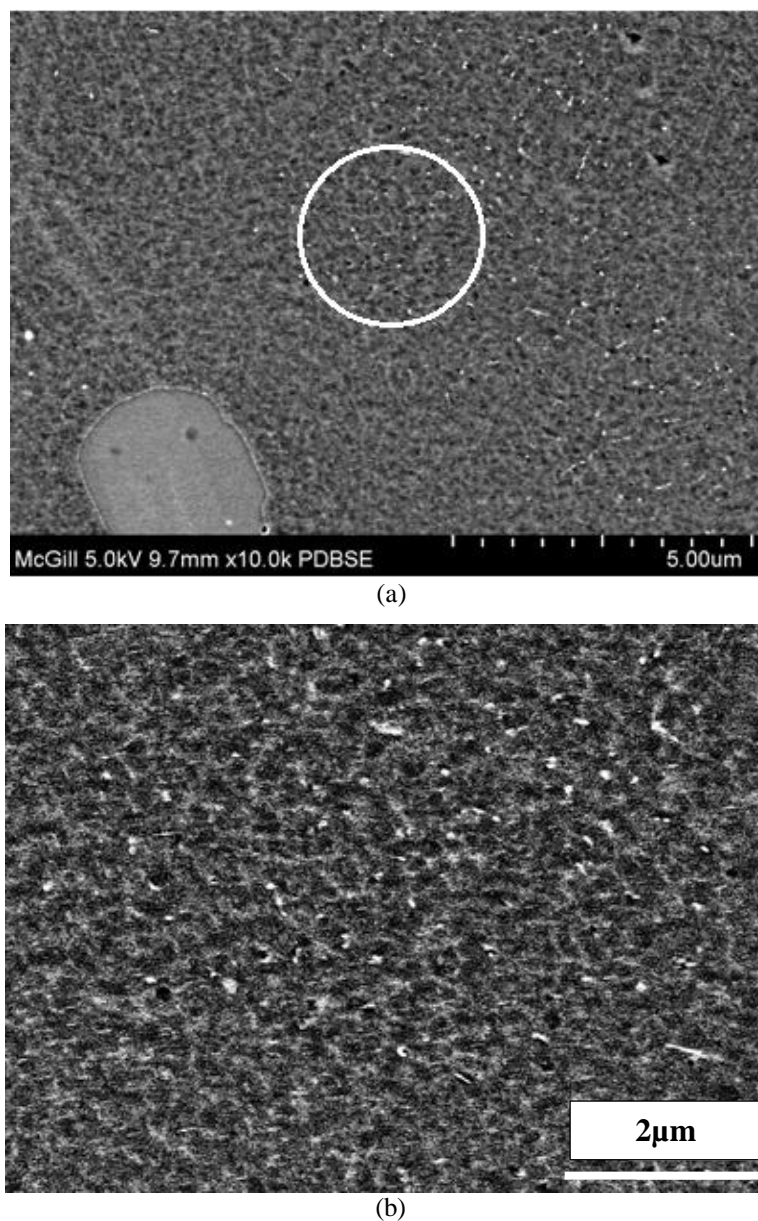


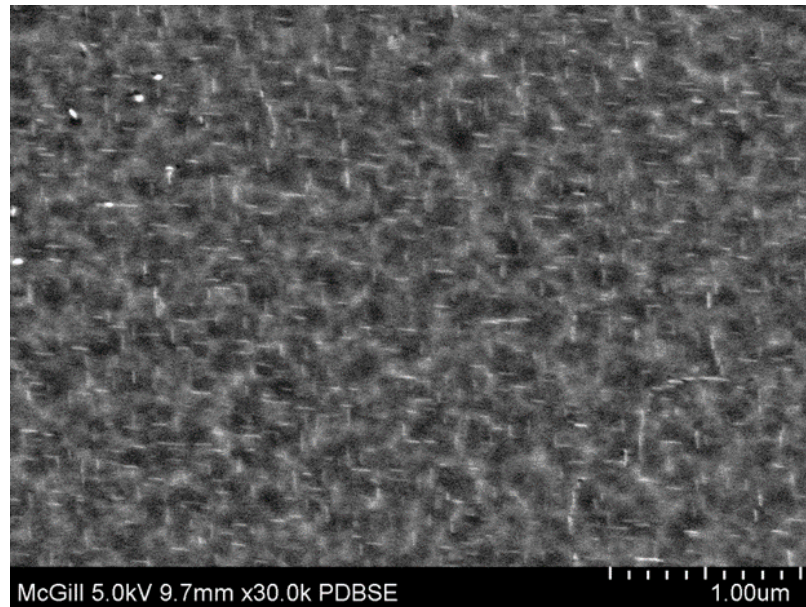
Figure 4.27 (a) Precipitation in T6-treated G1 base alloy deformed at 155°C after holding for 10 h, (b) enlarged image of circled area in (a).

Increasing the holding time to 100 h prior to deformation resulted in changing the morphology of the precipitates into thin platelets distributed in two perpendicular directions, as displayed in Figure 4.28. Similar observations were reported by Tavitas-Medrano *et al.*²⁵⁷ in 319 alloy samples aged at 240°C for 2h. The platelets were confirmed

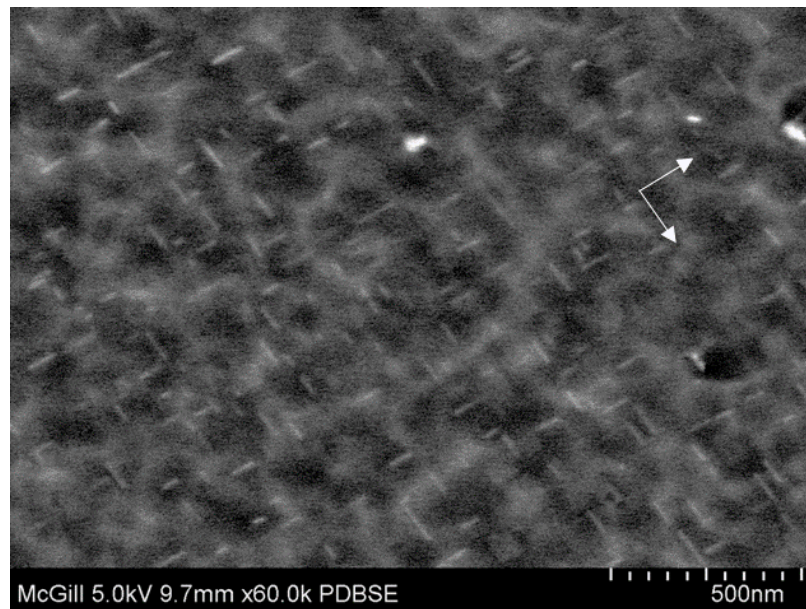
as being Al_2Cu phase particles, oriented in in the $\langle 110 \rangle$ directions. As mentioned previously, precipitation of the Al_2Cu phase starts with the formation of Guinier-Preston (GP) zones which consist of copper layers in the $\{100\}$ matrix planes, followed by precipitation of the coherent θ' phase, and finally formation of the equilibrium Al_2Cu phase.²⁴⁰

Figure 4.29(a) reveals that by increasing the testing temperature to 300°C , the density of precipitated particles markedly increased, visually reaching that obtained from samples held at 155°C for a 100 h. The morphology of the precipitates is more-or-less in the form of thin platelets, about $0.2\mu\text{m}$ in size, see Figure 4.29(b). The associated EDS spectra, see Figure 4.29(c), indicated that most of these precipitates are of Al_2Cu type.

Figure 4.30(a) presents the microstructure of G5 (G1 + 0.4wt% Ni + 0.4wt% Zr) alloy obtained after solution heat treatment/quenching, revealing the presence of Zr-rich phase particles (circled in red). The associated EDS spectrum, Figure 4.30(b), reveals strong reflections due to Al, Zr, Ti, and Ni elements. The appearance of a peak corresponding to Ag in the spectrum is the result of the sample preparation. In the investigations of Zaki²⁵⁸ it was shown that addition of Ag does not lead to formation of any specific intermetallics; rather, it is well distributed throughout the matrix. Zirconium, however, tends to interact with Ti forming a complex compound of $\text{Al}_x(\text{Zr,Ti})\text{Si}$.⁹² The presence of Ni in Figure 4.30(b) may be associated with Cu, forming Cu_3NiAl_6 phase²⁵⁹ which is insoluble during solution heat treatment.²⁶⁰ Figure 4.30(c) is an EDS generated from the arrowed area in (a), showing the possible presence of Al_9FeNi phase.



(a)



(b)

Figure 4.28 (a) Precipitation in T6-treated tensile G1 base alloy sample deformed at 155°C after holding for 100 h, (b) high magnification BSE image of (a) showing the presence of two perpendicular precipitate families – see white arrows.

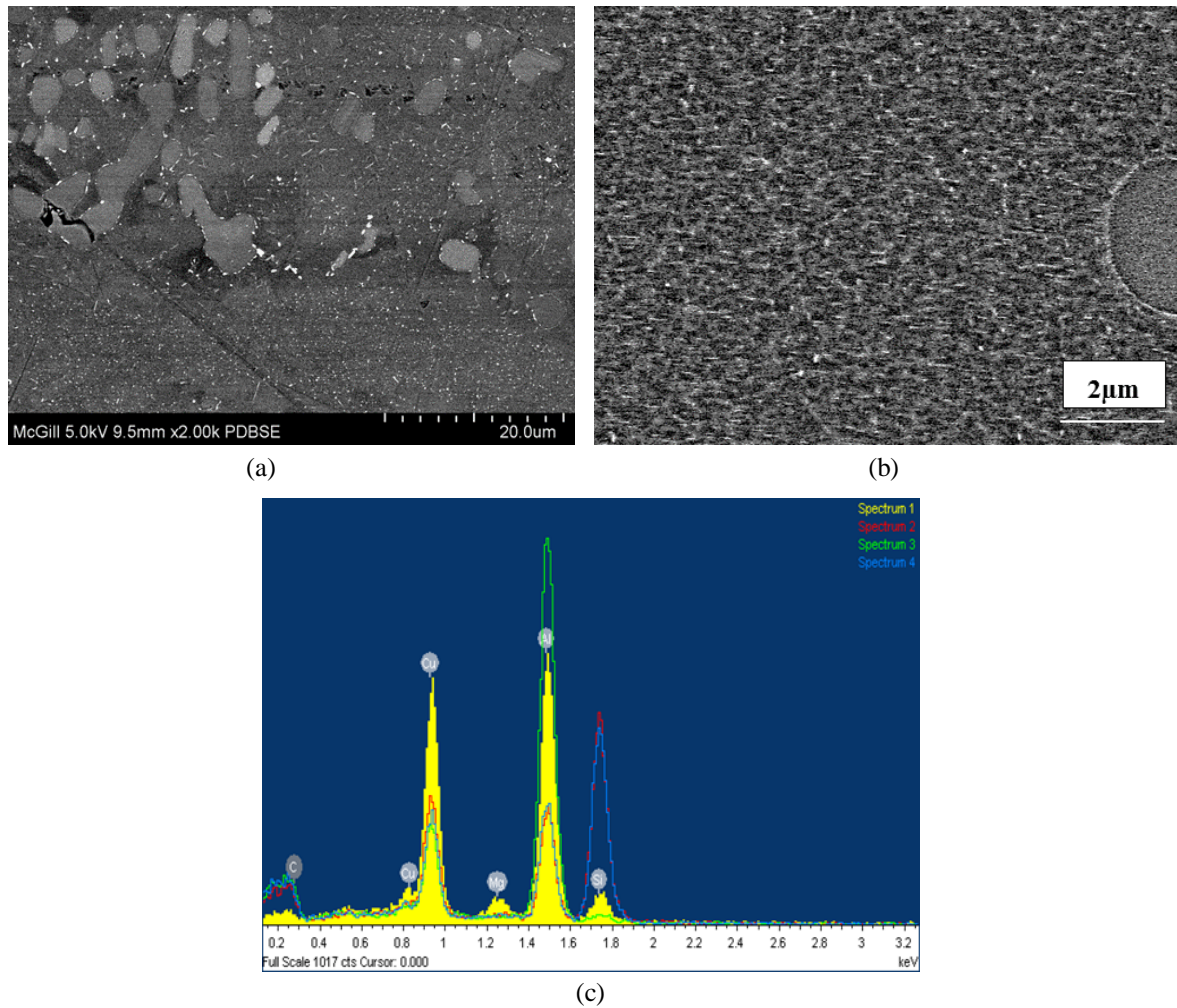


Figure 4.29 Backscattered electron images of T6-treated G1 base alloy tensile sample held for 10 h at 300°C prior to deformation (a) general view, (b) high magnification image, (c) EDS spectra obtained from different particles showing strong reflections of Al and Cu elements, corresponding to Al_2Cu .

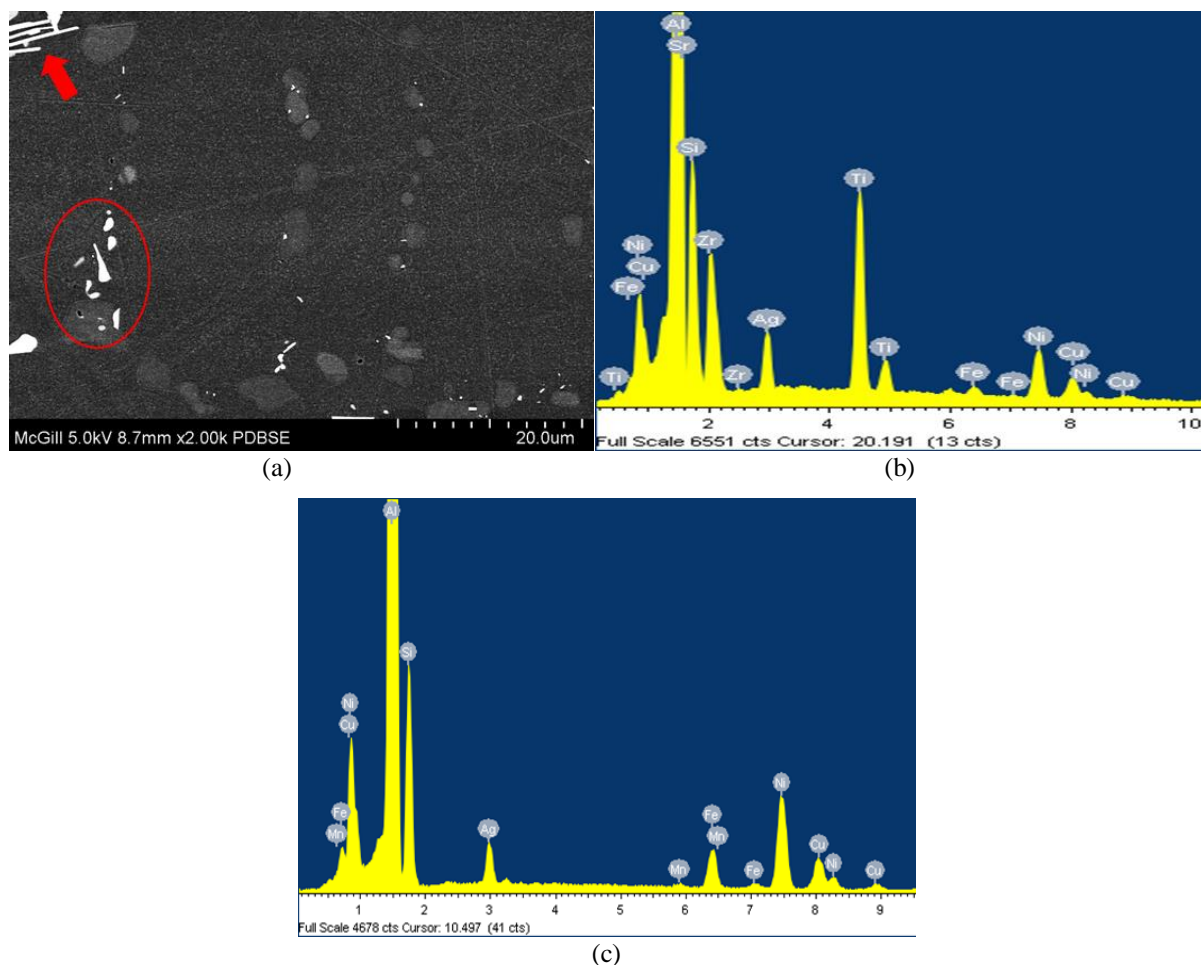
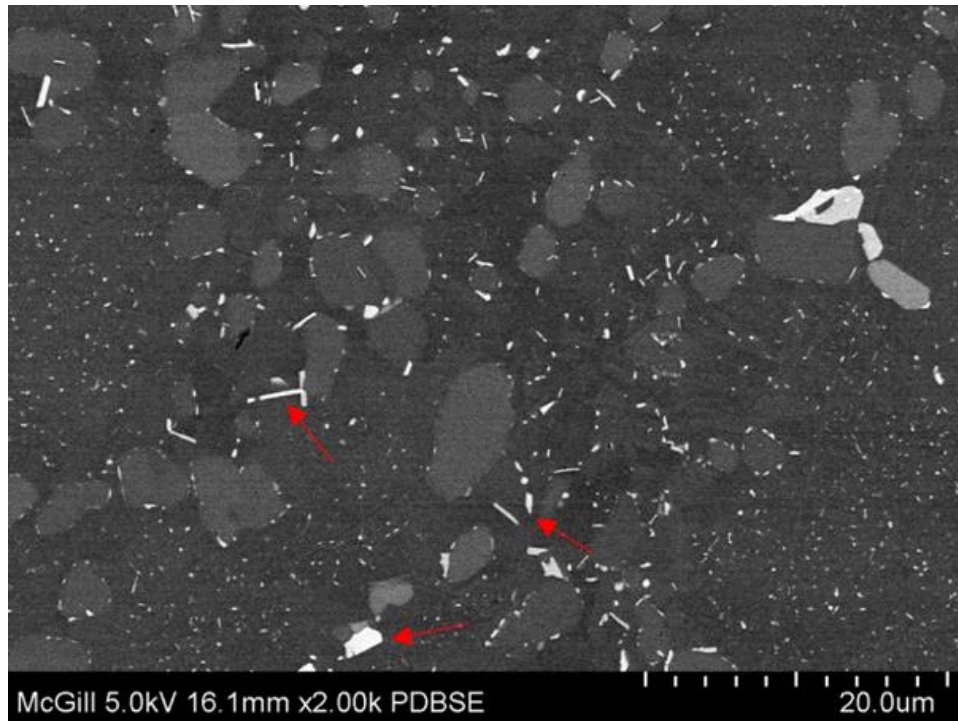


Figure 4.30 (a) Backscattered electron image of G5 alloy following solution treatment/quenching, (b) EDS spectrum corresponding to the circled area in (a) revealing presence of $\text{Al}_6\text{Cu}_3\text{Ni}$ phase, and (c) EDS spectrum obtained from the arrowed area in (a) corresponding to Al_9FeNi phase.

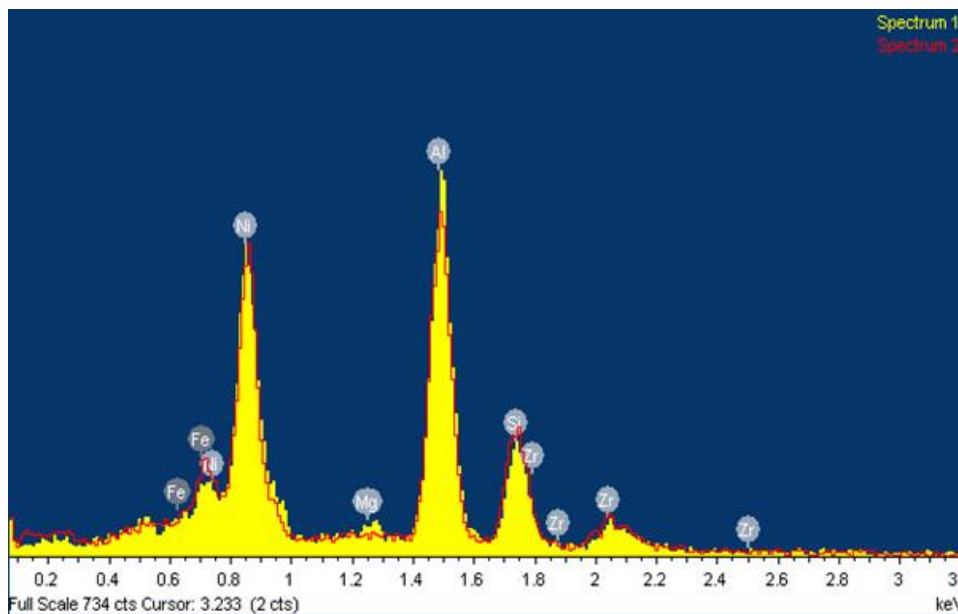
In the aged condition, the tiny L1_2 ($\text{Al}_3(\text{Zr},\text{Ti})$) type precipitates formed are coherent with the Al matrix, have high anti-phase boundary energy and low misfit. These precipitates have extreme thermal stability. Thus, with increasing temperature, they would coarsen at a low rate. These small and dispersed $\text{Al}_3(\text{Zr},\text{Ti})$ particles will provide a large force to retard the movement of dislocations and increase the alloy strength.²⁴⁰ This seems to be the most likely reason for the higher strength of the aged modified alloys.

The BSE image of Figure 4.31(a) is a general view of the T6-treated tensile sample of G5 alloy showing the precipitation which occurred during 10 h holding time at 300°C. Several bright particles may be observed, surrounding the pre-existing ones (see red arrows). The corresponding EDS spectrum in Figure 4.31(b) reveals that these particles are mainly Al₃Ni phase. The details of insoluble phases are shown clearly in Figure 4.32(a). The EDS spectra obtained from different locations in Figure 4.32(a), Figure 4.32(b) indicate the presence of *Q*-Al₅Mg₈Si₆Cu₂ phase (spectrum 1), and Al₃Ni phase (spectrum 2).

Figure 4.33(a) presents a high magnification image of the fine precipitates observed in Figure 4.31(a). The corresponding EDS spectra, shown in Figure 4.33(b), displays strong peaks of Al and Cu elements. Figure 4.34 exhibits the precipitation characteristics and distribution when the T6-treated tensile samples of G5 alloy were held for 100 h at 300°C before pulling to fracture. Figure 4.34(a) displays a general view, showing the size and distribution of the precipitated phase particles that formed under these holding conditions. It is interesting to note there is no precipitate free zones (PFZ) around the pre-existing phases (Figure 4.34(b)). Figure 4.34(c) and (d) indicate that these precipitates are mainly *Q*-phase phase. A relatively high magnification image of Figure 4.34(a) is shown in Figure 4.34(e) and reveals the platelet morphology (approximately 0.1μm thick and 1μm long) of the precipitated phase particles in two perpendicular directions, similar to those observed in the case of G1 base alloy samples under the same working conditions.

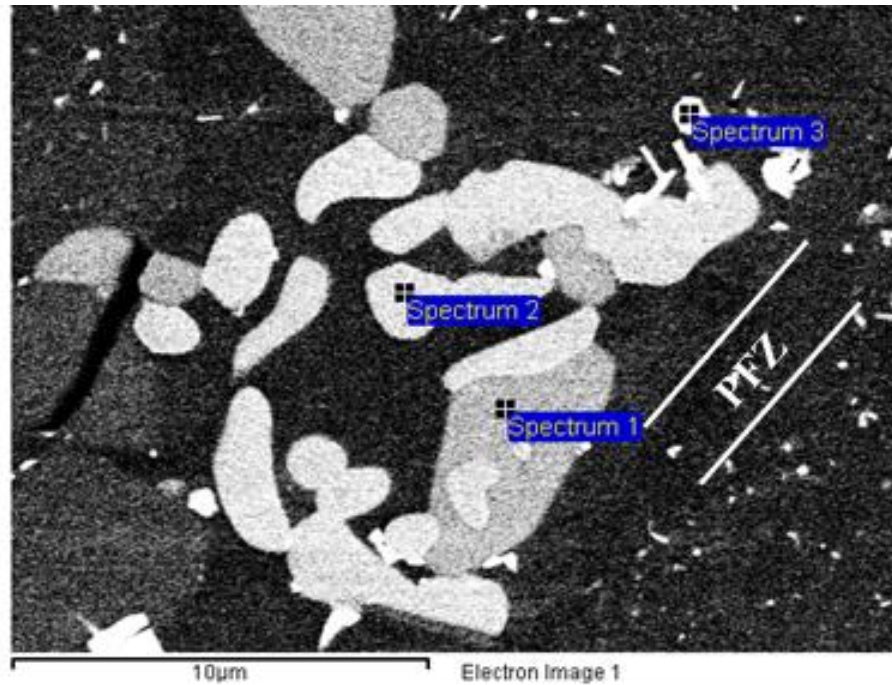


(a)

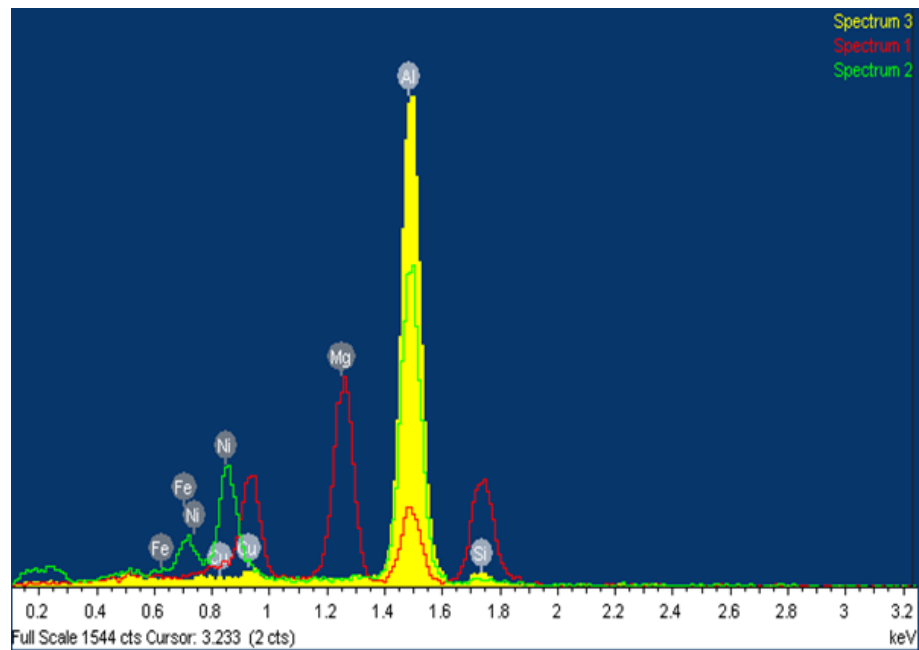


(b)

Figure 4.31 (a) BSE image of T6-treated tensile sample of G5 alloy held at 300°C/10 h prior to deformation, (b) EDS spectrum obtained from the bright particles arrowed in (a), reveals that these particles are mainly Al_3Ni phase.



(a)



(b)

Figure 4.32 (a) High magnification image of insoluble phases observed in G5 alloy, (b) EDS spectra corresponding to different areas in (a), indicate the presence of Q - $\text{Al}_5\text{Mg}_8\text{Si}_6\text{Cu}_2$ phase and Al_3Ni phase. Note the presence of precipitate free zones (marked PFZ) in (a).

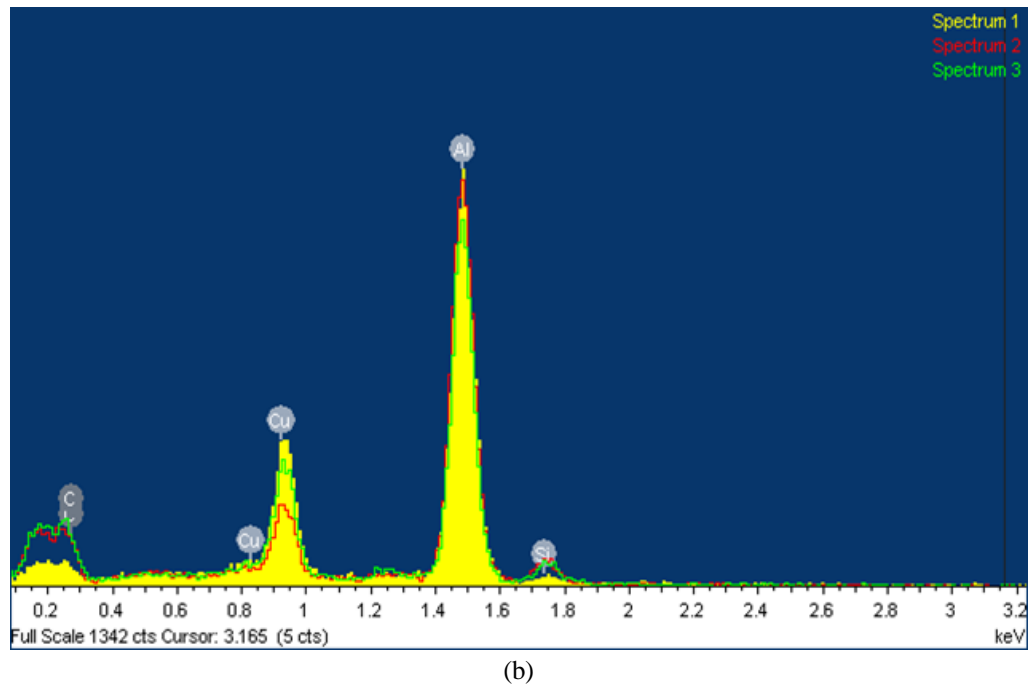
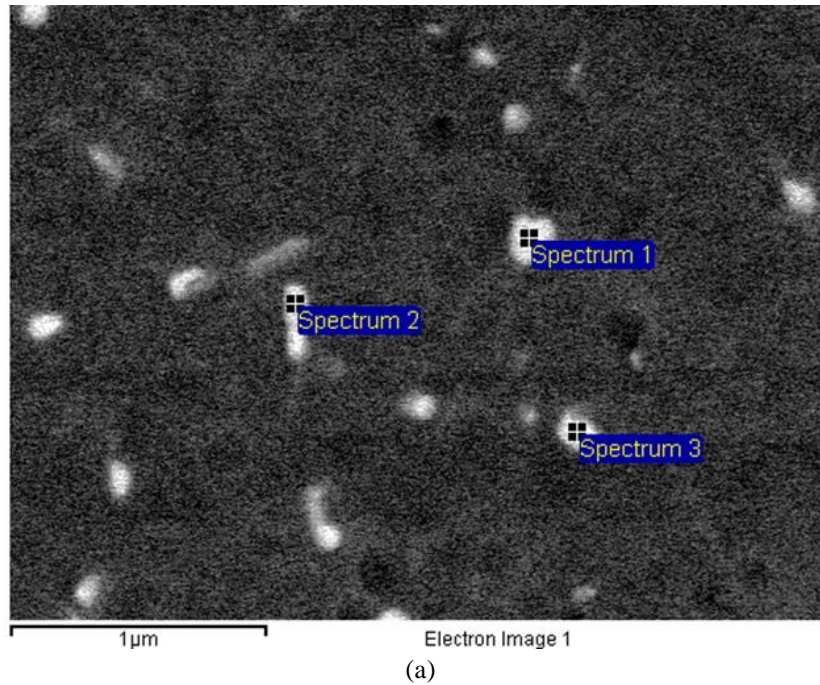
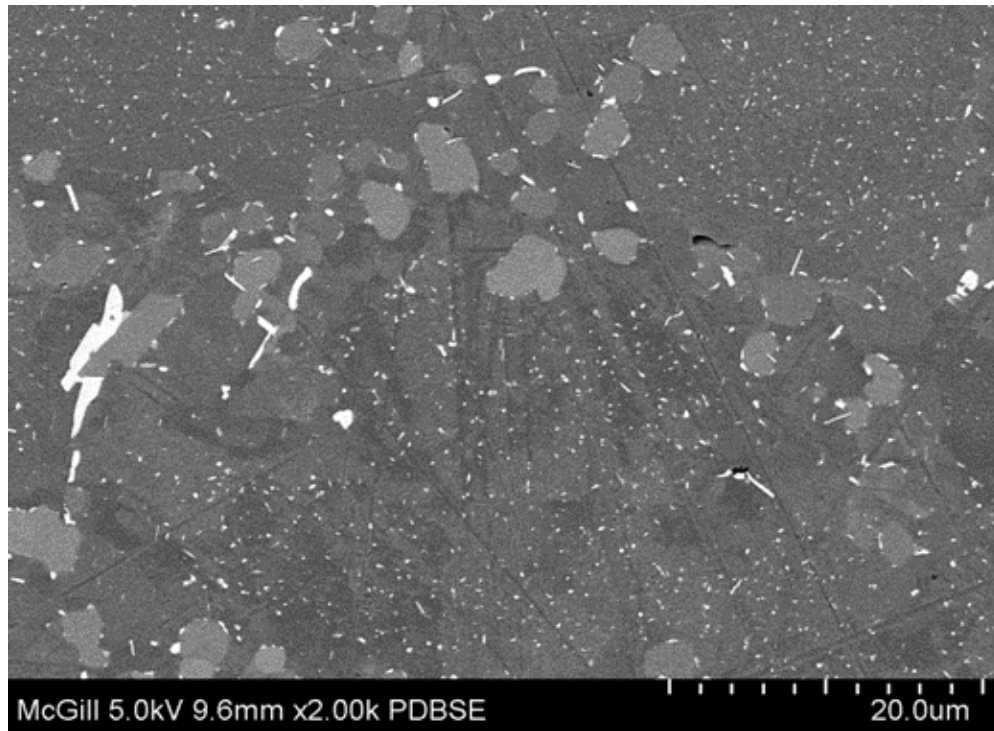
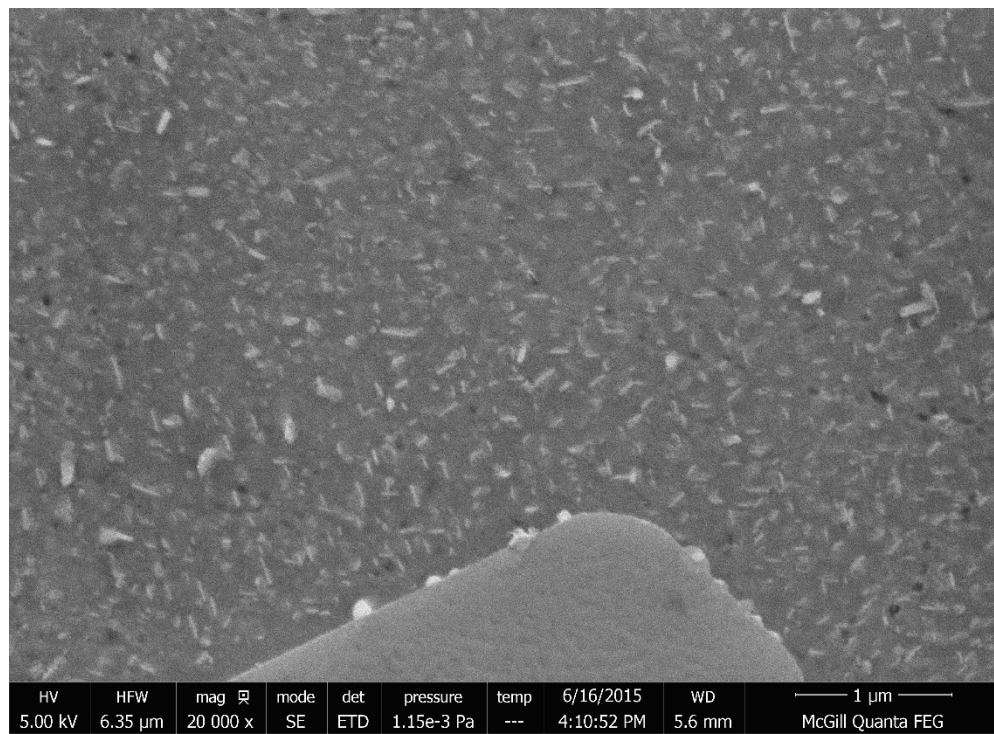


Figure 4.33 (a) Backscattered electron image of the fine precipitates observed in the T6-treated tensile sample of G5 alloy shown in Figure 4.31(a) and (b) EDS spectra corresponding to different particles in (a), displaying strong peaks of Al and Cu elements.



(a)



(b)

Figure 4.34 Cont.

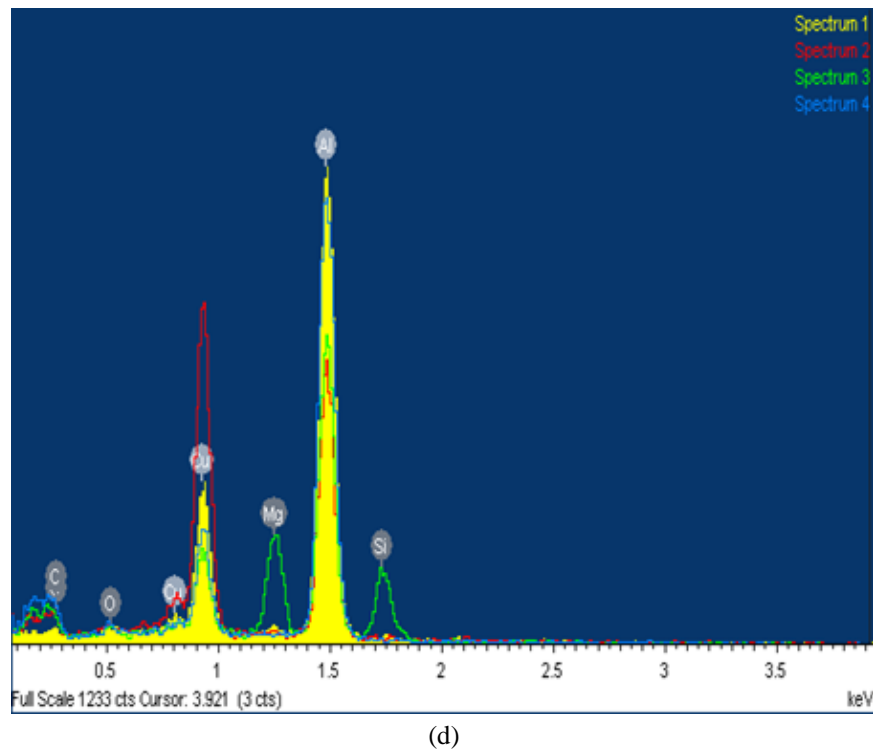
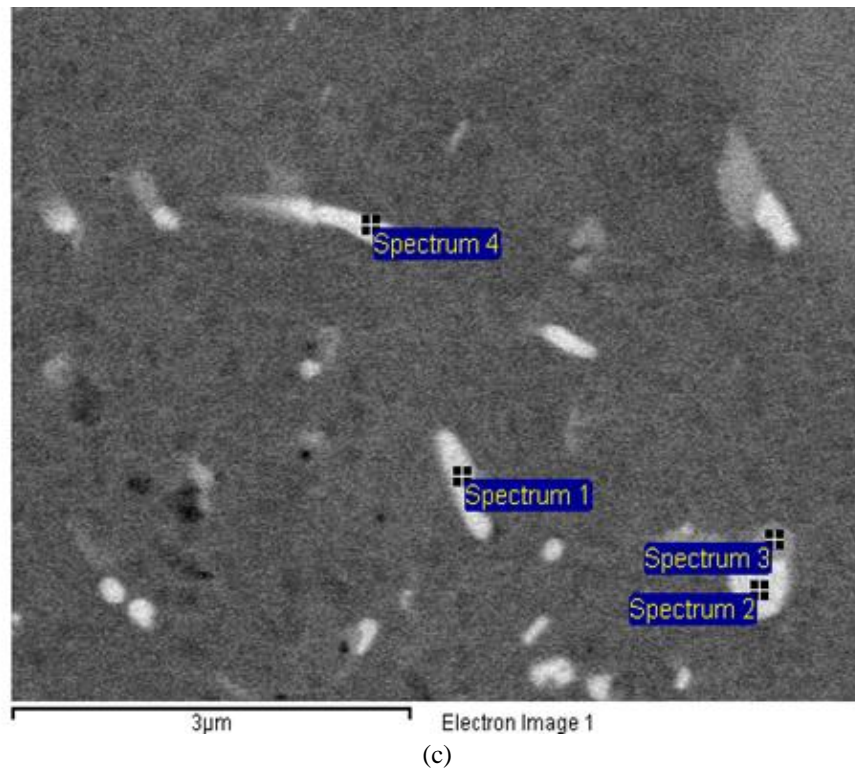
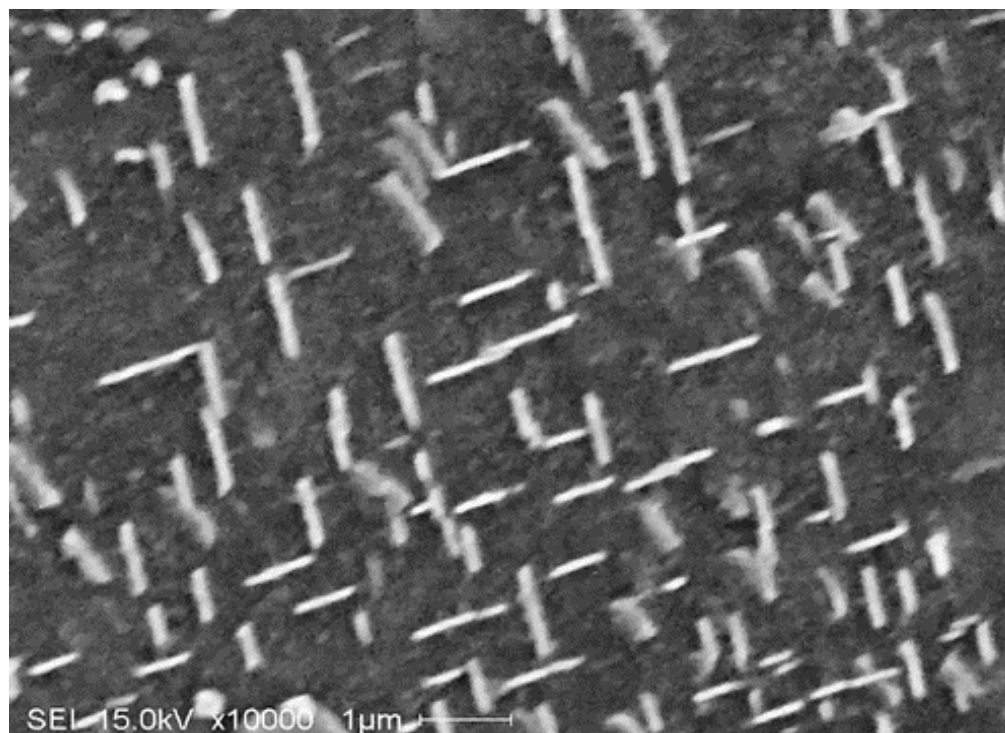


Figure 4.34 Cont.



(e)

Figure 4.34 (a) Backscattered electron (BSE) image, (b) BSE image showing no precipitate free zones (PFZ) around the pre-existing phases, (c) secondary electron image obtained from tensile sample of G5 alloy held at 300°C/100 h prior to deformation, (d) EDS spectra corresponding to (c) revealing presence of Al_2Cu , and (e) high magnification image of (a).

4.8 CONCLUSIONS

In this chapter the results pertaining to the influence of various metallurgical parameters on the tensile properties of Al-Si-Cu-Mg 354-type casting alloys were presented and discussed, with emphasis on acquiring an insight regarding the mechanical limits of Al-Si-Cu-Mg 354-type alloys in the context of these parameters, and to obtain an understanding of the effects of the addition of nickel and/or zirconium on alloy 354 with respect to the mechanical properties obtained at room temperature (as-cast and T6-treated conditions) and at high temperature (155°C and 300°C for holding times at temperature ranging from 10 to 100 hours). Based on an analysis of the results obtained, the following conclusions may be drawn.

1. The volume fraction of the undissolved phases in these alloys tends to increase with the addition of Ni and Zr, alone or in combination, in comparison with the base alloy G1. Alloy G5 exhibits the highest volume fraction with 6.48%, and has the highest level of Ni and Zr additions, 0.4wt% each. This may be explained by the dual presence of Zr and Ni, and their interaction with other elements present in the base alloy to form new phases and thus increase the total volume fraction of intermetallics in the alloy.
2. The mechanical behavior of 354-type cast alloys, measured by means of tensile testing, is strongly influenced by the testing temperature and by the holding time at temperature during high temperature testing.

3. The addition of copper to 354-type alloys plays a significant role in improving the strength of these alloys; the increase in strength obtained depends on the amount and homogeneity of the θ -Al₂Cu phase; the improvement occurs, however, at the expense of ductility.
4. Solution heat treatment of 354 alloys is considered to be a critical process because of the low melting point of the Al₂Cu phases present in the alloy. Limiting the solutionizing temperature to 505°C or less minimizes the possibility of incipient melting of the ternary eutectic structure α -(Al)-Si-Al₂Cu and the consequent formation of high levels of shrinkage porosity after quenching, thus avoiding reduction in the tensile properties.
5. The solution heat treatment temperature of 505°C/8h in combination with the aging temperature at 190°C/2h increases the UTS and YS (peak-strength), while ductility remains more or less the same as that in the as-cast condition.
6. The influence of minor additions of Ni and Zr 354-type alloys on their high-temperature performance is controlled by their T6-properties at room temperature, and by the temperature of testing and holding time prior to testing.
7. Addition of 0.2wt% Ni + 0.2wt% Zr (alloy G4) improves tensile properties considerably in the T6 heat treatment condition compared to the as-cast condition, although, the addition of 0.4wt% Ni + 0.4wt% Zr (alloy G5) is not sufficient to resist softening at 300°C/100h (*cf.* UTS: 52 MPa, YS: 45 MPa, %El: 23% with UTS: 361 MPa, YS: 343 MPa, %El 1.23%, observed after T6 treatment).

8. The addition of 0.4wt% Ni to alloy 354 (G2 and G5 alloys) leads to a decrease in the tensile properties, compared to the base alloy. This decrease may be attributed to a Ni-Cu reaction which could interfere with the formation of the Al_2Cu strengthening precipitates, thereby affecting the age hardening process.
9. The copper phase is seen mainly as small pockets of the block-like Al_2Cu . This can be explained by the high percentage of magnesium, and the strontium content, causing an increase of the segregation of this phase at the limits of the α -Al dendrites.
10. The percentage elongation increases with the testing temperature, from as-cast, to heat-treated, to T6-treated samples tested at high temperature (155°C and 300°C, respectively), in keeping with the accompanying reduction in the tensile strength of the alloy samples.
11. The microstructure beneath the fracture surface showed elongation of the dendrites in the direction of the loading axis. Coarse and deep dimples are observed on the fracture surface of 190°C/2h aged samples tested at high temperature while shallow dimples were observed in the room temperature tested samples (as-cast and T6 conditions).
12. In the T6-treated (190°C/2h) G1 alloy, the density of precipitated Al_2Cu particles (mostly spherical) markedly increases compared to the as-quenched condition. Increasing holding time during high temperature testing further increases the density.

13. At 155°C/100h in G1 alloy, the Al₂Cu precipitates appear in the form of thin platelets distributed in two perpendicular directions.
14. The L1₂ Al₃(Zr,Ti) phase, the block-like (Al,Si)₂(Zr,Ti) phase, and the needle-like (Al,Si)₃(Zr,Ti) phase are the main features observed in the microstructure of the tensile samples of alloys containing 0.2-0.4wt% Zr additions, viz., G3, G4 and G5 alloys, respectively.
15. The EDS spectra obtained from different locations in samples tested at 300°C after 10 h holding, indicated the presence of *Q*-Al₅Mg₈Si₆Cu₂ phase and Al₃Ni phase.
16. The formation of precipitate free zones around the pre-existing phases indicates that these precipitates are mainly Al₂Cu phase. High magnification electron images revealed the platelet morphology (approximately 0.1µm thick and 1µm long) of the precipitated phase particles in two perpendicular directions, similar to that observed in the case of G1 base alloy samples.
17. The good high temperature mechanical properties of the alloys are due to the presence of the L1₂ (Al₃(Zr,Ti)) type precipitates which are coherent to the Al matrix and hence, highly stable during long exposures at elevated testing temperatures.
18. The *Q*-phase (Al₅Cu₂Mg₈Si₆) and *θ*-Al₂Cu are the predominant precipitates found in the alloys studied. Precipitates of Al₃(Zr,Ti) with an ordered L1₂ structure are also observed.

CHAPTER 5

Stage II Alloys – Room Temperature Testing

MICROSTRUCTURE AND MECHANICAL

PROPERTIES

PART I

MICROSTRUCTURE CHARACTERIZATION

CHAPTER 5

Stage II Alloys - Room Temperature Testing

MICROSTRUCTURE AND MECHANICAL PROPERTIES

PART I

MICROSTRUCTURE CHARACTERIZATION

5.1 INTRODUCTION

This chapter is divided into two main sections. The first section presents the results obtained on the effects of different alloying/transition element additions, namely, iron, magnesium, manganese, nickel, scandium and zirconium, individually and/or in combination, on the microstructure and solidification sequence, of the Al-Si-Cu-Mg 354-type alloys studied using the thermal analysis technique and tensile test samples, (which provide low and high cooling rate conditions, respectively). The tensile test samples were studied in the as-cast condition and after solution heat treatment (500°C/8h). The low cooling rate (0.35°C/s) provided by the thermal analysis set-up/casting facilitates the detection and analysis of the phases which are formed in the respective alloys.

Major microstructural features such as silicon-particle characteristics, and volume fraction of intermetallic phases are presented in this part for both low and high cooling rate conditions.

The second section of this chapter will present the tensile properties of these alloys, with the goal of providing a better understanding of said properties in relation to the effects of the alloying additions made. The alloy/sample conditions investigated in this part include the as-cast, solution heat-treated, and aged conditions using different aging temperatures and times. The tensile test data and the quality index of the castings will be correlated to their microstructural characteristics, for purposes of interpreting the results obtained and setting the limits of the tensile properties, and to compare the mechanical behavior of the alloys to delineate the effects of the additions with respect to the aging treatments applied. Also, plots of ΔP ($P = \text{Property} = \text{UTS, YS and \%El}$) values were generated of the obtained at the different aging temperatures and times conditions, generated using the G1 base alloy as reference will be presented. This approach is expected to assist in better visualizing the effects and interactions of the various additions used and the different heat treatment conditions applied.

5.2 LOW COOLING RATE – THERMAL ANALYSIS

The cooling rate has a direct effect on the size and distribution of microstructural phases in a casting, and in turn, the mechanical properties. A decrease in the cooling rate of the casting lowers the mechanical properties of the alloy. This is a reflection of two aspects of the cast structure: i) the difficulty of obtaining a fine modified structure at very slow

cooling rates, and ii) the increased tendency for castings to be less sound if they solidify slowly.³² The cooling rate affects the pore size as well as the microstructure (mainly the dendrite arm spacing), which in turn, controls the threshold cell size and, hence, the pore size. An increase in cooling rate decreases both the average pore size and the total porosity in alloys (non-modified or modified).

Samples for microstructural analysis were sectioned from the castings obtained from the thermal analysis experiments, carried out for G1, and G6 through G10 alloy melts. Cylindrical specimens 15 mm thick were sectioned off from the center of each graphite mold casting close to the thermocouple tip for all of the compositions castings obtained; from these, metallographic samples were prepared for qualitative and quantitative microstructural analysis, as described in CHAPTER 3. The latter was carried out using an optical microscope-image analysis system. Thermal analysis provided information about the main reactions in the alloys studied, while electron probe microanalysis (EPMA) in conjunction with EDS and WDS analyses provided chemical compositions of the observed intermetallic phases.

5.2.1 SILICON PARTICLE CHARACTERISTICS AND VOLUME FRACTION

Table 5.1 lists the chemical analysis of the various alloys studied and their respective codes, as obtained from samplings taken for this purpose from the corresponding alloys used for this part of the study (Stage II alloys).

Table 5.1 Chemical composition of the alloys used in in this part of the study (wt%)

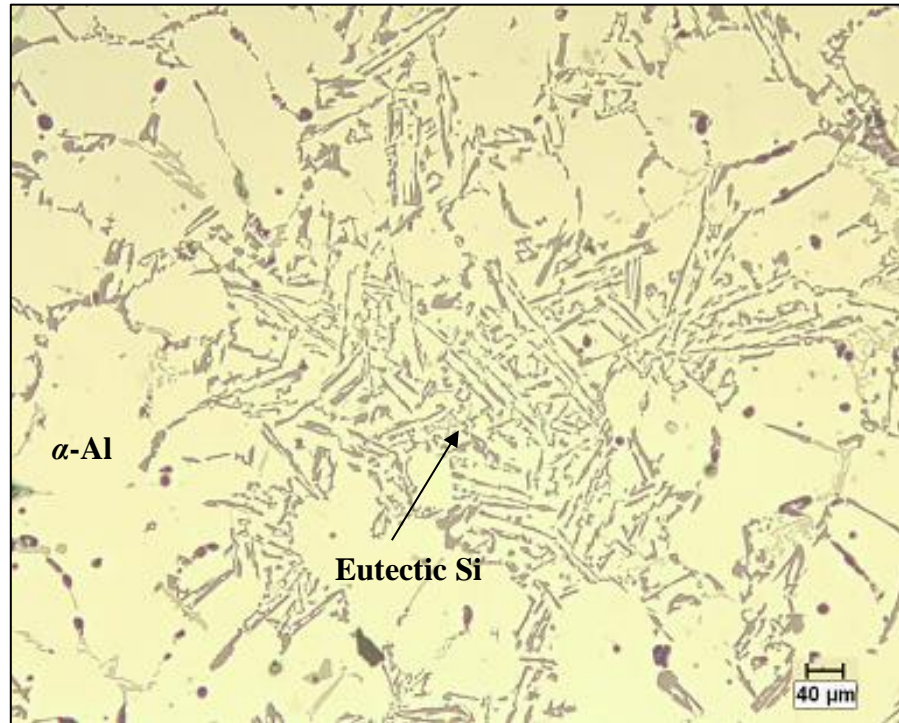
Alloy/Element	Si	Fe	Cu	Mn	Mg	Ti	Sr	Ni	Zr	Sc	Al	SF
G1	9.43	0.08	1.85	0.01	0.49	0.22	0.0150	~	~	~	Bal.	0.10
G6	8.70	0.18	1.89	0.02	0.73	0.15	0.0161	1.87	0.25	~	Bal.	0.22
G7	9.08	0.19	0.04	0.02	0.75	0.16	0.0170	1.86	0.25	~	Bal.	0.23
G8	8.92	0.18	1.88	0.75	0.74	0.15	0.0175	~	0.25	~	Bal.	1.68
G9	8.85	0.18	1.88	0.75	0.76	0.15	0.0168	1.87	0.25	~	Bal.	1.68
G10	8.95	0.19	1.87	0.03	0.75	0.15	0.0175	~	0.25	0.15	Bal.	0.25

The eutectic silicon particle characteristics were examined using a Clemex Vision PE4 optical microscope and image-analysis system as described and shown in CHAPTER 3. The morphology of the eutectic Si plays a vital role in determining the mechanical properties of Al-Si alloys. Particle size, shape, and spacing are all factors which characterize the Al-Si eutectic structure. Table 5.2 summarizes the silicon particle characteristics obtained from the alloys investigated. The addition of ~170 ppm Sr does not show a complete transformation of the morphology of Si particles from acicular to fibrous form for all alloys studied, which may be attributed to the low cooling rate of the thermal analysis casting.¹⁹ Examples of optical micrographs showing the incomplete transformation of Si particles are shown in Figure 5.1 for the ~170 ppm Sr-modified G1 (base), G8 (0.75wt% Mn + 0.25wt% Zr), and G10 (0.15wt% Sc + 0.25wt% Zr) alloys. Values obtained from the silicon particle measurements indicate that any further addition of alloying elements will decrease or weaken the effects of Sr as a modifier, as a result of their interaction with Sr to form complex intermetallic compounds.

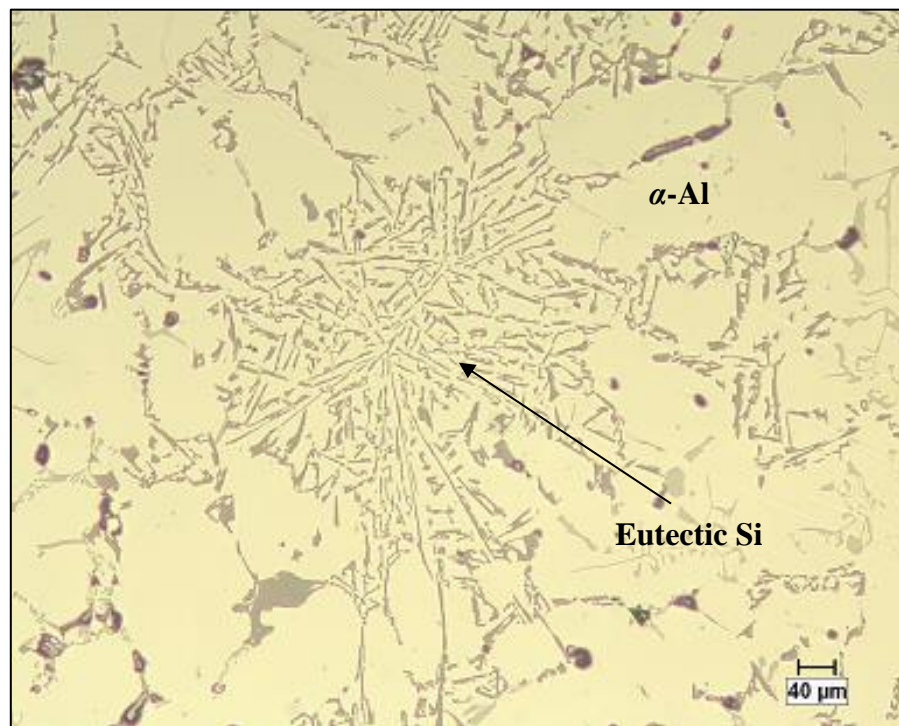
Table 5.2 Silicon particle measurements for the alloys studied using a graphite mold

Alloy Code Condition	Area (%)	Particle Area (μm^2)		Particle Length (μm)		Aspect Ratio		Roundness (%)	
	Av	Av	SD	Av	SD	Av	SD	Av	SD
G1	11.75	21.93	35.90	9.10	9.71	2.74	1.80	0.35	0.18
G6	11.95	23.10	37.50	9.12	10.10	2.54	1.41	0.36	0.19
G7	15.65	25.55	37.80	10.17	10.00	2.58	1.53	0.36	0.19
G8	14.85	35.48	52.90	12.20	10.97	2.74	1.59	0.33	0.18
G9	16.92	20.05	40.80	8.87	9.24	2.42	1.31	0.37	0.18
G10	10.81	24.03	51.15	9.40	9.20	2.40	1.36	0.38	0.17

It is interesting to note from Table 5.2 that the increase in the level of Mg and Fe and the addition of Mn, Ni, Sc and Zr, individually and/or in combination, to the alloys G6, G7, G9 and G10 has only a slight influence on the values of the average Si particle characteristics as compared to the G1 base alloy. On the other hand, alloy G8 containing 0.75wt% Mn + 0.25wt% Zr shows an overall increase in the average particle area and length of the Si particles. As shown in Table 5.2, the Si-particle length increases from 9.10 μm in the G1 alloy to 12.20 μm in the G8 alloy, while the average particle area increases from 21.93 μm^2 to 35.48 μm^2 , respectively. Moreover, the roundness and aspect ratio values of the Si particles stay stable for all alloys, at about 2.57% and 0.36%, respectively. The large standard deviations observed in Table 5.2 result from the presence of the large Si particles that appear in the microstructures (shown in Figure 5.1), mixed with the finer Si particles.

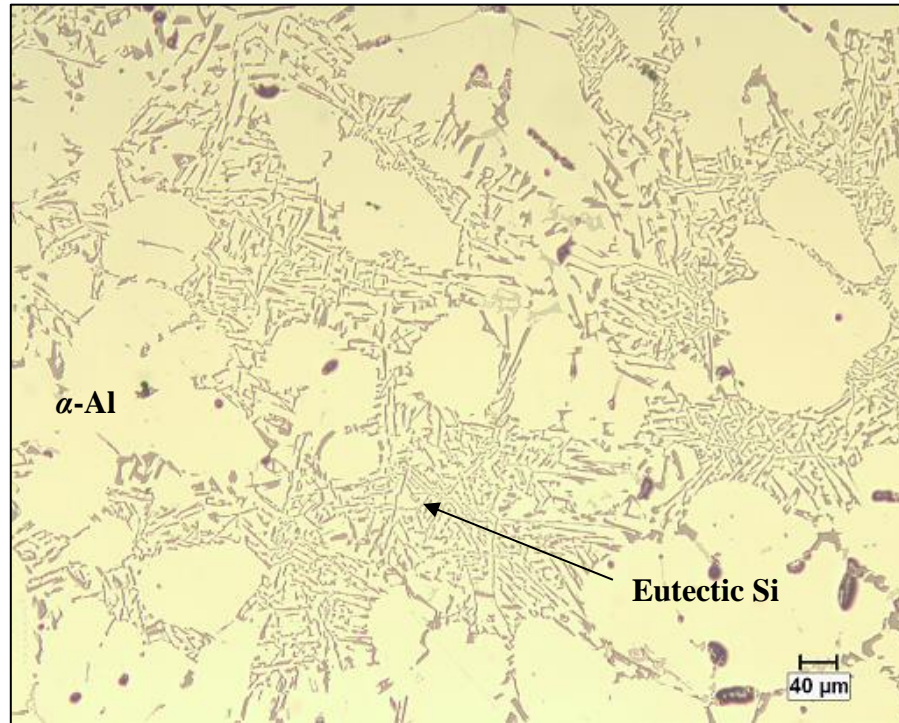


(a)



(b)

Figure 5.1 Cont.



(c)

Figure 5.1 Optical microstructure showing the incomplete transformation of Si particles at low cooling rate in Sr-modified: (a) G1 base alloy, (b) G8 alloy (0.75wt% Mn + 0.25wt% Zr), and (c) G10 alloy (0.15wt% Sc + 0.25wt% Zr).

The volume fraction of the undissolved phases in the matrix was measured using EPMA analysis. Table 5.3 lists the volume fractions obtained from the G1 and G6 through G10 alloy samples obtained from the thermal analysis castings.

Table 5.3 Volume fraction of undissolved phases observed in the matrix of alloys G1, and G6 through G10 used for this part of the study

Volume Fraction (%)	Alloy Code					
	G1	G6	G7	G8	G9	G10
TA Condition - Average	3.21	6.53	4.62	6.42	9.40	4.27
TA - Std. Deviation	0.41	0.74	0.68	0.81	0.64	0.51

As may be seen from Table 5.3, the volume fraction increases as the amount of such additives as Ni, Mn, Sc and Zr in the alloy increases. The highest volume fraction (9.4%) is exhibited by alloy G9, which is the alloy containing Ni (~2wt%), Mn (0.75wt%) and Zr (0.25wt%); followed by G6 alloy containing Ni (~2wt%) and Zr (0.25wt%), and G8 containing Mn (0.75wt%) and Zr (0.25wt%), the latter two alloys exhibiting similar volume fractions of 6.53% and 6.42%, respectively. Likewise, alloy G7 without Cu but with additions of Ni (~2wt%) and Zr (0.25wt%), and alloy G10 with additions of Sc (0.15wt%) and Zr (0.25wt%), show similar amounts of undissolved phases, 4.62% and 4.27%, respectively.

A comparison of the intermetallic volume fraction between the alloys studied are shown below:

- Comparing G8 to G9 alloy indicates that the addition of 2wt% Ni increases the vol% by ~3% (+1% Ni \approx +1.5vol%);
- Comparing G6 to G7 alloy indicates that the addition of 1.8wt% Cu increases the vol% by ~2% (+1wt% Cu \approx +1.1vol%);
- Comparing G6 to G9 alloy indicates that the addition of 0.75wt% Mn increases the vol% by ~3% (+1wt% Mn \approx +4vol%);
- Comparing G1 to G10 alloy indicates that the addition of 0.15wt% Sc and 0.25wt% Zr increases the vol% by ~1.06% (+1wt% Zr and Sc \approx +2.65vol%).
 - Showing that Mn has the maximum effect in increasing the total volume fraction (per 1% addition).

From these comparisons in volume fraction values, it may be reasonably deduced that transition elements such as Ni, Mn, and Zr in the G9 alloy must interact among themselves or with other elements contained in the base alloy, in order to form new phases, thereby increasing the overall volume fraction of intermetallics obtained. The increase in volume fraction may be also explained by the interaction between Fe and Mn and/or Cr if present, to form another version of the α -Fe phase, namely $\alpha\text{-Al}_{15}(\text{Fe,Mn})_3\text{Si}_2$, termed sludge.

5.2.2 THERMAL ANALYSIS: BASE ALLOY G1

The G1 base alloy contains around 9.4wt% Si, 0.08wt% Fe, 1.85wt% Cu, 0.5wt% Mg, 0.22wt% Ti, and ~170 ppm of Sr; it can hence be classified as an Al-Si-Cu-Mg type alloy. Based on this composition, the main phases expected for this alloy will be Cu- and Mg-rich intermetallic phases as well as Fe-rich intermetallic phases. In order to determine the main intermetallic phases and their formation reactions in the alloys studied, temperature-time cooling curves were obtained under low cooling rate conditions (0.35°C/s), using the thermal analysis set-up described in CHAPTER 3. The reactions observed for these alloys are listed in Table 5.4.

Table 5.4 Proposed main reactions occurring during solidification of alloys G1, G6 through G10^{19, 30, 36, 126, 261}

Reaction #	Suggested Temperature Range (°C)	Suggested Precipitated Phase
1	600-597	- Formation of α -aluminum dendritic network
2	560-558	- Precipitation of Al-Si eutectic - Precipitation of post-eutectic β -Al ₅ FeSi phase
3	555-556	- Precipitation of Al ₉ FeNi phase
4	540-538	- Precipitation of Mg ₂ Si phase
5	525-523	- Transforming of β -phase into π -Al ₈ Mg ₃ FeSi ₆ phase
6	523-520	- Precipitation of Al ₃ CuNi phase
7	500-496	- Formation of eutectic Al-Al ₂ Cu phase
8	485-489	- Precipitation of Q -Al ₅ Mg ₈ Cu ₂ Si ₆ phase

Based on the thermal analysis data obtained, the cooling curve and the first derivative were drawn, as shown in Figure 5.2 for base alloy G1. The numbers on the first derivative curve correspond to the same reaction numbers listed in Table 5.4. Similarly, the reactions observed in the other alloys are numbered on their first derivative curves, as will be presented later on in Figure 5.6, Figure 5.10, Figure 5.13, Figure 5.17 and Figure 5.21.

As may be seen from Figure 5.2, alloy G1 starts to solidify at 598°C (Reaction 1) through the development of the dendritic network followed by the precipitation of the Al-Si eutectic and the post-eutectic β -Al₅FeSi phase (Reaction 2) at 560°C, the Mg₂Si phase (Reaction 4) at 540°C, and the transformation of β -phase into π -Al₈Mg₃FeSi₆ phase (Reaction 5) at 525°C; following which the Al₂Cu and Q -Al₅Mg₈Cu₂Si₆ phases precipitate as the last reactions at 498°C and 488°C, respectively, toward the end of solidification.

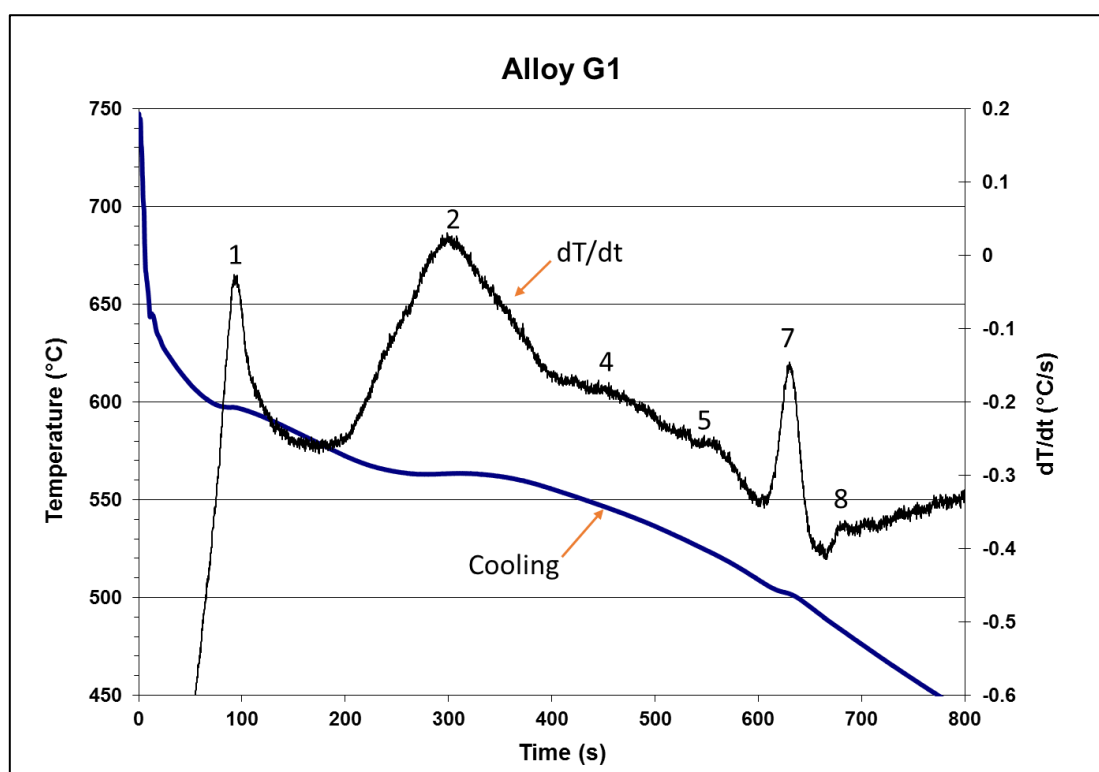
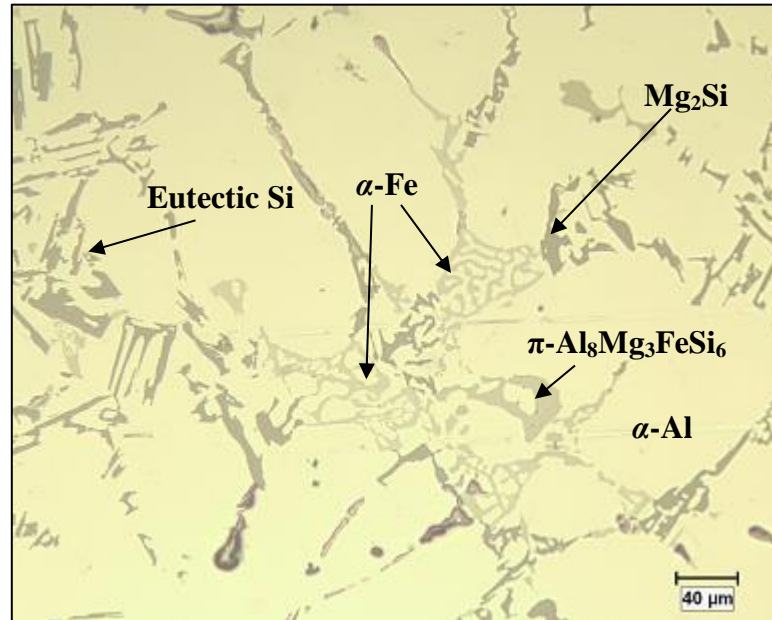


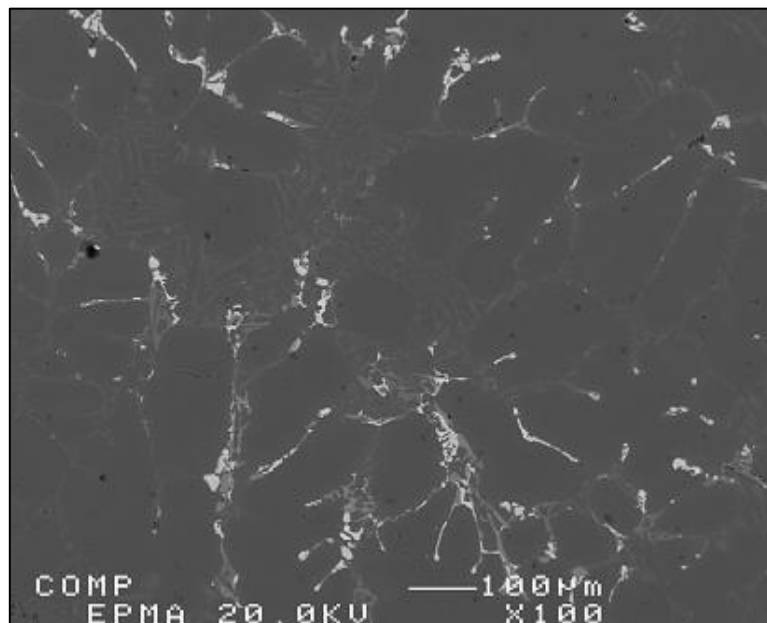
Figure 5.2 Temperature-time plot and first derivative obtained from the thermal analysis of base alloy G1.

The optical micrograph shown in Figure 5.3(a) for alloy G1 illustrates prominent phases such as the α -Al dendrites and the eutectic silicon phase in/at the interdendritic regions/boundaries of the primary Al grains and also the α -Fe phase script particles, the intermetallic phases being observed more clearly as the white particles in interdendritic regions away from the eutectic Si areas in the backscattered electron image shown in Figure 5.3(b). Figure 5.4 displays a higher magnification backscattered electron image showing clearly some of the other phases observed in the base alloy. These phases were identified by WDS, as shown in Table 5.5 and are those typically observed in Al-Si-Cu-Mg alloys.^{17, 19, 20, 49, 244} With regard to alloy G1, even if the Q -Al₅Mg₈Cu₂Si₆ phase reaction may only barely be perceived at 488°C, the solidification range is still one of 115°C, *i.e.* from 600°C to 485°C, similar to the solidification range observed for 319 alloy.¹⁹

With regard to the π -phase, the stoichiometry proposed by Closset *et al.*⁶³ and Bäckerud *et al.*,³⁶ is Al₈FeMg₃Si₆. In the present study, the calculated stoichiometry of the β - and π -phase iron intermetallic phases based on the composition obtained from WDS analysis of the alloy samples examined lie in the vicinity of the suggested formulas,³⁶ as presented in Table 5.5 and Figure 5.4, regardless of the Fe and Mg content of the alloys. The EDS spectra corresponding to Al₂Cu, β -Al₅FeSi, π -Al₈Mg₃FeSi₆, and Q -Al₅Mg₈Cu₂Si₆ phases observed in Figure 5.3(a) and Figure 5.4 are presented in Figure 5.5. These results are in keeping with the WDS analysis for the base alloy G1.



(a)



(b)

Figure 5.3 (a) Optical microstructure (200X) and (b) backscattered electron image of the G1 alloy sample obtained from the thermal analysis casting (cooling rate 0.35°C/s), showing different phases in the alloy.

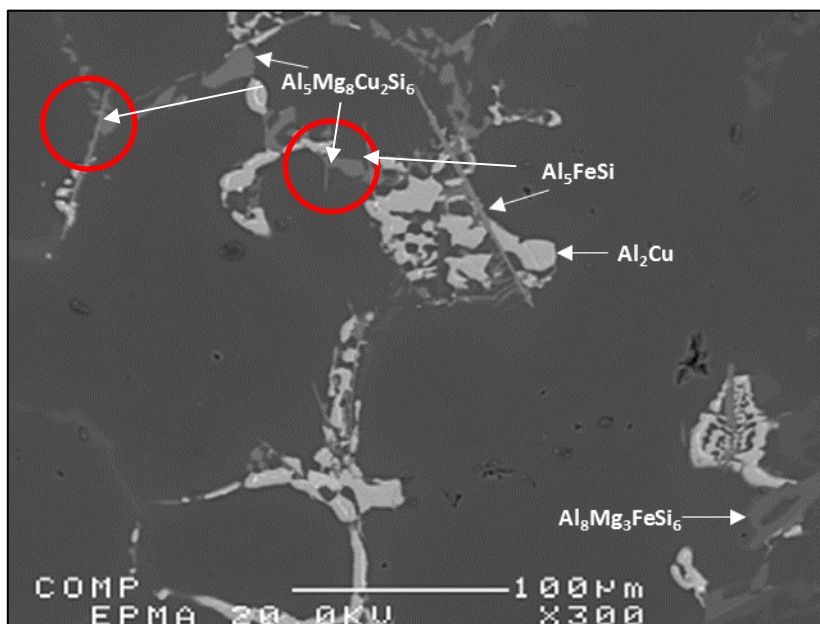
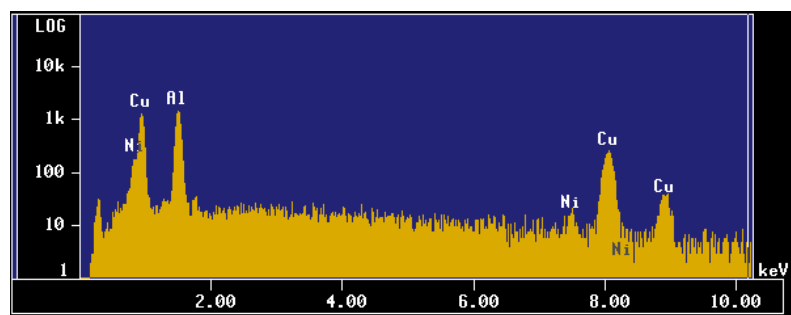


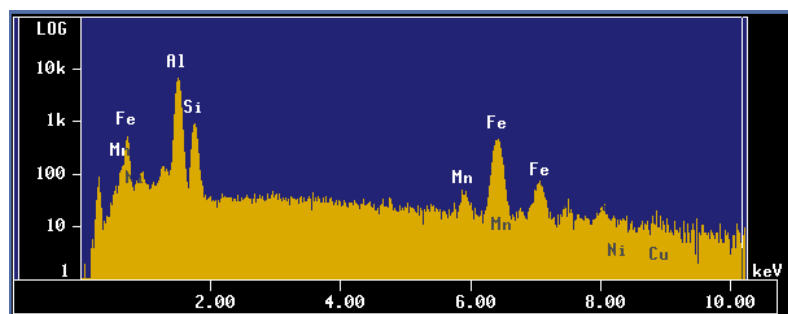
Figure 5.4 Backscattered electron image showing some of the phases observed in base alloy G1.

Table 5.5 WDS analysis of phases observed in base alloy G1

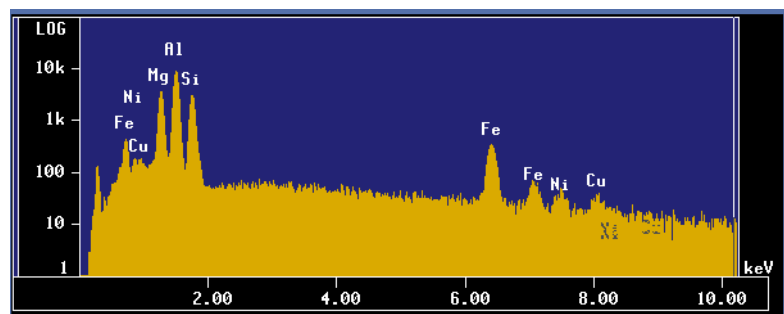
Alloy Code	Element	Wt%	At%	Calculated Formula	Suggested Formula
G1	Al	47.26	51.51	$\text{Al}_{10.6}\text{FeMg}_{4.02}\text{Si}_{4.7}$	$\text{Al}_8\text{FeMg}_3\text{Si}_6$
	Fe	9.20	4.85		
	Mg	16.15	19.53		
	Si	22.09	23.12		
	Total	94.70	99.01		
	Al	48.50	68.10	$\text{Al}_{2.25}\text{Cu}$	Al_2Cu
	Cu	50.70	30.21		
	Total	99.20	98.31		
	Al	17.18	18.30	$\text{Al}_{4.08}\text{Cu}_2\text{Mg}_{9.2}\text{Si}_7$	$\text{Al}_5\text{Cu}_2\text{Mg}_8\text{Si}_6$
	Cu	19.86	8.98		
	Mg	34.96	41.32		
	Si	30.65	31.35		
	Total	72.00	68.60		
	Mg	62.91	67.42	$\text{Mg}_{2.1}\text{Si}$	Mg_2Si
	Si	36.45	32.36		
	Total	62.91	67.42		



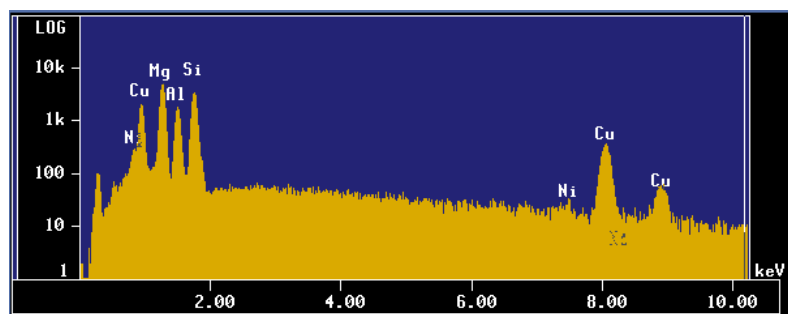
(a)



(b)



(c)



(d)

Figure 5.5 EDS spectra corresponding to Al_2Cu , $\beta\text{-Al}_5\text{FeSi}$, $\pi\text{-Al}_8\text{Mg}_3\text{FeSi}_6$, and $Q\text{-Al}_5\text{Mg}_8\text{Cu}_2\text{Si}_6$ phases observed in Figure 5.4.

When magnesium is added to the alloy, there is a tendency for segregation of the copper phase in localized areas, leading to the formation of the block-like, rather than the fine eutectic-like Al_2Cu phase. If iron is also present in the alloy, then it partially goes into solid solution in the matrix and, in part, forms intermetallic compounds (including the plate-like $\beta\text{-Al}_5\text{FeSi}$ and the script-like $\alpha\text{-Al}_{15}(\text{Mn,Fe})_3\text{Si}_2$ phases or $\text{Al}_8\text{Fe}_2\text{Si}$ in Al-Si-Mg alloys) during solidification. In the solidification process, $\beta\text{-Al}_5\text{FeSi}$ platelets are very active sites for the nucleation of the Al_2Cu phase. In Al-Si alloys, the size of the $\beta\text{-Al}_5\text{FeSi}$ intermetallic phase is directly dependent on the Fe content and cooling rate. An increase in the iron content easily increases the size of the β -iron phase platelets (or needles as they appear in the microstructure). A decrease in the cooling rate has the same effect, considering that the growth of β -iron intermetallic occurs at low driving forces or at slow cooling, *i.e.* at low degrees of undercooling.⁹⁰ The addition of Mg leads to the formation of the $\pi\text{-Al}_8\text{Mg}_3\text{FeSi}_6$ phase with script morphology. Under cooling rates close to equilibrium conditions for multicomponent 3xx type alloys, and at $\sim 540^\circ\text{C}$, the Mg_2Si and $\pi\text{-Al}_8\text{Mg}_3\text{FeSi}_6$ phases begin to precipitate. If the temperature is lowered to between 490°C - 530°C , precipitation of the Al_2Cu and $Q\text{-Al}_5\text{Mg}_8\text{Cu}_2\text{Si}_6$ phases occurs.²⁶²

Iron intermetallics in G1 base alloy were present in the form of acicular or platelet shaped $\beta\text{-Al}_5\text{FeSi}$ particles, as well as script-like $\pi\text{-Al}_8\text{Mg}_3\text{FeSi}_6$ particles. Also, other Mg and Cu intermetallic phases were observed, namely $Q\text{-Al}_5\text{Mg}_8\text{Cu}_2\text{Si}_6$ and Al_2Cu , as shown in Figure 5.4. It is expected that as solidification proceeds, the β -phase present will be transformed into the π -phase as a result of the peritectic reaction $\text{L} + \text{Al}_5\text{FeSi} \rightarrow \text{Al} + \text{Si} + \text{Al}_8\text{Mg}_3\text{FeSi}_6$. The π -phase affects ductility, as it assists in crack propagation. These effects

may contribute to the levelling off of mechanical properties at higher magnesium levels.^{81,}
^{91, 132} Increasing the solidification rate reduces the size of microstructural constituents, including eutectic silicon and intermetallics; this renders crack propagation through the material more difficult, thereby increasing the crack propagation energy.^{81, 91} The Al₂Cu phase precipitates in both block-like and eutectic-like forms whereas the *Q*-Al₅Mg₈Cu₂Si₆ phase appears as small particles growing out of the Al₂Cu phase. The absence of free Si in the microstructure implies that the Si content of the alloy was consumed in the formation of the *Q*-Al₅Mg₈Cu₂Si₆ and α -Fe phases.

The π -Al₈Mg₃FeSi₆ phase is often observed to be in close contact with β -Al₅FeSi phase platelets. Figure 5.4 shows the interface between the β - and π -phase is seamlessly fused together (see red circled areas), which may lead to the reasonable assumption that the β -Al₅FeSi phase will precipitate as a first step, followed by the growth of the π -Al₈Mg₃FeSi₆ phase from the surface of the β -Al₅FeSi thereafter, according to the reaction:

$$L + Al_5FeSi \rightarrow Al + Si + Al_8Mg_3FeSi_6.$$
³⁶

Table 5.6 through Table 5.10 present the chemical compositions of the phases examined in alloys G6 through G10, as obtained from the WDS analysis of the respective samples. For the sake of simplicity, these tables show only the WDS analysis of those phases which are not shared with the base alloy G1.

5.2.3 THERMAL ANALYSIS: ALLOY G6 (2wt% Ni + 0.25wt% Zr)

The cooling curve for alloy G6 containing 2wt% Ni + 0.25wt% Zr obtained from its time-temperature data and the first derivate plot are show in Figure 5.6. Apart from the α -Al dendrites and the eutectic Si particles observed in the interdendritic regions, other phases may also be observed, in the optical micrograph and in the backscattered images of G6 alloy shown in Figure 5.7. It is interesting to note that the eutectic Si particles observed in Figure 5.7, as well as those shown in Figure 5.1 and Figure 5.3(a) for base alloy G1, appear to be only partially modified even though the alloys contained over ~170 ppm Sr, as listed in Table 5.1. As mentioned previously, the incomplete modification of the eutectic silicon structure may be attributed to the slow cooling rate obtained in the thermal analysis experiments.

It has been reported^{99, 263} that increasing the Fe content to more than 0.1wt% changes the solidification sequence in Al-7Si-0.4Mg alloys. At 0.1wt% Fe, the β -Fe phase precipitates at low temperatures together with the Al-Si eutectic and is characterized by fine platelets in the microstructure. At more than 0.1wt% Fe, however, most of the β -phase will precipitate at a higher temperature, before the Al-Si eutectic. This β -phase is characterized by its large size in the microstructure. Consequently, increasing the Fe content will increase the quantity and size of the β -phase platelets in the microstructure, which is not favorable to the mechanical properties.^{90, 263}

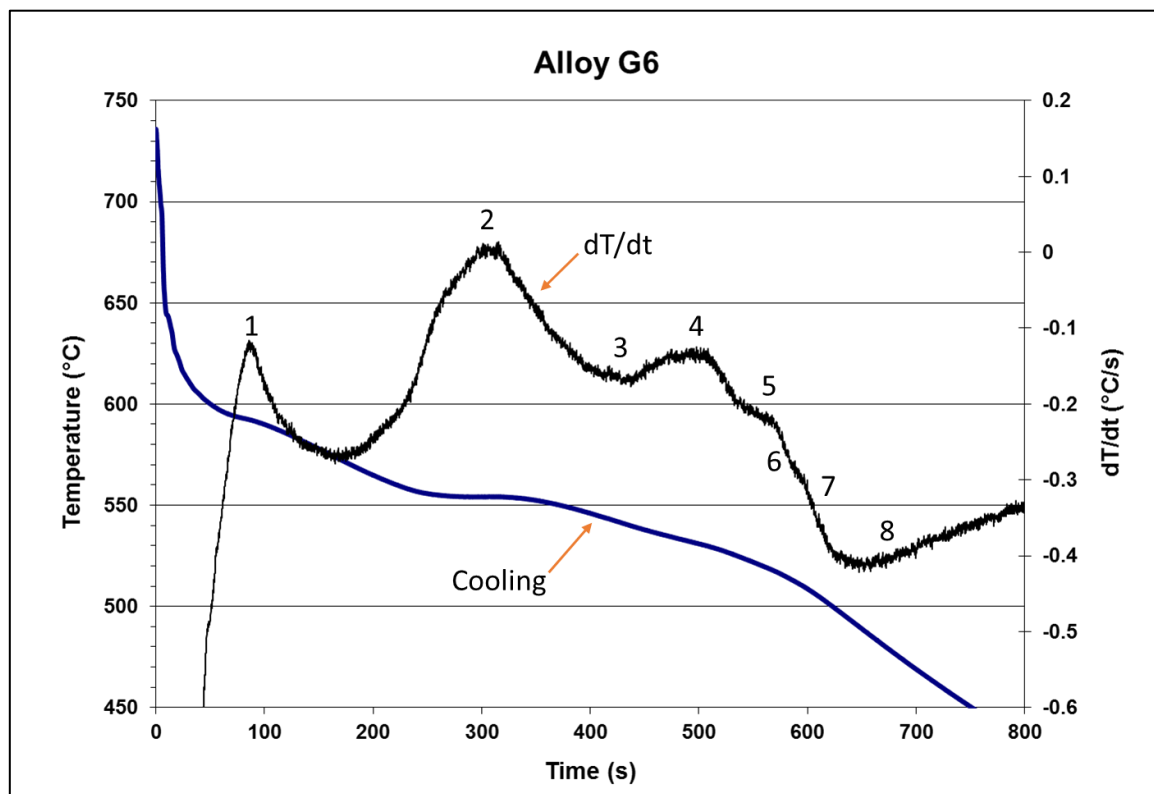
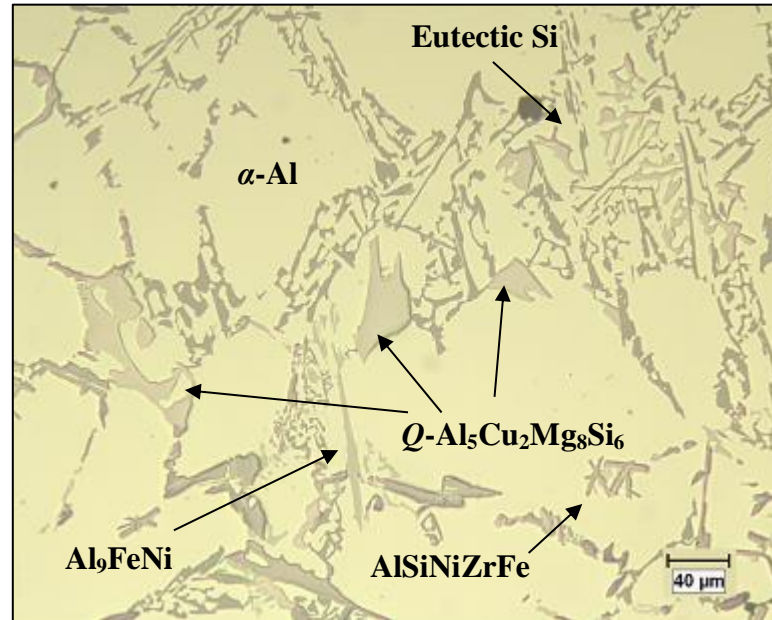
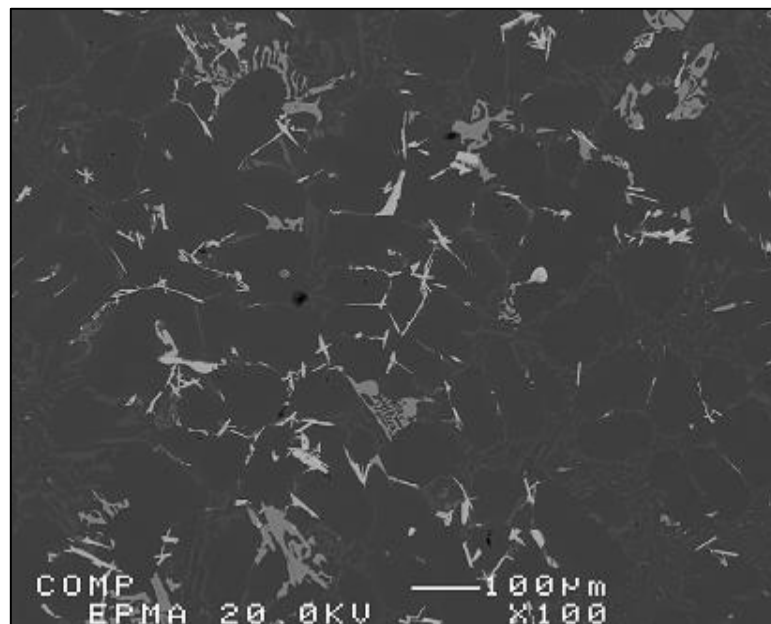


Figure 5.6 Temperature-time plot and first derivative from the thermal analysis of alloy G6 (containing 2wt% Ni + 0.25wt% Zr).

Figure 5.8 shows a backscattered image with some of the other phases observed in alloy G6. Figure 5.8(b) through (d) show the X-ray images, in which the different elements (Fe, Mg, Ni and Zr) concentrations may be seen, are all in keeping with the WDS analysis show in Table 5.6. Figure 5.9 shows the EDS spectrum of AlSiNiZrFe observed in Figure 5.8(a).

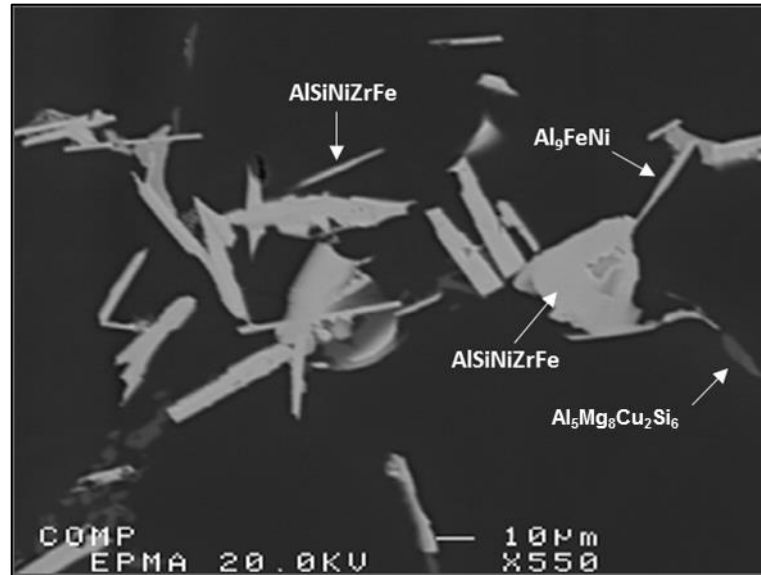


(a)



(b)

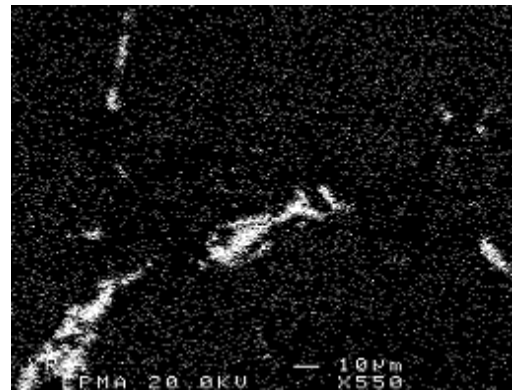
Figure 5.7 (a) Optical microstructure at 200X magnification, and (b) backscattered image of the G6 (2wt% Ni + 0.25wt% Zr) alloy sample, obtained from the thermal analysis casting (cooling rate 0.35°C/s), showing different phases present in the alloy.



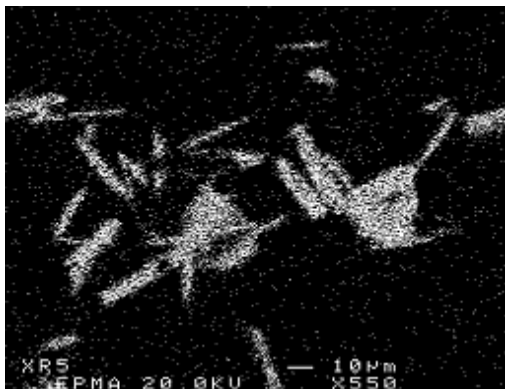
(a) BSE



(b) Fe



(c) Mg



(d) Ni



(e) Zr

Figure 5.8 (a) Backscattered electron image of G6 alloy (2wt% Ni + 0.25wt% Zr), showing the different intermetallic phases observed, and (b) through (e) corresponding X-ray images of Fe, Mg, Ni and Zr, respectively.

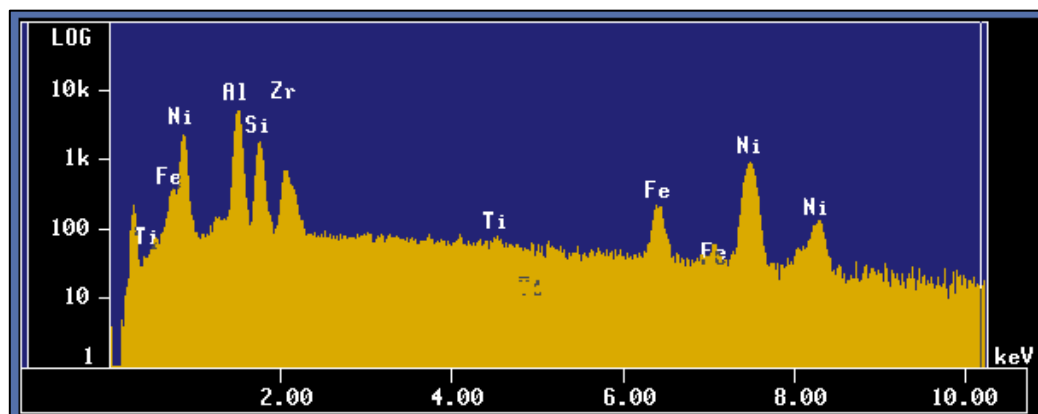


Figure 5.9 EDS spectrum corresponding to AlSiNiZrFe phase observed in Figure 5.8(a).

Table 5.6 WDS analysis of phases observed in alloy G6

Alloy Code	Element	Wt%	At%	Calculated Formula	Suggested Formula
G6	Al	66.69	80.44	$Al_{8.94}Fe_{0.25}Ni_{1.7}$	Al_9FeNi
	Fe	3.86	2.25		
	Ni	27.62	15.31		
	Total	99.85	98.86		
	Al	34.05	50.72	$Al_{15.98}FeSi_{5.18}$ $Ni_{7.03}Zr_{1.87}$	$Al_9FeSi_3Ni_4Zr$
	Fe	4.41	3.18		
	Si	11.50	16.46		
	Ni	32.59	22.31		
	Zr	13.48	5.94		
	Total	97.19	93.4		
	Al	39.32	60.44	$Al_{10.54}Si_{2.34}TiZr_{3.44}$	$(Al,Si)_3(Ti,Zr)$
	Si	9.09	13.43		
	Ti	6.61	5.73		
	Zr	43.4	19.74		
	Total	98.42	99.34		

The mechanism involved in Al_2Cu precipitation was proposed by Samuel *et al.*¹²³ as follows:

- i) During the first stages of solid fraction, the formation of the α -Al dendritic network is associated with the segregation of Si and Cu in the melt, ahead of the progressing dendrites;
- ii) When the solidification temperature approaches the eutectic temperature, Si particles precipitate, leading to a local concentration of Cu in the remaining areas, and because of this segregation, the Al_2Cu phase more often than not precipitates in the block-like form rather than in the fine eutectic form.

In the alloys containing nickel, the Al_3CuNi phase is observed situated adjacent to the Al_2Cu phase and both phases are located at the limits of the dendritic α -Al phase; this observation is in concordance with the fact that the reactions noted in the thermal analysis curves, namely Reaction 6 and 7, are contiguous to one another.

5.2.4 THERMAL ANALYSIS: ALLOY G7 (2wt% Ni + 0.25wt% Zr, no Cu)

The cooling curve of alloy G7 which, similar to alloy G6, contains 2wt% Ni + 0.25wt% Zr but no Cu, was obtained from its temperature-time data and is shown along with its first derivate plot in Figure 5.10. Apart from the α -Al dendrites and the eutectic Si particles observed in the interdendritic regions, other phases may also be observed in the optical micrograph and in the backscattered image of the alloy G7 sample, as shown in Figure 5.11(a) and Figure 5.11(b), respectively.

The optical micrograph of Figure 5.11(a) for G7 alloy displays large sized Mg_2Si particles with Chinese-script morphology, together with α -Fe script-like particles, Al_3Ni phase, and π - $Al_8Mg_3FeSi_6$ phase particles. The presence of the π - $Al_8Mg_3FeSi_6$ and Mg_2Si phases in the low cooling rate (thermal analysis) condition primarily depends on the Mg content. Although the π -phase and Mg_2Si phase reactions were observed in the first derivative curve of alloy G1, the proportion of Mg_2Si formed increased as the Mg level increased, as evidenced by Figure 5.10 and Figure 5.11 in the case of G7 alloy.

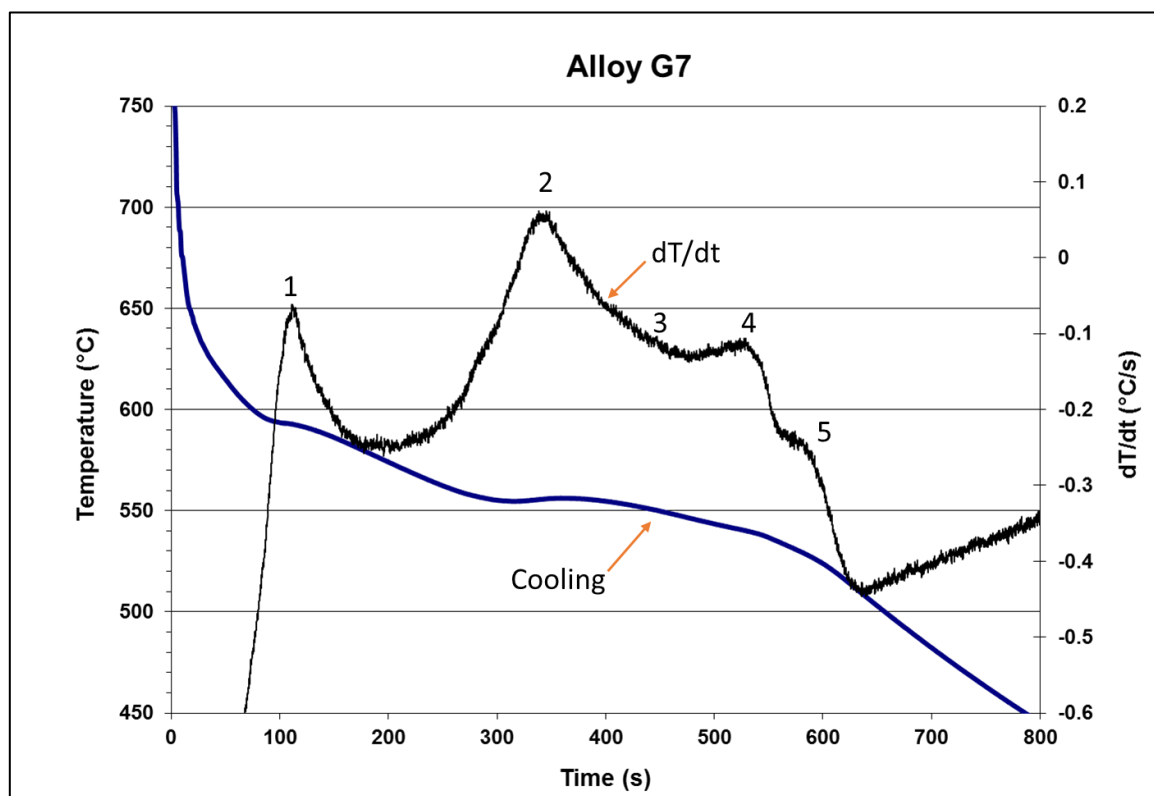
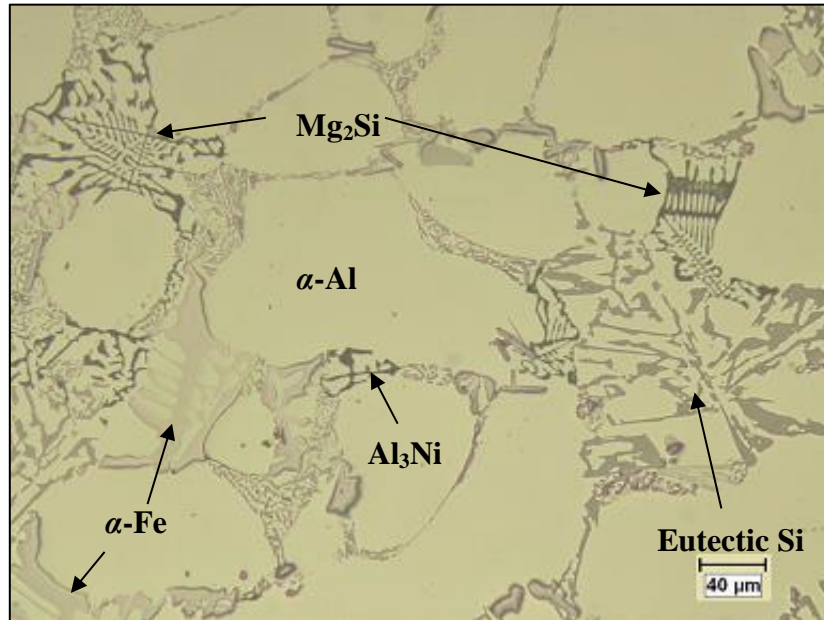
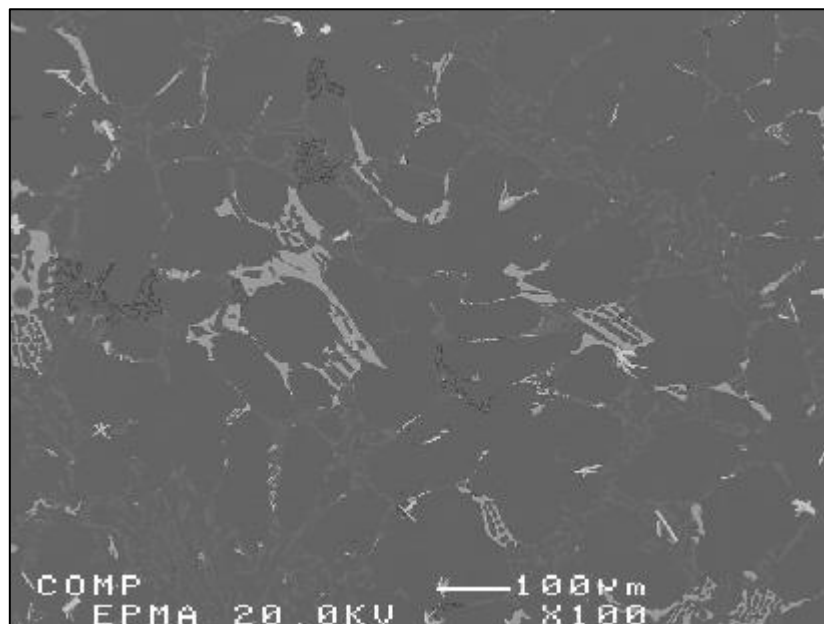


Figure 5.10 Temperature-time plot and first derivative from the thermal analysis of alloy G7 (containing 2wt% Ni + 0.25wt% Zr, but no Cu).



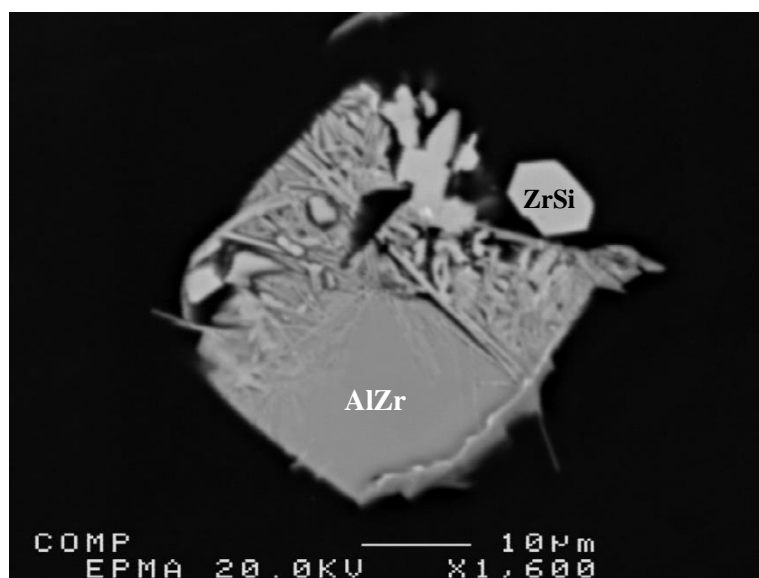
(a)



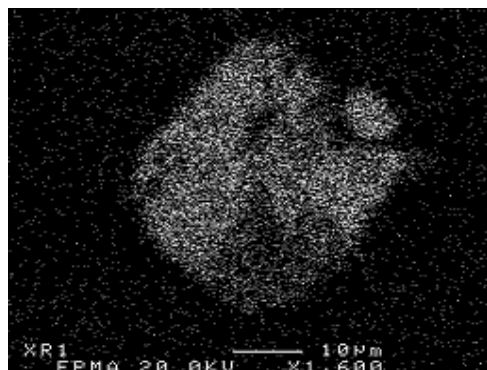
(b)

Figure 5.11 (a) Optical microstructure at 200X magnification and (b) backscattered electron image of the G7 (2wt% Ni + 0.25wt% Zr, but no Cu) alloy sample, obtained from the thermal analysis casting (cooling rate 0.35°C/s), showing the different phases present in the alloy.

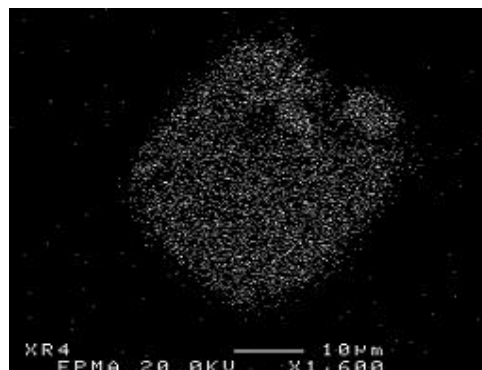
Figure 5.12(a) shows a high-magnification backscattered electron image taken from alloy G7 revealing the presence of ZrSi and AlZr or more correctly, (Zr,Ti)Si and (Al,Si)₃Zr phases; the corresponding X-ray images of Si and Zr shown in Figure 5.12(b) and (c) are in keeping with the WDS analysis shown. Table 5.7 for G7 alloy, and in Table 5.8 through Table 5.10 for the remaining alloys studied, which further confirmed that each of these two phases differs in its silicon and aluminum content.



(a) BSE



(b) Si



(c) Zr

Figure 5.12 (a) High-magnification backscattered electron image of alloy G7, showing different phases; (b) and (c) corresponding X-ray images of Si and Zr.

Table 5.7 WDS analysis of phases observed in alloy G7

Alloy Code	Element	Wt%	At%	Calculated Formula	Suggested Formula
G7	Si	23.90	50.12	$\text{Si}_{3.04}\text{Ti}_{1.33}\text{Zr}_{1.05}$	Si(Ti,Zr)
	Ti	0.98	1.20		
	Zr	70.23	45.35		
	Total	95.11	96.67		
	Zr	70.23	45.35	$\text{ZrSi}_{1.10}$	ZrSi
	Si	23.90	50.12		
	Total	94.13	95.47		
	Al	39.10	62.82	$\text{Al}_3\text{Si}_{0.56}\text{Zr}_{1.14}$	$(\text{Al,Si})_3\text{Zr}$
	Si	7.54	11.64		
	Zr	50.55	24.02		
	Total	97.19	98.48		

5.2.5 THERMAL ANALYSIS: ALLOY G8 (0.75wt% Mn + 0.25wt% Zr)

The cooling curve of alloy G8 (containing 0.75wt% Mn + 0.25wt% Zr), obtained from its time-temperature data and its first derivate plot are shown in Figure 5.13. Apart from the α -Al dendrites and the eutectic Si particles observed in the interdendritic regions, other phases may also be observed, in the optical micrograph and backscattered image of alloy G8 displayed in Figure 5.14(a) and (b), respectively.

Neutralization of Fe through the promotion of the less harmful α -Fe Chinese-script phase is sought at the expense of the brittle needle-like β -Fe phase with the goal of improving strength, ductility and other properties. At higher Mn:Fe ratios and/or in the presence of chromium, however, the iron, manganese and chromium form another version of the α -Fe phase, α -Al₁₅(Fe,Mn,Cr)₃Si₂, termed sludge. In this alloy an α -Al₁₅(Fe,Mn)₃Si₂

phase was observed, displaying a star-like morphology, and located within the α -Al dendrites, as shown in Figure 5.14(a) and (b).

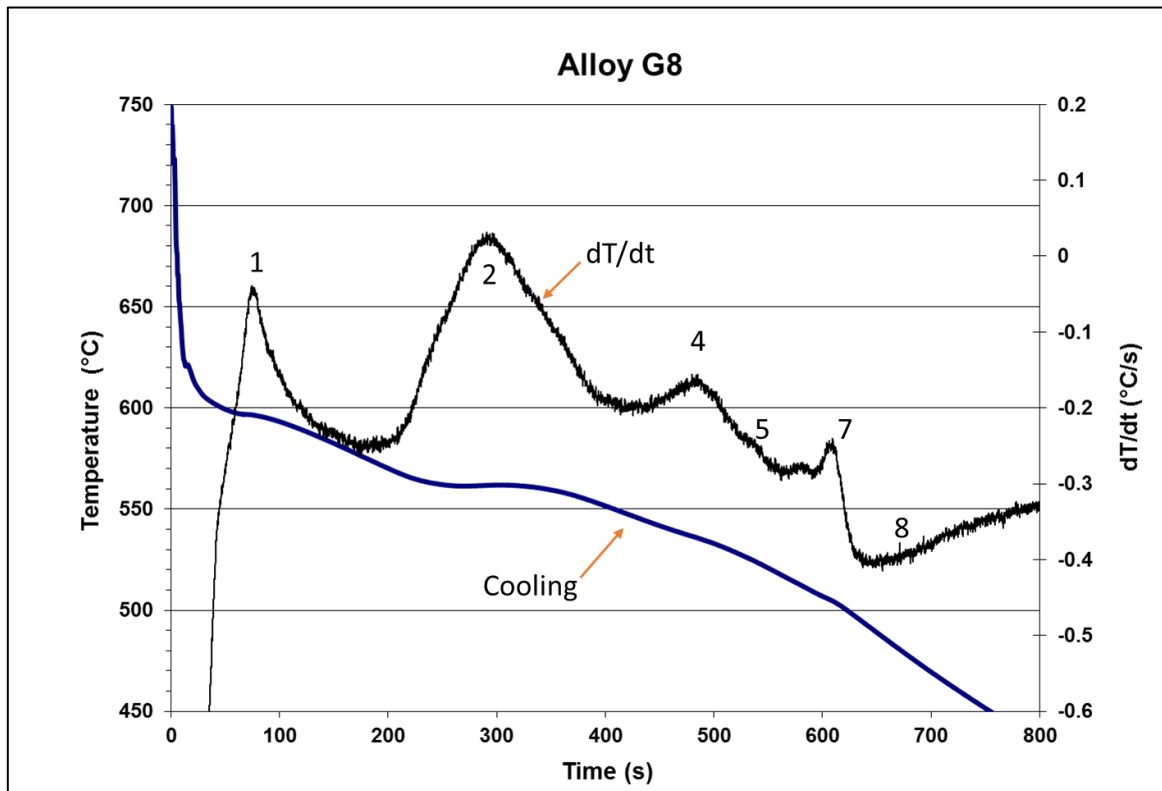


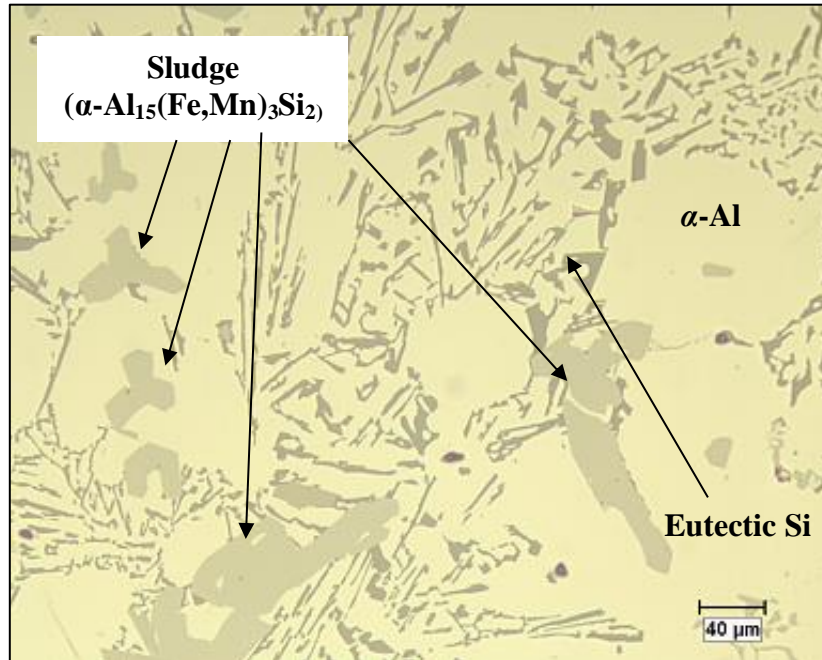
Figure 5.13 Temperature-time plot and first derivative from the thermal analysis of alloy G8 (containing 0.75wt% Mn + 0.25wt% Zr).

The precipitation of sludge particles need not necessarily be harmful to the alloy, as is commonly perceived in the literature, where sludge particles are usually observed in the interdendritic regions. This phenomenon of iron intermetallic precipitation within the α -Al dendrites proves very useful in the case of such Al-Si die-casting alloys as 380 alloy, containing 9wt% Si, where the proportion of α -Al dendrites is relatively higher.²⁶⁴

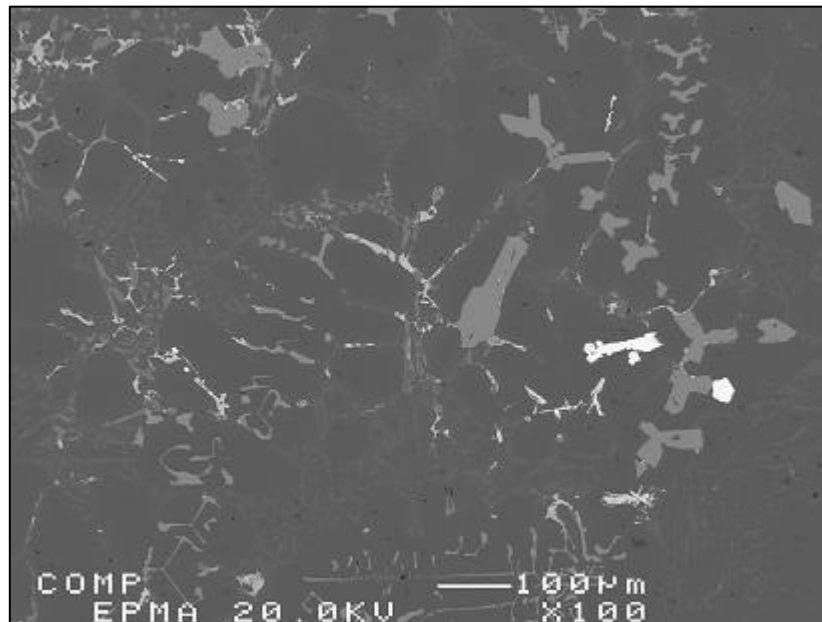
The tendency of a molten alloy to form sludge can be predicted by the holding temperature and its *sludge factor* ($SF = 1 \times \text{wt\% Fe} + 2 \times \text{wt\% Mn} + 3 \times \text{wt\% Cr}$).^{49, 54} This factor is an empirical formula applied to Al-Si-Cu alloys and is used to determine how much Fe, Mn, and Cr can cause sludge to form. At higher holding temperatures, or with an agitated bath as occurs in induction furnaces, a sludge factor of 1.8 will normally result in sludge formation if a casting temperature of 650°C or more is maintained; despite this, for lower holding temperatures, a sludge factor of 1.4 or less may have to be applied, since sludge formation is a temperature-dependent process in combination with the Fe, Mn, and Cr concentrations, independent of the Si content.

If Mg is also present with Si, π -phase can form, $\text{Al}_5\text{Si}_6\text{Mg}_8\text{Fe}_2$, having a script-like morphology. The Fe-rich sludge particles can be twice as large as the Si particles, and the cooling rate has a direct impact on the kinetics, quantities and size of this phase formed in the microstructure,²⁶⁵ as may be seen in Figure 5.14 for alloy G8 with its high content of Mn (0.75wt%) and, with an iron content of 0.18wt%, giving a sludge factor of 1.68.

For the purpose of this study, the backscattered image and X-ray mappings of the $(\text{Al,Si})_3(\text{Zr,Ti})$ phase were examined to further investigate the distribution of Al, Si, Ti, and Zr within this phase. The results are displayed in Figure 5.15. The EDS spectrum for the $(\text{Al,Si})_3(\text{Zr,Ti})$ phase which is an Al-rich phase and shows a stronger Al peak, is presented in Figure 5.16. These results are in keeping with the WDS analysis shown Table 5.8 for G8 alloy.



(a)



(b)

Figure 5.14 (a) Optical microstructure at 200X magnification and (b) backscattered electron image of the G8 (0.75wt% Mn + 0.25wt% Zr) alloy sample, obtained from the thermal analysis casting (cooling rate 0.35°C/s), showing different phases present in the alloy.

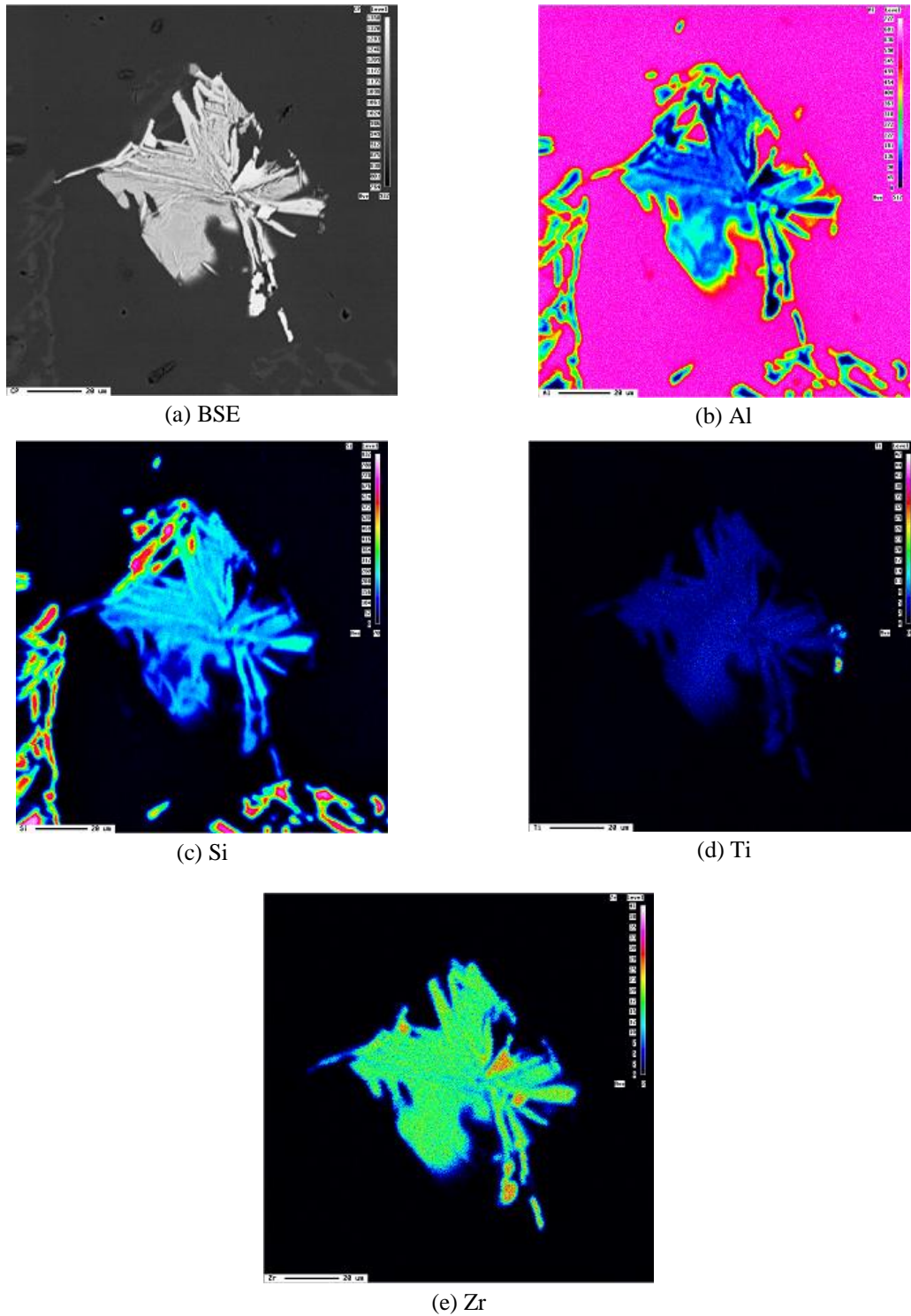


Figure 5.15 (a) Backscattered electron image of the G8 alloy (0.75wt% Mn + 0.25wt% Zr) sample showing the $(\text{Al,Si})_3(\text{Zr,Ti})$ phase; (b) through (e) corresponding X-ray images of Al, Si, Ti, and Zr.

Despite the fact that the thermal analysis curves did not detect any Zr-rich phase reaction, the EPMA, WDS, and EDS results clearly indicate that while there is no reaction of Zr with nickel, copper, strontium, it reacts with Ti, Si, and Al to form the block-like $(\text{Al,Si})_2(\text{Zr,Ti})$ phase with a high silicon content, and the needle-like $(\text{Al,Si})_3(\text{Zr,Ti})$ phase with a high Al content.

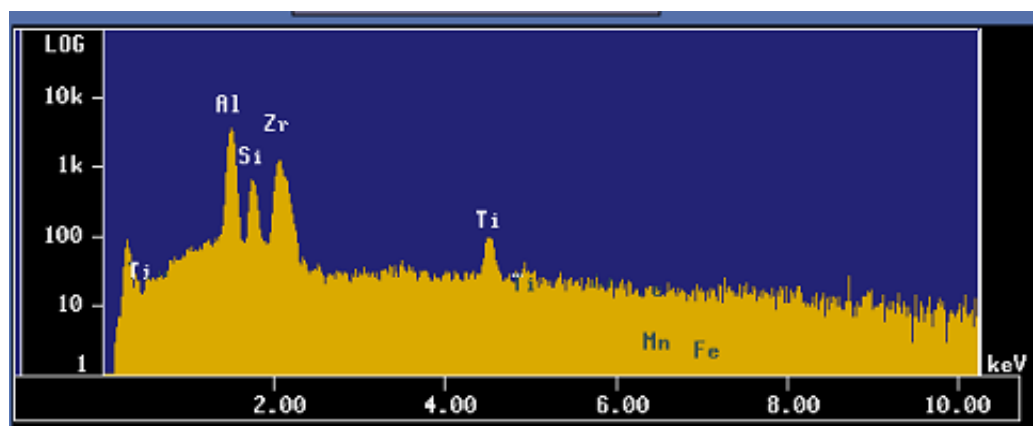


Figure 5.16 EDS spectrum corresponding to $(\text{Al,Si})_3(\text{Zr,Ti})$ phase observed in Figure 5.15(a).

Table 5.8 WDS analysis of phases observed in alloy G8

Alloy Code	Element	Wt%	At%	Calculated Formula	Suggested Formula
G8	Si	22.99	49.51	$\text{ZrSi}_{1.06}$	ZrSi
	Zr	70.35	46.65		
	Total	93.34	96.16		
	Al	39.43	60.88	$\text{Al}_{5.88}\text{Si}_{1.34}\text{Ti}_{0.25}\text{Zr}_{2.14}$	$(\text{Al,Si})_3(\text{Ti,Zr})$
	Si	9.39	13.92		
	Ti	2.97	2.59		
	Zr	49.21	22.47		
Total	101.00	99.86			

In Zr-containing alloys, Al_3Zr primary particles may appear in such different shapes as square, rectangular, and spherical. These primary particles are found to act as nucleation sites for Zr- and Sc-rich intermetallics. The composition of this phase was determined using WDS analysis, and was found to correspond to the Al_3Zr phase. As a result of the low cooling rate (0.35°C/s) and a zirconium content 0.25wt%, all Zr-containing alloys are located in the $\text{L} + \text{Al}_3\text{Zr}$ region of the Al-Zr phase diagram during the melting stage. This indicates that the coarse Al_3Zr particles are not formed from the melt during solidification but come instead directly from the Al-15wt% Zr master alloy added to the liquid melt. These particles do not dissolve in the melt, and they provide favored nucleation sites for the growth of the Zr-, Sc-, and Ti-intermetallics from the melt during solidification.^{92, 153}

5.2.6 THERMAL ANALYSIS: ALLOY G9 (2wt% Ni + 0.75wt% Mn + 0.25wt% Zr)

The cooling curve of alloy G9 containing 2wt% Ni + 0.75wt% Mn + 0.25wt% Zr, obtained from its time-temperature data and its first derivative plot are shown in Figure 5.17. Apart from the α -Al dendrites and the eutectic Si particles observed in the interdendritic regions, other phases may also be observed, as seen from the optical micrograph and backscattered image of alloy G9 displayed in Figure 5.18(a) and (b).

Figure 5.18(a) presents the optical microstructure of the G9 alloy showing a large sized α -Fe ($\text{Al}_{15}(\text{FeMn})_3\text{Si}_2$) phase particle in Chinese-script form, Al_9FeNi , Al_3CuNi , Al_2Cu , and π - $\text{Al}_8\text{Mg}_3\text{FeSi}_6$ phases, which were detected in the cooling curve and first derivative curve shown in Figure 5.17. Several examples of such large sized α -Fe particles

are clearly observed in the BSE image in Figure 5.18(b). Observation of the π - $\text{Al}_8\text{Mg}_3\text{FeSi}_6$ and Mg_2Si phases in the cooling curve primarily depends on the Mg and Si levels in the alloy

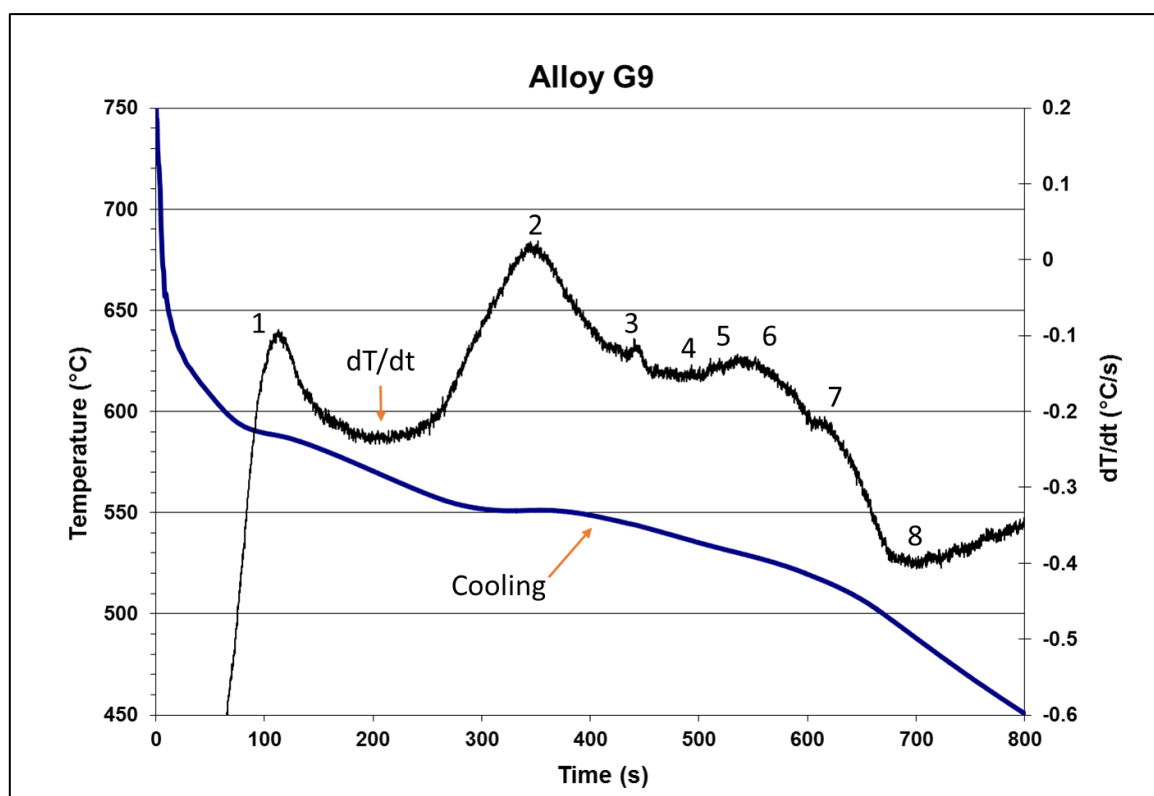
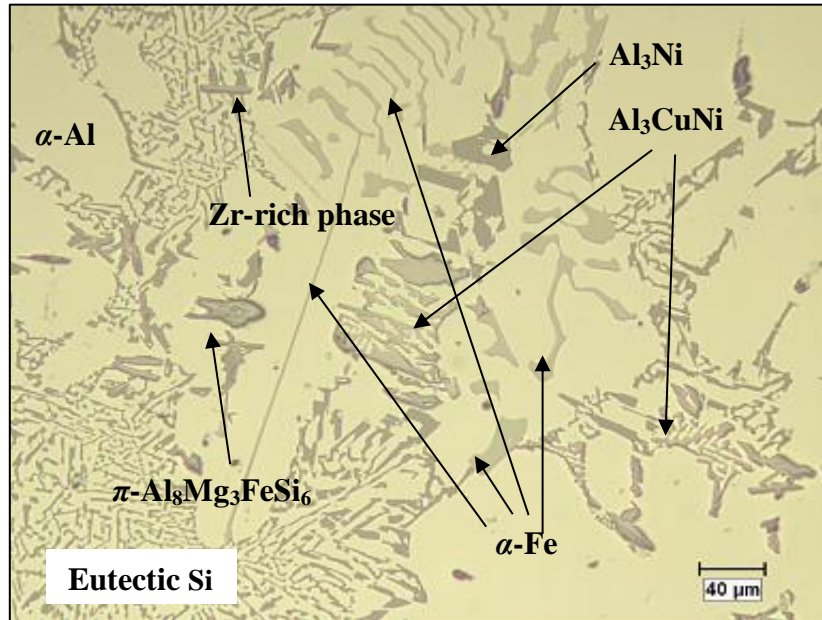
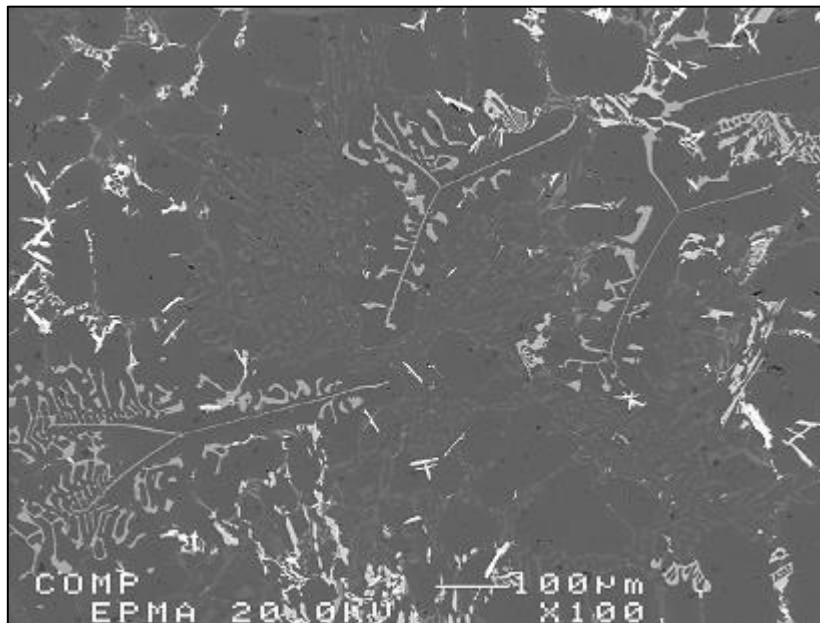


Figure 5.17 Temperature-time plot and first derivative from the thermal analysis of alloy G9 (containing 2wt% Ni + 0.75wt% Mn + 0.25wt% Zr).

Figure 5.19(a) is a high-magnification backscattered electron image taken from alloy G9 and shows the presence of Al_3CuNi (white) and Ni-rich Al_3Ni (gray) phase particles in the microstructure. The corresponding X-ray images of Cu and Ni are shown in Figure 5.19(b) and (c). Figure 5.20(a) shows the EDS spectrum of the Al_3CuNi phase particle observed in Figure 5.19(a). The WDS analysis shown in Table 5.9 confirmed these results.



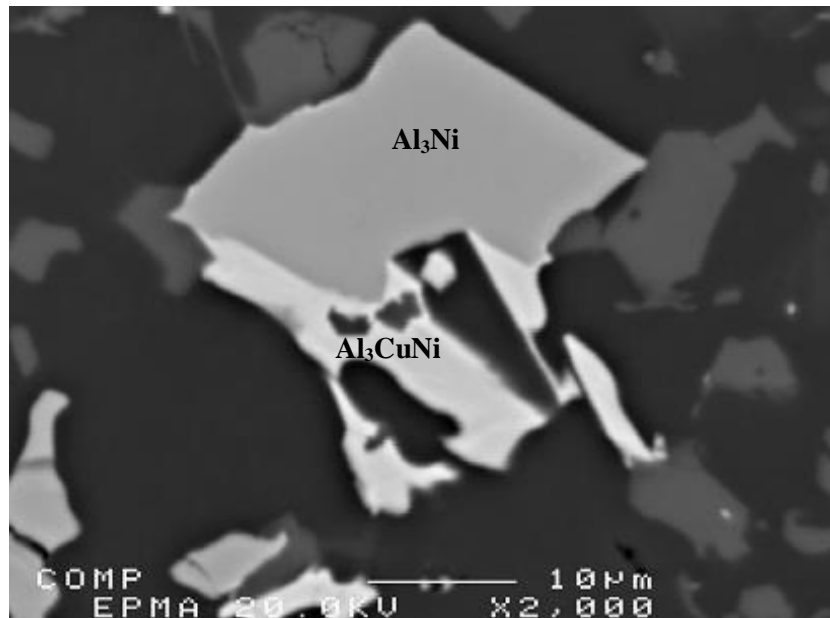
(a)



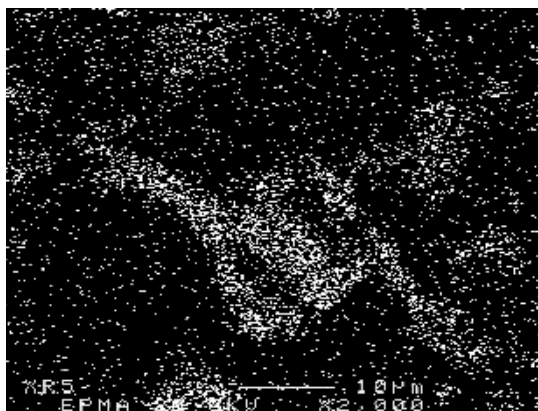
(b)

Figure 5.18 (a) Optical microstructure at 200X magnification and (b) backscattered electron image of the G9 (2wt% Ni + 0.75wt% Mn + 0.25wt% Zr) alloy sample, obtained from the thermal analysis casting (cooling rate 0.35°C/s), showing the different phases present in the alloy.

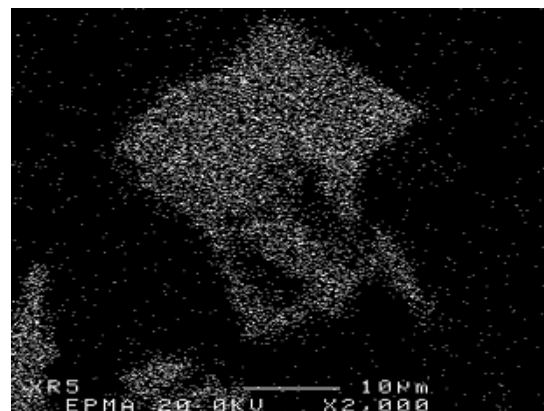
Another phase identified in the WDS analysis was the $(\text{Al,Si})_3(\text{Zr,Ti})$ phase, also listed in Table 5.9, which was confirmed by its EDS spectrum and is displayed in Figure 5.20(b).



(a) BSE

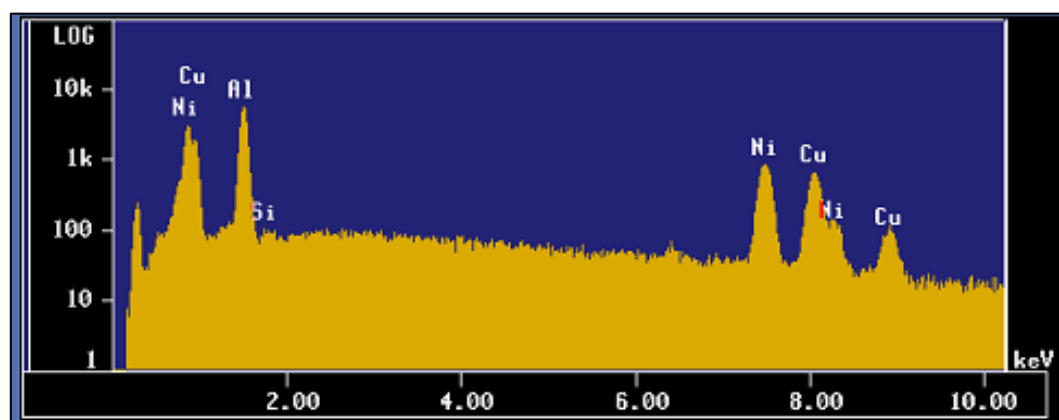


(b) Cu

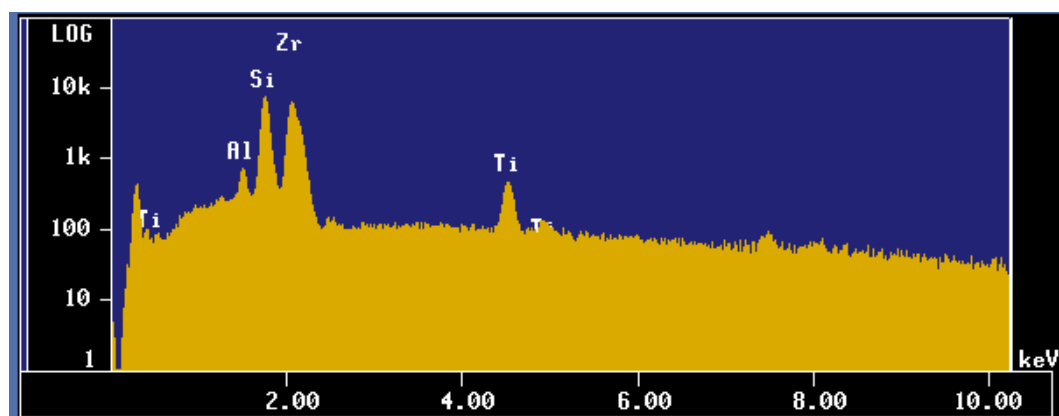


(c) Ni

Figure 5.19 (a) High-magnification backscattered electron image of the G9 alloy sample, showing Al_3CuNi and Ni-rich Al_3Ni phase; (b) and (c) corresponding X-ray images of Cu and Ni.



(a)



(b)

Figure 5.20 EDS spectra corresponding to (a) Al_3CuNi and (b) $(\text{Al,Si})_2(\text{Ti,Zr})$ phases listed in Table 5.9. See also Figure 5.19(a).

Table 5.9 WDS analysis of phases observed in alloy G9

Alloy Code	Element	Wt%	At%	Calculated Formula	Suggested Formula
G9	Al	37.67	58.41	$\text{Al}_{5.88}\text{Si}_{1.34}\text{Ti}_{0.25}\text{Zr}_{2.14}$	$(\text{Al},\text{Si})_3(\text{Ti},\text{Zr})$
	Si	10.94	16.29		
	Ti	3.79	3.31		
	Zr	47.14	21.62		
	Total	99.54	99.63		
	Al	6.32	7.85	$\text{AlSi}_{7.67}\text{Ti}_{1.49}\text{Zr}_{2.34}$	$(\text{Al},\text{Si})_2(\text{Ti},\text{Zr})$
	Si	35.98	60.24		
	Ti	14.96	11.76		
	Zr	37.85	18.42		
	Total	95.11	98.27		
	Si	24.36	49.53	$\text{Si}_{1.16}\text{Ti}_{0.11}\text{Zr}$	$\text{Si}(\text{Ti},\text{Zr})$
	Ti	4.06	4.85		
	Zr	68.17	42.69		
	Total	96.59	97.07		
	Al	40.77	61.03	$\text{Al}_{3.30}\text{Ni}_{1.13}\text{Cu}$	Al_3CuNi
	Ni	29.77	20.48		
Cu	28.44	18.07			
Total	98.98	99.58			

5.2.7 THERMAL ANALYSIS: ALLOY G10 (0.15wt% Sc + 0.25wt% Zr)

The cooling curve of alloy G10 containing 0.15wt% Sc + 0.25wt% Zr, obtained from its temperature-time data and first derivative plot are shown in Figure 5.21. The beneficial effects of the transition elements Zr, Sc, and Ti in refining the α -Al grain size in transforming the morphology from dendritic to a non-dendritic type lead, indirectly, to a noticeable reduction in the size of intermetallic compounds such as the Al_2Cu and α -Fe phases.⁹² Besides the α -Al dendrites and the eutectic Si particles, other phases may also be

formed, as shown in the optical micrograph and backscattered image of the microstructure of alloy G10 displayed in Figure 5.22(a) and (b).

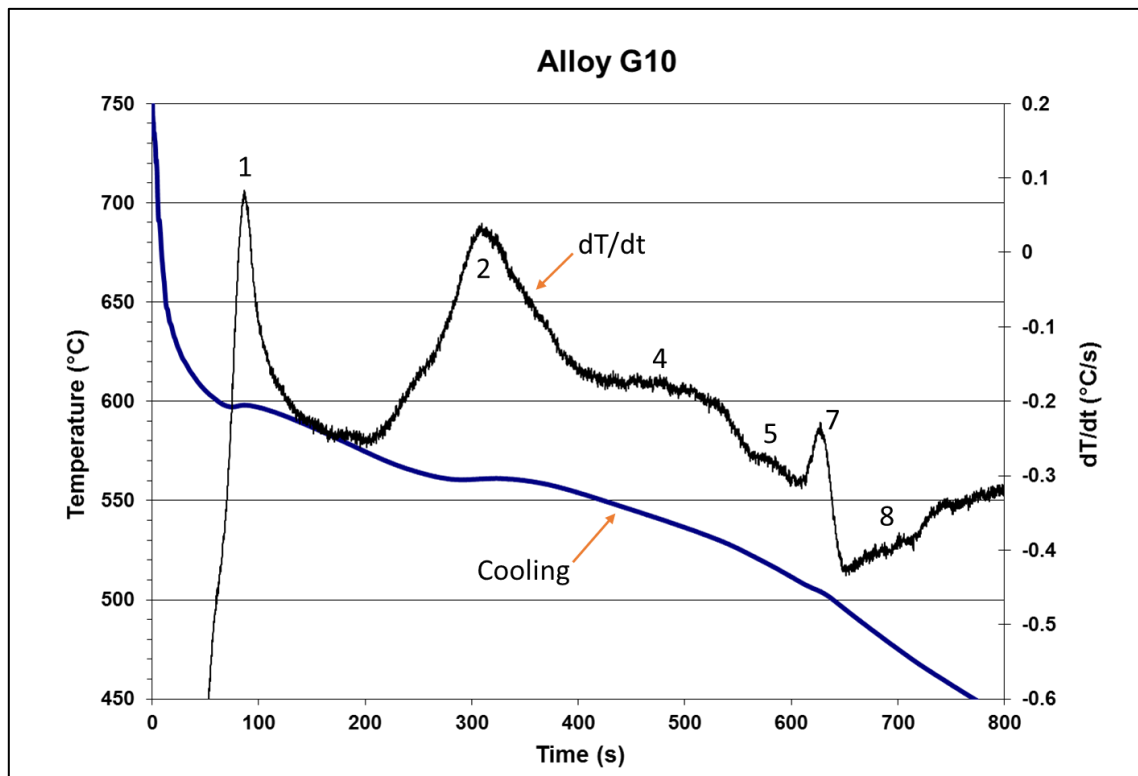
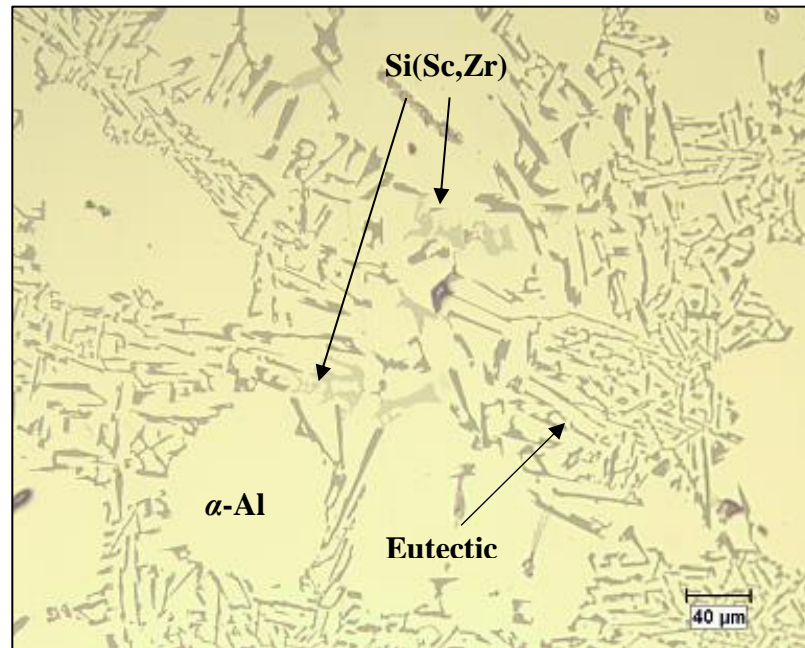
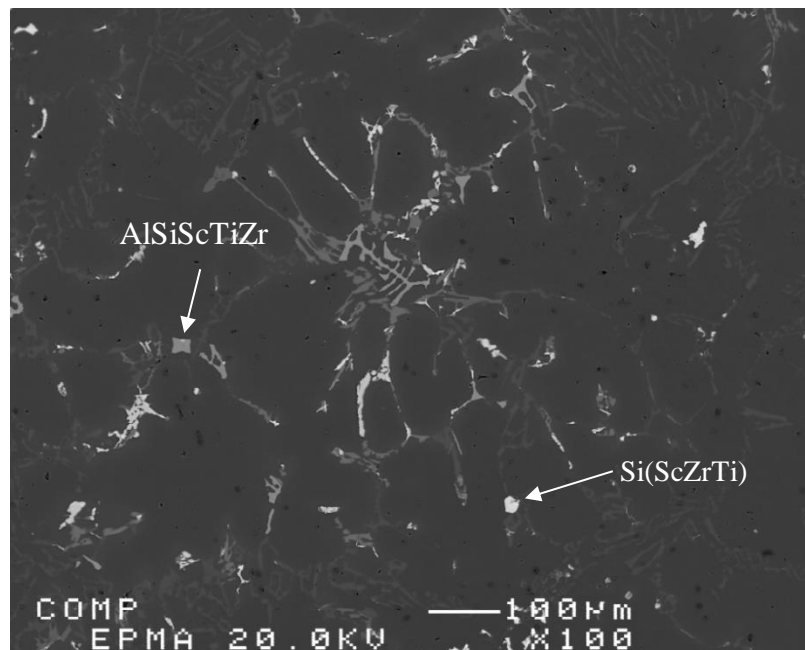


Figure 5.21 Temperature-time plot and first derivative from the thermal analysis of alloy G10 (containing 0.15wt% Sc + 0.25wt% Zr).



(a)



(b)

Figure 5.22 (a) Optical microstructure at 200X magnification and (b) backscattered image of the G10 (0.15wt% Sc + 0.25wt% Zr) alloy sample, obtained from the thermal analysis casting (cooling rate 0.35°C/s), showing the different phases present in the alloy.

The star-like phase, $\text{Al}_3(\text{Sc}_{1-x}\text{Zr}_x)$, is considered to be the most important of the Sc-Zr intermetallics because of its heightened efficiency in nucleating α -Al grains. This type of efficiency may be attributed to the L1_2 -crystal structure of the star-like phase which is characterized by its low mismatch with the α -Al lattice structure.²⁶⁵ In addition, as this phase forms within a temperature range of 655°C - 663°C which is higher than that of the α -Al phase, it has the possibility for being used as a potent grain refiner for a wide selection of aluminum alloys.^{21, 22} Nabawy⁹² found that when 0.2wt% Ti was added to Al-2wt% Cu, the composition of the star-like phase changed from $\text{Al}_{3.18}(\text{Sc}_{0.05}\text{Zr}_{0.5})$ to $\text{Al}_{3.05}(\text{Sc}_{0.46}\text{Zr}_{0.41}\text{Ti}_{0.13})$. These findings indicate that the content of transition elements in the alloy influences the composition of the star-like phase.

In the present study, the backscattered images of the AlSiScTiZr and Si(ScZrTi) phases observed in alloy G10 were further examined using X-ray mapping to examine the distribution of Al, Si, Sc, Ti and Zr within these phases. The results are displayed in Figure 5.23(a) and (b). The EDS spectra for the $(\text{Al,Si})_2(\text{Zr,Ti})$ and Si(Sc,Zr) phases are presented in Figure 5.24(a) and (b). These results are in keeping with the WDS analysis shown in Table 5.10 for alloy G10.

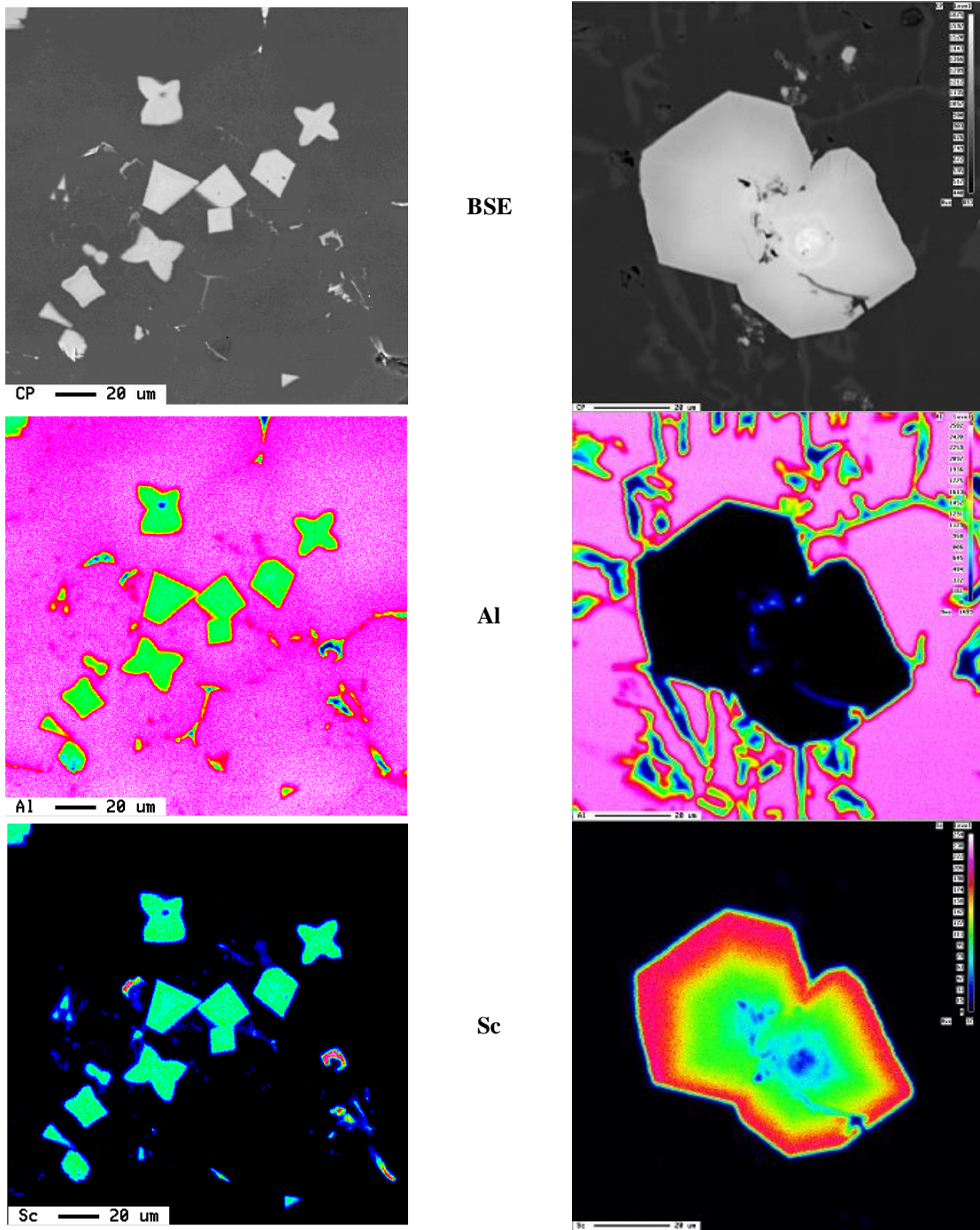


Figure 5.23 Cont.

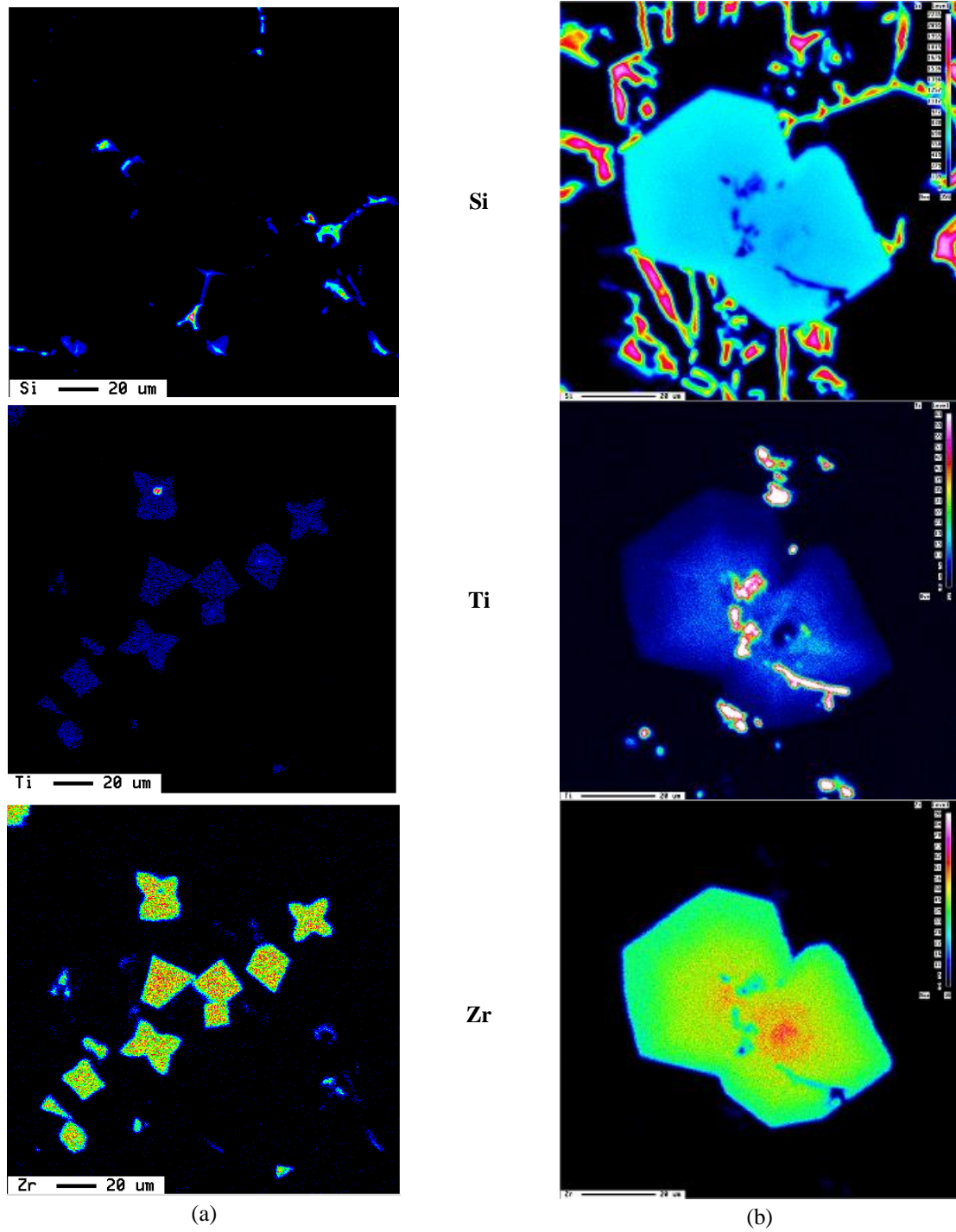
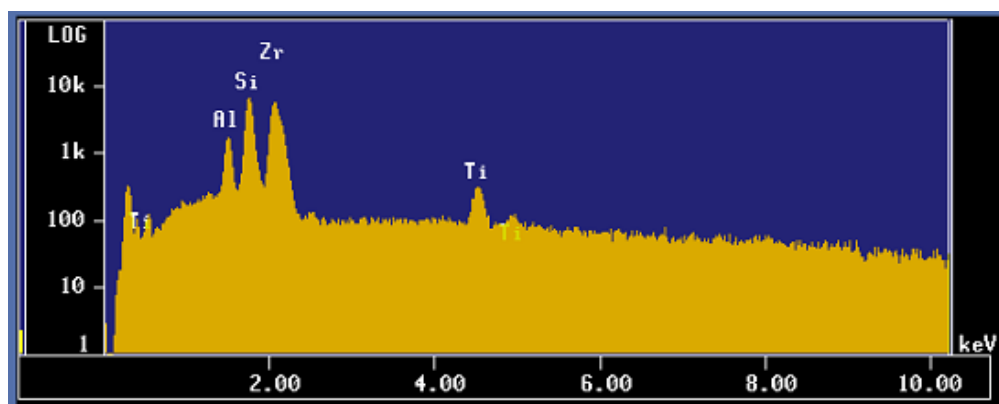
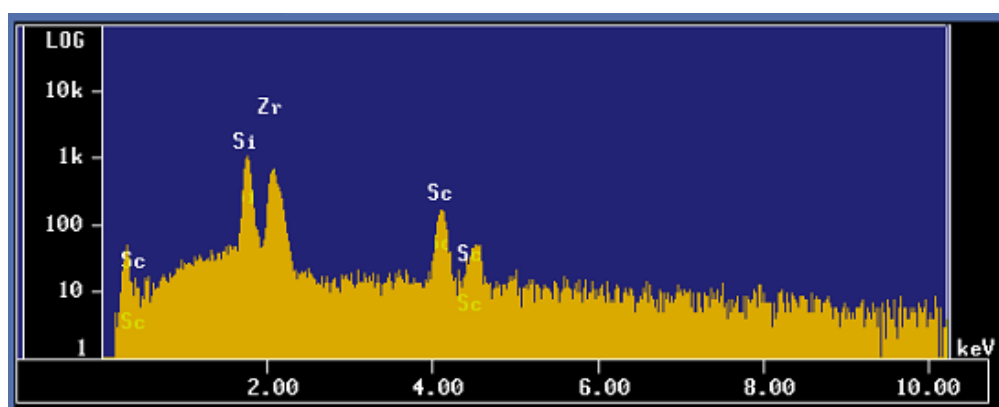


Figure 5.23 Backscattered electron image and corresponding X-ray images of Al, Sc, Si, Ti and Zr showing the distribution of these elements in (a) AlSiScTiZr, and (b) Si(ScZrTi) phase particles in G10 alloy sample.



(a)



(b)

Figure 5.24 EDS spectra corresponding to (a) $(\text{Al,Si})_2(\text{Zr,Ti})$ and (b) $\text{Si}(\text{Sc,Zr})$ phases observed in Figure 5.23(a) and Figure 5.23(b).

Table 5.10 WDS analysis of phases observed in alloy G10

Alloy Code	Element	Wt%	At%	Calculated Formula	Suggested Formula
G10	Si	26.89	50.75	$\text{Si}_{3.43}\text{Zr}_{2.16}\text{Sc}$	$\text{Si}(\text{Sc,Zr})$
	Zr	56.04	32.08		
	Sc	12.54	14.79		
	Total	95.47	97.623		
	Al	5.11	10.42	$\text{AlSi}_{4.43}\text{Ti}_{0.29}\text{Zr}_{3.81}$	$(\text{Al,Si})_2(\text{Ti,Zr})$
	Si	23.60	46.15		
	Ti	2.65	3.04		
	Zr	65.88	39.68		
Total	97.24	99.29			

5.3 HIGH COOLING RATE – TENSILE TEST SAMPLES

As mentioned earlier in the previous section, an increase in cooling rate decreases the total percentage porosity as well as the average pore size in both modified and non-modified alloys.²⁵¹ Also, increasing the solidification rate reduces the size of microstructural features including eutectic silicon and intermetallics; this renders crack propagation through the material more difficult, thereby increasing the alloy impact energy or toughness.^{81, 91} The thermal analysis experiments described in the beginning of this Chapter 5 provided evidence of the solidification sequence in which the phases form during solidification at low cooling rates. The cooling rate for the tensile test samples being relatively higher, certain differences between the precipitated phases may occur since the precipitation kinetics would be different in the two cases. The thermal analysis results are, however, of primary importance in this section because they are used as a reference for identifying the phases appearing in the microstructures of the tensile test samples.

High cooling rate has a direct effect on reducing the quantities of β , π , and Mg_2Si intermetallic phases observed within the microstructure of Al-7Si-Mg alloys.²³⁹ A rapid solidification process can also be used to suppress the formation of some precipitates or otherwise modify their morphologies.²³⁹ It has been reported that applying a high cooling rate produces fine microstructural constituents and suppresses the formation of iron intermetallics by minimizing their nucleation and eventual growth.²⁵⁹ The presence of strontium and magnesium leads to the segregation of the copper phase to areas free of eutectic silicon particles, as a result of which the Al_2Cu phase precipitates more often in

block-like form rather than in the fine eutectic form. Compared with the eutectic Al-Al₂Cu phase, the coarse block-like form of the phase is much more difficult to dissolve in the aluminum matrix. Segregation is also affected by the cooling rate, a high cooling rate being beneficial in contributing to a reduction in the amount of eutectic phase precipitation along the grain boundaries.

5.3.1 SILICON PARTICLE CHARACTERISTICS AND VOLUME FRACTION OF INTERMETALLICS

The presence of different alloying elements such as those mentioned before creates a more complicated microstructure in Al-Si alloys due to the formation of a variety of intermetallic phases. Each element in combination with others may promote the formation of a particular intermetallic microconstituent provided that its relative concentration is compatible with the expected intermetallic compound. All these variables (amount of silicon, DAS, amounts of alloying elements, amounts of intermetallic phases and casting process) may cause significant changes in the microstructure after proper heat treatment, which, in turn, would influence the resultant mechanical properties.

The eutectic Si morphology plays a vital role in determining the mechanical properties of Al-Si alloys, where the particle size and shape of the silicon particles are the factors which greatly influence the alloy performance. In the present study, quantitative measurements of the eutectic silicon particles were carried out on samples sectioned from G1, and G6 through G10 alloy castings obtained in the as-cast and the following solution heat-treated conditions:

1. Solution heat treatment of 500°C/8 h for alloys G1, G6, G8, G9, G10; and
2. Solution heat treatment of 540°C/8 h for alloy G7 (containing no Cu).

Samples for microstructural analysis were sectioned from the tensile-tested bars ~10 mm below the fracture surface, away from the deformed portion of the tensile bar. Quantitative measurements of the eutectic Si particle characteristics observed in the alloy samples tested were carried out using the optical microscope-image analysis system. The results are shown in Table 5.11. Solution heat treatment conditions together with Sr-modification result in transforming the morphology of the eutectic silicon particles from fibrous to globular.^{225, 226} Raising the solutionizing temperature and/or increasing the duration of the solution treatment time produce further improvements in the morphology of eutectic silicon particles.^{228, 229} The average Si particle area was seen to increase because of the coarsening brought about at high solutionizing temperatures and/or longer solutionizing time. On the other hand, the aspect ratio decreased because of the spheroidization of these same particles with the increase in the solution temperature/time conditions.

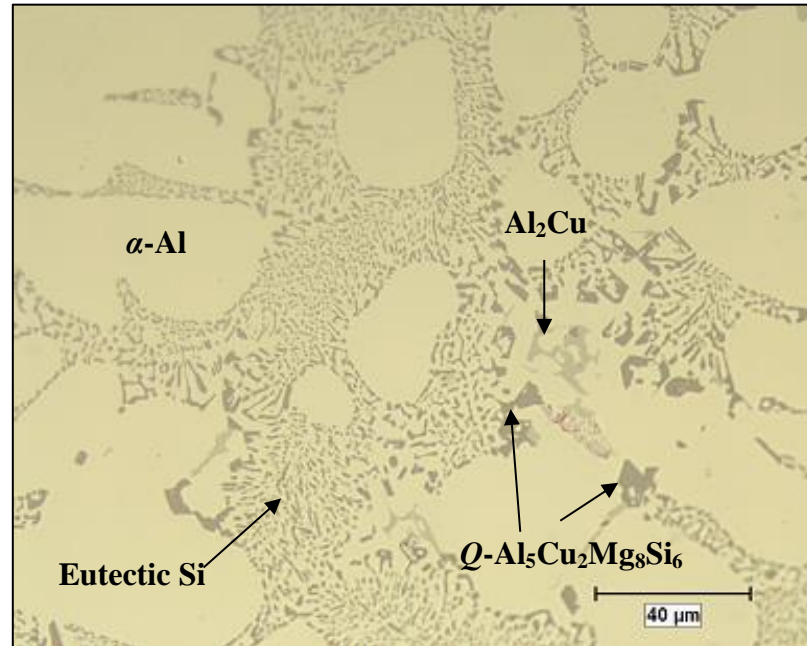
Figure 5.25(a) through Figure 5.30(a) show examples of the morphology of eutectic silicon particles of all alloys in the as-cast condition, while Figure 5.25(b) through Figure 5.30(b) show the change in particle morphology of the same alloys after applying solution heat treatment at 500°C/8 h for G1, G6, G8, G9 and G10 alloys; and at 540°C/8h for G7 alloy (without Cu). The points discussed at the start of this subsection are clearly reflected in the optical micrographs displayed in these figures. The microstructures reveal that certain Si areas are fully modified, whereas others are only partially modified. This observation is in satisfactory agreement with those of Joenoes and Gruzleski,⁵⁰ who reported that about 1% Mg is capable of refining the Si phase slightly and that it also has a negative effect on Sr modification, that is to say, it changes the microstructure from being a well-modified one to being a partially modified one, due to the fact that both Mg and Cu react with the Si and Sr in the alloy to form $Mg_2Sr(Si,Al)$ and Al-Cu-Sr compounds, respectively. As a result, there is less Sr available to obtain the same level of modification of the eutectic Si particle than would be expected with the ~170 ppm Sr amount that was added.

It has generally been reported that a higher Mg content increases the yield stress, while decreasing the ductility and the fracture toughness.¹²⁴ Aside from having an effect on the age-hardening potential, Mg also lowers the eutectic temperature and renders the eutectic Si structure more heterogeneous. It also appears to interfere with the modification of the eutectic structure when using Sr additions, resulting in a coarser and less uniform eutectic structure.^{81, 118, 128}

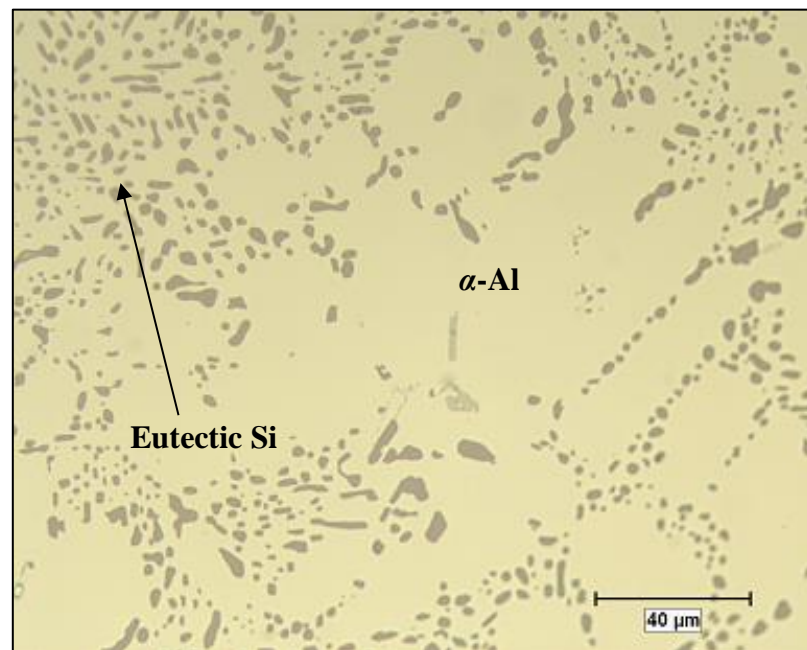
Table 5.11 Silicon particle characteristics for alloy G1 and G6 through G10

Alloy Code Condition	Area (%)	Particle Area (μm^2)		Particle Length (μm)		Aspect Ratio		Roundness (%)	
	Av	Av	SD	Av	SD	Av	SD	Av	SD
G1-AC	10.03	4.82	6.18	3.64	2.94	2.10	1.32	0.43	0.17
G1-SHT	9.83	6.31	6.64	3.66	2.43	1.68	0.62	0.59	0.16
G6-AC	12.80	10.53	8.80	5.42	4.58	2.06	0.87	0.41	0.17
G6-SHT	12.14	10.10	7.63	5.08	3.92	1.83	0.73	0.52	0.18
G7-AC	12.38	6.76	10.47	4.48	3.72	2.03	0.77	0.41	0.17
G7-SHT	11.10	10.07	12.73	5.00	3.18	1.65	0.56	0.56	0.17
G8-AC	9.89	7.22	9.51	4.15	3.32	1.99	0.79	0.45	0.17
G8-SHT	9.41	8.94	9.59	4.32	2.99	1.70	0.60	0.57	0.16
G9-AC	12.55	9.07	14.30	5.07	4.21	2.07	0.84	0.41	0.17
G9-SHT	10.09	10.05	11.67	4.95	3.37	1.76	0.49	0.53	0.17
G10-AC	10.43	6.66	10.40	4.57	4.25	2.09	0.86	0.42	0.17
G10-SHT	9.64	8.62	9.67	4.59	3.23	1.78	0.66	0.54	0.17

AC: As-cast; SHT: Solution heat-treated

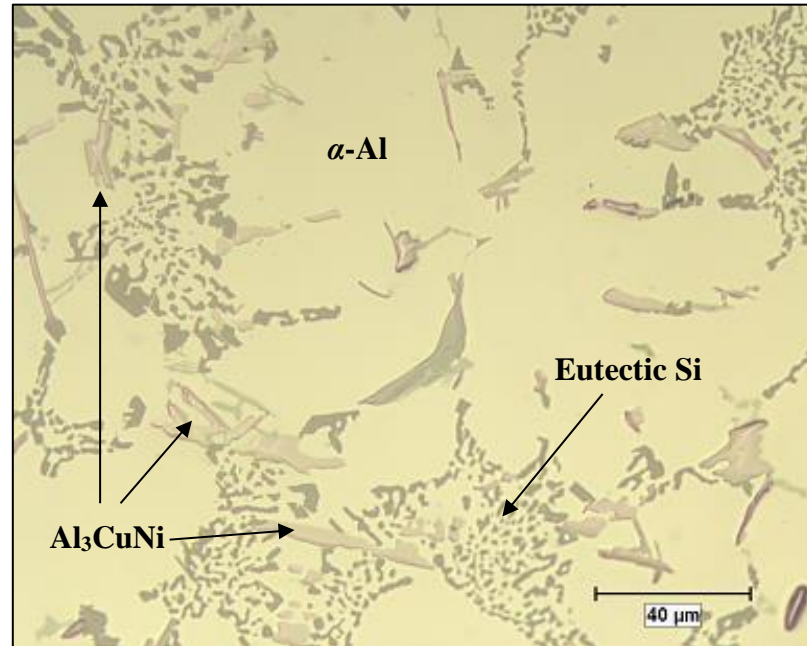


(a)

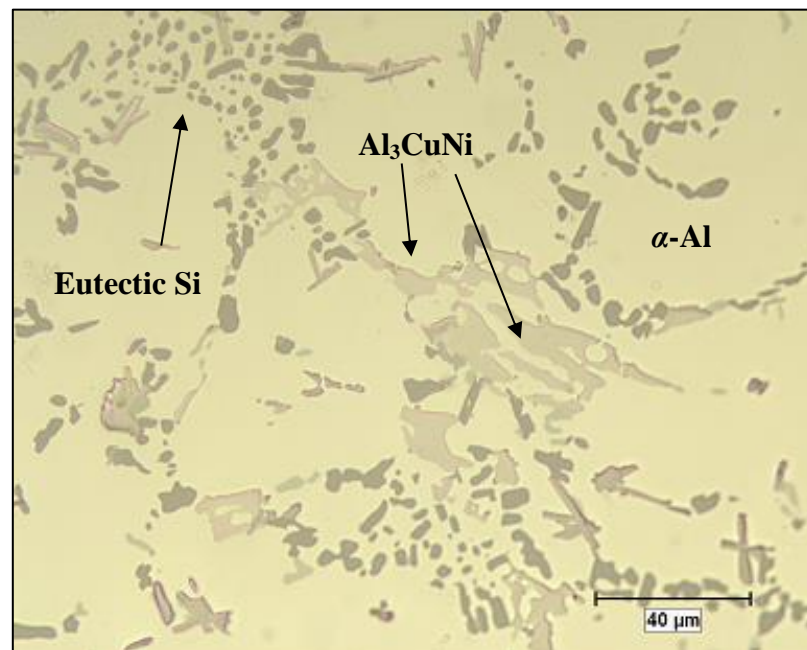


(b)

Figure 5.25 Optical micrographs at 500X showing the effect of solution heat treatment at 500°C on Si morphology in G1 base alloy for (a) 0 h and (b) 8 h solution treatment times.

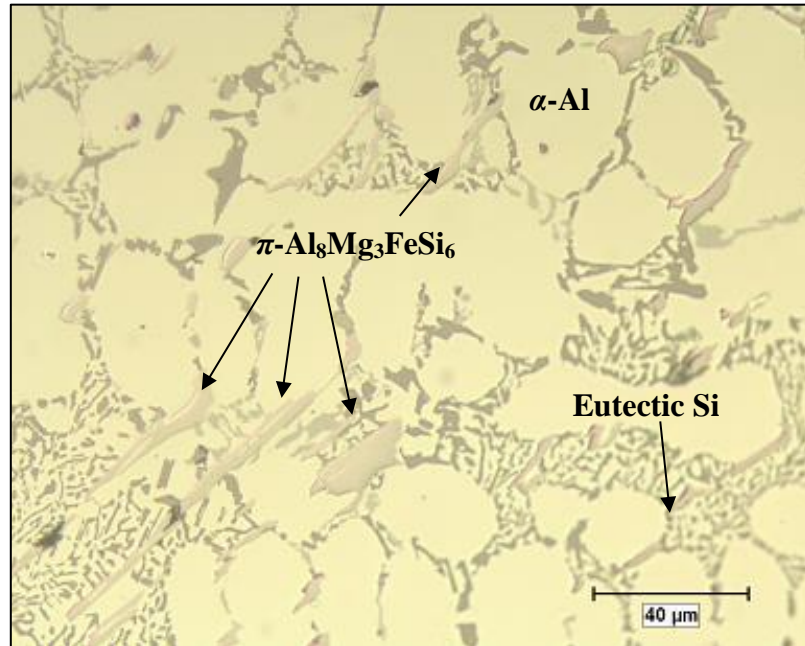


(a)

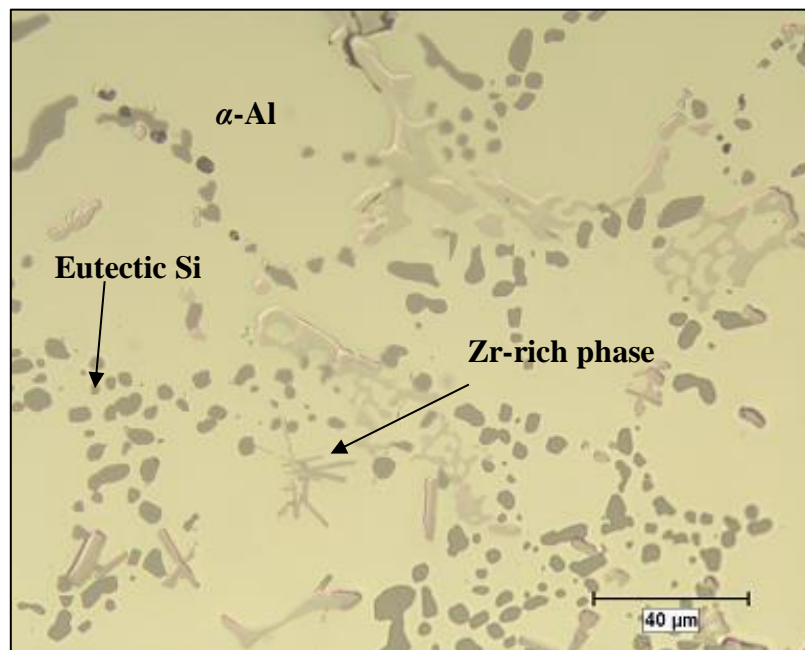


(b)

Figure 5.26 Optical micrographs at 500X showing the effect of solution heat treatment at 500°C on Si morphology in alloy G6 (containing 2wt% Ni + 0.25wt% Zr) for (a) 0 h and (b) 8 h solution treatment times.

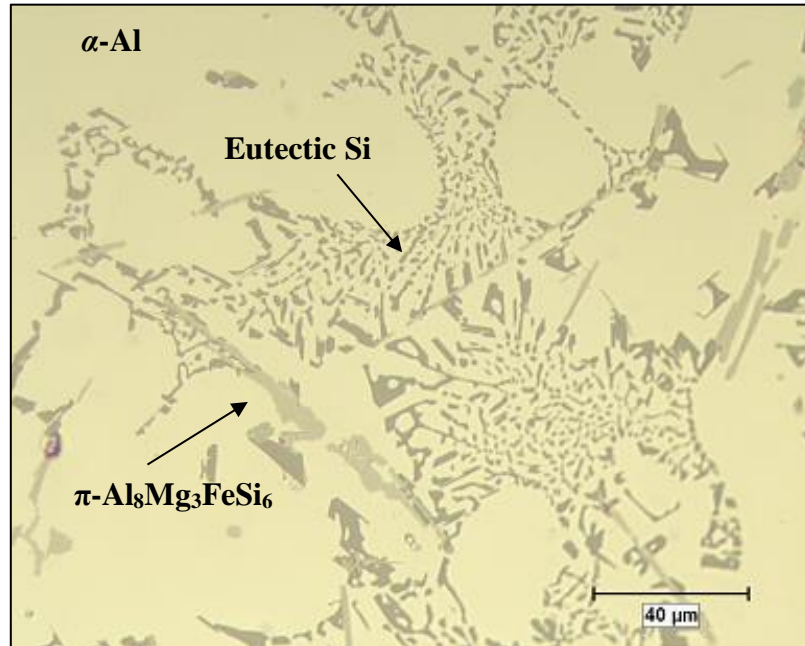


(a)

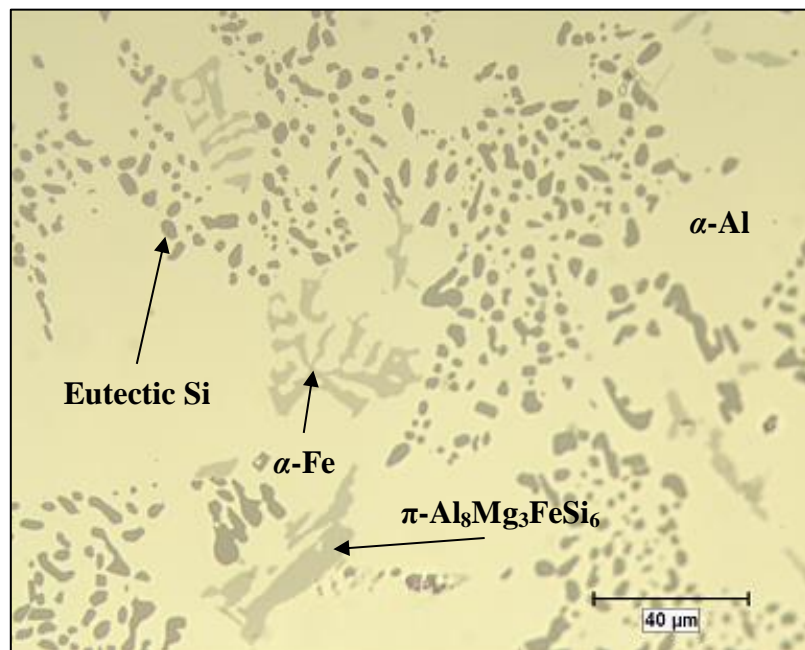


(b)

Figure 5.27 Optical micrographs at 500X showing the effect of solution heat treatment at 540°C on Si morphology in alloy G7 (containing 2wt% Ni + 0.25wt% Zr, but no Cu) for (a) 0 h and (b) 8 h solution treatment times.

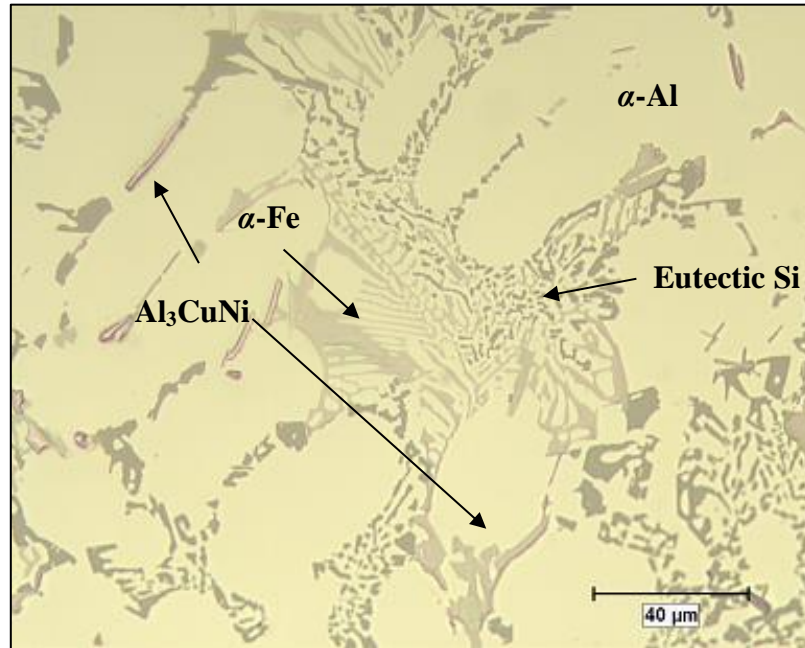


(a)

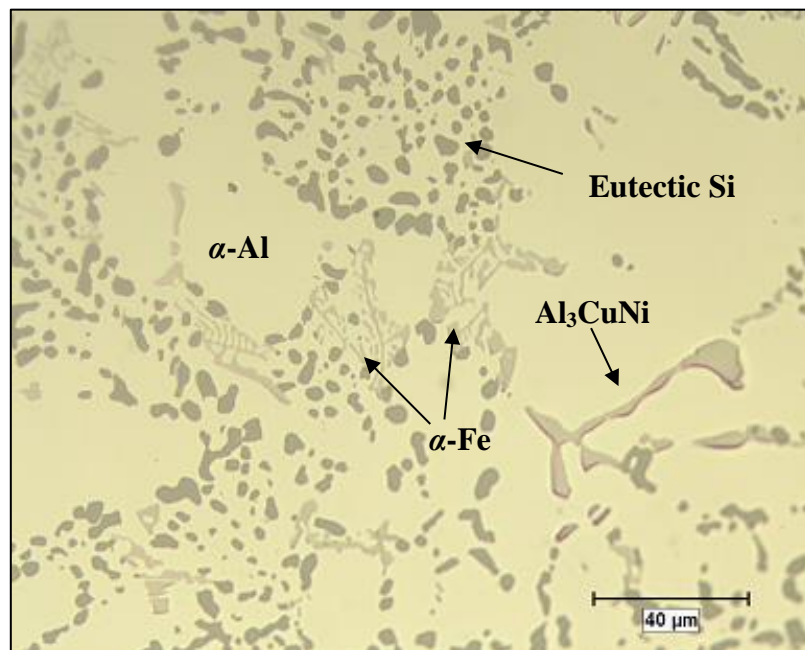


(b)

Figure 5.28 Optical micrographs at 500X showing the effect of solution heat treatment at 500°C on Si morphology in alloy G8 (containing 0.75wt% Mn + 0.25wt% Zr) for (a) 0 h and (b) 8 h solution treatment times.

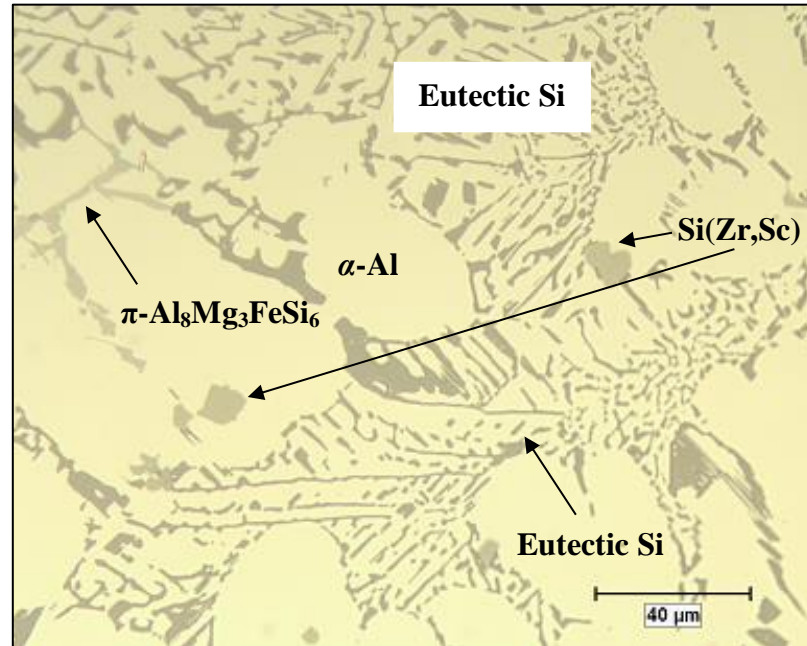


(a)

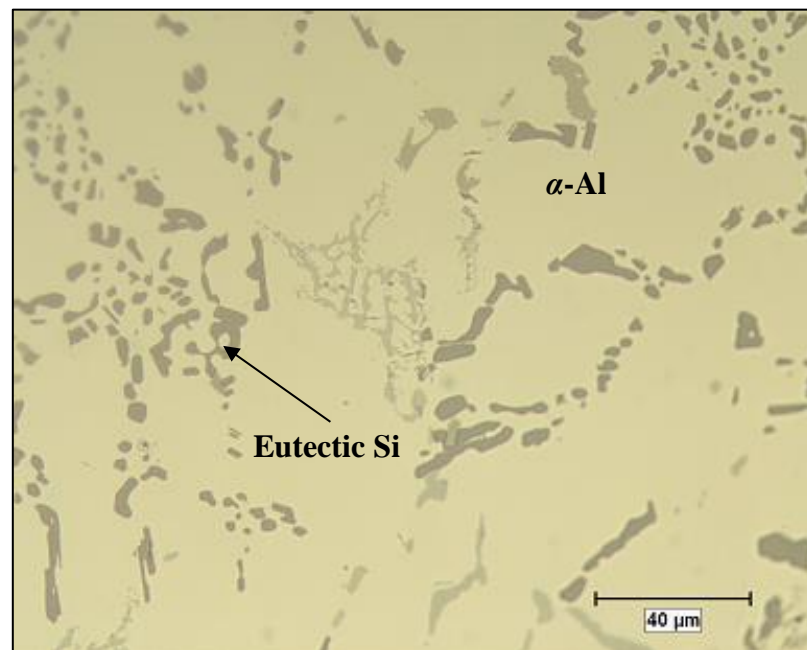


(b)

Figure 5.29 Optical micrographs at 500X showing the effect of solution heat treatment at 500°C on Si morphology in alloy G9 (containing 2wt% Ni + 0.75wt% Mn + 0.25wt% Zr) for (a) 0 h and (b) 8 h solution treatment times.



(a)



(b)

Figure 5.30 Optical micrographs at 500X showing the effect of solution heat treatment at 500°C on Si morphology in alloy G10 (containing 0.15wt% Sc + 0.25wt% Zr) for (a) 0 h and (b) 8 h solution treatment times.

Under normal cooling conditions, the eutectic silicon forms a network of interconnected irregular flakes, and may be chemically or thermally modified (using high temperature treatments) to a fine fibrous structure. In recent years, both chemical and thermal modification have been used in conjunction with each other to produce the desired properties of the casting. Several investigators have used quantitative metallographic techniques to monitor the changes in Si-particles morphology during solution heat-treatment.⁹⁵ One of the objectives of solution heat treatment is to allow the soluble hardening elements of the alloy to dissolve into solid solution and to homogenize castings. Because solubility and diffusion rate both increase with temperature, it is usually desirable to use the highest treatment temperature possible without causing incipient melting. When castings are heat-treated at temperatures lower than the normal range, dissolution is incomplete and mechanical properties obtained are not optimum.

Eutectic silicon is the discontinuous eutectic phase in Al-Si alloys. A common feature of eutectic alloys is that there is a certain degree of solubility of the discontinuous phase in the matrix at certain temperatures below the eutectic point. The solubility of Si in the matrix of Al-Si alloys, however, is not constant because Si has a different surface curvature and is an imperfect crystal having a different lattice deformation energy that varies so that the solubility of Si is affected. In general, the energy state, *i.e.* the surface curvature and the lattice deformation energy of the discontinuous eutectic phase, is inhomogeneous. Figure 5.31 shows a model of the granulation of unmodified eutectic Si illustrating three major stages during heat treatment: (a) the mass transport of solute which occurs from areas of intensified high energy state to areas of low energy state; (b) a

discontinuous phase fragmentation, and lastly, (c) spheroidization when the inhomogeneity of energy conditions is sufficiently high. Based on this model, the solubility of silicon particles is different from point to point depending on the surface morphology of the particles, *i.e.* the surface curvature or lattice deformation energy of eutectic silicon is greater at the roots of branches (A), and at the tips (B), than on the flat faces (C), as shown in Figure 5.31. The solubility of silicon in the matrix at locations A and B is thus larger than it is at location C. During heat treatment, the silicon atoms in the matrix at locations A and B diffuse to location C, resulting in the dissolution of eutectic silicon at A and B, and the precipitation of silicon on the eutectic silicon at C. This mass transport of silicon ultimately causes the fragmentation and spheroidization of eutectic silicon, the two processes being dependent on the diffusion of both solute atoms and matrix atoms.

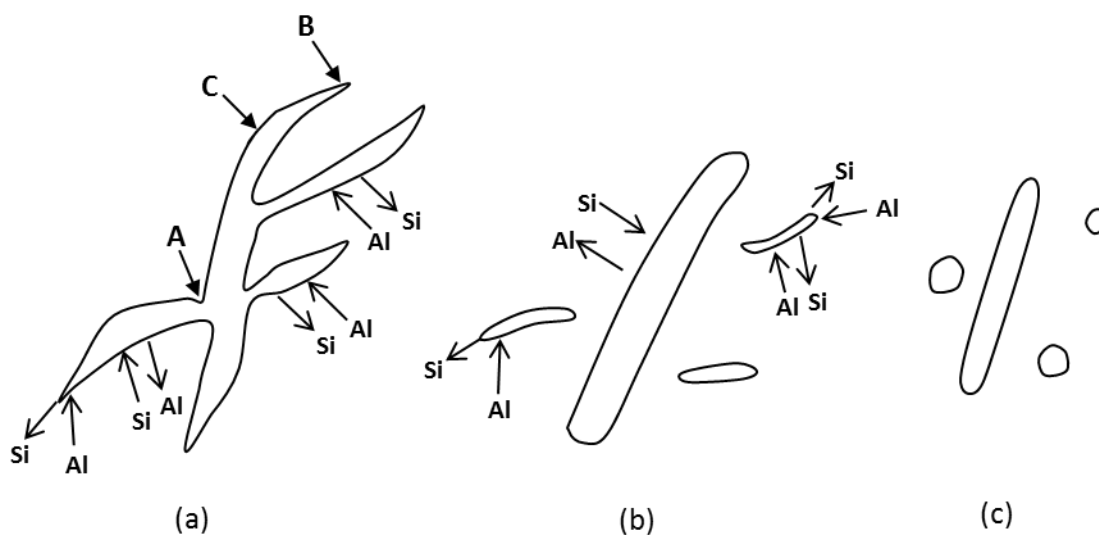


Figure 5.31 Model of granulation of unmodified eutectic Si during heat treatment. (a) transport of Si with the cooperation of Al begins; (b) transport continues after fragmentation; and (c) eutectic Si becomes spheroidized.²⁶⁶

Table 5.12 lists the volume fractions (%) from tensile test samples corresponding to the as-cast (AC) and solution heat treated (SHT) conditions for the alloys studied. As may be seen from the table, the volume fraction decreases for all alloys after solution heat treatment. This observation indicates that the difference in the volume fraction of intermetallic phases is slightly affected by the solution heat treatment applied. Normally, the percentage (volume fraction) of a phase may be represented by the average particle size (length or area) of that phase.

The base alloy G1 shows the lowest volume fraction of the undissolved phases in comparison with the other alloys, *viz.*, 2.06% and 1.26%, in the as-cast and solution heat-treated conditions, respectively. With the addition of transition elements and the amounts added, the volume fraction of intermetallics in the base alloy increases as reflected in the volume fractions of the other alloys.

As observed in the low cooling rate samples, the high cooling rate samples of alloy G9 (containing 2wt% Ni + 0.75wt% Mn + 0.25wt% Zr) continue to display the highest volume fractions of 9.34% and 9.00% in the as-cast and solution heat-treated conditions, respectively; followed by G6 alloy (containing 2wt% Ni + 0.25wt% Zr) with volume fractions of 7.63% (as-cast) and 6.81% (SHT), and G7 alloy (same additions as G6 alloy, but with no Cu) with volume fractions of 7.69% (as-cast) and 5.37% (SHT), respectively. Alloys G8 and G10 show similar behavior with respect to undissolved phases, presenting the lowest volume fractions among all the alloys, *viz.*, 5.47% and 5.13% in the as-cast condition, and 4.91% and 3.70% after solution heat treatment, respectively.

Table 5.12 Volume fraction of undissolved phases observed in the matrix of alloys G1, and G6 through G10 in the as-cast (AC) and solution heat-treated (SHT) conditions

Volume Fraction (%)	Alloy Code					
	G1	G6	G7	G8	G9	G10
AC Condition - Average	2.06	7.63	7.69	5.47	9.34	5.13
AC Condition - Std. Deviation	0.35	0.71	0.46	0.73	0.67	0.35
SHT Condition - Average	1.26	6.81	5.37	4.91	9.00	3.70
SHT Condition - Std. Deviation	0.38	0.36	0.42	0.52	0.65	0.50

From the above comparisons in volume fraction values it may be deduced that the transition elements Ni, Mn, and Zr present in the G9 alloy must interact between themselves, or with other elements contained in the base alloy, in order to form new phases and alter the total volume fraction of intermetallics. The interaction between Fe and Mn to form another version of the α -Fe phase, α -Al₁₅(Fe,Mn)₃Si₂ or sludge, would also increase the volume fraction of intermetallics in the alloy. The presence of hard sludge particles within the soft α -Al dendrites should lead to a more uniform distribution of the stresses throughout the alloy matrix and, hence, to improved mechanical properties. This shows that the precipitation of sludge particles need not necessarily be harmful to the alloy, as is commonly perceived in the literature, where sludge particles are usually observed in the interdendritic regions. This phenomenon of iron intermetallic precipitation within the α -Al dendrites proves very useful in the case of such Al-Si die-casting alloys as 380 alloy, containing 9%Si, where the proportion of α -Al dendrites is relatively higher.²⁶⁴ While the presence of Mn and Zr in alloy G8, and Sc and Zr in alloy G10 increase the volume fraction of intermetallics to twice that observed in the base alloy, alloys G6, G7 and G9 containing Ni all show much higher volume fractions, as may be seen from Table 5.12. The highest

volume fraction of intermetallics is exhibited by alloy G9, and may be explained by the large size of the intermetallic particles formed through the interaction between Fe, Ni and Mn, thereby increasing the volume fraction. Compared to alloy G8 which has the same Fe and Mn additions but no Ni, it may be seen that the addition of Ni increases the volume fraction by close to 42% in both as-cast and solution heat-treated conditions.

The beneficial effects of combined Zr-Sc additions in reducing grain size is attributed to the profuse formation of the $\text{Al}_3(\text{Sc}_{1-x}\text{Zr}_x)$ star-like phase as the primary phase during solidification, which in turn acts as a potent nucleant for α -Al.⁹² The presence of titanium enhances the efficiency of the star-like phase as an α -Al nucleant in that it reduces the lattice misfit between the $\text{Al}_3(\text{Sc}_{1-x}\text{Zr}_x)$ phase and the α -Al. The beneficial effects of the transition elements Ti, Sc, and Zr in refining the α -Al grain size and transforming the morphology from a dendritic to a non-dendritic type leads, indirectly, to a noticeable reduction in the size of the intermetallic compounds such as the Al_2Cu and α -Fe phases.

The measurement of secondary dendrite arm spacing (SDAS) was carried out for the base alloy G1 and alloys G6 through G10, in the as-cast (AC) condition as shown in Table 5.13. The technique for measuring the SDAS is the same as the one applied for eutectic Si particles using a Clemex Vision PE optical microscope and image-analysis system.

It was observed that SDAS did not show any significant difference among the alloys studied. The average SDAS of the six alloys samples was $\sim 18 \mu\text{m}$. A finer structure resulting from a higher cooling rate will produce a smaller SDAS value and *vice versa*.¹⁹

The higher solidification rate effect will be observed in the improved modification and more refined phases and grain structures than those appearing in the thermal analysis samples.^{125, 261} The smaller the SDAS value, the smaller the size of defects such as segregation, microshrinkage, and gas porosity, which are detrimental to mechanical properties.²⁵⁹ It is well known that SDAS has a strong influence on the mechanical properties of cast aluminum alloys.²⁵⁸ High cooling rate has a direct effect on reducing the quantities of β , π , and Mg_2Si intermetallic phases observed within the microstructure of Al-7Si-Mg alloys.²⁵⁹

Table 5.13 Average SDAS measured for the alloys G1 and G6 through G10 (samples were obtained from the tensile test bars samples)

Alloy Code						
SDAS (μm)	G1	G6	G7	G8	G9	G10
AC Condition	16.3	18.5	16.9	19.8	19.7	17.0

5.3.2 CHARACTERISTICS OF INTERMETALLIC PHASES

The separation of high melting-point intermetallic compounds from liquid metal may occur by means of precipitation and gravity segregation. These intermetallics are, in actual fact, solid solutions which have a substantial capacity for dissolving other elements. Although expressed by definite chemical formulae, these compounds exhibit a wide range of compositions and precipitation. Caceres *et al.*²⁶⁷ showed that an increased Si-content in Al-Si-Cu-Mg alloys does indeed have a size-refining effect on the β - Al_5FeSi platelets; this may be ascribed to the tendency in the alloys containing high levels of Si to form large particles of pre-eutectic β - Al_5FeSi and α - $Al_{15}(Mn,Fe)_3Si_2$ particles during solidification as a

result of a reduction in the available growth period. The size-refining effect of a high Si-content is also evident in other intermetallics such as α -Al₁₅(Mn,Fe)₃Si₂ and Al₂Cu which form from the eutectic liquid in Al-Si-Cu-Mg alloys. Thus, the evidence suggests that an increased Si-content tends not only to refine the size of intermetallic particles but also to redistribute them in a more uniform dispersion within the intermetallic and intergranular regions compared with a lesser Si-content which promotes long clusters of intertwined particles along the grain boundaries.

5.3.2.1 AS-CAST AND SOLUTION HEAT-TREATED CONDITIONS

The characteristics of intermetallic phases observed in alloys G1, and G6 through G10 were examined using EPMA analysis for the as-cast and heat-treated conditions. Figure 5.32 through Figure 5.37 show backscattered electron images in the as-cast condition and after solution heat treatment, respectively, at 500°C/8 h for G1, G6, G8 through G10, and at 540°C/8 h for alloy G7 (containing no Cu). The volume fraction was observed to decrease after applying the solution heat treatment for all alloys studied, as illustrated in Table 5.12. The principal partially soluble phases in the 354 casting alloys are the β -Al₃FeSi, π -Al₈Mg₃FeSi₆, Q -Al₅Mg₈Cu₂Si₆, Al₉FeNi, Mg₂Si, sludge, and Al₃CuNi phases, as may be seen from Figure 5.32 through Figure 5.37. In the presence of copper, the increase in the volume fraction of the partially soluble phases is related to the formation of Cu-containing phases such as the Q -Al₅Mg₈Cu₂Si₆ and Al₃CuNi phases.

In addition to the silicon structure, another important consideration from the point of view of microstructure is controlling the Fe-content of the alloy. Accurate identification of

the relatively coarse Fe-rich intermetallic phases commonly found in Al-Si casting alloys is also important, since some of these phases are associated with reduced mechanical properties. Solution heat treatment parameters, *viz.*, time and temperature, have a significant effect on the solubility of both soluble and partially soluble phases.

The solid-state solubility of Fe in aluminum is very low, the greater part of the Fe being present in the form of intermetallic compounds, the nature of which depends mainly on the alloying elements present. Of the many existing AlFeSi intermetallics, the most important are generally thought to be the α -Fe, β -Fe, and sludge intermetallic phases. The conditions which control the formation of the α -Fe phase, as opposed to the β -phase, are still not completely understood. In this study, it was observed at low and high cooling rate that addition of Sr in the presence of transition elements such as Mn in alloys G8 and G9, is capable of promoting the development of the intermetallic α -Fe phase in its commonly observed Chinese-script morphology. The formation of the α -Fe phase reduces the possibility of the formation of the β -phase.

The large size of these particles indicates the existence of a high diffusion rate of Fe occurring at high melt temperatures. The α -Fe phase may precipitate either in the form of the Chinese-script phase or else as compact polygonal or star-like shaped particles (sludge) with a composition close to that of the α -Fe phase. Precipitation of sludge particles depends upon the levels of Fe, Mn, and Cr present in the alloy, and the processing parameters, namely, melt holding temperature, pouring temperature, melt additives, and cooling conditions. When the iron content increases from ~0.1wt% in the G1 base alloy to ~0.2wt%

in G8 and G9 alloys, Chinese-script α -Fe and platelet-like β -Fe compounds form, with the same level of Mn, *i.e.* ~0.54wt%.

A further similarity between the thermal analysis of 319 and 354 alloys may be observed at 500°C where the copper phase reaction appears clearly; this observation reveals that the solution heat treatment temperature should be less than ~505°C in order to avoid the risk of incipient melting of the Al₂Cu phase. This similarity between the solidification of both alloys should be considered for future analysis in relation to the heat treatment of 354 alloys since most of the literature recommends a solution temperature which is higher than 515°C for this particular alloy.^{19, 20, 89, 232}

Solution temperatures have been found to affect not only the volume fraction of the completely soluble phases and partially soluble compounds but also the nature and the morphology of the iron-bearing phases, whether π or β . When applying solutionizing treatment, the β -phase platelets were affected by both the modifying effect of Sr and solution heat treatment, leading ultimately to the breakdown of the β needles into small thin fragments via two mechanisms:¹²⁹ (i) splitting of the needle/platelets into two halves through the formation of longitudinal cracks, which is enhanced greatly by the brittle nature of the β -Fe phase, and (ii) fragmentation through Si rejection. It was found that the volume fraction of iron phases increased with the addition of Ni and increasing levels of Fe and/or Mn, as presented in Table 5.12.

Alloying elements such as Cu and Mg determine which constituents will precipitate. Copper is a significant alloying addition made to aluminum because of its observable

solubility and marked strengthening effect. Consequently, many commercial alloys contain Cu as either the major addition or as one of the principal alloying elements. Copper is frequently used in combination with magnesium, thereby improving the aging characteristics of the alloys. The presence of Mg improves strain hardenability and strengthens the material according to the amount present in solid solution. The increase of Mg content in solid solution contributes to the precipitation phenomenon since clusters of Mg are the precursors in the formation of Mg_2Si in Al-Mg-Si alloys.^{44, 96, 256}

Copper forms the intermetallic phase Al_2Cu with aluminum which precipitates during solidification. Depending on the cooling rate and the local concentration of segregated Cu atoms, Al_2Cu may precipitate in a block-like form directly from the liquid, at a Cu concentration of ~53.5wt%, especially in the presence of the β -phase; or in the form of eutectic (Al + Al_2Cu); or, as in many cases, as a mixture of both.¹²³ It was also observed that heightened Mg levels promote the precipitation process. In Mg-containing alloys, the $\pi-Al_8Mg_3FeSi_6$ results from the transformation of the β -phase, while the $Q-Al_5Mg_8Cu_2Si_6$ phase is reported to occur at the end of the Al- Al_2Cu eutectic reaction. The amount of this phase is found to increase progressively with an increase in Mg content. Thus, increasing the Mg content to ~0.74wt%, results in the formation of thick plates of $Q-Al_5Mg_8Cu_2Si_6$, which normally appear to be growing out of the Al_2Cu phase particles.

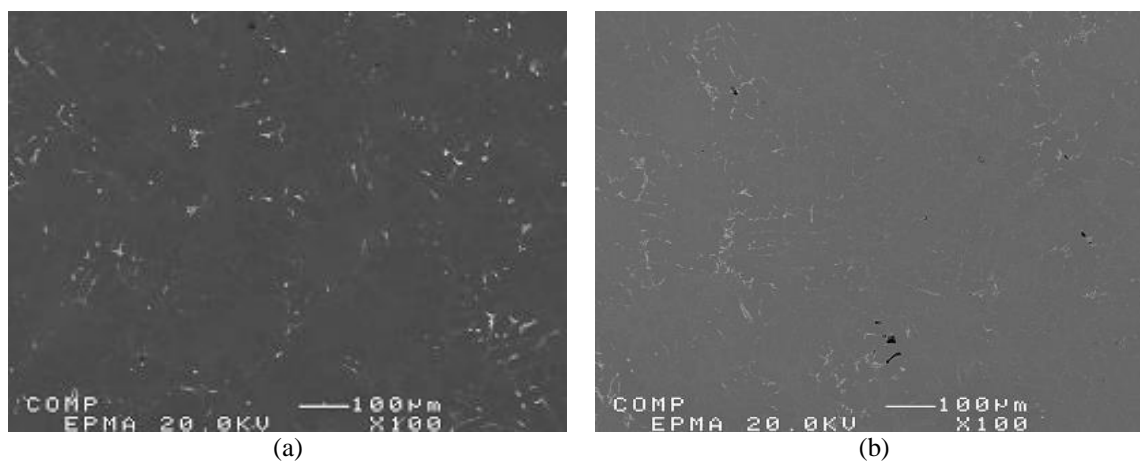


Figure 5.32 Backscattered electron images of G1 base alloy samples: (a) as-cast, and (b) after solution heat treatment.

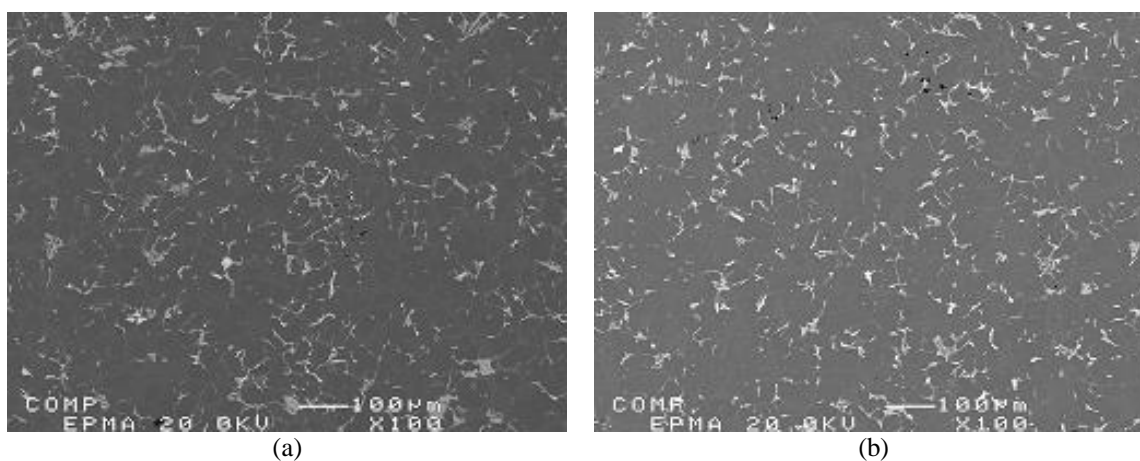


Figure 5.33 Backscattered electron images of G6 (2wt% Ni + 0.25wt% Zr) alloy samples: (a) as-cast, and (b) after solution heat treatment.

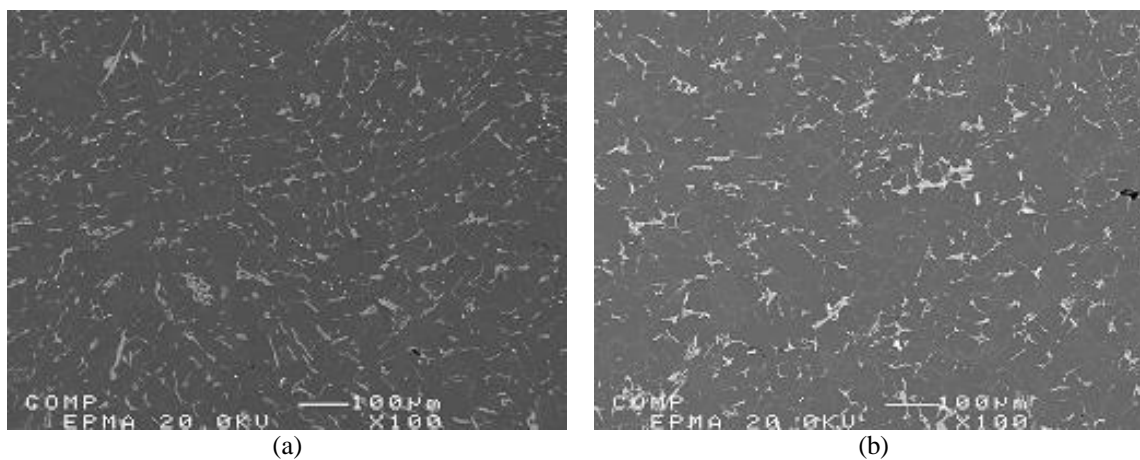


Figure 5.34 Backscattered electron images of G7 (2wt% Ni + 0.25wt% Zr, no Cu) alloy samples: (a) as-cast, and (b) after solution heat treatment.

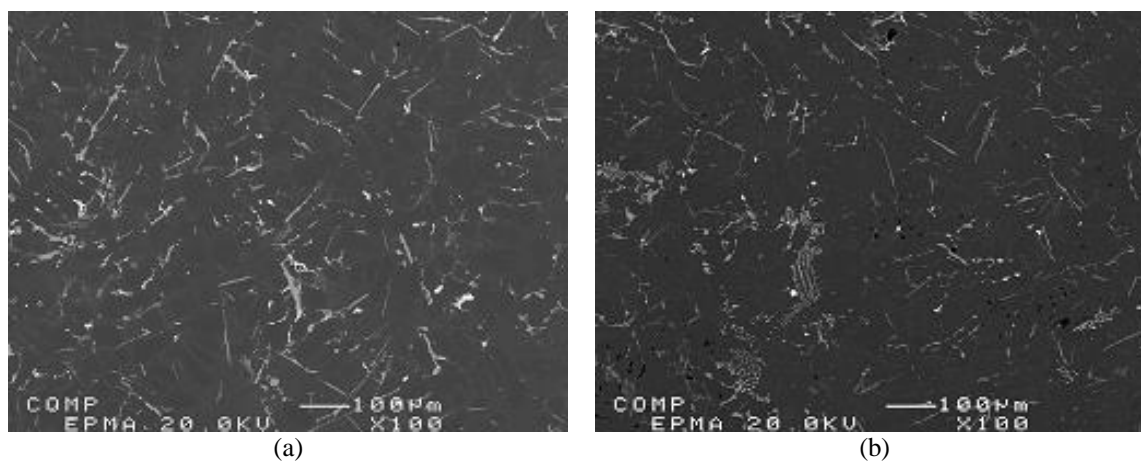


Figure 5.35 Backscattered electron images of G8 (0.75wt% Mn + 0.25wt% Zr) alloy samples: (a) as-cast, and (b) after solution heat treatment.

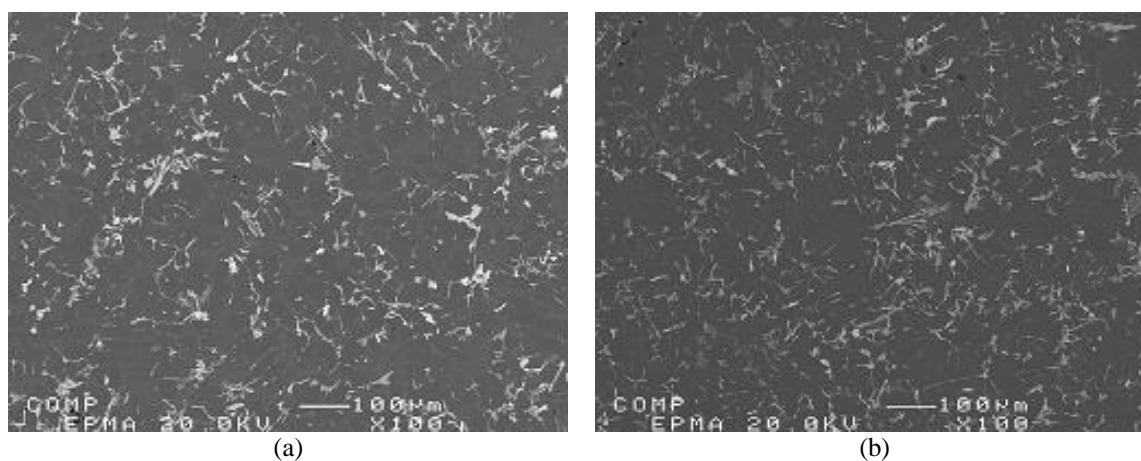


Figure 5.36 Backscattered electron images of G9 (2wt% Ni + 0.75wt% Mn + 0.25wt% Zr) alloy samples: (a) as-cast, and (b) after solution heat treatment.

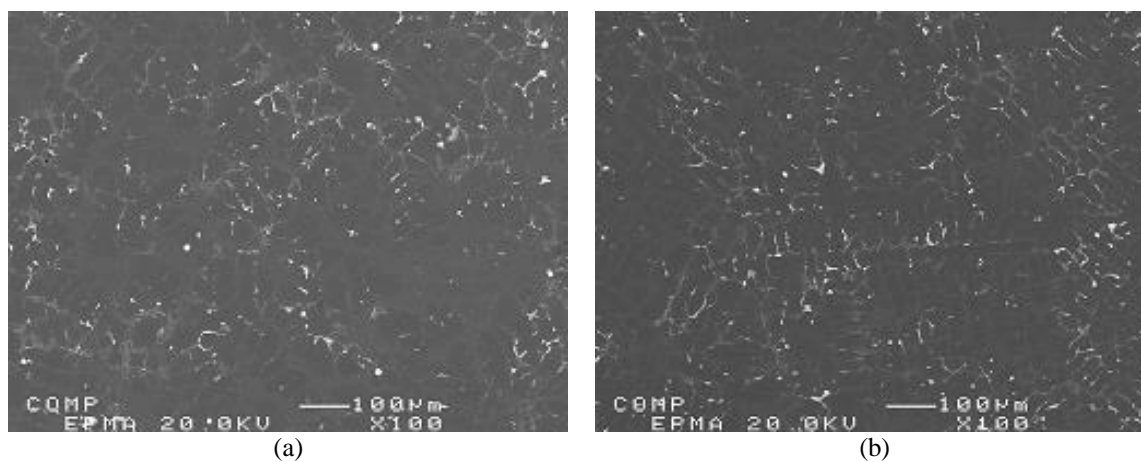


Figure 5.37 Backscattered electron images of G10 (0.15wt% Sc + 0.25wt% Zr) alloy samples: (a) as-cast, and (b) after solution heat treatment.

5.4 CONCLUSIONS

Based on the microstructural results and thermal analysis data presented in this first part of Chapter 5, the following conclusions may be drawn:

1. The thermal analysis experiments provide evidence of the solidification sequence in which phases appear during solidification at low cooling rate. Tensile test samples, obtained at high cooling rate, supply evidence of the alloy behavior in the as-cast condition and after solution heat treatment (at 500°C/8h for G1, G6, G8 through G10 alloy; and at 540°C/8h for G7 alloy (containing no Cu)).
2. The volume fraction of the undissolved phases (vol%) in the low cooling rate condition increases in the matrix with the addition of Ni, Mn, Sc, and Zr. A comparison of the intermetallic volume fraction between the alloys studied are shown below:
 - Comparing G8 to G9 alloy indicates that the addition of 2wt% Ni increases the vol% by ~3% (+1% Ni \approx +1.5vol%);
 - Comparing G6 to G7 alloy indicates that the addition of 1.8wt% Cu increases the vol% by ~2% (+1wt% Cu \approx +1.1vol%);
 - Comparing G6 to G9 alloy indicates that the addition of 0.75wt% Mn increases the vol% by ~3% (+1wt% Mn \approx +4vol%);
 - Comparing G1 to G10 alloy indicates that the addition of 0.15wt% Sc and 0.25wt% Zr increases the vol% by ~1.06% (+1wt% Zr and Sc \approx +2.65vol%).
 - Showing that Mn has the maximum effect in increasing the total volume fraction (per 1% addition).

3. Image analysis, optical microscopy, and EPMA techniques make it possible to quantify the microstructural changes occurring in the experimental 354 type alloys.
4. Similar to the 319 alloy, the 354 alloy presents well-defined reactions at temperatures below 500°C, related to Cu- and Mg-containing phases.
5. Six main reactions are detected during the solidification of the 354 base alloy: the formation of an α -Al dendritic network at 598°C followed by the precipitation of the Al-Si eutectic and the post-eutectic β -Al₅FeSi phase at 560°C, Mg₂Si phase and the transformation of the β -phase into π -Al₈Mg₃FeSi₆ phase at 540°C and 525°C; and then Al₂Cu and Q -Al₅Mg₈Cu₂Si₆ precipitate almost simultaneously as a last reaction at 498°C and 488°C. Also, two main reactions are detected with the addition of 2wt% of Ni, *i.e.*, the formation of Al₉FeNi and Al₃CuNi phases.
6. Of the two cooling rates used in the present study, it is important to note that in the industry, the high cooling rate is the more significant parameter in controlling the silicon particles and the volume fraction of intermetallic phases.
7. Based on the composition of G1 base alloy (9.4wt% Si, 0.08wt% Fe, 1.85wt% Cu, 0.5wt% Mg, 0.22wt% Ti, and ~170 ppm Sr), the main phases for this alloy are restricted to Cu-, Mg-, and Fe-rich intermetallic phases.
8. At low cooling rate and with an increase in the alloy Mg and Fe levels, the Si-particle size (area and length) increases. An increase in the Mg level at high cooling rate results in an increase in the Si-particle size (particle area and length) in the as-cast and solution heat-treated conditions; aspect ratio and roundness ratio are not affected, however, by the increase of Mg at both cooling rates, thereby, in effect, diminishing

the modifying influence of Sr. The addition of Fe and/or Mn has no significant effect on the Si particle characteristics as seen in G8 and G9 alloys.

9. The SDAS does not differ much among the alloys studied. The average of SDAS (as-cast tensile samples) of the six alloys was $\sim 18 \mu\text{m}$.
10. Minimum iron content is always recommended in the production of the 354 casting alloys. With regard to the castings which contain high iron levels, appropriate solution heat treatment procedures may partially neutralize the deleterious effects of the iron-bearing phases.
11. The presence of hard sludge particles within the soft α -Al dendrites in G8 alloy, would lead to a uniform distribution of stresses through the alloy matrix, thereby improving the alloy properties.
12. The Al_2Cu phase particles are more or less completely dissolved in the Al matrix after solution heat treatment in all the alloys studied.
13. Increasing the Mg and Fe levels in the base 354 alloy G1 increases the amount of the π -intermetallic phase formed.
14. The Q - $\text{Al}_5\text{Cu}_2\text{Mg}_8\text{Si}_6$, α -Fe, and sludge intermetallics are insoluble, whereas the platelet-like β -Fe phase dissolves partially during solution heat treatment.
15. Qualitative and quantitative analyses of solution heat-treated alloy samples reveal a high degree of decomposition of π -phase into β -phase during solution heat treatment for all the 354 alloys studied.
16. Using solution treatment time for 8 hours improves the π -phase decomposition to a large extent and increases the concentration of Mg in the matrix to the highest level

compared to the as-cast condition; large amounts of Mg_2Si will thus be expected to precipitate during the aging of such solution-treated samples.

17. Despite the fact that the thermal analysis curves did not detect any Zr-rich and Sc-rich phase reactions, the EPMA, WDS, and EDS results clearly indicate that while there is no reaction of Zr and Sc with Ni, Cu and Sr. Zirconium and scandium react only with Ti, Si, and Al in the alloys examined to form the phases $Si(Ti,Zr)$, $ZrSi$, $(Al,Si)_3Si$, Al_3Zr , $Si(Sc,Zr)$, $(Al,Si)_2(Zr,Ti)$, and $(Al,Si)_3(Zr,Ti)$.
18. Zr-rich intermetallic phases observed in this study appear in two different forms: the $(Al,Si)_2(Zr,Ti)$ phase which contains a higher level of Si and appears in block-like form, and the $(Al,Si)_3(Zr,Ti)$ phase containing a higher level of aluminum, and which appears in needle-like form.
19. The beneficial effects of the transition elements Zr, Sc, and Ti in refining the α -Al grain size and transforming the morphology from a dendritic to a non-dendritic type lead, indirectly, to a noticeable reduction in the size of such intermetallics as the Al_2Cu and α -Fe phases, as they appear under both low and high cooling rate conditions. In general, the Zr-containing intermetallic compounds appear to be refined and more uniformly distributed in the matrix when Sc is present in the alloy.

CHAPTER 5

Stage II Alloys – Room Temperature Testing

MICROSTRUCTURE AND MECHANICAL

PROPERTIES

PART II

TENSILE PROPERTIES

CHAPTER 5

Stage II Alloys - Room Temperature Testing

MICROSTRUCTURE AND MECHANICAL

PROPERTIES

PART II

TENSILE PROPERTIES

5.5 INTRODUCTION

This second part of Chapter 5 will document and analyze the tensile test results for the alloy studied in this work, in the as-cast, solution heat-treated, and aged conditions, using different aging temperatures and times, with the goal of providing a better understanding of the alloy properties in relation to the various alloying additions used. Quality index charts will be generated with the purpose of setting the limits of the tensile properties, as well as to compare the properties of the alloys studied, to delineate the effects of the additions made in relation to the heat (aging) treatment applied. Plots of ΔP will also be presented, with P representing Property (*i.e.*, UTS, YS and %El) and ΔP representing the

difference in property value obtained for a specific alloy composition/heat treatment condition, taking the G1 alloy as the base line. This approach helped to better visualize the effects and interactions of the various additions used and the different heat treatment conditions. The tensile test data are provided in the form of tables and graphs in the sections that follow. For the sake of simplicity, only selected data have been highlighted in this chapter.

5.6 AS-CAST AND SOLUTION HEAT-TREATED CONDITIONS

The mechanical properties of Al-Si-Mg-Cu castings are controlled mainly by their microstructure, in particular, by the SDAS, the morphology of Si particles, the Mg_2Si precipitation, and the nature of the iron intermetallics.^{16, 69, 126} It is important to mention that the results for the base alloy G1 presented in this part have been taken directly from the work of Hernandez-Sandoval¹⁹ since the same alloy and same heat treatment and testing procedures were used by him as in the present case for the new alloys proposed in this part of the study. Only the quality index (Q) values for alloy G1 presented in this chapter were calculated.

The appropriate solution treatment temperature for the 354 casting alloys was selected via a critical selection process because of the high copper content (1.8wt% Cu) of the alloys, after an extensive investigation of the effects of solution temperature on the tensile properties. Although the temperature selected was 500°C, which might appear to be over-conservative, it was deemed necessary to avoid the risk of any incipient melting of the copper phases, which could have the potential for deteriorating the mechanical properties of

the alloys to a great extent. On the other hand, increased strength after the treatment is normally to be observed in similar 354 alloys which use a solution heat treatment temperature of 525°C, over a 2-3 h period, in conjunction with analogous aging treatments.^{232, 268} The solution heat treatment for the alloys were carried out at 500°C for 8 h, with the exception of alloy G7 (containing 2wt% Ni and 0.25wt% Zr but without Cu), which was solution heat-treated at 540°C for 8 h. This increase in solution temperature improved the strength of the castings compared to the as-cast condition.

The UTS, YS, and %El values for all alloys investigated for both as-cast (AC) and solution heat-treated (SHT) conditions are displayed in Table 5.1 and in Figure 5.38. The X-axis represents the condition in which the samples were tested, while the primary Y-axis represents the strength values (UTS and YS), and the secondary Y-axis represents the percent of elongation to fracture (%El) values obtained for each condition. Using a solution heat treatment temperature to within the specified limits for the 354 alloys results in homogenizing the microstructure, since higher temperatures provide a greater driving force for the segregated atoms to diffuse through the metal matrix, producing a homogeneous structure.^{17-20, 31}

It will be observed that the strength and ductility values for G6 through G10 alloys in the as-cast condition increase by as much as 60-90 MPa (UTS), by about 55-85 MPa (YS), and vary from -0.1 to 0.8% (%El), respectively, in comparison with the base alloy G1. In the solution heat-treated condition the UTS and YS values increase by about 15-50 MPa (UTS), 38-73 MPa (YS), whereas the ductility decreases by 1.0 to 3.5%, respectively, compared to G1 alloy.

In the as-cast condition, the microstructures of the alloys investigated contain mainly coarse particles of the solidified intermetallics or phases such as Al_2Cu , Q - $\text{Al}_5\text{Mg}_8\text{Cu}_2\text{Si}$, $\text{Al}_{15}(\text{Mn,Fe})_3\text{Si}_2$ and Si. These particles have a deleterious effect on the tensile strength and ductility of the alloy because of their sharp edges which act as crack initiators.^{17, 18, 223, 224} During tensile testing, cracking is usually initiated by the breaking up of these hard intermetallics or by the decohesion of the intermetallic particles from the surrounding matrix.^{57, 126} In the solution heat-treated condition, these intermetallics break down and dissolve in the matrix, producing a supersaturated solid solution of α -Al; the latter strengthens the matrix by increasing the resistance to dislocation movement during deformation of the test bars as testing progresses.^{30, 102} Microstructure and soundness of the casting are the main controlling factors which influence ultimate tensile strength. This increase in mechanical properties is related to the changes occurring in the morphology of the silicon particles during solution heat treatment, such that they become more rounded, resulting in a decrease in their aspect ratio and density.^{19, 20}

Alloys G6 (containing 2wt% Ni and 0.25wt% Zr) and G9 (containing 2wt% Ni, 0.75wt% Mn, and 0.25wt% Zr) showed similar as-cast (AC) and solution heat-treated (SHT) tensile properties. In these two conditions, alloy G6 displayed, respectively, UTS values of 318 MPa (AC)/323.5 MPa (SHT), YS values of 233.3 MPa/205.3 MPa, and ductility values of 1.81%/ 3.55%, while alloy G9 showed UTS, YS and ductility values of 310.6 MPa/319 MPa UTS, 230.2 MPa/205.6 MPa YS, and 1.55%/ 2.85% for the same two conditions. These results indicate that the presence of Mn has virtually no effect on either the as-cast properties or those obtained after solution heat treatment. Overall, the highest

tensile properties for the two conditions were obtained with alloy G7, namely, 306.5 MPa/354.4 MPa (UTS), 208.8 MPa/234.5 MPa (YS), and 2.41%/4.88%, the latter %El value of 4.88% being only slightly lower to that obtained for alloy G10 (5.4%). Alloys G8 and G10 also displayed an increase in UTS and %El in the as-cast (323.8 MPa (G8)/298.5 MPa (G10) and 2.05%/2.32%) and solution heat-treated (328.4 MPa/333.1 MPa and 4.62%/5.40) conditions, respectively. On the other hand, the results obtained for YS in both alloys, presented a decrease from 238.9 MPa (G8)/228.1 MPa (G10) to 203.4 MPa/199.4 MPa, respectively.

Table 5.1 Mean values of UTS, YS, %El obtained for alloy studied in the as-cast and solution heat-treated conditions, Q values obtained with Equation 1

Mean values of UTS and YS (MPa) and %El used to obtain Q				
Identification	$Q = \text{UTS} + 150\log (\% \text{El})$		Eq. 1	
	UTS (MPa)	YS (MPa)	Total Strain (%El)	Q (MPa) (Eq.1)
G1-AC	234.69	154.41	1.63	267
G1-SHT	304.48	161.50	6.36	425
G6-AC	317.96	233.30	1.81	357
G6-SHT	323.53	205.31	3.55	406
G7-AC	306.50	208.83	2.41	364
G7-SHT	354.44	234.47	4.88	458
G8-AC	323.79	238.90	2.05	371
G8-SHT	328.44	203.43	4.62	428
G9-AC	310.62	230.15	1.55	339
G9-SHT	319.03	205.61	2.85	387
G10-AC	298.50	228.09	2.32	353
G10-SHT	333.09	199.36	5.40	443

*Total strain: total strain elastic + plastic strain at failure.

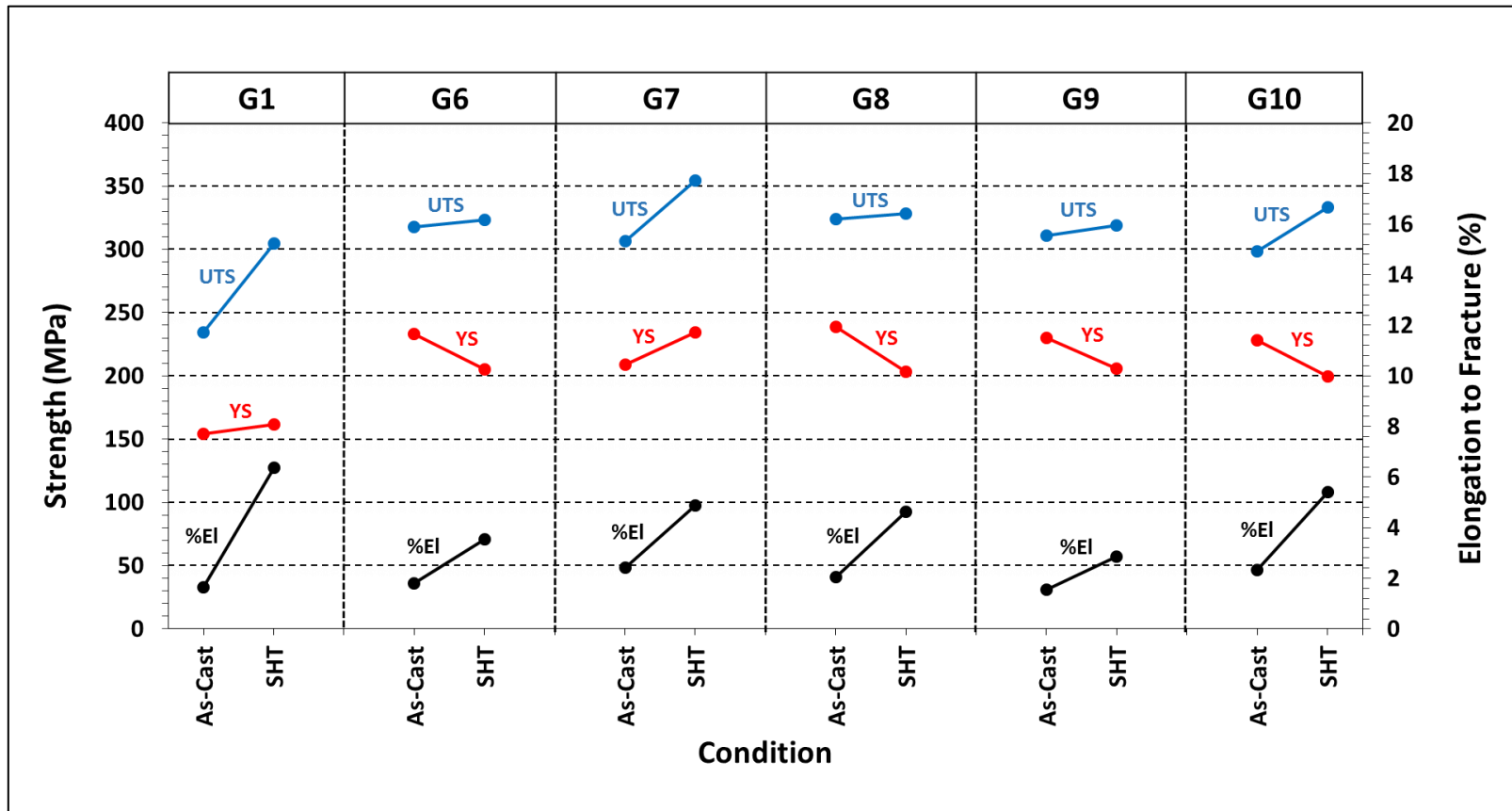


Figure 5.38 Variation in ultimate tensile strength (MPa), yield strength (MPa), and percent elongation to fracture (%El) for as-cast and solution heat-treated samples.

The change in ductility may be explained as follows: in the as-cast condition, the brittle acicular silicon particles serve as stress concentrators since they are harder than the matrix. Such particles tend to promote crack propagation during load application thereby decreasing the ductility of the alloy. The increased solution treatment temperature of 540°C for the G7 alloy (without Cu), provided significant thermal modification, producing a considerable change in the size and morphology of the eutectic silicon particles as was observed earlier in Part 1 of Chapter 5, which resulted in improving both the alloy strength and ductility; these results are in accordance with the work of Ammar.^{17, 223} The mechanism of thermal modification of the eutectic silicon particles involves the necking, fragmentation, spheroidization, and coarsening of the eutectic Si particles.^{17, 84, 228, 256}

The tensile properties (UTS, YS and %El) are usually considered separately when the effect of one or more parameters on these properties is studied. As described in Chapter 2, Drouzy *et al.*¹³⁰ proposed another method for interpreting tensile properties in a more general way. Two variables, quality index (Q) and probable yield strength (YS) were obtained as functions of the ultimate tensile strength UTS and percentage of elongation to fracture (%El) on a chart which plotted UTS vs. log %El. According to these authors, such variables would facilitate the interpretation of the data regarding tensile properties of the alloy and also vary independently of each other.

Quality charts were generated for evaluating the influence of metallurgical parameters on the tensile properties and the quality indices of 354-type casting alloys. An example of the quality chart obtained for the as-cast and solution heat-treated conditions for the various 354 alloys is show in Figure 5.39. Equations 1 and 2 (described in Chapter 2)

were used to generate *iso-Q* lines and *iso-yield strength* lines, respectively. The *iso-Q* and *iso-YS* lines in these charts facilitate knowing which additions are beneficial in this respect.

By increasing the copper content, it is possible to improve the strength of the alloys, although this will result in a reduction in ductility.^{15, 110, 223} The strengthening effect obtained by adding copper to an Al-9wt%Si-0.5wt%Mg alloy is based on the formation of Cu- and Cu-Mg-containing precipitates such as θ -Al₂Cu, S -Al₂CuMg, Q -Al₅Cu₂Mg₈Si₆,^{112, 113, 115} and may be further optimized by applying adequate heat treatment procedures. Table 5.1 and in Figure 5.38 show that the low Cu-content in the base alloy G1 and the no Cu-content in alloy G7, present the best performer after solution treatment. This behavior may be related to the combination of Mg, Cu, Ni, Mn, Zr and Sc. Suitable heat treatments applied to castings containing the same copper content ultimately lead to improvements in the strength and quality of these castings, as shown in Figure 5.39. The quality of these castings, however, will be affected according to the net amount by which the increase in strength is balanced by the reduction in ductility.

The main purpose of solution heat treatment is to maximize dissolution of the hardening elements in solid solution, to convert the acicular eutectic silicon to fragmented and spheroidized particles, as well as cause the fragmentation and dissolution of undissolved phases, namely Fe-intermetallics, and to achieve a homogeneous structure for improving the ductility and the quality of Al-Si cast alloys.^{147, 210-223} These improvements are reflected in the alloy properties and *Q* values obtained in the solution heat-treated condition compared to the as-cast values listed in Table 5.1 and displayed in the Quality chart of Figure 5.39.

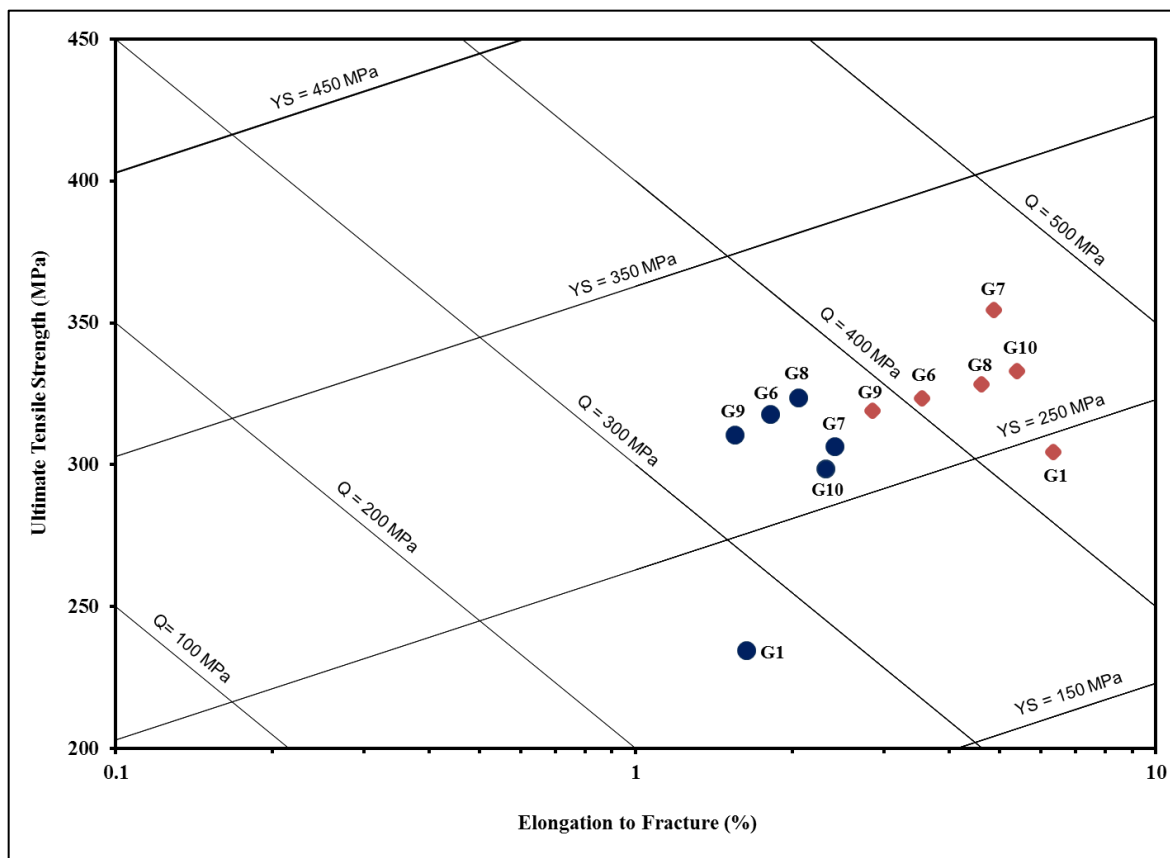


Figure 5.39 Quality chart generated using Equations 1 and 2, showing the influence of different additions on the tensile properties and the quality indices (Q) of test bars in the as-cast (blue) and solution heat-treated (red) conditions.

The application of a solutionizing treatment leads to significant improvement in the strength and quality of the castings, even for the alloys containing a higher Fe-level (alloys G6 through G10) than the base alloy G1, as may be seen from Figure 5.38, Figure 5.39, and Table 5.1. Such improvement is related to the changes which occur in the volume fraction, size, and/or morphology of the Fe-containing phases after solution heat treatment, specifically the reduction in volume fraction due to the dissolution, thinning, necking and fragmentation of the β -phase and the dissolution and/or transformation of the π -phase into clusters of fine needles of the β -phase.^{17, 18} The deleterious effects of iron are thereby

reduced. It will be clear from Figure 5.38 and Figure 5.39 that, for the alloys studied, solution heat treatment provided a considerable improvement in reducing the compromise between strength and quality, as since both parameters were increased after solution heat treatment.

An improvement in the tensile properties and alloy quality are noted upon solution heat treatment for all alloys, indicating that although the solution heat treatment is mainly responsible in improving the alloy quality, the presence of Ni and Zr in alloy G7 in the absence of Cu, and of Sc and Zr into the alloy G10 provides even further improvement, since these alloys show the best Q and YS values. Zirconium and scandium as transition elements form dispersoid precipitates of Al_3Zr , Al_3Sc , $Al_3(Zr_{1-x}Sc_x)$, and $Al_3(Sc_{1-x}Zr_x)$ throughout the α -Al matrix, producing an intensified hardening effect. These precipitates form during the course of solidification when passing through the temperature formation range of the dispersoids. Their presence would explain why the yield strengths of the Sc- and Zr-containing alloy is higher than the base alloy G1 in the as-cast condition.

The increase in the Mg-content from 0.5wt% to 0.75wt% leads to an improvement in the strength of the castings and to a slight decrease in ductility, but without any noticeable change in quality, as may be seen from the quality chart shown in Figure 5.39. These observations relate to the fact that the amount by which the strength of the alloy is increased compensates for the amount by which the ductility is decreased. The improved strength of the castings obtained by increasing the Mg-level is directly related to the precipitation of Mg_2Si phase. While a higher Mg content should produce a larger amount of

these hardening precipitates, on the other hand, it will also bring about the precipitation of a large volume fraction of the π - $\text{Al}_8\text{Mg}_3\text{Si}_6$ phase; this phase, known for its deleterious effect on both strength and ductility, will consequently affect the quality of the casting.^{16, 126, 218}

The negative effect of the π - $\text{Al}_8\text{Mg}_3\text{Si}_6$ phase on the strength of the castings results directly from the decrease in the density of Mg_2Si precipitates due to the reduction in magnesium available to go into solid solution for the Mg_2Si precipitation which occurs after aging treatment.^{17, 18} This would also explain the slight increase in the strength values of the alloys with Mg levels up to 0.76wt%. The π -phase also has a deleterious effect on the alloy ductility due to its brittle nature so that its particles act as preferred crack initiation sites where the fracture is triggered easily. After solution heat treatment at 500°C, the π -phase was observed to dissolve or transform into a cluster of very fine β -phase platelets, as was described in Part I of Chapter 5.

The fulfilment of the objectives of this research relies strongly on the use of Quality index charts as a useful tool for illustrating, in an accessible way, the general behavior of the alloys with respect to tensile properties as the aging temperatures and times increase.

5.7 INFLUENCE OF AGING PARAMETERS

Aging treatment of the castings was carried out to investigate the influence of aging temperature and aging time on the tensile properties of the 354 alloys studied. During aging, the excess of solute atoms in the supersaturated solid solution of α -Al ultimately precipitate after a certain period of time, depending on the aging temperature applied to the castings.⁴⁷ The vacant sites in the lattice structure, resulting from the solution and

quenching treatments, provide the means for the diffusion of the excess solute atoms through the metal matrix. Five aging temperatures of 155°C, 190°C, 240°C, 300°C, and 350°C were used over a wide range of aging times, namely 2 h, 4 h, 6 h, 8 h, 10 h, 20 h, 48 h, and 100 h.

5.7.1 AGING BEHAVIOR OF BASE ALLOY G1

Figure 5.40 shows the tensile properties of the base alloy G1, for the various aging times and temperatures applied during the aging treatment. The maximum value of UTS, ~382 MPa may be obtained with two different sets of aging conditions, *i.e.* 155°C/100h and 190°C/2h. The greatest mechanical stability for the aging treatments was observed at 155°C and then at 190°C. Considering the yield strength value in the solution heat-treated condition, with artificial aging, it was possible to increase the yield strength by more than 100%, with the maximum yield strength achieved after 100 hours at 155°C aging temperature, and after 2 hours at 190°C.

The greatest decrease in tensile strength was observed at 240°C, going from 312 MPa at 2 h to 240 MPa at 100 h. Similarly, a significant decrease in strength was also observed at 190°C going from 381.8 MPa at 2 h to 314 MPa at 100 h. Even though such a decrease in alloy strength across the 2-100 h range of aging time is not evident at 300°C and 350°C, nonetheless, the greatest mechanical deterioration is expected to be observed after less than 2 hours of aging treatment. This assumption is based on a consideration of the tensile properties of the solution heat-treated alloy, namely 304.5 MPa UTS and 161.5 MPa YS, implying that the over-aged samples tend to lose between 15% and 40% of their

original strength within the first 2 hours of aging at 300°C and 350°C. As will be observed in Figure 5.40, the ductility ranges from 1 to 6%, where any value greater than 3% is considered as a high ductility value in the context of hypoeutectic Al-Si alloys.⁴⁶

The high silicon content of the base alloy G1, which is 9wt% Si, seems to reflect this behavior with respect to elongation. At the low silicon content of hypoeutectic Al-Si alloys, *i.e.*, 5 to 7wt%, the eutectic liquid solidifies in narrow bands surrounding the aluminum grains, and therefore the intermetallics which precipitate out of this liquid are observed to form along these narrow bands as entwined clusters. In contrast, in the case of high Si alloys, with a greater volume fraction of eutectic liquid, rather than just forming wide bands of particles around the grains, they form within the complex networks of interdendritic and intergranular liquid pools; these are bounded by the more orthogonal dendritic Al grains and ultimately lead to the formation of more uniformly dispersed intermetallic phases.^{132, 267} In general, the ductility of alloy G1 is found to decrease on going from 155°C to 190°C. The lowest ductility value is observed at the 190°C/20h aging condition. The ductility begins to increase again when the aging temperature is increased above 190°C. The greatest ductility is observed at 300°C/100h and at 350°C aging temperature, although none of the aging conditions achieves the higher ductility value observed in the solution heat-treated condition. This observation may be considered evidence that the mechanical behavior displayed by alloy G1 is common to that of Al-Si-Cu-Mg alloys whose strength is obtained at the expense of ductility.^{19, 20, 132, 269}

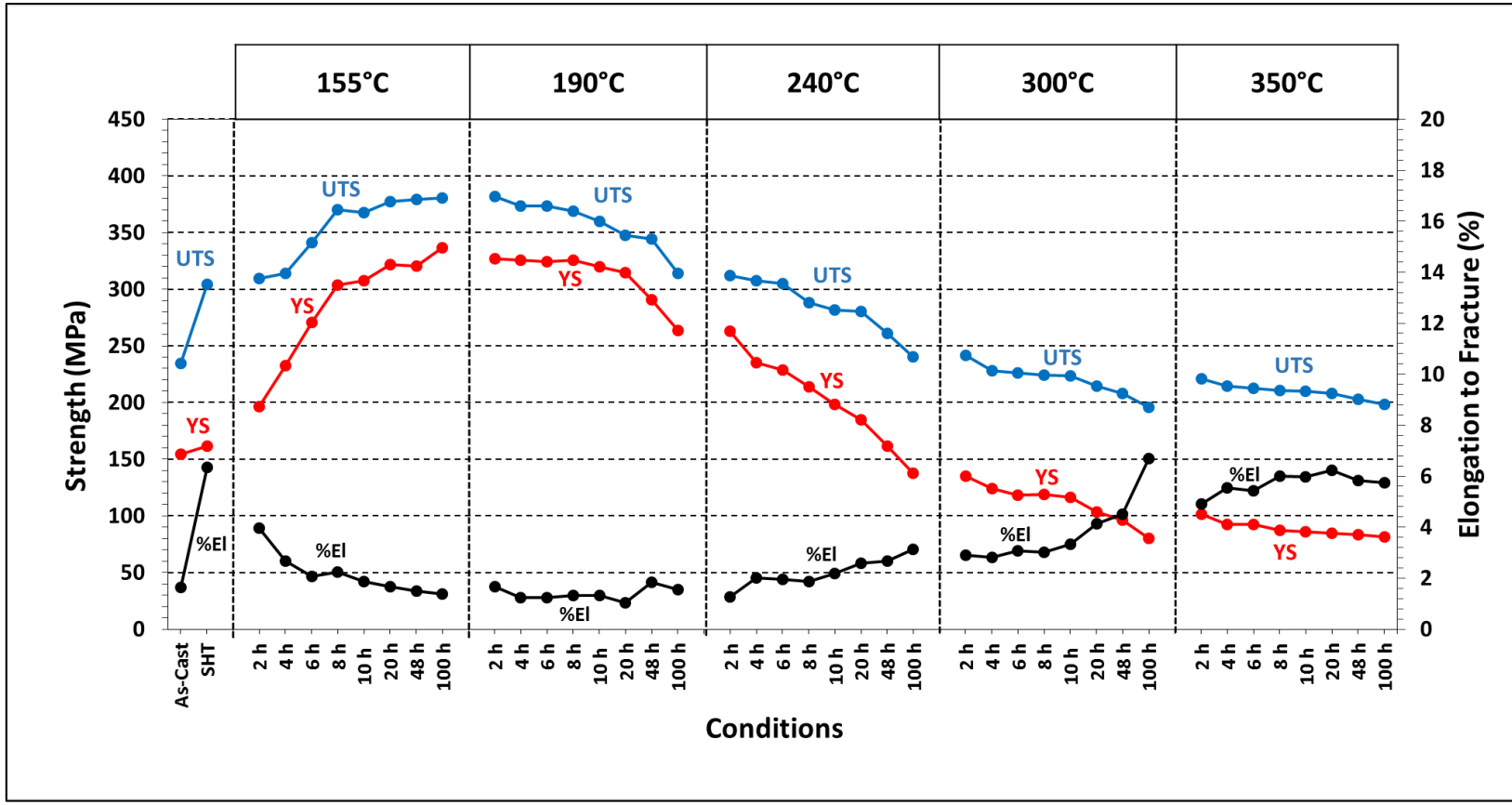


Figure 5.40 Variation in UTS (MPa), YS (MPa), and %El observed in base alloy G1 as a function of aging conditions.

The tensile strength attains the highest value after 2 hours of aging at 190°C while exhibiting a low ductility in such condition applied. The yield strength appears to be most stable at this temperature, showing a variation of about 50 MPa in YS values over the range of aging times studied. Aging at 155°C results in a continuous increase in strength with increase in aging time up to 100 hours at which point maximum strength is obtained. This is accompanied by a reduction in ductility up to the peak aging point. It is interesting to note how the same strength values may be achieved after only 2 hours of aging when the aging temperature is raised to 190°C, which is significant in terms of heat treatment and, therefore, production costs.

The aging times required to reach the peak strength are 100 h, 2 h, 2 h, 2 h and 2 h, at aging temperatures of 155°C, 190°C, 240°C, 300°C and 350°C, respectively. It should be noted that the peak-aging time for each temperature is determined from the corresponding yield strength curve shown in Figure 5.40.

The best combination of properties for alloy G1 is achieved after aging at 190°C for 2 hours: 382 MPa UTS, 327 MPa YS, and 1.66 %El. This condition may therefore be considered as the appropriate T6 heat treatment for the base 354 alloy. The redistribution of the solute atoms in the early stages of aging results in the formation of coherent Guinier-Preston (GP) zones accompanied by an improvement in the alloy strength. A further increase in the aging time results in the formation of coherent and semi-coherent transition phases at the GP zone sites, by means of which a further increase in the strength of the casting may be attained up to a maximum level at peak-aging. Any further aging beyond

the peak-strength results in overaging in which equilibrium and coarser phases form and lead to a reduction in the strength of the casting.

The Quality Index values for alloy G1 are presented in Table 5.2. For constructing the quality index (Q) charts with regard to the as-cast, solution heat-treated, and aging conditions for the six alloys studied. Equations 1 and 2 were used to calculate the quality index (Q), the *iso-Q* lines and the *iso-YS* lines, respectively. Figure 5.41 presents a Quality Index chart showing the lowest and highest mechanical quality occurring for the conditions mentioned above.

In order to analyze mechanical quality by means of the quality index charts, 17 conditions per alloy were selected from among all the conditions used, and include the as-cast and solution heat-treated conditions plus 15 aging conditions corresponding to 2, 10, and 100 h aging times at each of the five aging temperatures (155°C, 190°C, 240°C, 300°C, and 350°C). The reason for taking only 17 conditions out of a total of 42 per alloy was principally to avoid an overcrowded quality index chart in which it would not be possible either to discern or to show the general mechanism/behavior covering all of the experiments carried out for this research. The criterion applied for these 17 conditions was to take into consideration the extreme values, particularly those concerning the percentage elongation to fracture and yield strength, and including the as-cast and solution heat-treated conditions.

Table 5.25 Mean values of UTS, YS, %El obtained for base alloy G1 subjected to different heat treatment conditions, Q values obtained with Equation 1

Mean values of UTS and YS (MPa) and El (%) used to obtain Q				
Q = UTS + 150log (%El)			Eq. 1	
Identification	UTS (MPa)	YS (MPa)	Total Strain (%El)	Q (MPa) (Eq.1)
As-Cast	234.69	154.41	1.63	267
SHT	304.48	161.50	6.36	425
155°C-2 h	309.45	196.20	3.96	399
155°C-4 h	313.65	232.75	2.68	378
155°C-6 h	340.81	270.44	2.08	388
155°C-8 h	370.19	303.56	2.24	423
155°C-10 h	367.27	307.69	1.86	408
155°C-20 h	377.56	321.80	1.68	411
155°C-48 h	379.39	320.65	1.50	406
155°C-100 h	380.22	336.44	1.38	401
190°C-2 h	381.84	327.07	1.66	415
190°C-4 h	373.11	325.38	1.23	386
190°C-6 h	373.46	324.17	1.23	387
190°C-8 h	369.14	325.85	1.31	387
190°C-10 h	360.04	319.60	1.32	378
190°C-20 h	347.85	314.44	1.05	351
190°C-48 h	344.04	290.78	1.84	384
190°C-100 h	314.01	263.64	1.56	343
240°C-2 h	312.01	262.63	1.25	327
240°C-4 h	307.44	234.93	2.00	353
240°C-6 h	304.87	228.89	1.97	349
240°C-8 h	288.37	213.73	1.88	329
240°C-10 h	281.66	198.21	2.17	332
240°C-20 h	280.39	184.68	2.58	342
240°C-48 h	260.80	161.57	2.68	325
240°C-100 h	240.02	137.44	3.12	314
300°C-2 h	241.65	134.89	2.89	311
300°C-4 h	228.09	123.97	2.81	295
300°C-6 h	225.80	118.12	3.07	299
300°C-8 h	224.44	119.19	3.03	297
300°C-10 h	223.25	116.25	3.33	302
300°C-20 h	214.66	103.60	4.14	307
300°C-48 h	208.09	96.10	4.52	306
300°C-100 h	195.67	80.35	6.70	320
350°C-2 h	221.13	101.53	4.90	325
350°C-4 h	214.38	92.30	5.53	326
350°C-6 h	212.77	92.35	5.43	323
350°C-8 h	210.78	87.33	6.00	327
350°C-10h	209.79	85.97	5.98	326
350°C-20 h	208.22	84.34	6.24	328
350°C-48 h	203.09	83.17	5.83	318
350°C-100 h	198.36	81.16	5.76	312

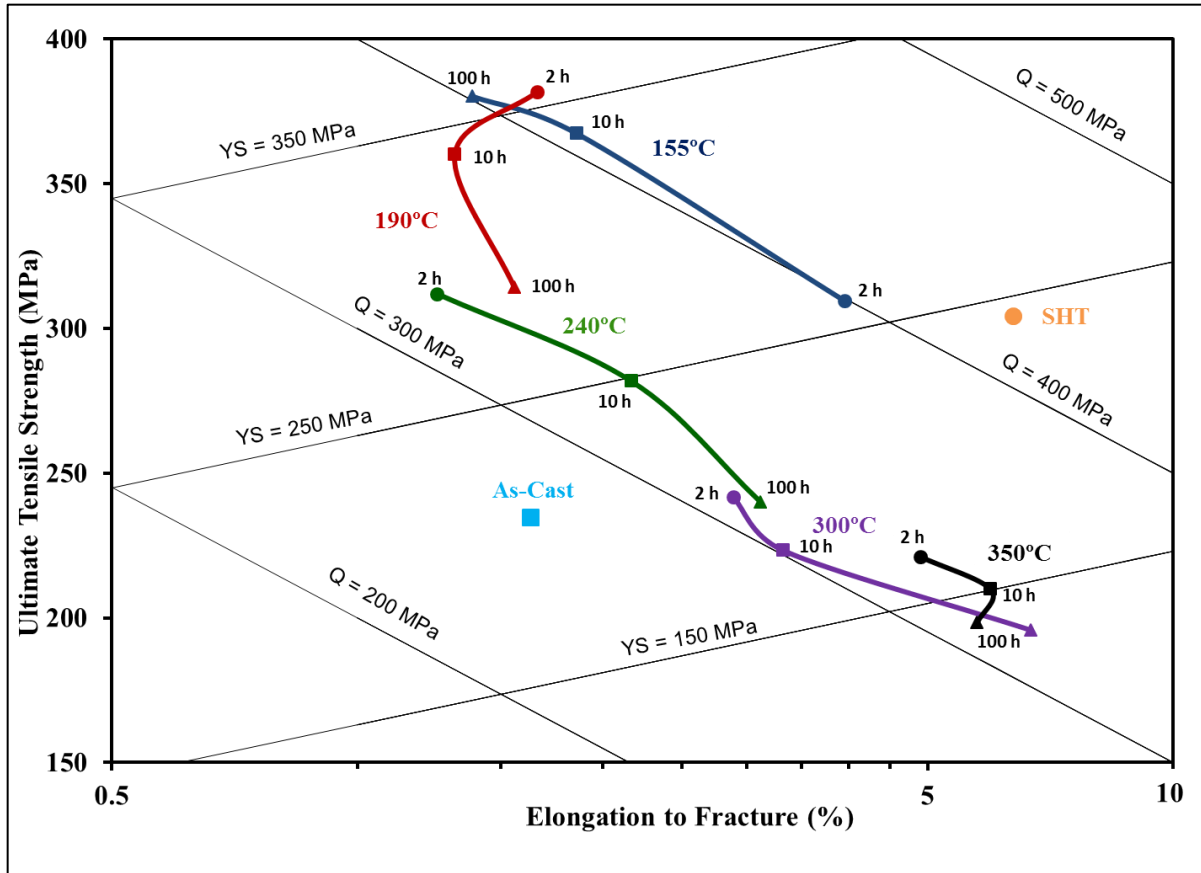


Figure 5.41 Quality chart generated using Equations 1 and 2 showing the tensile properties and the quality indices (Q) of G1 base alloy test bars in the as-cast, solution heat-treated, and aged conditions (five aging temperatures used and aging times of 2, 10, and 100 hours).

Figure 5.41 shows the maximum and minimum tensile properties obtained for alloy G1 over all the conditions examined in this study. Taking into consideration all the aging temperatures listed in this figure, it becomes possible to detect a trend in mechanical behavior similar to that reported for alloy 319, as evidenced by the curvilinear aspect of the quality index as it emerges throughout the aging process of the material.^{20, 224, 269} The contoured curves observed in the quality index chart can be related to changes in the yield

strain and strain-hardening which result principally from the effects of aging time and temperature on the precipitation-hardening of the copper phase particles.

In the current study, β -Al₅FeSi, π -Al₈Mg₃FeSi₆, Al₉FeNi, and Al₁₅(Fe,Mn)₃Si₂, intermetallic phases were the main Fe-containing phases formed in these castings at low cooling rate, as was shown in Part I of Chapter 5. The size and morphology of the phases mentioned are the main source of the detrimental effect of iron on the tensile properties and quality index of the castings.^{88, 91, 137} As mentioned previously, a number of studies have reported that the β -phase is the most deleterious Fe-bearing intermetallic because of its platelet-like shape, with the platelet edges producing areas of high stress concentration. The formation of such stress raisers throughout the microstructure results in impaired mechanical properties and an impoverished quality of the castings.

As shown in Figure 5.41, the YS reaches a maximum value and then decreases after the 190°C/2h condition when the strain-hardening coefficient reaches a minimum followed by an increase. Below the 190°C/2h condition, GP zones and θ' precipitates develop that are coherent with the matrix.^{110, 269} The YS is thus increased because of the strain fields associated with these precipitates, which are sheared by the dislocations and subsequently lead to a low strain-hardening rate. Slotz and Pelloux²⁷⁰ mentioned the formation of Al₂Cu precipitates at temperatures of 190°C and above. These precipitates are incoherent with the matrix and cannot be sheared by dislocations, thereby promoting lower strength values and high strain-hardening rates resulting from the accumulation of Orowan loops around these particles.

5.7.2 AGING BEHAVIOR OF ALLOY G6 (2wt% Ni + 0.25wt% Zr)

Figure 5.42 shows the tensile properties obtained for the G6 alloy, containing 2wt% Ni and 0.2wt% Zr for the various aging times and temperatures applied during heat treatment. Compared to the as-cast condition, although the same behavior (*viz.*, an increase in value) is observed for UTS and %El as the base alloy G1, the YS value is decreased after solution heat treatment. With respect to the UTS, YS and %El curves obtained for the aged G1 and G6 alloys, at first glance, Figure 5.40 and Figure 5.42 appear to be very similar in nature. However, the tensile and yield strength values of G6 alloy samples are higher and more stable across the range of aging times studied for all aging temperatures.

Figure 5.42 reveals that the aging times required to reach the peak strength are 100 h, 2 h, 2 h, 2 h and 2 h, at the five aging temperatures, respectively. The yield strength curve is used to determine the peak-aging time for each temperature. The yield strength tends to be more responsive to artificial aging since this property is less influenced by the soundness of the casting than ultimate tensile strength and more influenced by the microstructural condition of the alloy.^{29, 30} The formation of coherent precipitates is the main source of strengthening in the G6 alloy and leads to an increase in strength to a maximum at 100 h at 155°C, which, in this case, is considered to be the peak-aging time. Increasing the aging temperature to 190°C or above results in considerably reducing the time required to reach peak aging to only 2 hours.

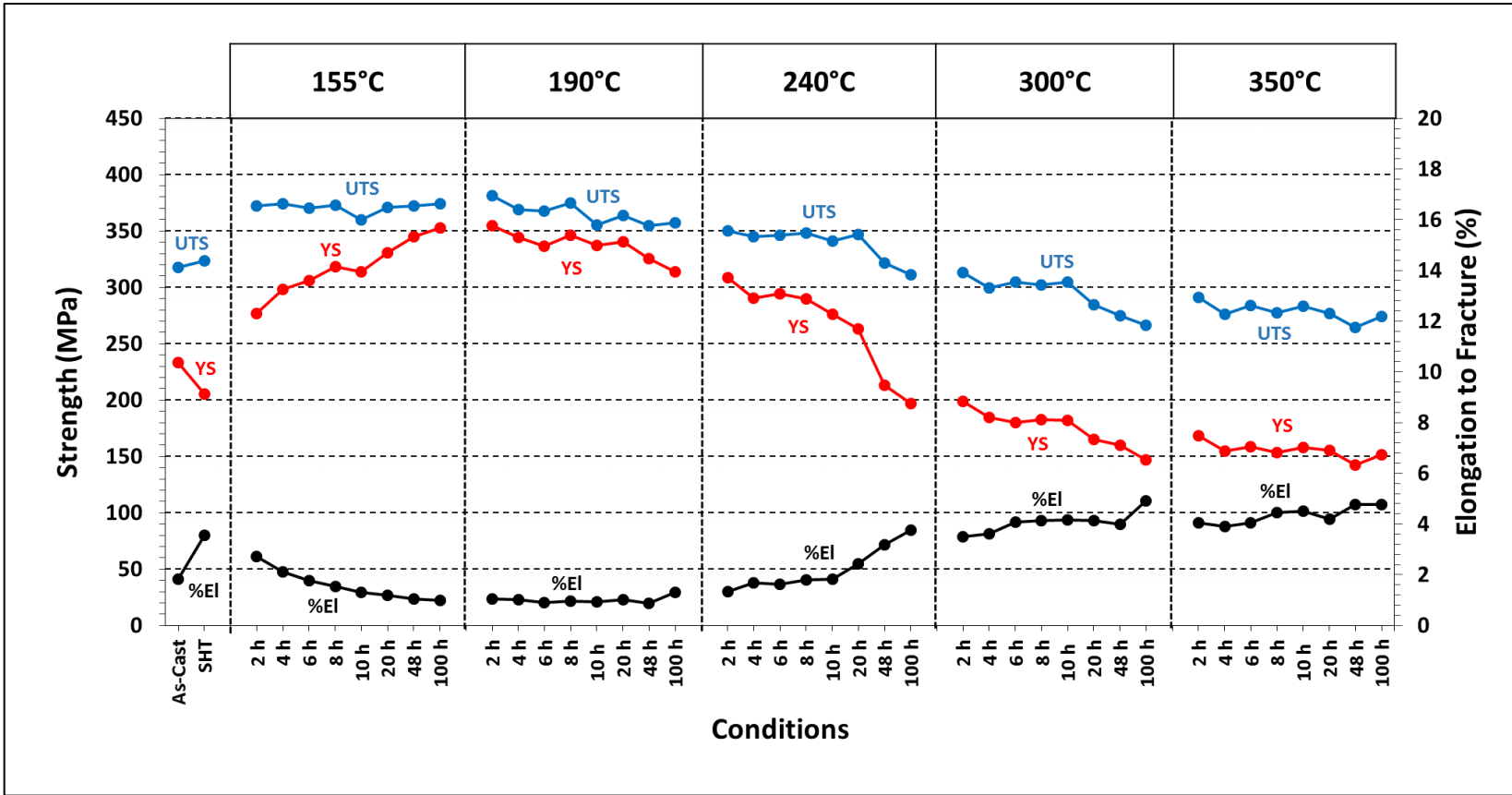


Figure 5.42 Variation in UTS (MPa), YS (MPa), and %El observed in alloy G6 (2wt% Ni + 0.25wt% Zr) as a function of aging conditions.

This behavior may be attributed to the overaging conditions which occur upon increasing the aging time for durations longer than the specified peak-aging time with respect to each temperature, and because a rapid aging is related to the high rate of atomic diffusion accompanying high aging temperatures and the direct precipitation of the coherent and semi-coherent phases, which are the main sources responsible for peak strength.¹⁸ The results concerning the aging treatment of the G6 alloy show that increasing the aging temperature decreases UTS as well as YS and increases the %El.

The best combination of properties is achieved after 2 hours of aging at 190°C, the corresponding properties being 381 MPa UTS, 355 MPa YS, and 1.05 %El. This condition may therefore be considered as the appropriate T6 heat treatment for the alloy G6 containing additions of Ni and Zr.

Figure 5.43 shows the quality index chart for the 17 selected heat treatment conditions for alloy G6. In this figure, the general behavior of alloy G6 appears to be similar to that of the base alloy G1 at aging temperatures above 190°C. Based on a comparison of the tensile properties of alloys G6 and G1, it will be observed that below aging temperatures of 240°C, the tensile properties/quality of alloy G6 decrease. This behavior may be ascribed to the fact that the decrease in ductility is more substantial than the slight increase in YS and UTS values observed at low aging temperatures.

Iron has been observed to affect the strength, ductility, and quality of 354-type castings in a detrimental way; thus, by increasing the iron level in these alloys, the strength is decreased, the ductility is reduced, and the alloy quality is diminished. The yield

strength, however, does not change significantly when the Fe-level is increased from 0.08wt% to 0.18wt%, since it is comparatively independent of impurity elements such as Fe, but is strongly related to the hardening effects which result from the addition of hardening elements or/and the application of a suitable aging treatment. With the increase in iron content, there is a concomitant increase in the volume fraction of intermetallics in the microstructure, as was reported in Table 5.12 in Part I of this Chapter.

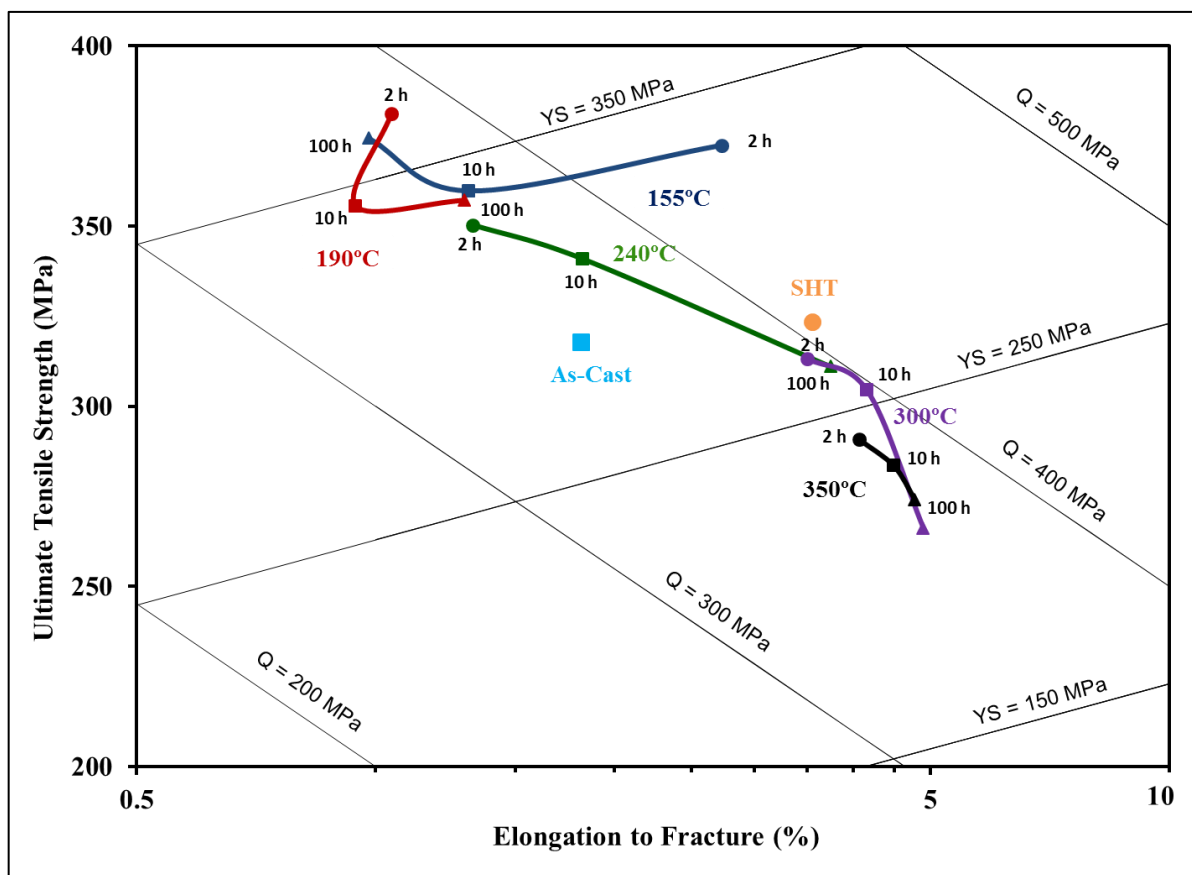
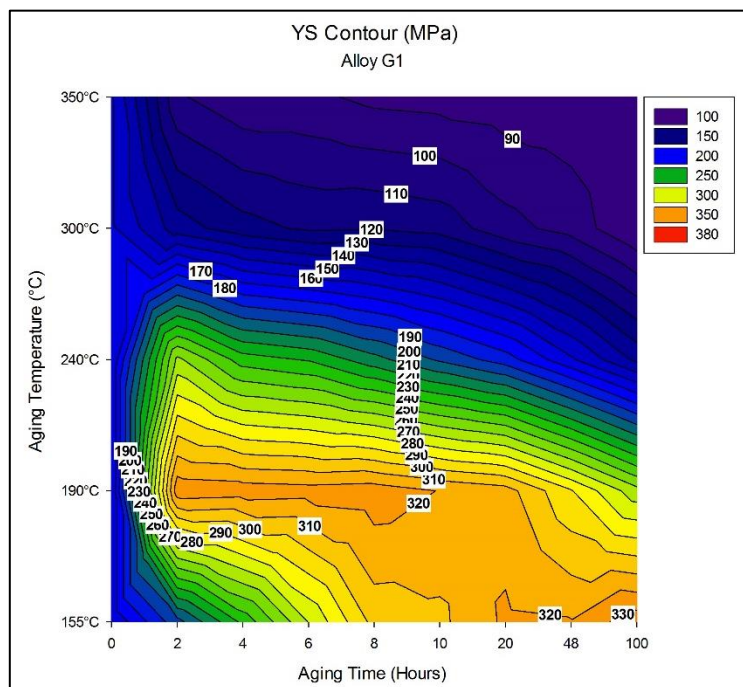


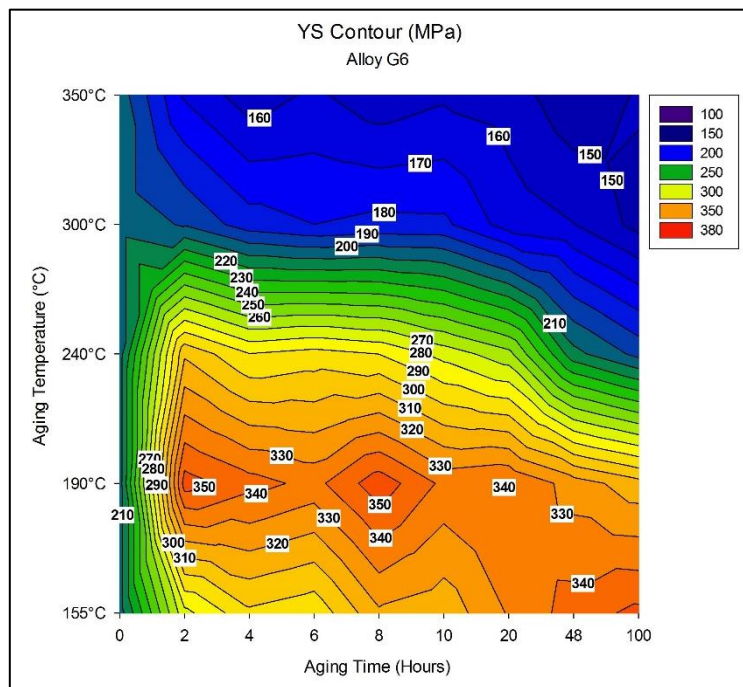
Figure 5.43 Quality chart generated using Equations 1 and 2 showing the tensile properties and the quality indices (Q) of G6 (2wt% Ni + 0.25wt% Zr) alloy test bars in the as-cast, solution heat-treated, and aged conditions (at the five aging temperatures used and aging times of 2, 10, and 100 hours).

Color-contour maps are 2D vector plots that display a field of vectors in x,y coordinates where both direction and magnitude are represented. It is a tool that can help to present the tensile results obtained in a different way, whereby one can observe how the properties vary with the aging conditions, according to the change in color and magnitude of the contour regions. Each contour line represents a specific value of the property being considered. As an example, Figure 5.44(a) and (b) show the yield strength (YS) color-contour maps for alloys G1 and G6, respectively. These charts reveal that the yield strength of alloy G6 shows a significant increase (~40 MPa) with the progress in aging time compared with that of the base alloy.

Increasing the solidification rate reduces the size of the microstructural features including eutectic silicon and intermetallics. This makes propagation of a crack through the material more difficult thereby increasing elongation in particular but also ultimate tensile strength. An increase in solidification rate does not affect the matrix strength and hence yield strength is not greatly impacted. Changing the aging condition from underaged to peak-aged increases the size of the Mg-Si precipitates formed. This raises the stress on the atomic lattice making dislocation movement more difficult. The ultimate tensile strength and yield strength of the material are increased; however, the ductility is reduced as was seen previously in Figure 5.40 and Figure 5.42 for alloys G1 and G6.



(a)



(b)

Figure 5.44 Yield strength-color contour charts for the base alloy G1 and alloy G6 (2wt% Ni + 0.25wt% Zr), comparing the effect of aging conditions.

5.7.3 AGING BEHAVIOR OF ALLOY G7 (2wt% Ni + 0.25wt% Zr, no Cu)

Figure 5.45 shows the tensile properties of alloy G7 (containing 2wt% Ni and 0.25wt% Zr, and no Cu) for the various aging times and temperatures applied. Aging at 155°C, results in an increase in the UTS up to peak-aging which is observed at 48 h. The increase in strength is accompanied by a corresponding reduction in ductility. The aging behavior at this temperature is related to the precipitation of the various precursors of the Mg₂Si phase in the alloy matrix according to the aging time applied.

Any further increase in the aging temperature and time beyond 48 hours results in overaging when the strength starts diminishing and the ductility begins to increase. As in the case of G6 alloy, for the G7 alloy also, there is a possibility for peak-aging to be attained in a shorter aging time with increase in aging temperature. The aging times required to reach the peak strength are 48 h at 155°C, and 2 h thereafter at higher aging temperatures. Aging treatments above 190°C result in increasing the alloy strength up to peak-aging, at the expense of ductility. Overaging takes place after reaching the peak strength for each temperature, whereupon the strength begins diminishing and the ductility starts to increase, as illustrated in Figure 5.45. The decrease in the alloy strength which accompanies overaging is related to the loss of the coherency strain surrounding the precipitates.¹⁷

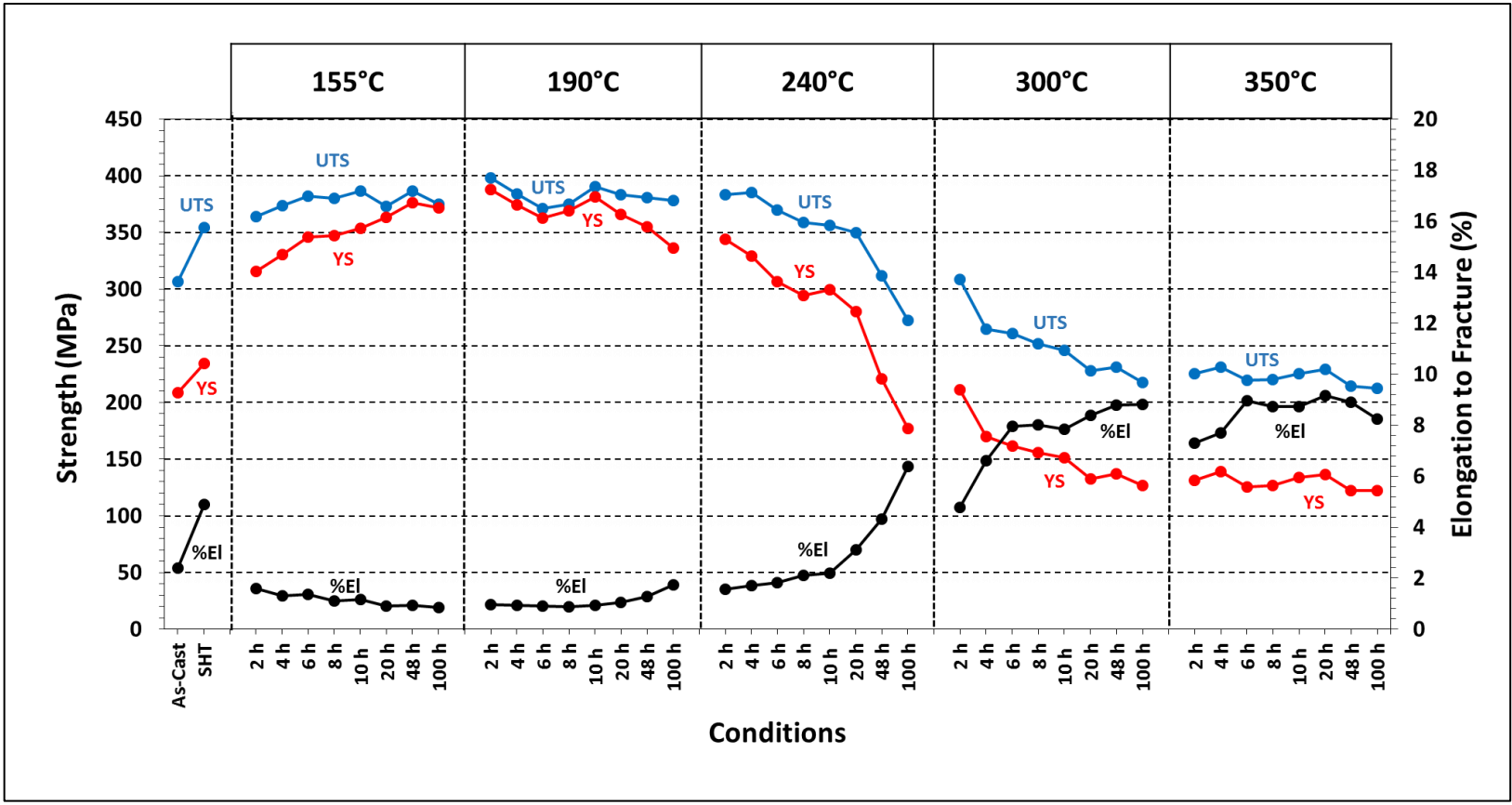


Figure 5.45 Variation in UTS (MPa), YS (MPa), and %El observed in alloy G7 (2wt% Ni + 0.25wt% Zr, no Cu) as a function of aging conditions.

The best combination of properties is achieved after aging at 190°C for 2 h and the corresponding properties observed are 398 MPa UTS, 388 MPa YS, and 0.97 %El. This condition may therefore be considered as the appropriate T6 heat treatment for the alloy G7 containing additions of Ni and Zr but without Cu-content.

The increase in the aging temperature provides a high rate of atomic diffusion and, in so doing, accelerates the precipitation process thus reaching peak strength faster than when the aging is carried out at lower temperatures. For example, for aging at 240°C, the peak strength is attained after only 2 h as compared to 48 h at 155°C. The UTS, YS, and %El values obtained for peak-aging at 155°C are 361 MPa, 352 MPa and 0.86%, respectively, while those obtained at 240°C are 332 MPa, 219 MPa and 4.9%, respectively.

Figure 5.46 shows the quality index chart for the 17 selected heat treatment conditions for alloy G7. In this figure, the general mechanical behavior of alloy G7 appears to follow that of the base alloy G1 and alloy G6 at aging temperatures above 190°C. From a comparison of the tensile properties of alloy G7 with those of alloys G1 and G6, it is observed that, below aging temperatures of 240°C, the quality index of alloy G7 decreases. As mentioned previously, this behavior may be ascribed to the fact that the decrease in ductility is more substantial than the slight increase in YS and UTS values observed at low aging temperatures.

The quality index provides a useful comparison of the relative merits of different alloys since the relationship between yield strength and elongation may be controlled by means other than alloy composition. The quality index is particularly useful in the present

case where increasing the Mg content compared to the base alloy influenced both yield strength and the number of brittle particles formed.

The aging rate can be accelerated when treating the alloy/casting at a higher temperature, so as to enhance the diffusion of solute atoms and precipitation of secondary phases. The degree of strengthening will depend on the system involved, the volume fraction and size of the second phase particles, as well as on their interactions with the dislocations.^{196, 246, 249}

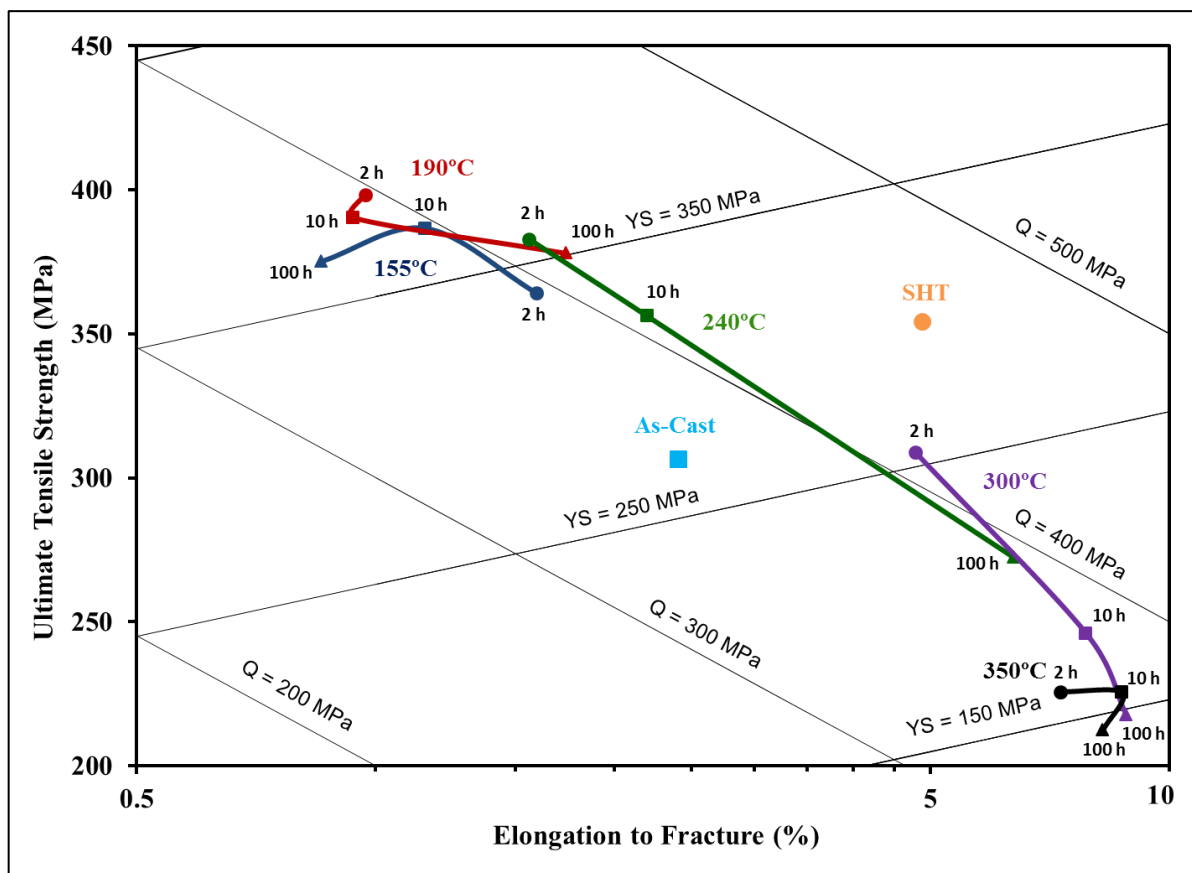
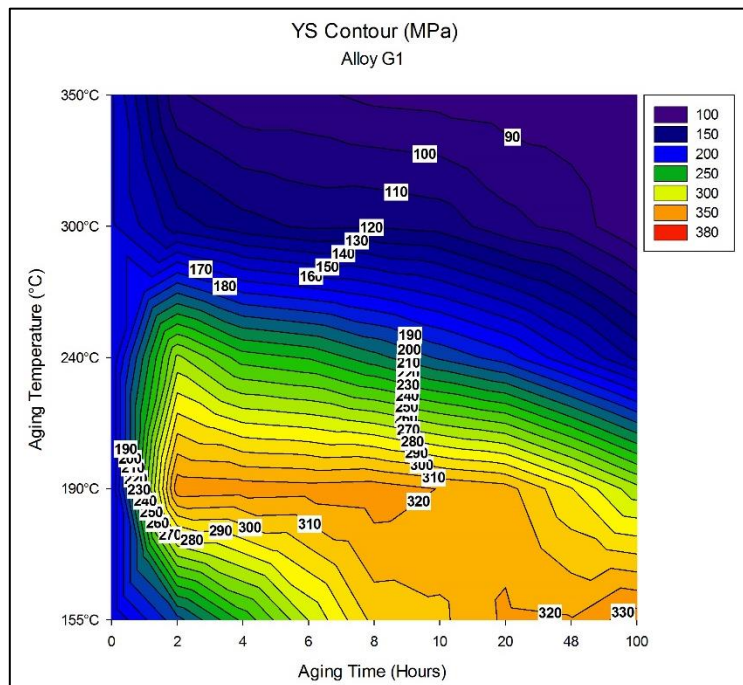


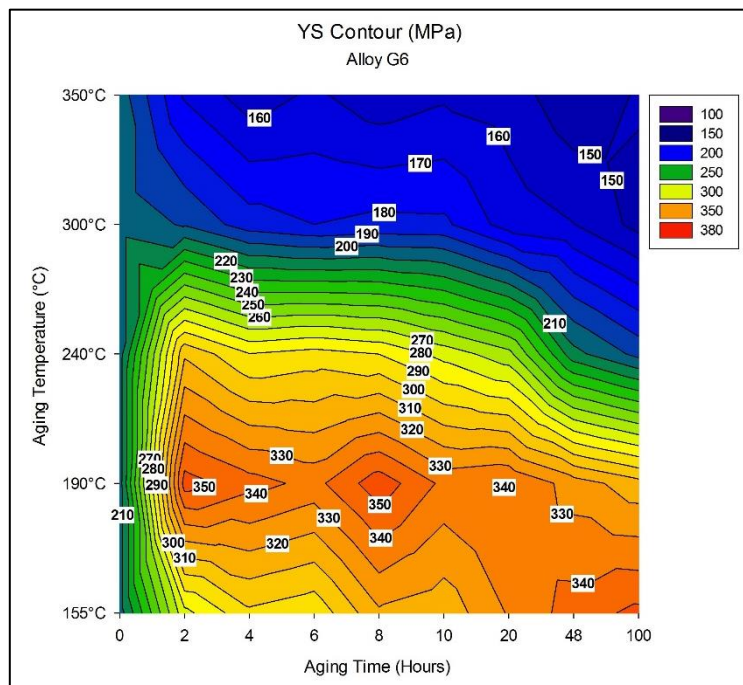
Figure 5.46 Quality chart generated using Equations 1 and 2 showing the tensile properties and the quality indices (Q) of G7 (2wt% Ni + 0.25wt% Zr, no Cu) alloy test bars in the as-cast, solution heat-treated, and aged conditions (at the five aging temperatures used and aging times of 2, 10, and 100 hours).

Higher magnesium levels increase the number of Mg-Si precipitates which form during aging. These precipitates strengthen the aluminum matrix by stressing the atomic lattice, making dislocation movement difficult thereby increasing the yield strength (significantly) and the ultimate tensile strength of the material. As the yield strength is increased to a greater extent than ultimate tensile strength, ductility is reduced. At specific magnesium levels, magnesium can also combine with iron to form π phase. As detailed earlier, the π phase particles adversely affect ductility as they assist in crack propagation. The π phase is also detrimental in that it removes magnesium from solution, decreasing Mg-Si precipitation. Both these features may contribute to the levelling off of mechanical properties at higher magnesium levels.

Figure 5.47(a to c) shows the yield strength (YS) color-contour maps for alloys G1, G6, and G7, respectively. These maps reveal that the strength, particularly the yield strength, shows a significant increase with the progress in aging time, ~60 MPa and ~40 MPa, respectively, compared to that noted for alloys G1 and G6.



(a)



(b)

Figure 5.47 Cont.

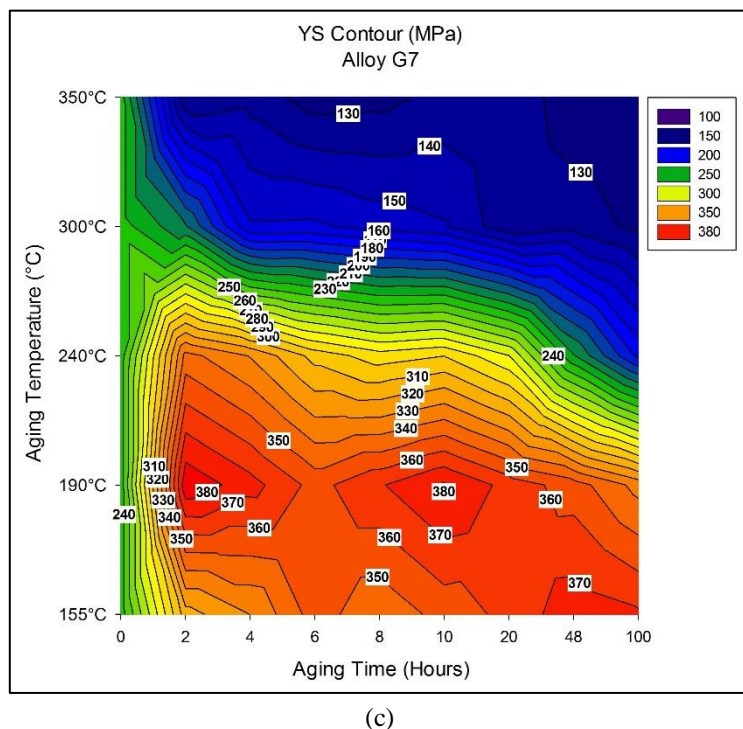


Figure 5.47 Yield strength-color contour charts for alloys G1, G6 (2wt% Ni + 0.25wt% Zr), and G7 (2wt% Ni + 0.25wt% Zr, no Cu) comparing the effect of aging conditions.

5.7.4 AGING BEHAVIOR OF ALLOY G8 (0.75wt% Mn + 0.25wt% Zr)

Figure 5.48 shows the tensile properties of alloy G8 (containing 0.75% Mn and 0.25% Zr) for the aging times and five aging temperatures applied. The aging times required to reach peak strength were determined to be 48 h at 155°C, 2 h and 20 h at 190°C, and 2 h thereafter, at each of the three higher aging temperatures, respectively. Aging at 155°C results in an increase in the tensile strength up to peak-aging which occurs at 48 h, accompanied by a reduction in ductility which may be attributed to the dispersion of massive Fe-rich phase particles throughout the matrix, in addition to the formation of the age-hardening compounds.⁴⁹ Any further increase in aging time produces overaging, where

the strength starts diminishing and the ductility begins to increase. The UTS, YS, and %El at peak-aging at 155°C are 411 MPa, 367 MPa and 1.40% respectively, while those obtained at peak-aging upon increasing the aging temperature to 240°C are 371 MPa, 355 MPa and 1.75%, respectively, after 2 h of aging. It is interesting to observe the rapid decline in yield strength at this temperature, whereas at 190°C, the yield strength is more or less stable, as are the tensile strength and ductility, across the range of aging times used. Thus, with respect to alloy G8, an aging temperature of 190°C appears to be the best heat treatment choice from the application point of view.

The highest decrease in tensile strength is also observed at 240°C, going from 371 MPa at 2h to 309 MPa at 100 h, with a corresponding increase in ductility from <2% after 2 h to ~4.5% at 100 h. At 300°C and 350°C aging temperatures, the greatest mechanical deterioration is expected to be observed after less than 2 h of aging treatment. This assumption is based on a consideration of the tensile properties of the alloy upon solution heat treatment, namely, 328 MPa UTS and 203 MPa YS, implying that the overaged samples tend to lose between 15% and 40% of their original strength within the first 2 hours of being subjected to aging at these temperatures. With regard to ductility, the %El values decrease from ~4% in the solution heat-treated condition to about 1%, as the aging temperature changes from 155°C to 190°C, as shown in Figure 5.48. Above 190°C, the ductility increases as the aging temperature increases, the highest ductility values being observed at 350°C, in the order of ~5%.

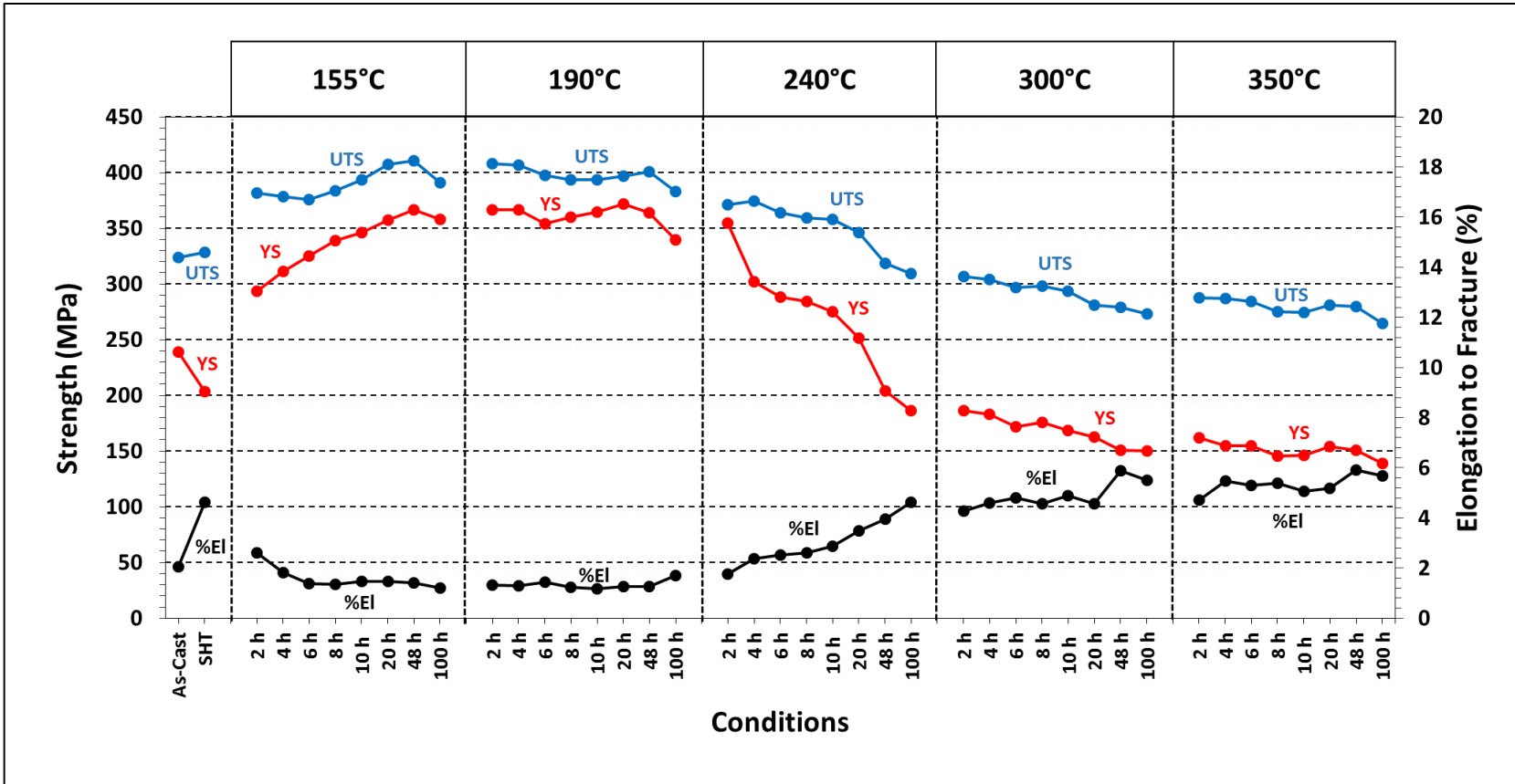


Figure 5.48 Variation in UTS (MPa), YS (MPa), and %El observed in alloy G8 (0.75wt% Mn + 0.25wt% Zr) as a function of aging conditions.

The best combinations of properties are achieved at the aging temperatures of 155°C and 190°C, after 48 h, and after 2 h and 20 h at the two temperatures, respectively. These conditions may therefore be considered as the appropriate T6 heat treatment for 357-type alloys having the same composition (Mn and Zr additions) as alloy G8.

Figure 5.49 shows the quality index chart for the 17 selected heat treatment conditions for alloy G8. In this Figure 5.49, the general mechanical behavior of alloy G8 appears to be similar to that of the base alloy G1, and alloys G6 and G7 at aging temperatures above 190°C. It will be observed that, below aging temperatures of 240°C, the quality index of alloy G8 decreases. The chemical composition of 354 casting alloys contains three hardening elements, namely, copper, magnesium and silicon. The application of an aging treatment to these alloys causes an entire range of precipitates to form according to the temperature and time applied.

The aging behavior observed when applying aging temperature at 155°C is related to the precipitation of the Cu- and Mg-containing phases. The features of these precipitates vary according to the aging time applied to the casting. The aging curves in the case of aging at high temperatures display curvilinear forms. This specific form of the aging curves is a result of the overaging conditions, which occur upon increasing the aging time for duration longer than the specified peak-aging times with respect to each temperature. A further increase in the aging time results in a decrease in the alloy strength and quality, an increase in the ductility at 240°C, 300°C and 350°C, respectively.

The increased ductility has compensated for the decreased strength in Equation 1, thus, the overall quality does not display any significant change within this range of time. Such a decrease in strength and increase in the ductility of the alloy is related to the softening which occurs as a result of the overaging conditions at which the equilibrium precipitates form, leading to the loss of the coherency strain between the precipitates and the matrix. In addition, the overaging result in the continuous growth of the large precipitates at the expense of the smaller ones, ultimately leading to the coarser precipitates with less density in the metal matrix having large inter-particle spacing.¹⁷

Figure 5.50(a) and (b) show the yield strength (YS) color-contour maps for alloys G1 and alloy G8, respectively. These maps also reveal that, as in the case of alloy G6 and G7, the yield strength significantly increase (~45 MPa) with the progress in aging time compared with that of the base alloy.

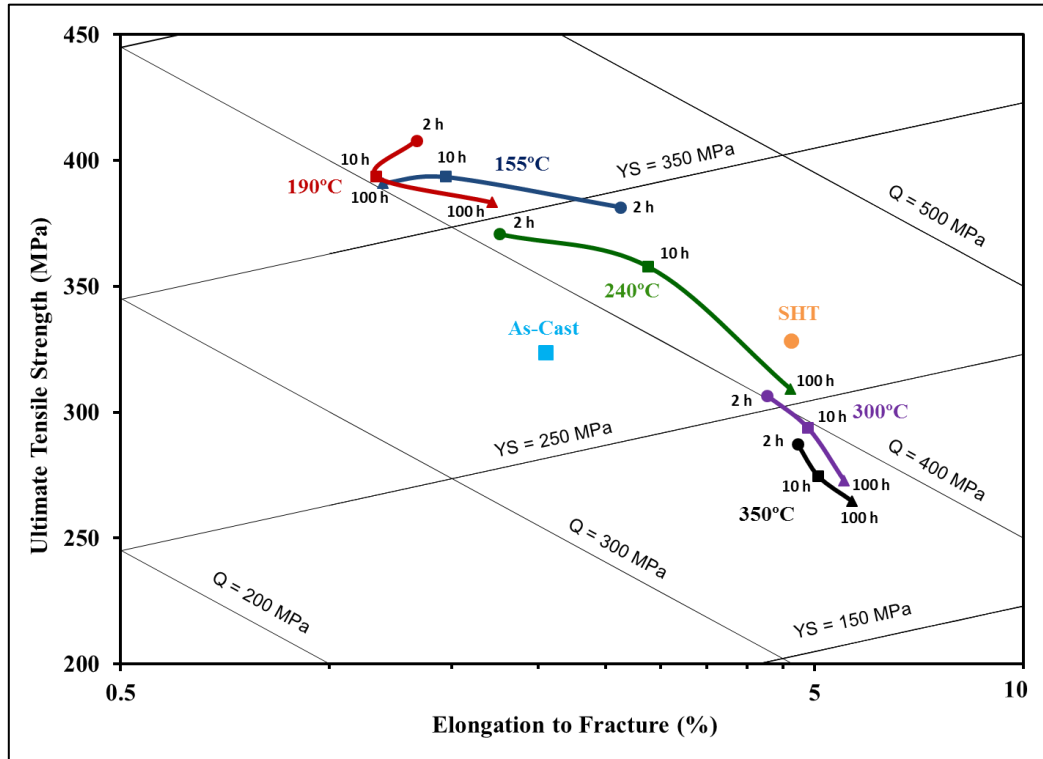


Figure 5.49 Quality chart generated using Equations 1 and 2 showing the tensile properties and the quality indices (Q) of G8 (0.75wt% Mn + 0.25wt% Zr) alloy test bars in the as-cast, solution heat-treated, and aged conditions (at the five aging temperatures used and aging times of 2, 10, and 100 hours).

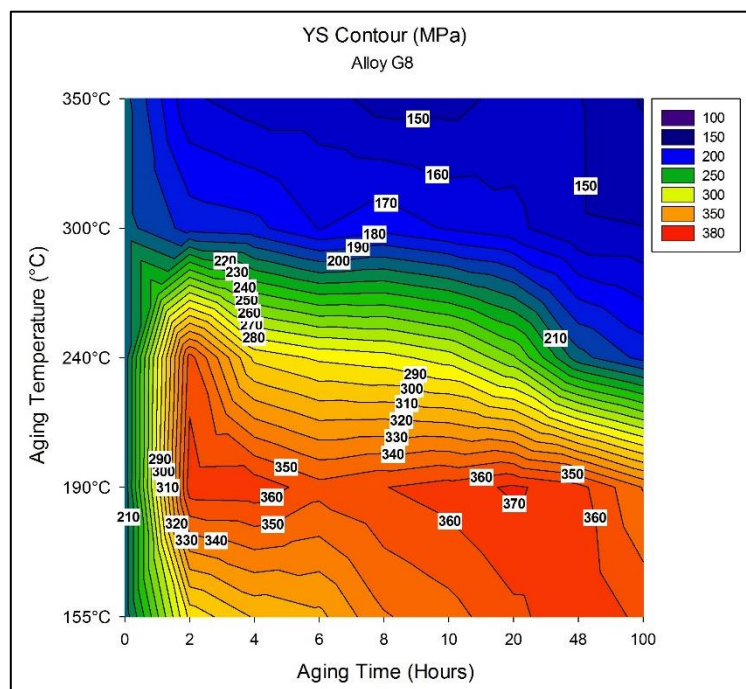
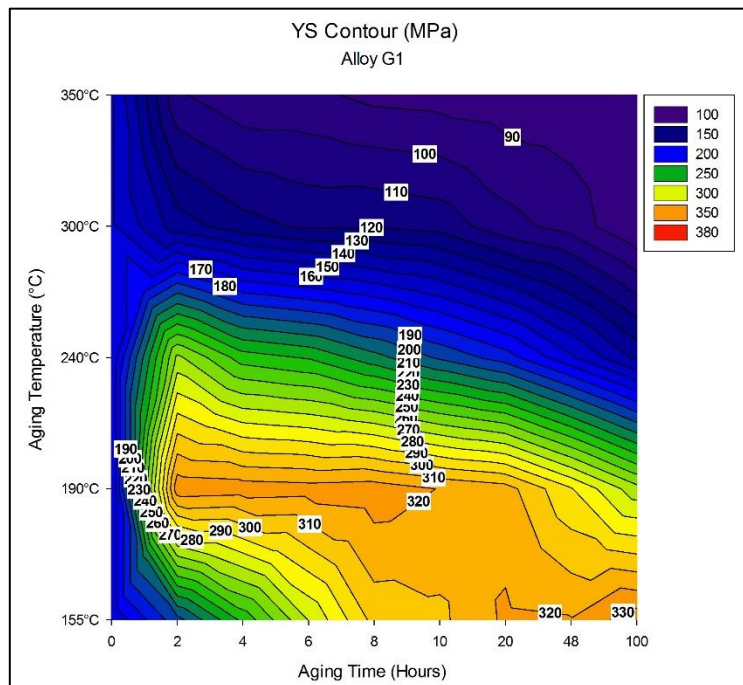


Figure 5.50 Yield strength-color contour charts for the base alloy G1 and alloy G8 (0.75wt% Mn + 0.25wt% Zr), comparing the effect of aging conditions.

5.7.5 AGING BEHAVIOR OF ALLOY G9 (2wt% Ni + 0.75wt% Mn + 0.25wt% Zr)

Figure 5.51 shows the tensile properties of alloy G9, containing 2wt% Ni, 0.75wt% Mn, and 0.25wt% Zr at the different aging times and temperatures employed for the heat treatment, where the aging times required to reach the peak strength are 100 h at 155°C, 4 h at 190°C, and 2 h thereafter at higher aging temperatures, respectively. As mentioned previously, the yield strength curve was used to determine the peak-aging time for each temperature.

The maximum tensile strength was obtained at 155°C/2h, ~380 MPa, with the UTS displaying an overall average of ~368 MPa over the remaining holding times at this temperature. Likewise, a similar average UTS value of ~368 MPa was obtained at the 190°C testing temperature, for holding times of 4 h, 6 h, 8 h, 10 h, 20 h, and 48 h. As Figure 5.51 reveals, the greatest mechanical stability for the aging treatments is observed at 155°C and at 190°C. Considering the yield strength value in the solution heat-treated condition, in conjunction with the artificial aging conditions used, it was possible to increase the YS value by more than 150 MPa. The maximum yield strength was reached after 100 h at 155°C, and after 4 h at 190°C aging temperature, (364 MPa and 357 MPa, respectively). The greatest decrease in YS may be observed at 240°C, which shows a sharp decline with increase in aging time, going from 317 MPa at 2 h to 216 MPa at 100 h.

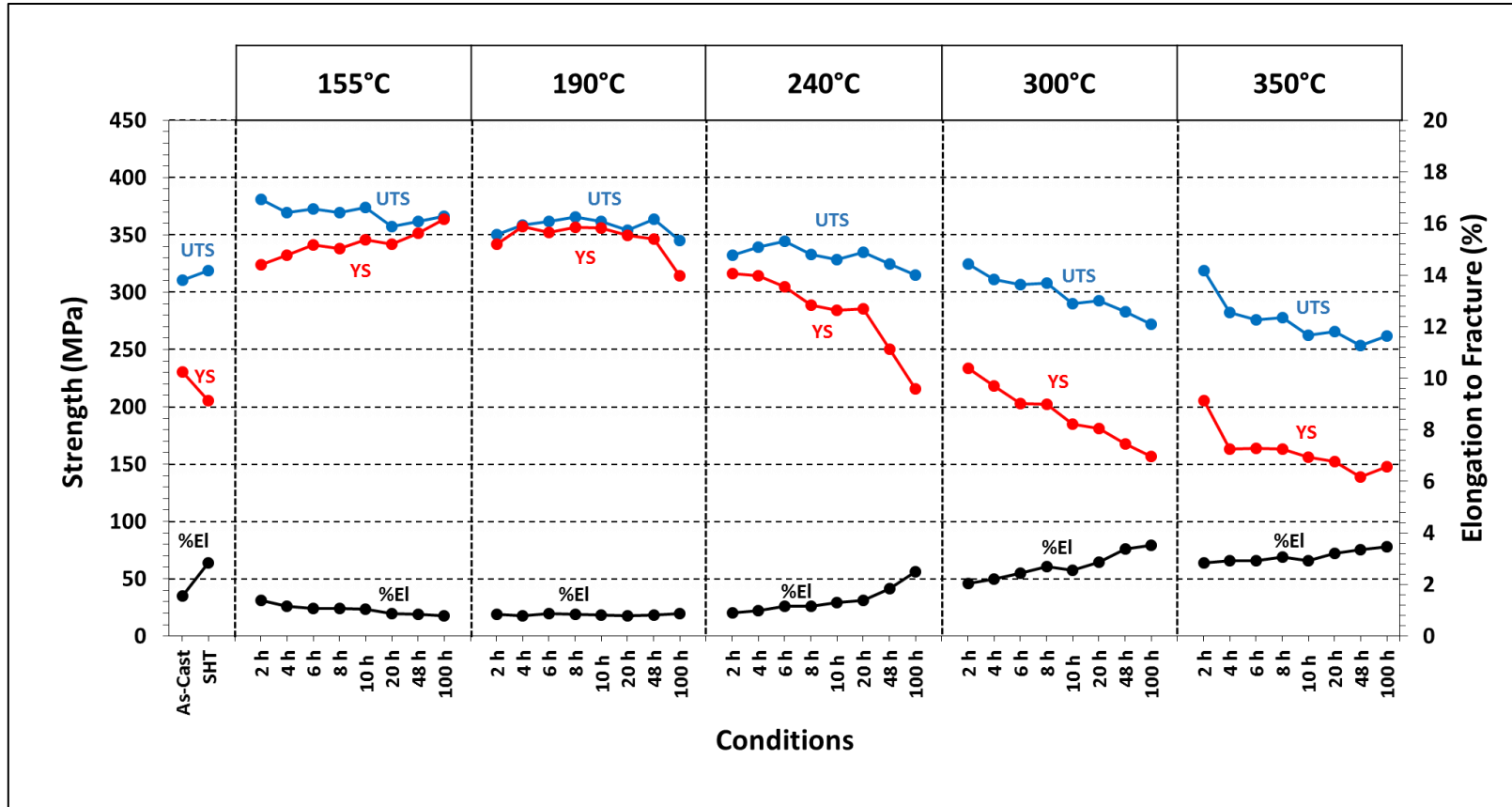


Figure 5.51 Variation in UTS (MPa), YS (MPa), and %El observed in alloy G9 (2wt% Ni + 0.75wt% Mn + 0.25wt% Zr) as a function of aging conditions.

Likewise, the UTS also decreases, going from 332 MPa at 2 h to 315 MPa at 100 h at 240°C, with a corresponding increase in ductility from ~1% to about 2.5% over the same range of aging times. Overall, the yield strength behavior appears to be the most stable at 190°C aging temperature, showing a variation of ~15 MPa in yield strength values for aging times between 2 and 48 h. The best combination of properties is achieved after aging at 190°C for 4 h and the corresponding properties observed are 359 MPa UTS, 357 MPa YS, and 0.80%El. This condition may therefore be considered as the appropriate T6 heat treatment for alloy G9 of 354-type alloys containing additions of Ni, Mn, and Zr.

As will be seen from Figure 5.51, ductility displays values ranging from 1 to 3.5%, where any value greater than 3% is considered high when considering the ductilities normally exhibited by hypoeutectic Al-Si alloys.⁴⁶ The ductility behavior of alloy G9 shows a decrease in %El values on going from 155°C to 190°C, as shown in Figure 5.51. Lower ductility values are observed for alloy G9 at 190°C than those displayed by the G1 base alloy at the same aging temperature, over all aging times used. The maximum ductility values are obtained between the 300°C and 350°C aging temperatures as, once past the point of peak aging, softening occurs. It is seen that the presence of 2wt% Ni in alloy G9 has a limited effect on the tensile properties after solution heat treatment and aging, presenting similar strength and a lower ductility compared with alloy G6 which contains the same 2wt% Ni and 0.25wt% Zr additions but no Mn.

The higher iron and magnesium levels in this alloy compared to the base alloy increase the number and size of iron-containing intermetallics namely β and π phases. The

β phase is very detrimental as it is large in size, may have a large aspect ratio and is brittle. These features facilitate crack initiation and the propagation of cracks through the matrix thereby reducing ductility, compared to the base alloy and the other alloys studied in this work. The ultimate tensile and yield strengths are not affected as much as ductility, as the particles mainly influence/affect crack growth after the material has yielded. The π phase, although also large, has a much more compact morphology than the β phase and is therefore less detrimental. It does, however, occupy a larger volume fraction for equivalent amounts of iron.⁸¹

Figure 5.52 shows the quality index chart for the 17 selected heat treatment conditions for alloy G9. In his studies on the tensile properties and quality indices of Al-Si-Cu-Mg and Al-Si-Mg alloys, Ammar¹⁷ reported that aging time up to peak strength does not affect the quality index values. The application of an aging treatment to such alloys causes an entire variety of precipitates to form according to the temperature and time applied. Such an observation is related to the fact that increasing the aging time up to 100 h at low aging temperature, results in a continuous increase in the strength of the casting at the expense of its ductility, although the increase compensates for the reduction in ductility in accordance with Equation 1.

With regard to the influence of aging time and temperature, it may be noted from the quality charts shown in Figure 5.43, Figure 5.46, Figure 5.49, and Figure 5.52 that a prolonged aging time decreases the strength and the quality index values of these alloys significantly. The aging behavior observed at 155°C is related to the precipitation of the

Cu- and Mg-containing phases in the metal matrix. The features of these precipitates vary according to the aging time applied to the castings. The formation of coherent precipitates is the main source of strengthening in the 354 casting alloys and leads to an increase in strength to a maximum level at 155°C/100h and 190°C/4h which, in this case, is considered to be the peak-aging time for these alloys. It should be noted that peak-strength may also be attained in the presence of both coherent and semi-coherent precipitates. The semi-coherent precipitates which may be present in the peak-aged conditions are the needle-like β' (Mg_2Si), the plate-shaped θ'' (Al_2Cu), and the lathlike S' (Al_2CuMg) phases.¹⁷⁻²⁰

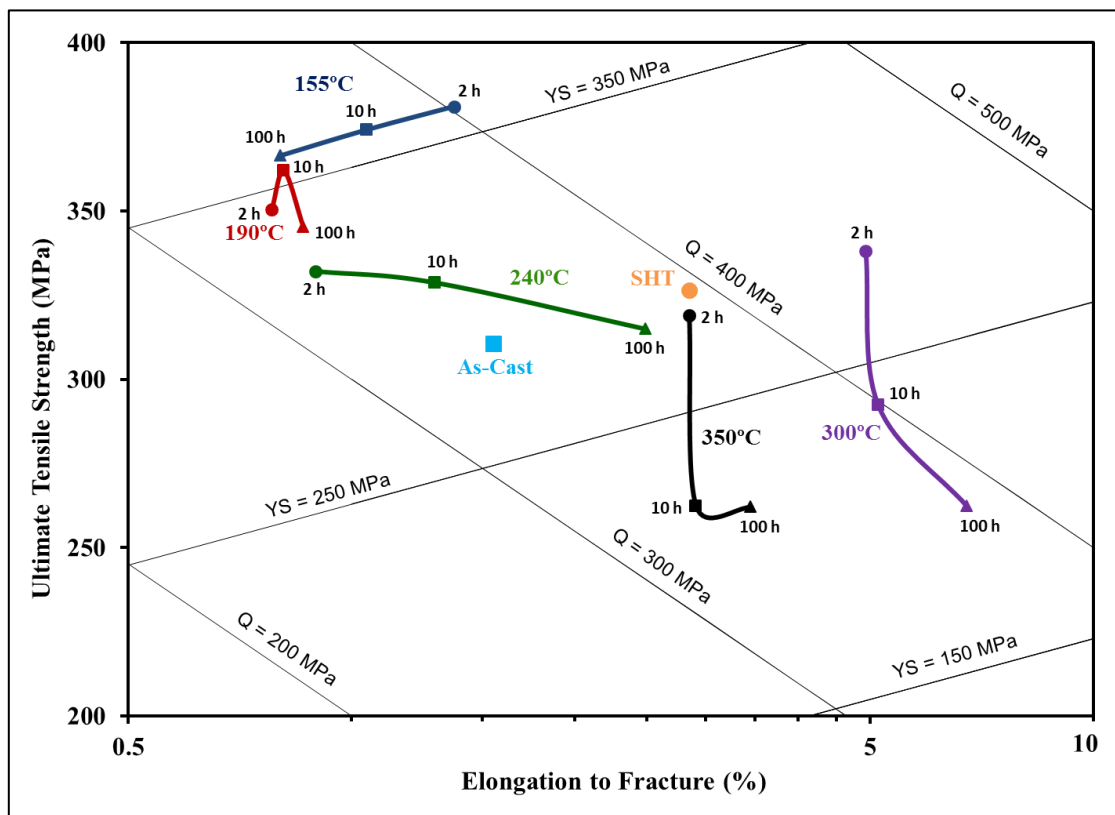
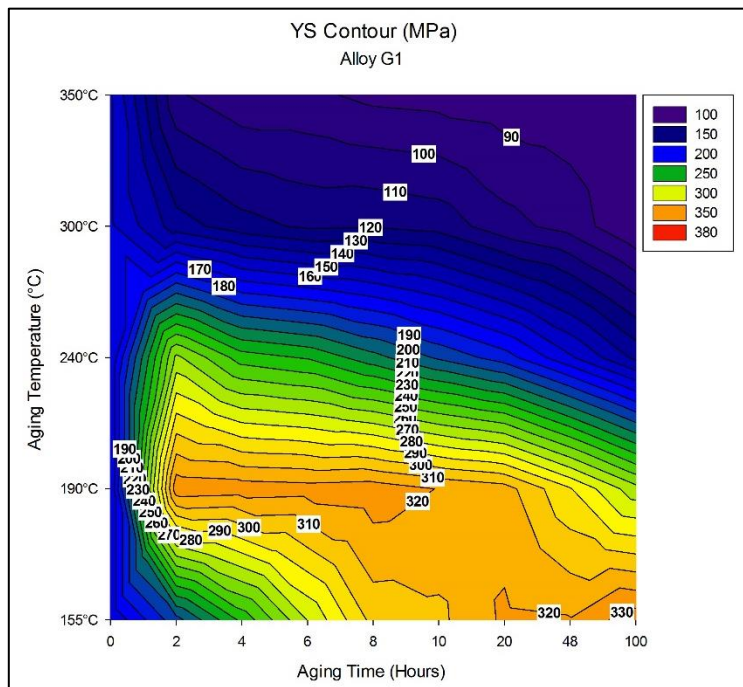


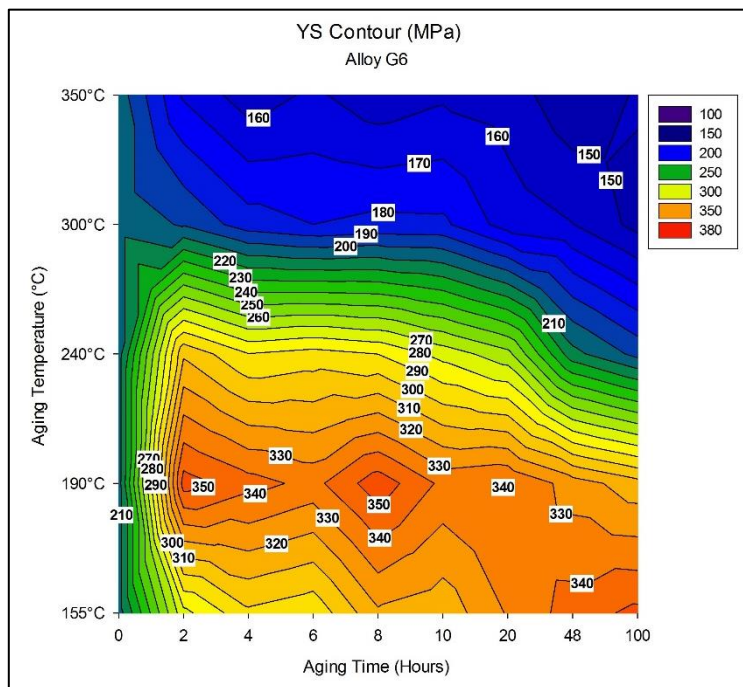
Figure 5.52 Quality chart generated using Equations 1 and 2 showing the tensile properties and the quality indices (Q) of G9 alloy test bars in the as-cast, solution heat-treated and aged conditions (at the five aging temperatures used and aging times of 2, 10, and 100 hours).

Increasing the solidification rate reduces the size of microstructural constituents and features including the eutectic silicon and intermetallic phases; this makes propagation of a crack through the material more difficult, thereby increasing elongation in particular but also ultimate tensile strength.^{81, 91} Changing the aging condition from under-aged to peak-aged increases the size of the Mg-Si precipitates formed, which then increases the stress on the atomic lattice, making dislocation movement more difficult. The ultimate tensile strength and yield strength of the material are increased, however, the ductility is reduced as the material has less ability to yield plastically.^{81, 102} With increasing magnesium, the morphology and composition of the iron intermetallics change. These microstructural changes result in altering the behavior by which the material deforms and fractures.

Figure 5.53(a to e) compares the yield strength (YS) color-contour maps for alloys G1, G6, G8, and G9. On comparing the four color-contour charts shown in Figure 5.53, an increase in the strength of alloy G9 was observed in comparison with the base alloy G1 and G6, as indicated by the color/intensity of the chart at certain aging conditions. A decrease in YS is observed with the addition of 2wt% Ni compared with the alloy G8, which does not contain Ni. This decrease in strength through the addition of Ni, is related to the interaction between copper and nickel to form precipitates of Al_3CuNi in the microstructure.^{19, 20, 152, 199, 271} The Al_3CuNi phase was detected in the thermal analysis experiments. Since copper, as well as magnesium, determine the precipitation strengthening of Al-Si-Cu-Mg alloys, the available copper would form Al_2Cu precipitates through the solution heat/treatment/quenching/aging process (except at the highest aging temperatures), thereby strengthening the cast alloys.

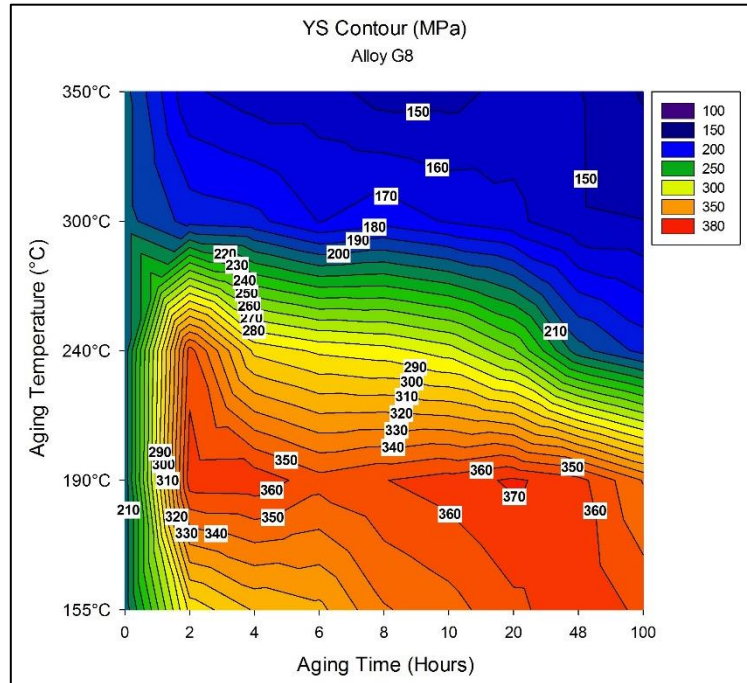


(a)

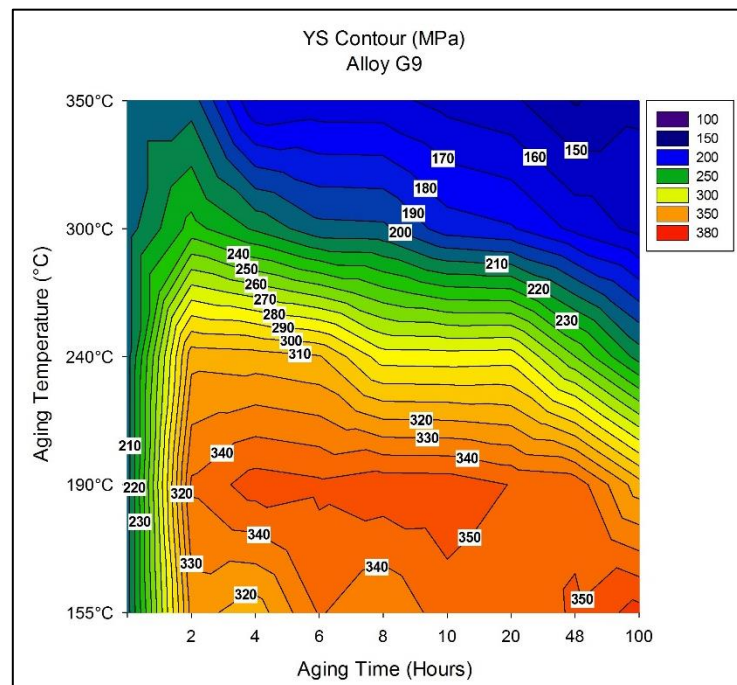


(b)

Figure 5.53 Cont.



(c)



(d)

Figure 5.53 Yield strength-color contour charts for alloys (a) G1; (b) G6; (c) G8; and (d) G9 comparing the effect of aging conditions.

The formation of Al-Cu-Ni precipitates would thus subtract part of the copper content available for strengthening; this is the principal reason why a slight decrease in yield strength is observed with the addition of 2wt% Ni to alloy G9

5.7.6 AGING BEHAVIOR OF ALLOY G10 (0.15wt% Sc + 0.25wt% Zr)

Figure 5.54 shows the tensile properties of alloy G10 for the aging times and temperatures applied during heat treatment. For this alloy, the aging times required to reach peak strength are 48 hours at 155°C, and 2 hours thereafter, at higher aging temperatures. It may be observed that a combined addition of 0.25wt% Zr with 0.15wt% Sc has a beneficial effect on the alloy strength.⁹² In particular, the as-cast properties of alloy G10 show a considerable improvement over those obtained for the base alloy. Figure 5.54 shows that the ductility improves from 2 to 5% with solution heat treatment.

With increase in the aging temperature above 155°C, the time required to reach peak aging is reduced to 2 hours, whereupon over-aging sets in and the alloy begins to soften, with a continuous decline in strength and a corresponding increase in ductility. The lowest values of ductility observed for alloy G10 were obtained at 190°C aging temperature at the different aging times. At 350°C, the alloy is completely softened, exhibiting the lowest strength and highest ductility values, in the range of ~6%. Of interest to note is that all three properties are more or less constant across the range of aging times studied.

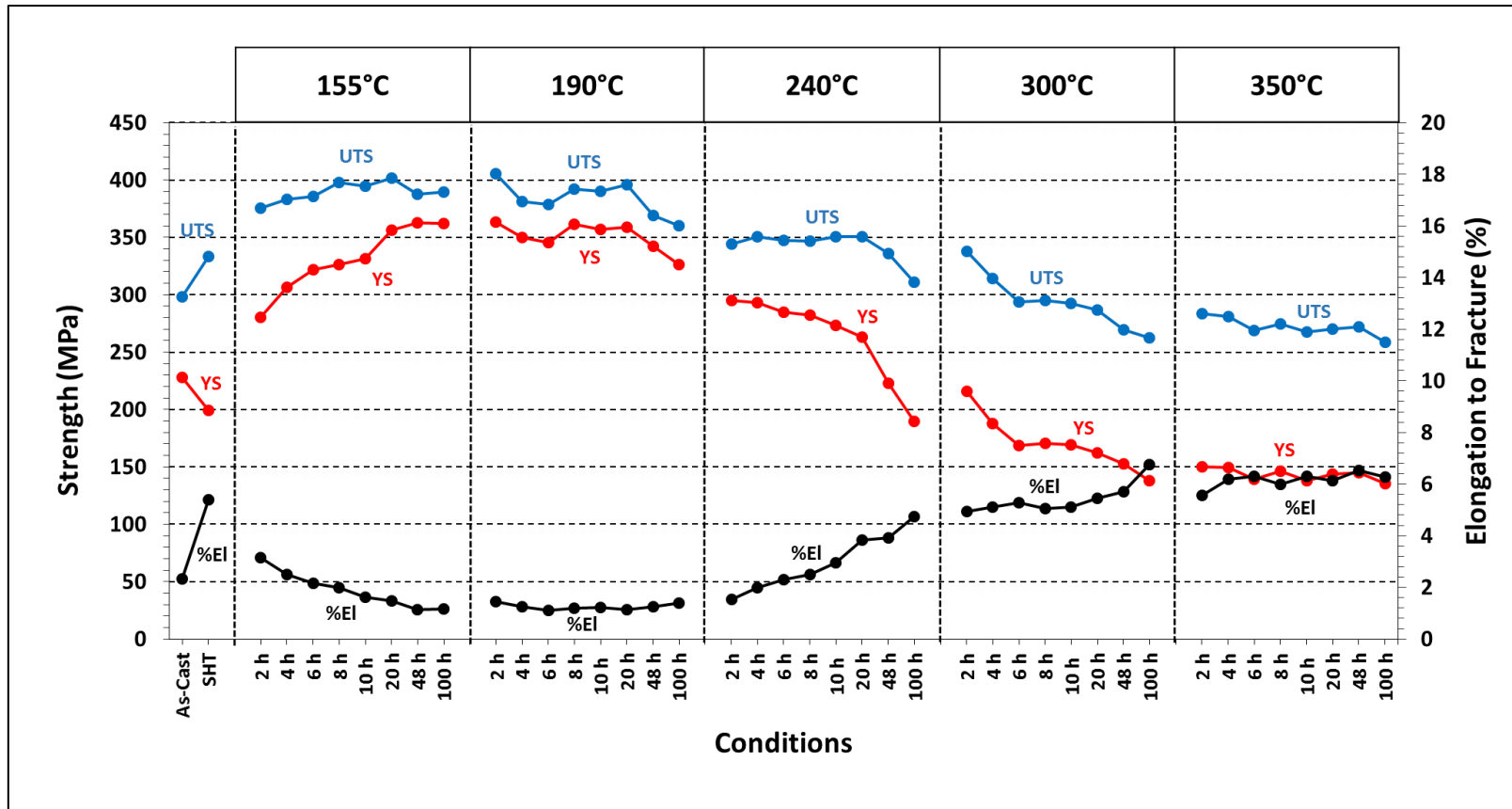


Figure 5.54 Variation in UTS (MPa), YS (MPa), and %El observed in alloy G10 (0.15wt% Sc + 0.25wt% Zr) as a function of aging conditions.

The best combination of properties is achieved after aging at 190°C for 2 h and the corresponding properties observed are 405 MPa UTS, 363 MPa YS, and 1.45 %El. This condition may therefore be considered as the appropriate T6 heat treatment for the alloy G10 containing additions of Sc and Zr.

The combined addition of Zr and Sc increases the yield strength of the as-cast G10 alloy compared to that of the as-cast base alloy G1 (~235 MPa vs. ~155 MPa); the YS then decreases subsequently after solution heat treatment. The increase and decrease in yield strength are attributed respectively to the formation of transition-elements dispersoids, followed by their rapid coarsening during solution heat treatment. Zirconium additions are known to increase the ambient temperature tensile strength and recrystallization resistance of Al(Sc) alloys. Additions of Sc and Zr to commercial 2618 (Al-Cu-Mg-Fe-Ni), 5083 (Al-Mg-Mn), and 5754 (Al-Mg-Mn) aluminum alloys have been shown to increase the tensile strength over Zr-free alloys, an effect attributed to the pinning of grain- and subgrain-boundaries by the highly stable $\text{Al}_3(\text{Sc}_{1-x}\text{Zr}_x)$ precipitates.^{172, 179, 183}

Aging at higher temperatures introduces a technologically useful strategy for this particular alloy system in that, with the noticeable reduction in aging time to reach peak strength (only 2 hours), a significant economic gain is achieved in the form of several benefits including lower energy consumption, longer lifetime for the heating furnaces, greater productivity, lower labor costs, and a number of other analogous advantages.

Figure 5.55 shows the quality index chart for the 17 selected heat treatment conditions for alloy G10. In this figure, the general mechanical behavior of alloy G10

appears to be similar to that of the alloy G8 containing 0.75wt% Mn and 0.25wt% Zr. It is known that the simultaneous addition of Sc and Zr has a more pronounced effect than if either of these elements is added alone; the effect of a simultaneous addition of Sc and Zr is evidently favorable.^{152, 158} Minor Sc and Zr combined additions affect not only as-cast grain refinement of the microstructure but also the softening process. Figure 5.56 shows the yield strength (YS) color-contour maps for the base alloy G1 and alloy G10, respectively. It may be observed that, compared to the base alloy, the yield strength of alloy G10 shows a significant increase with the progress in aging time.

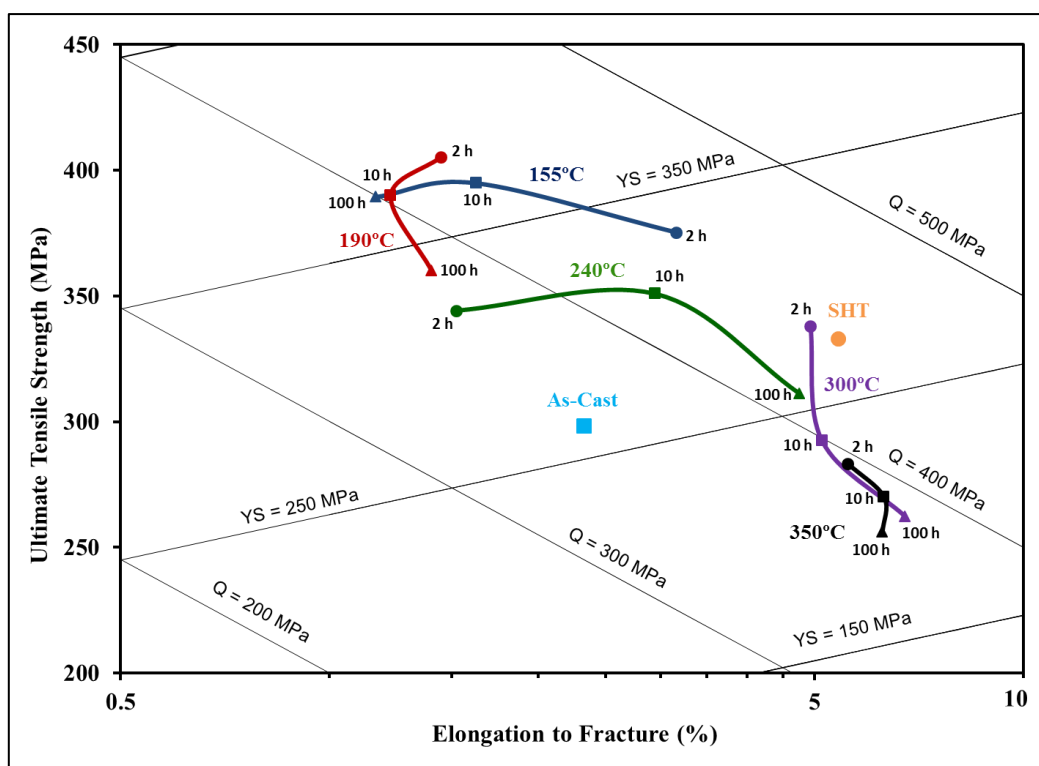


Figure 5.55 Quality chart generated using Equations 1 and 2 showing the tensile properties and the quality indices (Q) of G10 (0.15wt% Sc + 0.25wt% Zr) alloy test bars in the as-cast, solution heat-treated and aged conditions (at the five aging temperatures used and aging times of 2, 10, and 100 hours).

The addition or presence of scandium and zirconium has an observable effect on the precipitation process from a number of aspects; the Al_3Sc and Al_3Zr dispersoids provide heterogeneous nucleation sites for the age-hardening phase. The Zr additions produce a refined non-dendritic structure, which in turns reduces the porosity level and the amount of the undissolved Al_2Cu , thus improving alloy strength.⁹²

The aging curves in Figure 5.54 at high temperatures display curvilinear forms. This specific form of the aging curves is a result of the overaging which occurs upon increasing the aging time for durations longer than that required for peak-aging with respect to each temperature. A decrease in strength and increase in the ductility of the alloy is related to the softening which occurs as a result of such overaging conditions at which the equilibrium precipitates form, leading to the loss of the coherency strain between the precipitates and the matrix. In addition, overaging results in the continuous growth of the large precipitates at the expense of the smaller ones, ultimately leading to coarser precipitates with less density in the metal matrix, and having large inter-particle spacing. All these changes which accompany overaging contribute to the decrease in the strength of the casting, and thereby to an increase in the ductility.

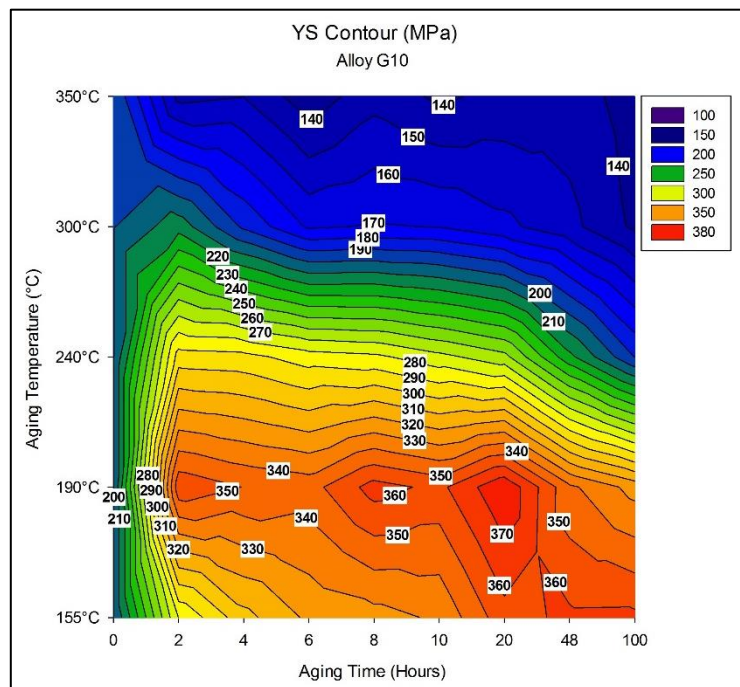
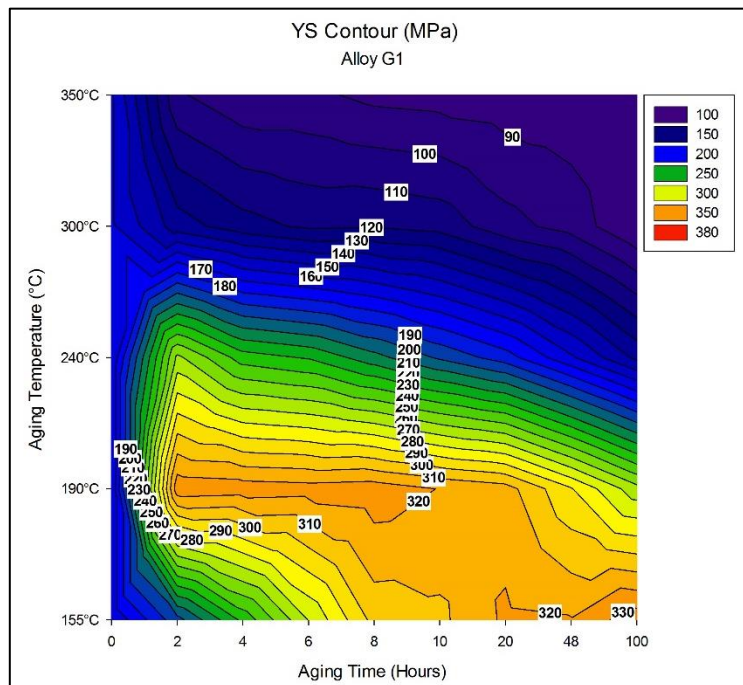


Figure 5.56 Yield strength-color contour charts for the base alloy G1 and alloy G10, comparing the effect of aging conditions.

5.7.7 QUALITY INDEX CHARTS: COMPARISON BETWEEN AGING BEHAVIORS OF ALLOY G1, AND ALLOYS G6 THROUGH G10

Figure 5.57 through Figure 5.61 show a comparison between the aging behaviors of the six alloys observed at each aging temperature for the three specified aging times of 2, 10, and 100 hours. The quality chart shown in Figure 5.57 illustrates the strength and the quality indices obtained for the base alloy G1 and for alloys G6 through G10 at 155°C aging temperature; Figure 5.58 compares the aging behavior at 190°C for the same aging times, while the quality charts shown in Figure 5.59 through Figure 5.61 compare the aging behaviors of the alloys at 240°C, 300°C, and 350°C aging temperatures, respectively.

An associated increase in the volume fraction of intermetallics is expected with an increase in the iron content. As a result, the detrimental influence of the β -phase on the strength and quality of the castings will become apparent the quality charts.¹⁷ The effects of Fe-content on the strength, ductility, and quality of aluminum castings have been reported and discussed in a number of earlier studies^{78, 130, 147} in which these effects were also evaluated by using quality charts. The results obtained in the present study are in agreement with those obtained in these previous studies. Thus, reducing the iron level in 354 type alloy castings may be considered an engineering objective and is to be recommended strongly for the purposes of developing greater strength and optimum quality values in such castings.

The ultimate tensile strength (UTS) is normally used for the specification and quality control of the casting, while the ductility of the casting, expressed as percent elongation to fracture, is usually used as an indicator of casting quality because of its

sensitivity to the presence of any impurity or defect in the cast structure.^{28, 102} On the other hand, yield strength does not represent the quality of the casting since it is a material property which is not affected by the level of defects or impurities present in the casting, but is influenced, rather, by the movement of dislocations in the casting structure, and depends on the resistance expected by the hardening precipitates against the moving dislocations.¹⁷ In general, therefore, quality charts provide a simple tool for estimating and recommending the appropriate processing conditions to obtain specified properties and hence to facilitate the selection of castings to meet these specifications.

According to the studies carried out by Andrade-Gonzalez²³⁷ and Tavitas-Medrano²⁴⁹ for 319 alloys under similar conditions as those prevailing in the present work, the structural changes during the age-hardening process are, in reality, not so easy to distinguish. With an increase in either aging temperature or time, different decomposition and precipitation processes occur, in some cases sequentially and, in others, simultaneously. These precipitation processes may be illustrated in detail after examining the 319 alloys used. In these alloys, five stages of structural changes were determined during the heat-treating operations, as summarized in Table 5.3.²³⁷

Table 5.3 Age-Hardening Behavior of Al-Si-Cu-Mg alloys²³⁷

Stage	Heat Treatment	Phases
I	None	Mostly precipitated as equilibrium CuAl_2 phases
II	Solution treatment at 500°C and rapid cooling	All Cu in solution Most Mg phases in solution
III	Natural aging at room temperature	Segregation into GP I zones (coherent)
IV	Age-hardening at 180°C	Dissolution of GP I zones Segregation into GP II zones (coherent) Precipitation of S' phase (CuAl_2Mg)
	Further age-hardening at 180°C	Increased diffusion into GP II zones and precipitation as θ phase (partially coherent) Precipitation of S' phase (CuAl_2Mg) Precipitation of β'' phase Precipitation of traces of Si
V	Overaging resulting from treatment time too long	Precipitated as θ phase, the equilibrium phase (incoherent)

The first stage represents the structure prior to solution heat treatment. The precipitates may originate either in the cast structure or in any previous thermal treatment. In the second stage, the copper atoms that had precipitated previously are taken into solid solution at 500°C . The solution heat treatment also removes any previous cold work or precipitation hardening. The material is then quenched from the solution treatment temperature to room temperature, developing helical dislocations. During natural aging, the dissociation of the supersaturated solid solution begins by coherent precipitation of copper-rich GP zones only a few atoms thick. These precipitates stress the aluminum lattice, and because of their great number, form a dense network that impedes the movement of dislocations during deformation. The extremely small zones that originate at room temperature are called GP I zones and do not grow further during subsequent artificial aging, but actually re-dissolve in a short time at temperatures between 150 to 200°C ,

leading to a temporary reduction in hardness. This regression suggests that the arrangement of the strengthening atoms after artificial aging is basically different from that after natural aging. Artificial aging at elevated temperatures causes new enrichment of copper atoms in GP II zones soon after the end of the reversion.

As the artificial aging continues at approximately 180-220°C, the formation of a metastable phase, θ , takes place, which corresponds to the equilibrium phase CuAl_2 in composition, but has a different crystal lattice. Maximum hardness is obtained during the appearance of the GP II zones and sometimes for a mixture of GP II, θ' , and a mixture of S' + θ' + β' and precipitating Si.

Although a number of authors^{235, 245} have reported that they observed the Q' phase, these precipitates have electron diffraction patterns which are very close to those of the β'' or β' phase. Also, copper and excess of silicon refine β'' precipitates, while Mg facilitates the formation of the θ' phase instead of θ'' . As soon as only θ' particles are present, the stage of overaging is attained, characterized by a reduction in hardness and strength. When aged for longer times, the equilibrium phase, Al_2Cu , forms a relatively coarse precipitate which is visible under the optical microscope.

The change of phase composition is known to affect the aging response and mechanical properties of the alloy. Impurities and small additions can affect the hardening behavior of Al-Si-Cu-Mg alloys to a considerable extent, mainly due to the binding of main alloying elements in the form of insoluble particles, thereby decreasing the Cu and Mg content in the supersaturated solid solution.

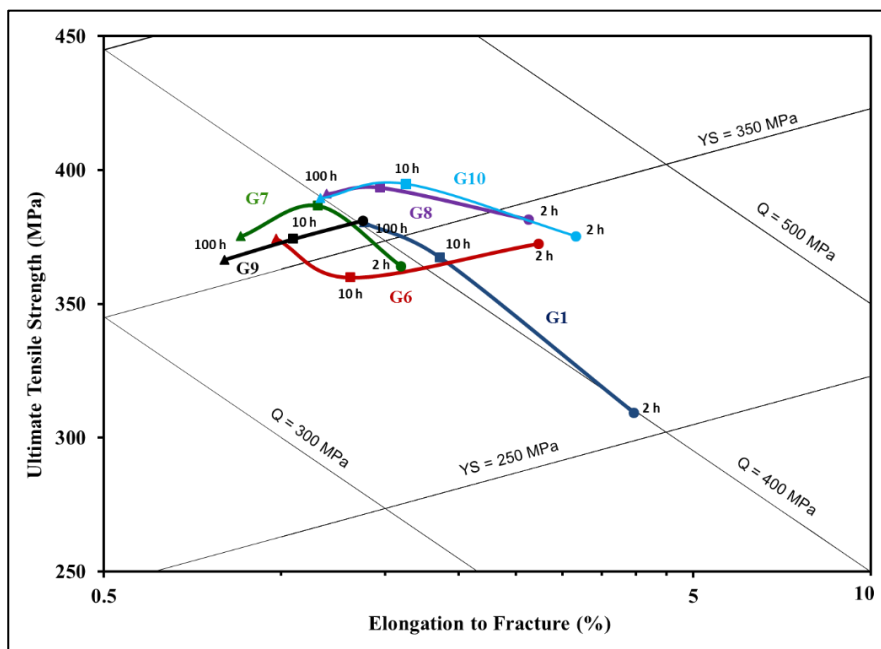


Figure 5.57 Quality chart generated using Equations 1 and 2 to compare the strength and quality of the alloys studied, after aging treatment at 155°C for aging times of 2, 10, and 100 hours.

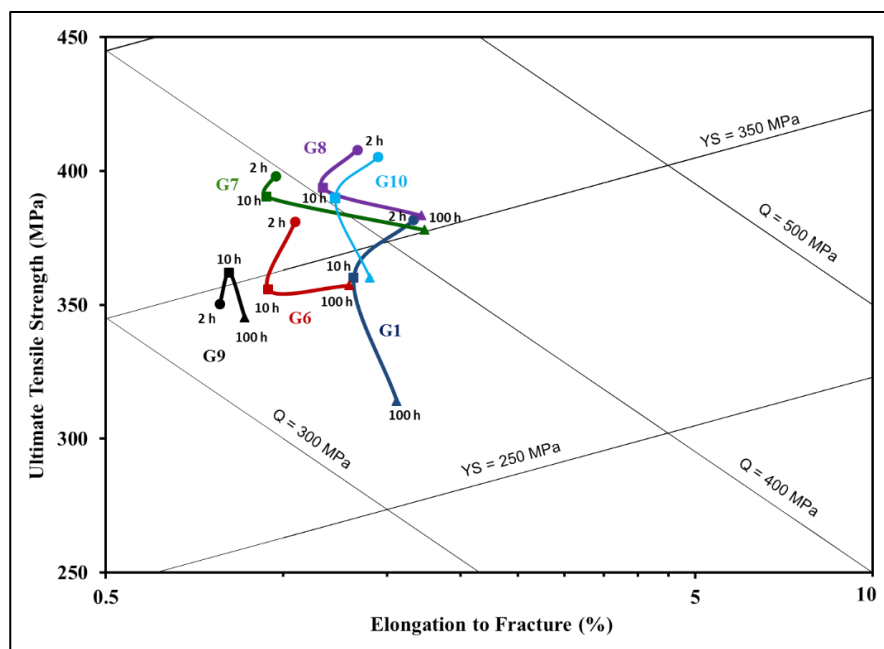


Figure 5.58 Quality chart generated using Equations 1 and 2 to compare the strength and quality of the alloys studied, after aging treatment at 190°C for aging times of 2, 10, and 100 hours.

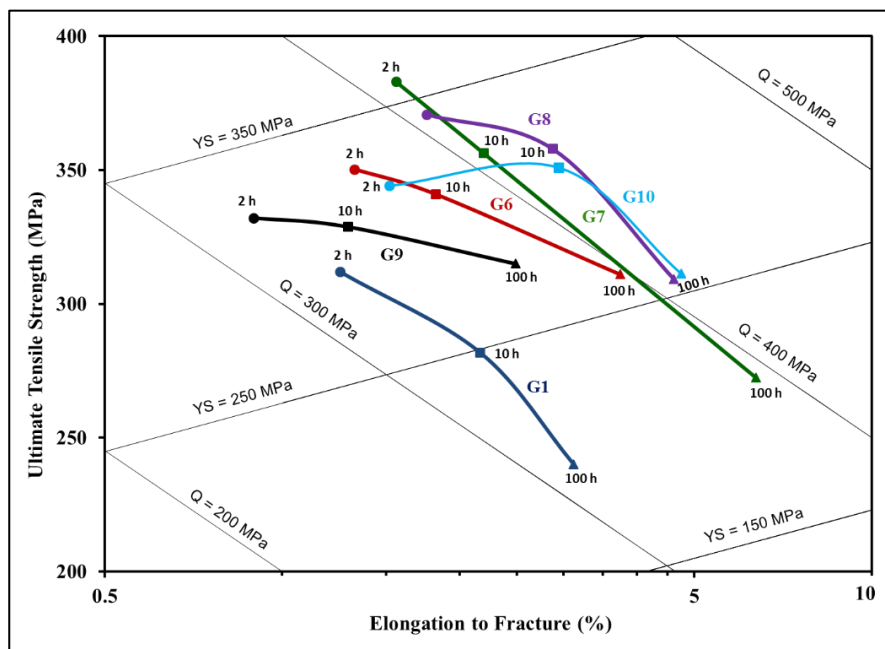


Figure 5.59 Quality chart generated using Equations 1 and 2 to compare the strength and quality of the alloys studied, after aging treatment at 240°C for aging times of 2, 10, and 100 hours.

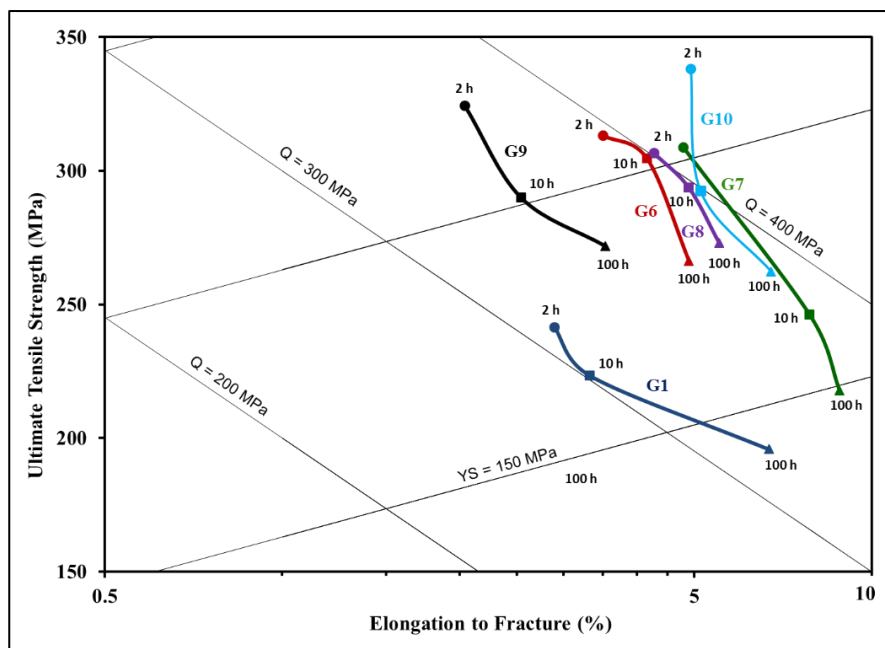


Figure 5.60 Quality chart generated using Equations 1 and 2 to compare the strength and quality of the alloys studied, after aging treatment at 300°C for aging times of 2, 10, and 100 hours.

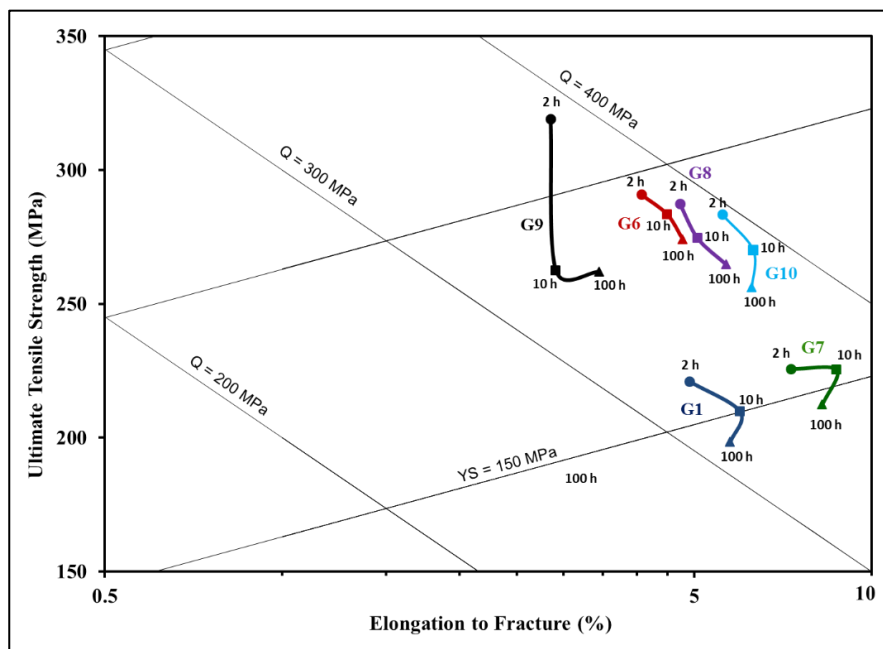


Figure 5.61 Quality chart generated using Equations 1 and 2 to compare the strength and quality of the alloys studied, after aging treatment at 350°C for aging times of 2, 10, and 100 hours.

5.8 STATISTICAL ANALYSIS

Figure 5.62 depicts the tensile properties obtained for alloys G6, G7, G8, G9 and G10 at the 155°C (lowest) and 350°C (highest) aging temperatures, relative to the values obtained for the G1 base alloy, *i.e.*, subtracting the values obtained for the base alloy G1 in each case, and plotted as ΔP values on the Y-axis ($P = \text{Property} = \text{YS, UTS or \%El}$), with the X-axis representing the base line for alloy G1. This approach helps to better visualize the effects and interactions of the various additions used and the different heat treatment conditions, so as to arrive at a better understanding of the effects of Ni, Mn, Sc and Zr on the mechanical properties of 354 casting alloys.

As may be seen from Figure 5.62, additions of these elements improve the alloy performance *i.e.*, the tensile properties at 155°C and 350°C, respectively. Figure 5.62(a) shows that after 8 h aging time at 155°C, however, the comparative UTS (or ΔP_{UTS}) values start to decrease as the aging time increases, indicating that these elements provide little or no improvement in mechanical properties. On the other hand, the comparative yield strength (or ΔP_{YS}) values of all alloys are improved, as shown in Figure 5.62(b), and are stabilized after 8 h aging time, while Figure 5.62(c) shows that the $\Delta P_{\% \text{EI}}$ or percent elongation to fracture values for all alloys are much lower than those of the G1 base alloy, which is to be expected, in light of the results shown in Figure 5.62(a). At 350°C aging temperature, an overall improvement in the ΔP values for all alloys is noted for UTS and YS with respect to the base alloy G1, with alloy G7 showing improvements going up to only 20 MPa. It is interesting to note how the YS values of all alloys are stable, appearing within a band ranging from about 30 to 80 MPa. Alloys G7 (Ni + Zr, no Cu) and G10 (Sc + Zr) show good ductility at 350°C compared to G8 (Mn + Zr), G6 (Ni + Zr) and G9 (Ni + Mn + Zr) alloys which exhibit ductility values much lower than that of G1 alloy.

Figure 5.63 compiles the strength-ductility values obtained for all the 354 alloys investigated. These values fall into regions corresponding to peak aging, under-aging, and overaging. Using regression analysis, the UTS versus %EI relationship may be expressed as follows.

$$\text{UTS} = -20.63x + 392.23 \quad \text{with a fit of } R^2 = 0.8208$$

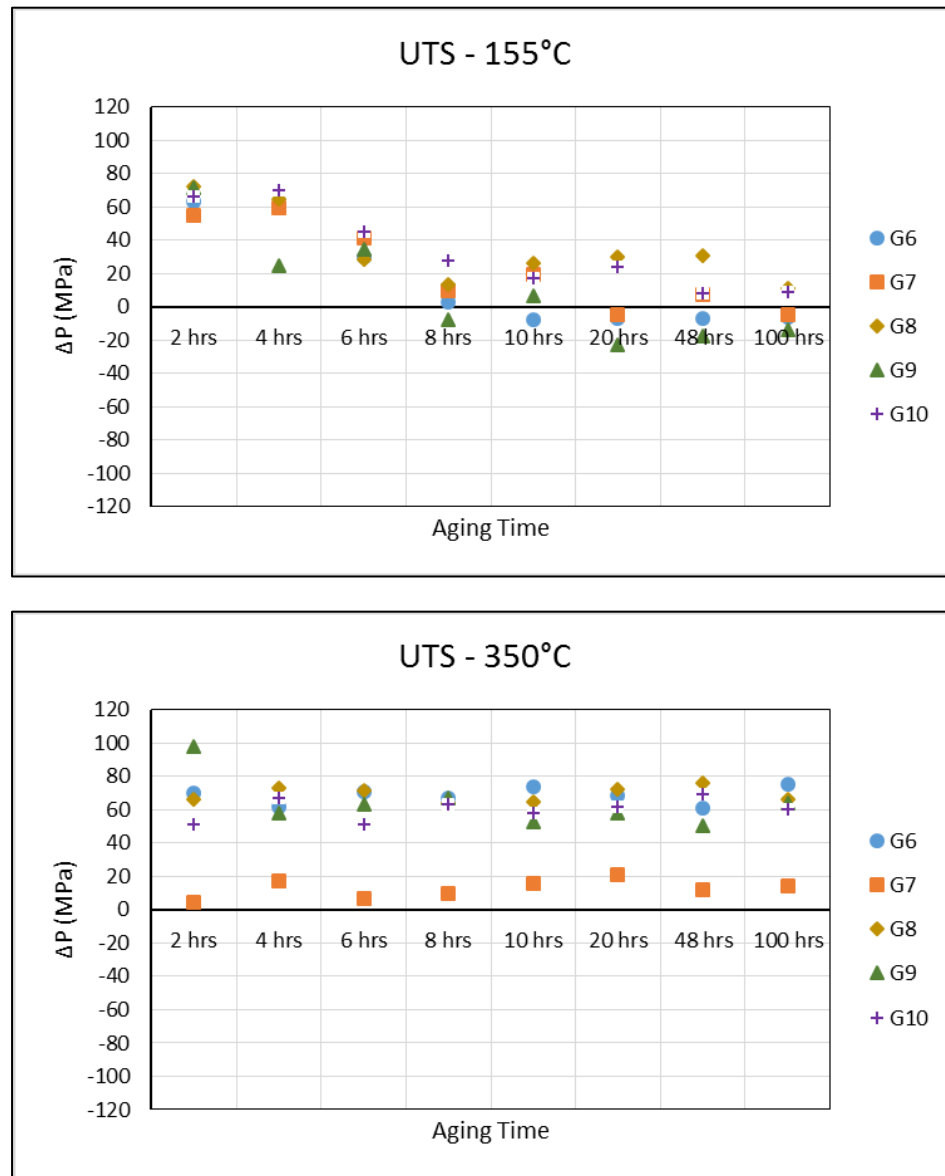
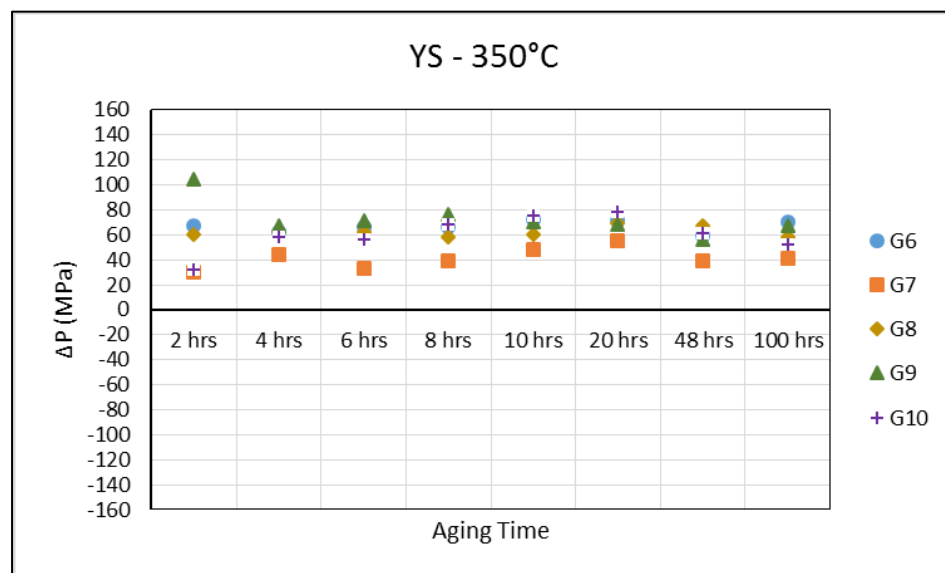
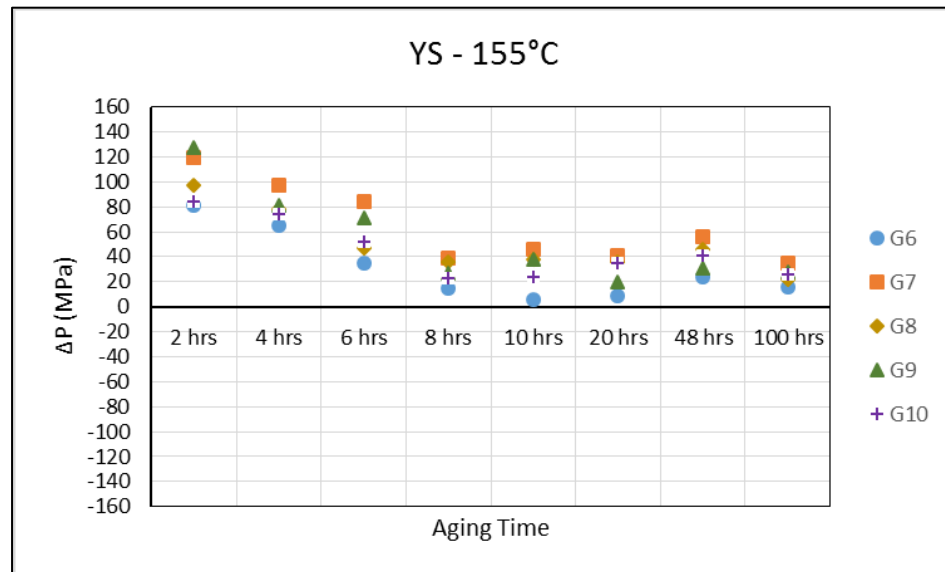
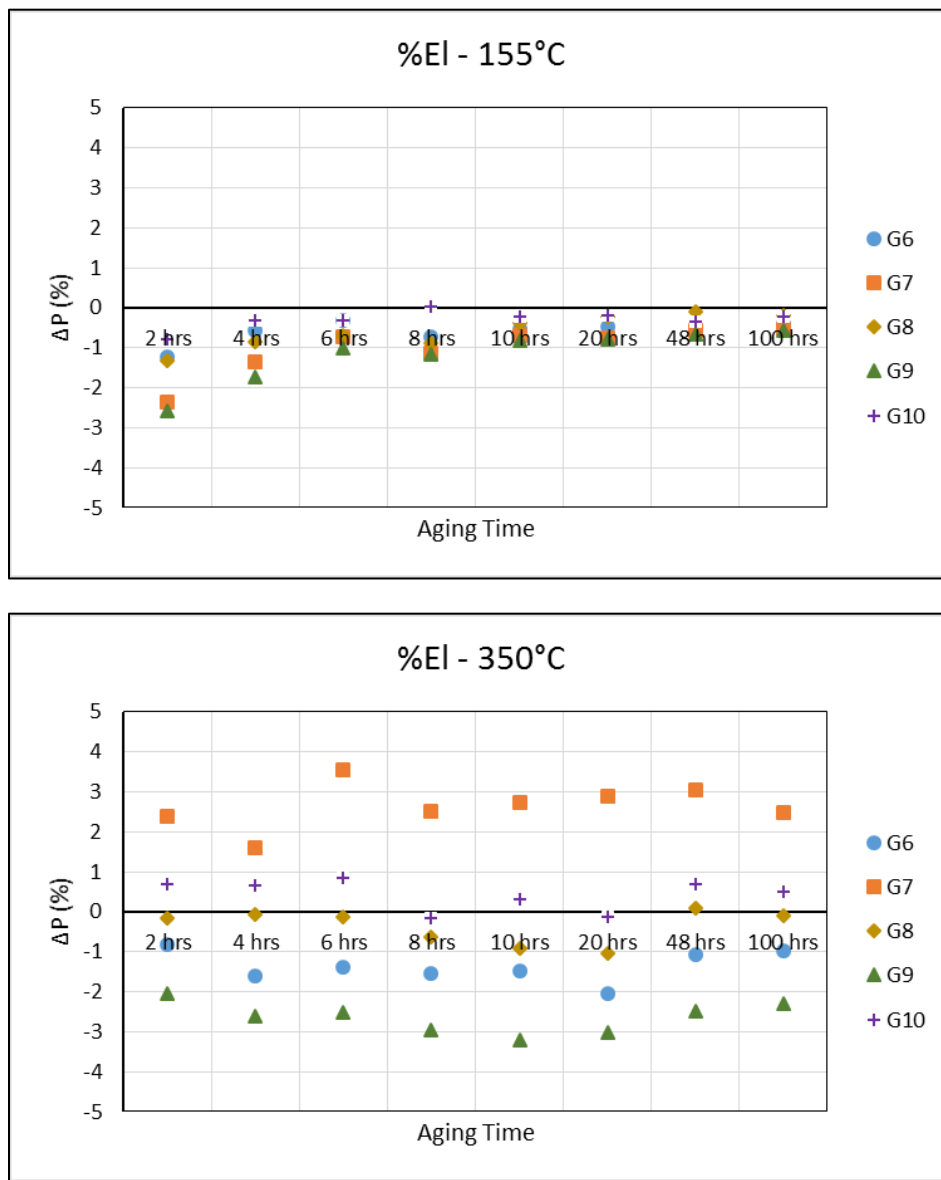


Figure 5.62 Cont.



(b)

Figure 5.62 Cont.



(c)

Figure 5.62 Comparison of tensile properties of G6, G7, G8, G9, G10 alloys relative to those of G1 alloy: (a) UTS, (b) YS, and (c) %EI at 155°C and 350°C.

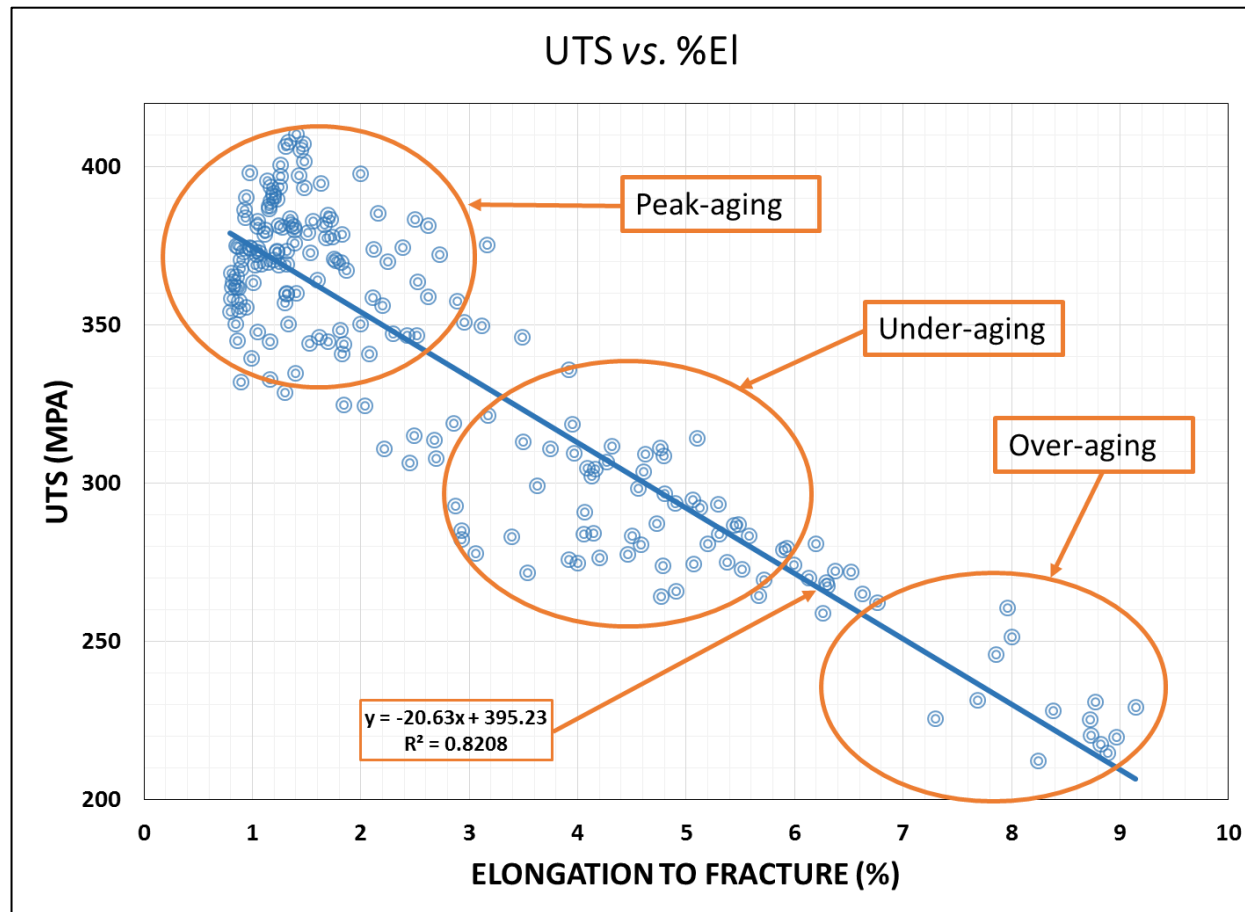


Figure 5.63 UTS vs. %El relationship for heat-treated 354 alloys, depicting the peak-, under-, and over-aged regions within the heat treatment conditions used in this study.

5.9 CONCLUSIONS

Based on the results presented in this part of Chapter 5 on the tensile properties of the 354 alloys investigated, the following conclusions may be drawn.

1. Among the alloys containing transition element additions (G6 through G10), the highest tensile and yield strength values were obtained with alloy G7 (containing 2wt% Ni and 0.25wt% Zr but no Cu) in the as-cast and solution heat-treated (540°C/8h) conditions, namely 306.5 MPa (UTS)/208.8 MPa (YS) and 354.4 MPa (UTS)/234.5 MPa (YS), respectively, with an increase in the ductility from 2.41 to 4.88% after solution heat treatment.
2. Alloys G8 (with 0.75wt% Mn and 0.25wt% Zr) and G10 (with 0.1wt% Sc and 0.25wt% Zr) displayed a significant increase in UTS and %El in the as-cast and solution heat-treated (500°C/8h) conditions from 323.8 MPa/298.5 MPa (AC) to 328.4 MPa/333.1 MPa (SHT) and an increase in the percentage elongation from 2.05%/2.32% (AC values) to 4.62%/5.40 (SHT values), respectively. The YS decreased in both conditions, however, from 238.9 MPa (G8)/228.1 MPa (G10) to 203.4 MPa/199.4 MPa (SHT), respectively.
3. The application of a solutionizing treatment leads to significant improvement in the strength and quality of the castings, even if these alloys (G6 to G10) contain higher Fe and Mg levels than the base 354 alloy G1.
4. An improvement in the tensile properties and alloy quality are noted upon solution heat treatment for all alloys, indicating that although the solution heat treatment is

mainly responsible in improving the alloy quality (~190 MPa), the presence of Ni and Zr in alloy G7 with no Cu (458 MPa) compared with alloy G6 with Cu (406 MPa), and the addition of Mn and Zr in alloy G8, and Sc and Zr in alloy G10 provides improvement in the quality index values of 428 MPa and 443 MPa, respectively, as these alloys show the best Q and YS values.

5. When adding the hardening elements Cu and Mg to 354 type alloys, the quality index of the alloy castings is controlled by the net amount by which the strength is increased and the ductility is reduced.
6. The addition of different amounts/combinations of Ni, Zr, Sc, Mn (alloys G6, and G8 to G10) and also the absence of Cu in alloy G7 improves the tensile properties compared to those exhibited by the 354 base alloy G1.
7. Among the alloys containing transition element additions (G6 through G10) and the base alloy G1, the highest tensile results and quality index values - obtained at the two peak-aging conditions are displayed below (best aging condition is 190°C/2h).

Code Alloy	155°C/100h (G1, G6, G9) 155°C/48h (G7, G8, G10)				190°C/2h (G1, G6, G7, G8, G10) 190°C/4h (G9)			
	UTS (MPa)	YS (MPa)	%El	Q (MPa)	UTS (MPa)	YS (MPa)	%El	Q (MPa)
G8	410.46	366.71	1.40	432	408.01	366.24	1.33	427
G10	387.55	363.03	1.15	397	405.24	363.29	1.49	429
G7	386.47	376.23	0.92	381	398.25	387.82	0.97	396
G6	374.27	352.65	0.98	373	381.14	354.68	1.05	384
G9	366.46	363.92	0.80	352	358.53	357.20	0.80	344
G1	380.22	336.44	1.38	401	381.84	327.07	1.66	415

8. Aging treatment of 354-type alloy castings produces a wide range of tensile properties based on the aging temperatures and times applied. Depending on the

required tensile properties, suitable aging conditions may be recommended based on the best possible compromise between strength, quality, and aging time involved in the process.

9. The best combination of properties is achieved after aging at 190°C/2h for all alloys studied, with an exception of alloy G9 that showed the best combination at 190°C/4h. These conditions may therefore be considered as the appropriate T6 treatment for these alloys.
10. Any value greater than 3% is considered high when considering the ductilities usually exhibited by hypoeutectic Al-Si alloys. The highest ductility values are attained at 240°C, 300°C and at 350°C aging temperature (alloys G7, G8, and G10) across the range of aging times. This behavior is normally expected in Al-Si-Cu-Mg alloys whose strength is obtained at the expense of ductility.
11. Aging treatment at the five temperatures studied results in a continuous increase in the alloy strength accompanied by a reduction in ductility up to the peak aging point. Aging times required for reaching peak strength in alloys lie between 48 h and 100 h at 155°C, from 2 h to 4 h at 190°C, and 2 h for the higher aging temperatures of 240°C, 300°C and 350°C.
12. Aging treatment at higher temperatures (240°C, 300°C and 350°C) is accompanied by a reduction in the tensile properties and quality index values of the castings; however, it also introduces the possibility of a significant economical strategy for minimizing the time and the cost of this same treatment.

13. Increasing the aging time after reaching the peak strength at each temperature leads to overaging, whereupon the alloy strength starts to decrease and the ductility to increase.
14. Multiple aging peaks are observed in the age-hardening curves of alloys G6 to G10 (aging temperatures of 155°C, 190°C, and 240°C). These peaks are related to the precipitation sequence which occurs in each alloy. The first hardness peak is related to the formation of the GP zones, while the subsequent peaks correspond to the various stages of formation of the type of hardening precipitates formed in the alloy.
15. The quality charts developed in the course of the current research facilitate the interpretation and evaluation of the tensile properties of 354 alloy. Such charts provide a logical evaluation tool for an accurate prediction of the influence of the various metallurgical parameters investigated on the alloys. Based on the quality charts developed, it is possible to make a rigorous selection as to the most suitable parameters to be applied to 354 type alloys so as to obtain the best possible cost-effective compromise between alloy strength and quality.
16. Aging at 190°C introduces a technologically useful strategy for this particular alloy system in that it becomes possible to contribute a significant economic benefit in the form of a noticeable reduction in the aging time required to reach peak strength (2 h or 4 h for all the 354 alloys studied). Other associated benefits include lower energy consumption, longer lifetime for the heating furnaces, greater productivity, lower production costs, etc.

RECOMMENDATIONS FOR FUTURE WORK

RECOMMENDATIONS FOR FUTURE WORK

Based on the results obtained in the present study, further investigations are suggested along the following lines to complement this study.

- It would be interesting to extend the work to investigate the effects of different solution heat treatment temperature/time conditions on the resulting mechanical properties of 354 alloys containing different Mn, Ni, Sc, and Zr additions.
- One of the main criteria which control the alloy application is the role played by the alloying elements in preserving the tensile properties under high temperature service conditions. Therefore, it is suggested that a study should be undertaken to investigate this aspect further in 354 alloys with Mn, Ni, Sc, and Zr additions and lower Mg and Fe contents will be useful.
- Investigating the possibility of producing 354-type alloy castings using other casting technologies such as lost foam, precision sand, and low pressure die casting.

REFERENCES

REFERENCES

1. T. Udomphol, "Aluminum and its alloys", Suranaree University of Technology, May-Aug 2007.
2. D. Raymond and F. Philip, "Manufacturing Feasibility of All-Aluminum Automotive Engines via Application of High Silicon Aluminum Alloy", SAE Inc., (2000).
3. M. Tadashi, "Advanced Near Dry Machining System," Horkos Corp, 2000.
4. R. Molina, P. Amalberto and M. Rosso, "Mechanical characterization of aluminum alloys for high temperature applications Part 1: Al-Si-Cu alloys," *Metallurgical Science and Technology*, Vol. 29-1, 2011, pp. 5-15.
5. T. Tanaka and T. Akasawa, "Machinability of Hypereutectic Silicon-Aluminum Alloys," *Journal of Materials Engineering and Performance*, Vol. 8(4), 1999, pp. 463-468.
6. National Research Council (U.S.), Effectiveness and Impact of Corporate Average Fuel Economy (CAFÉ) Standards, National Academy Press, Washington, D.C., 5A-4, 2001.
7. D.E. Malen and K. Reddy, "Preliminary Vehicle Mass Estimation using Empirical Subsystem Influence Coefficients," Auto Steel Partnership, May 2007.
8. C. Bjelkengren, "The Impact of Mass Decompounding on Assessing the Value of Vehicle Lightweighting," Master's Thesis, MIT, Massachusetts, Country (2008).

9. M.W. Verbrugge, "Mass Decoupling and Vehicle Lightweighting," *Materials Science Forum*, Vol. 5, 2009, pp. 618-619.
10. J.A. Lee and P. Chen, High Strength Aluminum Alloy for High Temperature Applications, US Patent No. 6918970, 2002.
11. J.A. Lee, "Cast Aluminum Alloy for High Temperature Applications," *The Minerals, Metals & Materials Society*, Sand Diego Convention Center, San Diego, CA, 2003, pp. 1-8.
12. J.D. Robson and P.B. Pragnell, "Modeling Al_3Zr dispersoid precipitation in multicomponent aluminum alloys," *Materials Science and Engineering A*, Vol. 352 2003, pp. 240-250.
13. Y.J. Li, S. Brusethaug and A. Olsen, "Influence of Cu on the Mechanical Properties and Precipitation Behavior of AlSi7Mg0.5 Alloy during Aging Treatment," *Scripta Materialia*, Vol. 54, 2006, pp. 99-103.
14. M.A. Moustafa, F.H. Samuel, H.W. Doty and S. Valtierra, "Effect of Mg and Cu Additions on the Microstructural Characteristics and Tensile Properties of Sr Modified Al-Si Eutectic Alloys," *International Journal of Cast Metals Research*, Vol. 14, 2002, pp. 235-253.
15. A.L. Dons, G. Heiberg, J. Voje, J.S. Maeland, J.O. Loland and A. Prestmo, "On the Effect of Additions of Cu and Mg on the Ductility of Al-Si Foundry Alloys Cast with a Cooling Rate of Approximately 3 K/s," *Materials Science and Engineering A*, Vol. 413-414, 2005, pp. 561-566.
16. Q.G. Wang and C.H. Cáceres, "Mg Effects on the Eutectic Structure and Tensile Properties of Al-Si-Mg Alloys," *Materials Science Forum*, Vol. 242, 1997, pp. 159-164.

17. H. Ammar, "Influence of Metallurgical Parameters on the Mechanical Properties and Quality Indices of Al-Si-Cu-Mg and Al-Si-Mg Casting Alloys," PhD. Thesis, Université du Québec à Chicoutimi, Chicoutimi, Quebec, Canada (2010).
18. H.R. Ammar, A.M. Samuel, F.H. Samuel, E. Simielli, G.K. Sigworth and J.C. Lin, "Influence of Aging parameters on the Tensile Properties and Quality Index of Al-9 Pct Si-1.8 Pct Cu-0.5 Pct Mg 354-Type Casting Alloys," *Metallurgical and Materials Transactions A*, Vol. 43A, 2012, pp. 61-73.
19. J. Hernandez-Sandoval, "Improving the Performance of 354 Type Alloy," PhD. Thesis, Université du Québec à Chicoutimi, Chicoutimi, Quebec, Canada (2010).
20. J. Hernandez-Sandoval, G.H. Garza-Elizondo, A.M. Samuel, S. Valtierra and F.H. Samuel, "The ambient and high temperature deformation behavior of Al-Si-Cu-Mg alloy with minor, Ti, Zr, Ni additions," *Material and Design*, Vol. 58, 2014, pp. 89-101.
21. D. Jing-Zhi, H. Yu-Feng, and C. Jun, "Effect of Sc and Zr on Microstructures and Mechanical Properties of As-Cast Al-Mg-Si-Mn Alloys," *Transactions of Nonferrous Metals Society of China*, Vol. 19, 2009, pp. 540-544.
22. Y. Yi-Cong, H. Liang-Ju, and L. Pei-Jie, "Differences of Grain-Refining Effects of Sc and Ti Additions in Aluminum by Empirical Electron Theory Analysis," *Transactions of Nonferrous Metals Society of China*, Vol. 20, 2010, pp. 465-470.
23. I.N. Fridlyander, V.G. Sister, O.E. Grushko, V.V. Berstenev, L.M. Sheveleva and L.A. Ivanova, "Aluminum Alloys: Promising Materials in the Automotive Industry," *Metal Science and Heat Treatment*, Vol. 44 (9-10), 2002, pp. 365-370.
24. <http://www.drivealuminum.org/research-resources/PDF/Webinars/2014/2015-ducker-worldwide-survey-of-automakers>, The Aluminum Association Presents: 2015 Ducker

Worldwide Automaker Survey, Drive Aluminum An Aluminum Association Webinar, 2015.

25. <http://www.drivealuminum.org/research-resources/PDF/Speeches%20and%20Presentations/2012/Aluminum-Growth-in-Auto-Body-Today-to-2020-Murphy.pdf>, Aluminum Growth in Auto Body Today to 2020, Mike Murphy – Vice President Global Automotive, ALCOA, 2012.
26. http://www.alcoa.com/car_truck/en/pdf/2014_Ducker_Executive_Summary.pdf, 2015 North American Light Vehicle Aluminum Content Study, Drive Aluminum, Ducker Worldwide, June 2014.
27. T. Murat and J. Staley, *Physical Metallurgy and the Effect of Alloying Additions in Aluminum Alloys*, Handbook of Aluminum Volume 1 - Physical Metallurgy and Processes, Marcel Dekker, Inc., New York, 2003.
28. J.R. Davis, *Aluminum and Aluminum Alloys*, ASM Specialty Handbook, ASM International, Materials Park, OH, U.S.A., 1993.
29. J.G. Kaufman and E.L. Rooy, *Aluminum Alloy Castings: Properties, Processing, and Applications*, ASM International, Materials Park, Ohio, U.S.A., 2004.
30. J.E. Hatch, *Aluminum: Properties and Physical Metallurgy*, American Society for Metals, Metals Park, OH, U.S.A., 1984, pp. 55-120.
31. ASM Handbook Vol. 2, *Properties and Selection: Nonferrous Alloys and Special-Purpose Materials*, ASM International, Materials Information Society, U.S.A., 1990.
32. J.E. Gruzleski and B.M. Closset, *The Treatment of Liquid Aluminum-Silicon Alloys*, American Foundrymen's Society, Inc., Des Plaines, IL, U.S.A., 1990.

33. L. Heusler and W. Schneider, "Influence of Alloying Elements on the Thermal Analysis Results of Al-Si Cast Alloys," *Journal of Light Metals*, Vol. 2, 2002, pp. 17-26.
34. L. Lu, K. Nogita and A.K. Dahle, "Combining Sr and Na Additions in Hypoeutectic Al-Si Foundry Alloys," *Materials Science and Engineering A*, Vol. 399, 2005, pp. 244-253.
35. L. Lu and A.K. Dahle, "Effects of Combined Additions of Sr and AlTiB Grain Refiners in Hypoeutectic Al-Si Foundry Alloys," *Materials Science and Engineering A*, Vol. 435-436, 2006, pp. 288-296.
36. L. Bäckerud, G. Chai and J. Tamminen, *Solidification Characteristics of Aluminum Alloys, Vol. 2 Foundry Alloys*, AFS/Skanaluminium, Des Plaines, IL, U.S.A., 1190.
37. M. Warmuzek, *Aluminum-Silicon Casting Alloys: Atlas of Microfractographs*, ASM International, Materials Park, OH, U.S.A., 2004.
38. J. Asesio-Lozano and B. Suarez-Peña, "Effect of the Addition of Refiners and/or Modifiers on the Microstructure of Die Cast Al-12Si Alloys," *Scripta Materialia*, Vol. 54, 2006, pp. 943-947.
39. J.L. Jorstad, "Hypereutectic Al-Si Casting Alloys: 25 Years, What's Next," *AFS Transactions*, Vol. 104, 1996, pp. 669-671.
40. J. Li, M. Elmadagli, V.Y. Gerstman, J. Lo and A.T. Alpas, "FIB and TEM Characterization of Subsurface of an Al-Si Alloy (A390) Subjected to Sliding Wear," *Materials Science and Engineering A*, Vol. 421, 2006, pp. 317-327.
41. M. Zuo, X. Liu and Q. Sun, "Effects of Processing Parameters on the Refinement of Primary Si in A390 Alloys with A New Al-Si-P Master Alloy," *Journal of Materials Science*, Vol. 44, 2009, pp. 1952-1958.

42. V.C. Srivastava, R.K. Mandal and S.N. Ojha, "Evolution of Microstructure in Spray Formed Al-18%Si Alloy," *Materials Science and Engineering A*, Vol. 383, 2004, pp. 14-20.
43. A.S. Lee, "A Study on the Economics of Hypereutectic Aluminum-Silicon (Al-Si) Alloy Machining," *International Journal of Advanced Manufacturing Technology*, Vol. 16, 2000, pp. 700-708.
44. J.E. Hatch, (Ed.), *Aluminum: Properties and Physical Metallurgy*, American Society for Metals, Metals Park, OH, 1993, pp. 135-160.
45. F.H. Samuel, A.M. Samuel, "Effect of Heat Treatment on the Microstructure, Tensile Properties, and Fracture Behavior of Permanent Mold Al-10wt%Si-0.6wt%Mg/SiC/10_p Composite Castings," *Metallurgical and Materials Transactions A*, Vol. 25A, 1994, pp. 2247-2263.
46. H. Ammar, "Effect of Casting Imperfections on the Fatigue Properties of Aluminum-Silicon Casting Alloys," Master's Thesis, Université du Québec à Chicoutimi, Chicoutimi, Quebec, Canada (2006).
47. J.L. Jorstad, W.M. Rasmussen and D.L. Zalensas, *Aluminum Casting Technology*, 2nd Edition, The American Foundrymen's Society, Inc., Des Plaines, IL, U.S.A., 1993.
48. E.L. Roy, *ASM Handbook, Castings*, 9th Edition, ASM International, Materials Park, OH, Vol. 15, 1992, pp. 743-769.
49. A.M.A. Mohamed, "Effect of Additives on the Microstructure and Mechanical Properties of Aluminum-Silicon Alloys," PhD. Thesis, Université du Québec à Chicoutimi, Chicoutimi, Quebec, Canada (2008).
50. A.T. Joenoes and J. Gruzleski, "Magnesium Effects on the Microstructure of Unmodified and Modified Al-Si Alloys," *Cast Metals*, Vol. 4(2), 1991, pp. 62-71.

51. R. Dunn and W. Dickert, "Magnesium Effect on the Strength of A380.0 and 383.0 Aluminum Die Casting Alloys," *Die Casting Engineer*, Vol. 19, 1975, pp. 12-20.
52. B. Closset and J.E. Gruzleski, "Mechanical Properties of A356.0 Alloys Modified with Pure Strontium," *AFS Transactions*, Vol. 90, 1982, pp. 453-464.
53. S. Bercovici, "Control of Solidification Structure and Properties of Al-Si Alloys," Paper presented at 45th Congress of International Foundry, 1978.
54. E.E.M. Elgallad, "Effect of Additives on the Mechanical Properties and Machinability of a New Aluminum-Copper Base Alloy," PhD. Thesis, Université du Québec à Chicoutimi, Chicoutimi, Quebec, Canada (2010).
55. G.K. Sigworth, "Theoretical and Practical Aspects of the Modification of Al-Si Alloys," *AFS Transactions*, Vol. 91, 1983, pp. 7-16.
56. S.Z. Lu and A. Hellawell, "The Mechanical of Silicon Modification in Aluminum Silicon Alloys: Impurity Induced Twinning," *Metallurgical Transactions*, Vol. 18A, 1987, pp. 1721-1733.
57. A.T. Joenoes, "The Role of Magnesium on Eutectic Silicon Microstructure," Master's Thesis, McGill University, Montreal, Canada (1991).
58. Pacz, United States Patent 1, 387, 900 (August 16, 1921).
59. L.F. Mondolfo, *Metallography of Aluminum Alloys*, Wiley, New York, 1943.
60. J.E. Gruzleski, "The Art and Science of Modification 25 Years of Progress," *AFS Transactions*, Vol 100, 1992, pp. 673-683.
61. Dahle, K. Nogita, S. McDonald, C. Dinnis, and L. Lu, "Eutectic Modification and Microstructure Development in Al-Si Alloys," *Materials Science and Engineering A*, Vol. 413-414, 2005, pp. 243-248.

62. G. Nagel and R. Portalier, "Structural Modification of Aluminum-Silicon Alloys by Antimony Treatment," *International Cast Metals Journal*, Vol. 5(4), 1980, pp. 2-6.
63. B. Closset and J.E. Gruzleski, "A Study on the Use of Pure Metallic Strontium in the Modification of Al-Si Alloys," *AFS Transactions*, Vol. 89, 1981, pp. 801-808.
64. M. Hafi and T. Kobayashi, "Mechanical Properties of Modified and Non-modified Eutectic Al-Si Alloys," *Journal of Japan Institute of Light Metals*, Vol. 44(1), 1994, pp. 28-34.
65. N. Fat-Halla, "Structural Modification of Al-Si Eutectic Alloy by Sr and its Effect on Tensile and Fracture Characteristics," *Journal of Materials Science*, Vol. 24, 1989, pp. 2488-2490.
66. B. Kulunk and D. Zuliani, "Application and Quality of Low Pressure Aluminum Castings," *AFS Transactions*, Vol. 96, 1988, p. 249-260.
67. K. Nogita, P.L. Schaffer, S.D. McDonald, L. Lu, and A.K. Dahle, "Modification of Al-Si Alloys," *Aluminum Dusseldorf*, Vol. 81(4), 2005, pp. 330-335.
68. S.D. McDonald, A.K. Dahle, J.A. Taylor, and D.H. StJohn, "Modification-Related Porosity Formation in Hypoeutectic Aluminum-Silicon Alloys," *Metallurgical and Materials Transactions B*, Vol. 35B, 2004, pp. 1097-1106.
69. F. Paray and J.E. Gruzleski, "Microstructure-Mechanical Properties Relationships in 356 Alloy. Part I: Microstructure," *Cast Metals*, Vol. 7(1), 1994, pp. 29-40.
70. J.E. Gruzleski, *Microstructure Development during Metal Casting*, American Foundry Society, Des Plaines, IL, 2000.
71. L.F. Mondolfo, S. Farooq, and C. Tse, "Grain Refinement of Aluminum Alloy by Titanium and Boron," *Solidification Processing*, 1987, pp. 133-136.

72. M.M. Guzowski, G.K. Sigworth, and D.A. Sentner, "The Role of Boron in the Grain Refinement of Aluminum with Titanium," *Metallurgical and Materials Transactions A*, Vol. 18A, 1987, pp. 603-620.
73. P.S. Mohanty, F.H. Samuel, and J.E. Gruzleski, "Studies on Addition of Inclusions to Molten Aluminum Using a Novel Technique," *Metallurgical and Materials Transactions B*, Vol. 26(1), 1995, pp. 907-912.
74. G.K. Sigworth and M.M. Guzowski, "Grain Refining of Hypoeutectic Al-Si Alloys," *AFS Transactions*, Vol. 93, 1985, pp. 907-912.
75. P.S. Mohanty, R.I.L. Guthrie and J.E. Gruzleski, "Studies on the Fading Behavior of Al-Ti-B Master Alloys and Grain Refinement Mechanism Using LiMCA," *Light Metals*, The Minerals, Metals, and Materials Society, Warrendale, PA, 1995, pp. 859-868.
76. M.C. Flemings, *Solidification Processing*, McGraw-Hill, New York, 1974.
77. ASM Handbook, *Vol.4: Heat Treating of Aluminum Alloys*, 10th Edition, American Society for Metals, Materials Park, OH (1991).
78. G.K. Sigworth, "Controlling Tensile Strength in Aluminum Castings," Private Communication, Alcoa Primary Metals, Rockdale, TX (2006).
79. J.R. David, *ASM Speciality Handbook: Aluminum and Aluminum Alloys*, ASM International, Materials Park, OH (1993).
80. E. Sjölander and S. Seifeddine, "Artificial Ageing of Al-Si-Cu-Mg Casting Alloys," *Materials Science and Engineering*, Vol. 528 (24), 2011, pp. 7402-7409.
81. J. Barresi, M.J. Kerr, H. Wang, and M.J. Couper, "Effect of Magnesium, Iron, and Cooling Rate on Mechanical Properties of Al-7Si-Mg Foundry Alloys," *AFS Transactions*, 2000, pp. 63-70.

82. J. Gauthier, P. Louchez, and F.H. Samuel, "Heat Treatment of 319.2 Al Automotive Alloy: Part 1, Solution Heat Treatment," *Cast Metals*, Vol. 8(1), 1995, pp. 91-106.
83. D.O. Northwood, X. Sun, G. Byczynski, J.H. Sokolowski, "The development of a two-stage solution treatment for cast Al-Si-Cu alloys," *IMMA ADCA Conference Proceedings*, Vol. 4, 1995, pp. 15-19.
84. J.H. Sokolowski, X.C. Sun, and A. Esseltine, "The Removal of Copper-Phase Segregation and the Subsequent Improvement in Mechanical Properties of Cast 319 Aluminum Alloys by a Two-Stage Solution Heat Treatment," *Journal of Materials Processing Technology*, Vol. 53, 1995, pp. 385-392.
85. P. Shiang Wang, S.L. Lee, and M.T. Jahn, "Effects of Solution Temperature on Mechanical Properties of 319.0 Aluminum Casting Alloys Containing Trace Beryllium," *Journal of Materials Research*, Vol. 15, 2000, pp. 2027-2035.
86. J. Gauthier, P.R. Louchez, and F.H. Samuel, "Heat Treatment of 319.2 Aluminum Automotive Alloy: Part 2, Aging Behavior," *Cast Metals*, Vol. 8(2), 1995, pp. 293-299.
87. P. Ouellet, F.H. Samuel, D. Gloria, and S. Valtierra, "Effect of Mg content on the Dimensional Stability and Tensile Properties of Heat Treated Al-Si-Cu (319) Type Alloys," *International Journal of Cast Metals Research*, Vol. 10, 1997, pp. 67-78.
88. P.N. Crepeau, "Effect of Iron in Al-Si Casting Alloys: A Critical Review," *AFS Transactions*, Vol. 110, 1995, pp. 361-366.
89. M. Tash, F.H. Samuel, F. Mucciardi, and H.W. Doty, "Effect of Metallurgical Parameters on the Hardness and Microstructural Characterization of As-Cast and Heat-Treated 356 and 319 Aluminum Alloys," *Materials Science and Engineering A*, Vol. 443A, 2007, pp. 185-201.

90. Z. Ma, A.M. Samuel, F.H. Samuel, H.W. Doty, and S. Valtierra, "A Study of Tensile Properties in Al-Si-Cu and Al-Si-Mg Alloys: Effect of β -iron Intermetallics and Porosity," *Materials Science and Engineering A*, Vol. 490, 2008, pp. 36-51.
91. T.O. Mbuya and B.O. Odera, "Influence of Iron on Castability and Properties of Aluminum Silicon Alloys: Literature Review," *International Journal of Cast Metals Research*, Vol. 16, 2003, pp. 451-465.
92. A.M. Nabawy, "Influence of Zirconium and Scandium on the Microstructure, Tensile Properties, and Hot-Tearing Susceptibility of Al-2wt%Cu-Based Alloys," PhD. Thesis, Université du Québec à Chicoutimi, Chicoutimi, Quebec, Canada (2010).
93. T. Croucher and B. Butler, "Polymer Quenching of Aluminum Castings," 26th *National SAMPE Symposium*, April 26-28, 1982, pp. 527-535.
94. G.E. Totten and D.S. Mackenzie, "Aluminum Quenching Technology: A Review," *Materials Science Forum*, Vols. 331-337, 2000, pp. 589-594.
95. A.V. Sverdlin, G.E. Totten, and G.M. Webster, "Polyalkyleneglycol Base Quenching Media for Heat Treatment of Aluminum Alloys," *Metallovedenie Termicheskaya Obrabotka Metallov*, Vol. 6, 1996, pp. 17-19.
96. D. Emadi, L.V. Whiting, M. Sahoo, J.H. Sokolowski, P. Burke and M. Hart, "Optimal Heat Treatment of A356.2 Alloy," *Light Metals*, The Minerals, Metals, and Materials Society, Warrendale, PA, 2003, pp. 983-989.
97. A.J. Garcia-Celis, R. Colas, and S. Valtierra, "Aging in Heat Treatable Cast Aluminum Alloy," *The 1st International Automotive Heat Treating Conference*, Puerto Vallarta, Mexico, 13-15 July, 1998, pp. 372-375.
98. R. Howard, N. Bogh, D.S. MacKenzie, "Heat Treating Processes and Equipment," in *Handbook of Aluminum Volume 1 - Physical Metallurgy and Processes*, Marcel Dekker, Inc., New York, 2003.

99. H.M. Kandil, "None-Combustible Water-Based Quenchants in Forging Shops for Automotive Parts - Latest Development," *The 1st International Automotive Heat Treating Conference*, Puerto Vallarta, Mexico, 13-15 July, 1998, pp. 106-109.
100. S. Seifeddine, "The influence of iron and mini content on the microstructure and tensile properties of cast Al-Si-Mg alloys," *Vilmer Project-5.2 Casting*, The School of Engineering Component Technology Sweden (2007).
101. G.H. Garza Elizondo, "Machinability of Al-(7-11%)Si Casting Alloys: Role of Free-Cutting Elements," Master's Thesis, Université du Québec à Chicoutimi, Chicoutimi, Quebec, Canada (2010).
102. G.E. Dieter, *Mechanical Metallurgy*, SI Metric Edition, McGraw-Hill, London, 1988.
103. D.A. Porter and K.E. Easterling, *Phase Transformations in Metals and Alloys*, 2nd Edition, Chapman and Hall, New York, 1992.
104. D.R. Askeland, *The Science and Engineering of Materials*, 3rd Edition, Chapman and Hall, Boston, MA, 1996.
105. D.R. Askeland, P.P. Fulay, and W.J. Wright, *The Science and Engineering of Materials*, 6th Edition, CENGAGE Learning (Pub.), Stamford, 2001, pp. 458-484.
106. D.G. Eskin, "Decomposition of Supersaturated Solid Solutions in Al-Cu-Mg-Si Alloys," *Journal of Materials Science*, Vol. 38, 2003, pp. 279-290.
107. S.K. Son, M. Takeda, M. Mitome, Y. Bando, and T. Endo, "Precipitation Behaviour of an Al-Cu Alloy during Isothermal Aging at Low Temperatures," *Materials Letters*, Vol. 75, 2005, pp. 629-632.
108. S.P. Ringer and K. Hono, "Microstructural Evolution and Age Hardening in Aluminum Alloys: Atom Probe Field-Ion Microscopy and Transmission Electron Microscopy Studies," *Materials Characterization*, Vol. 44, 2000, pp. 101-131.

109. C.R. Hutchinson and S.P. Ringer, "Precipitation Processes in Al-Cu-Mg Alloys Microalloyed with Si," *Metallurgical and Materials Transactions A*, Vol. 31A, 2000, pp. 2721-2733.
110. S. Abis, M. Massazza, P. Mengucci, and G. Tiontino, "Early Ageing Mechanisms in a High-Copper AlCuMg Alloy," *Scripta Materialia*, Vol. 45, 2001, pp. 685-691.
111. G.E. Totten and D.S. Mackenzie, "*Handbook of Aluminum, Vol. 1: Physical Metallurgy and Processes*," Marcel Dekker, NY, U.S.A., 2003.
112. S.C. Wang, M.J. Starink, and N. Gao, "Precipitation Hardening in Al-Cu-Mg Alloys Revisited," *Scripta Materialia*, Vol. 54, 2006, pp. 287-291.
113. P. Ratchev, B. Verlinden, P. De Smet, and P. Van Houtte, "Effect of Cooling Rate and Predeformation on the Precipitation Hardening of an Al-4.2wt%Mg-0.6wt%Cu Alloy," *Scripta Materialia*, Vol. 38(8), 1998, pp. 1195-1201.
114. Charai, T. Walther, C. Alfonso, A.M. Zahra, and C.Y. Zabra, "Coexistence of Clusters, GPB Zones, S''-, S' – and S-Phases in an Al-0.9%Cu-1.7%Mg Alloy," *Acta Materialia*, Vol. 48, 2000, pp. 2751-2764.
115. P. Ratchev, B. Verlinden, P. De Smet, and P. Van Houtte, "Precipitation Hardening of an Al-4.2wt%Mg-0.6wt%Cu Alloy," *Acta Materialia*, Vol. 46(10), 1998, pp. 3523-3533.
116. C. Cayron and P.A. Buffat, "Transmission Electron Microscopy Study of the β' Phase (Al-Mg-Si Alloys): Ordering Mechanism and Crystallographic Structure," *Acta Materialia*, Vol. 48, 2000, pp. 2639-2653,
117. K. Matsuda, D. Teguri, T. Sato, and S. Ikeno, "EFTEM Observation of Q' Phase in Al-Mg-Si-Cu Alloy," *Materials Science Forum*, Vol. 396-402, 2002, pp. 947-952.

118. J.Y. Hwang, R. Banerjee, H.W. Doty, and M.J. Kaufman, "The Effect of Mg on the Structure and Properties of Type 319 Aluminum Casting Alloys," *Acta Materialia*, Vol. 57, 2009, pp. 1308-1317.
119. G. Wang, Q. Sun, L. Feng, L. Hui, and C. Jing, "Influence of Cu Content on Aging Behavior of AlSiMgCu Cast Alloys," *Materials and Design*, Vol. 28, 2007, pp. 1001-1005.
120. J. Buha, R.N. Lumley, and A.G. Crosky, "Microstructural Development and Mechanical Properties of Interrupted Aged Al-Mg-Si-Cu Alloy," *Metallurgical and Materials Transactions A*, Vol. 37A, 2006, pp. 3119-3129.
121. G.A. Edwards, K. Stiller, G.L. Dunlop, and M.J. Couper, "The Precipitation Sequence in Al-Mg-Si Alloys," *Acta Materialia*, Vol. 46, 1998, pp. 3893-3904.
122. I.J. Polmear, "Role of Age Hardening in Modern Aluminum Alloys," *Proceedings of the 3rd International Conference on Aluminum Alloys: ICAA3*, The Norwegian Institute of Technology, Trondheim, Norway, 1992, pp. 371-384.
123. F.H. Samuel, A.M. Samuel, and H.W. Doty, "Factors Controlling the Type and Morphology of Cu-Containing Phases in 319 Al Alloy," *AFS Transactions*, Vol. 104, 1996, pp. 893-901.
124. M.F. Ibrahim, "Effects of Magnesium Content and Aging Conditions on the Impact Toughness of 319-Type Al-Si-Cu-Mg Alloys," Master's Thesis, Université du Québec à Chicoutimi, Chicoutimi, Quebec, Canada (2010).
125. D. Apelian, "Aluminum Cast Alloys: Enabling Tools for Improved Performance," Worldwide Report, NADCA, Wheeling, Illinois, 2009.
126. Q.G. Wang, "Microstructural Effects on the Tensile and Fracture Behavior of Aluminum Casting Alloys A356/357," *Metallurgical and Materials Transactions A*, Vol. 34A, 2003, pp. 2887-2891.

127. L. Narayanan, F.H. Samuel, and J.E. Gruzleski, "Crystallization Behavior of Iron-Containing Intermetallic Compounds in 319 Aluminum Alloy," *Metallurgical Transactions A*, Vol. 25A, 1994, pp. 1761-1773.
128. Y. Awano and Y. Shimizu, "Non-Equilibrium Crystallization of AlFeSi Compound in Melt-Superheated Al-Si Alloy Castings," *AFS Transactions*, Vol. 98, 1990, pp. 889-895.
129. A.M. Samuel, F.H. Samuel, and H.W. Doty, "Observations on the Formation of β -Al₅FeSi Phase in 319 Type Al-Si Alloys," *Journal of Materials Science*, Vol. 31, 1996, pp. 5529-5539.
130. M. Drouzy, S. Jacob, and M. Richard, "Interpretation of Tensile Results by Means of Quality Index and Probable Yield Strength," *AFS International Cast Metals Journal*, Vol. 5, 1980, pp. 43-50.
131. G.K. Sigworth, "Aluminum Casting Alloys," Special Communication, 2008.
132. C.H. Cáceres, I.L. Svensson, and J.A. Taylor, "Strength-Ductility Behaviour of Al-Si-Cu-Mg Casting Alloys in T6 Temper," *International Journal of Cast Metals Research*, Vol. 15, 2003, pp. 531-543.
133. S. Murali, A. Trivedi, K.S. Shamanna, and K.S. Murthy, "Effect of Iron and Combined Iron and Beryllium Addition on the Fracture Toughness and Microstructures of Squeeze-Cast Al-7Si-0.3Mg Alloy," *Journal of Materials Engineering and Performance*, Vol. 5(4), 1996, pp. 462-468.
134. Y. Choi, J. Lee, W. Kim, and H. Ra, "Solidification Behavior of Al-Si-Fe Alloys and Phase Transformation of Metastable Intermetallic Compound by Heat Treatment," *Journal of Materials Science*, Vol. 34, 1999, pp. 2163-2168.
135. R.M. Young and T. Clyne, "An Al-Fe Intermetallic Phase Formed During Controlled Solidification," *Scripta Metallurgica*, Vol. 15, 1981, pp. 1211-1216.

136. Miki, H. Kosuge, and K. Nagahama, "Supersaturation and Decomposition of Al-Fe Alloys during Solidification," *Journal of Japan Institute of Light Metals*, Vol. 25, 1975, pp. 1-9.
137. Couture, "Iron in Aluminum Casting Alloys – A Literature Survey," *AFS International Cast Metals Journal*, Vol. 6, 1981, pp. 9-17.
138. G. Gustafsson, T. Thorvaldsson, and G.L. Dunlop, "The Influence of Fe and Cr on the Microstructure of Cast Al-Si-Mg Alloys," *Metallurgical Transactions A*, Vol. 17A, 1986, pp. 45-52.
139. H. Iwahori, H. Takamiya, K. Yonekura, Y. Yamamoto, and M. Nakamura, *Casting* (in Japanese), Vol. 60(9), 1988, pp. 590-595.
140. Franek, J. Pazdernik, and A.K. Hanna, "On the Morphology of the Eutectic and Phases in Aluminium-Silicon 12-Iron and Aluminium-Silicon 20-Iron Alloys," *Praktische Metallographie*, Vol. 10, 1973, pp. 582-587.
141. S.G. Shabestari, "The Effect of Iron and Manganese on the Formation of Intermetallic Compounds in Aluminum-Silicon Alloys," *Materials Science and Engineering A*, Vol. 383, 2004, pp. 289-298.
142. S.G. Shabestari, M. Mahmudi, M. Emani, and J. Campbell, "Effect of Mn and Sr on intermetallics in Fe-rich eutectic Al-Si alloy," *International Journal of Cast Metals Research*, Vol. 15, 2002, pp. 17-24.
143. J.L. Jorstad, "Understanding Sludge," *Die Casting Engineer*, Nov-Dec 1986, pp. 30-36.
144. D.L. Colwell and R.J. Kissling, "Die and Permanent Mold Casting Aluminum Alloy Minor Elements," *AFS Transactions*, Vol. 69, 1961, pp. 610-615.

145. W. Khalifa, "Rôle des inclusions dans la germination de la phase α -aluminium des intermétalliques contenant du fer dans le coin riche en aluminium du système ternaire Al-Si-Fe," PhD. Thesis, Université du Québec à Chicoutimi, Chicoutimi, Quebec, Canada (2003).
146. S.A. Musmar, "In-situ Thermal Analysis Probe," Ph.D Thesis, McGill University, Montreal, Canada (2006).
147. G.K. Sigworth and C.H. Cáceres, "Quality Issues in Aluminum Net Shape Castings," *AFS Transactions*, Vol. 112, 2004, pp. 1-15.
148. G.E. Totten and D.S. McKenzie (Eds.), *Handbook of Aluminum – vol. 1: Physical Metallurgy and Process*, Marcel Dekker Inc., New York, NY, 2003.
149. D. Srinivasan and K. Chattopadhyay, "Metastable phase evolution and hardness of nanocrystalline Al-Si-Zr alloys," *Materials Science and Engineering A*, Vols. 304-306, 2001, pp. 534-539.
150. P. Seperband, R. Mahmudi, and F. Khomamizadeh, "Effect of Zr addition on the aging behavior of A319 aluminum cast alloy," *Scripta Materialia*, Vol. 52, 2005, pp. 253-257.
151. R. Mahmudi, P. Sepehrband, and H.M. Ghasemi, "Improved properties of A319 aluminum casting alloy modified with Zr," *Materials Letters*, Vol. 60, 2006, pp. 2606-2610.
152. N.A. Belov, A.N. Alabin, D.G. Eskin, and V.V. Istomin-Kastrovskii, "Optimization of Hardening of Al-Zr-Sc Cast Alloys," *Journal of Materials Science*, Vol. 41, 2006, pp. 5890-5899.
153. D. Srinivasan and K. Chattopadhyay, "Non-equilibrium Transformations Involving, $L1_2$ -Al₃Zr in Ternary Al-X-Zr Alloys," *Metallurgical and Materials Transactions A*, Vol. 36A, 2005, pp. 311-320.

154. N. Ryum, "Precipitation and Recrystallization in an Al-0.5wt Percent Zr Alloy," *Acta Metallurgica*, Vol. 17, 1969, pp. 269-278.
155. E. Nes, "Precipitation of the Metastable Cubic Al₃Zr-Phase in Subperitectic Al-Zr Alloys," *Acta Metallurgica*, Vol. 20(4), 1972, pp. 499-506.
156. J.D. Robson and P.B. Pragnell, "Predicting recrystallised volume fraction in aluminium alloy 7050 hot rolled plate," *Materials Science and Technology*, Vol. 18, 2002, pp. 607-614.
157. B. Morere, C. Maurice, R. Shahani, and J. Driver, "The influence of Al₃Zr dispersoids on the recrystallization of hot-deformed AA 7010 alloys," *Metallurgical and Materials Transactions A*, Vol. 32A, 2001, pp. 626-632.
158. Z. Yin, Q. Pan, Y. Zhang, and F. Jiang, "Effect of Minor Sc and Zr on the Microstructure and Mechanical Properties of Al-Mg Based Alloys," *Materials Science and Engineering A*, Vol. A280, 2000, pp. 151-155.
159. B. Forbord, H. Hallem, and K. Marthinsen, "The Effect of Alloying Elements on Precipitation and Recrystallisation in Al-Zr Alloys," *Proceedings of the 9th International Conference on Aluminum Alloys*, Brisbane Australia, 2004, pp. 1179-1185.
160. Z. Jia and G. Hu, "Effect of Homogenization and Alloying Elements on Resistance of Al-Zr-Mn Alloys," *Materials Science and Engineering A*, Vol. 444A, 2007, pp. 284-290.
161. J.L. Murray, Alcoa, Alcoa Center PA, Personal Communication, 2005.
162. Z. Liu, "Thermodynamics of nanoscale precipitate strengthened Fe-Cu and Al-Transition-Metal system from first principles calculations, PhD. Thesis, Northwestern University, Evanston, IL (2006).

163. K.E. Knipling, "Development of a Nanoscale Precipitation-Strengthened Creep-Resistant Aluminum Alloy Containing Trialuminide Precipitates," PhD Thesis, Northwestern University, Evanston, IL, (2006).
164. W.L. Manknis and S. Lamb, "Nickel and nickel alloys," *Metals Handbook, Vol. 2, Properties and Selection: Nonferrous Alloys and Special-Purpose Materials*, 10th Edition, Materials Park, Ohio (1990).
165. L. Sang-Yong, L. Jung-Hwan, and L. Young-Seon, "Characterization of Al 7075 alloys after cold working and heating in the semi-solid temperature range," *Journal of Materials Processing Technology*, Vol. 111, 2001, pp. 42-47.
166. P. Nash, M.F. Singleton, and J.L. Murray, *ASM Handbook, Vol. 3: Alloy-Phase Diagrams*, 10th Edition, ASM, Materials Park, Ohio (1992).
167. J.G. Kaufman, *Properties of aluminum alloys: Tensile, creep, and fatigue data at high and low temperatures*, ASM International, Materials Park, Ohio, 1999, pp. 714-724.
168. Z. Asghar, G. Requena, and F. Kubel, "The role of Ni and Fe aluminides on the elevated temperature strength of an AlSi12 alloy," *Materials Science and Engineering A*, Vol. A527, 2010, pp. 5691-5698.
169. C.L. Chen, A. Ritcher, and R.C. Thomson, "Investigation of mechanical properties of intermetallic phases in multi-component Al-Si alloys using hot-stage nanoindentation," *Intermetallics*, Vol. 18(4), 2010, pp. 499-508.
170. E. Tillová and M. Panusková, "Effect of solution treatment on intermetallic phases morphology in AlSi9Cu3 cast alloy," *Metalurgija/METABK*, Vol. 47(3), 2008, pp. 207-210.
171. D.N. Seidman, E.A. Marquis, and D.C. Dunand, "Precipitation Strengthening at Ambient and Elevated temperatures of Heat-Treatable Al(Sc) Alloys," *Acta Materialia*, Vol. 50, 2002, pp. 4021-4035.

172. V.G. Davydov, T.D. Rostova, and V.I. Yelagin, "Scientific Principles of Making an Alloying Addition of Scandium to Aluminum Alloys," *Materials Science and Engineering A*, Vol. 280A, 2000, pp. 30-36.
173. S. Iwamura and Y. Miura, "Loss in Coherency and Coarsening Behavior of Al₃Sc Precipitates," *Acta Materialia*, Vol. 52, 2004, pp. 591-600.
174. E.A. Marquis and D.N. Seidman, "Nanoscale Structural Evolution of Al₃Sc Precipitates in Al(Sc) Alloys," *Acta Materialia*, Vol. 49, 2001, pp. 1909-1919.
175. M.S. Kaiser and A.S.W. Kurny, "Effect of scandium on the grain refining and ageing behavior of cast Al-Si alloy," *Iranian Journal of Materials Science & Engineering*, Vol. 8(4), 2011, pp. 1-8.
176. L. Yuntao, L. Zhiyi, X. Qingkun, and L. Yanbin, "Grain refinement of the Al-Cu-Mg-Ag alloy with Er and Sc additions," *Metallurgical and Materials Transactions A*, Vol. 38A, 2007, pp. 2853-2858.
177. <http://www.himikatus.ru/art/phase-diagr1/Al-Sc.php>, The phase diagram of the system Fe-O.
178. V.V. Zakharov, "Effect of Scandium on the Structure and Properties of Aluminum Alloys," *Metal Science and Heat Treatment*, Vol. 45, 2003, pp. 246-253.
179. L.S. Toropova, D.G. Eskin, M.L. Kharaktrova, and T.V. Dobakina, *Advanced Aluminum Alloys Containing Scandium: Structure and Properties*, Gordon and Breach Science Publishers, Canada, 1998.
180. K.B. Hyde, A.F. Norman, and P.B. Prangnell, "The Effect of Cooling Rate on the Morphology of Primary Al₃Sc Intermetallic Particles in Al-Sc," *Acta Materialia*, Vol. 49, 2001, pp. 1327-1337

181. A.F. Norman, P.B. Prangnell, and R.S. McEwen, "The Solidification Behaviour of Dilute Aluminum-Scandium Alloys," *Acta Materialia*, Vol. 46, 1998, pp. 5715-5732.
182. O.N. Senkov, M.R. Shagiev, S.V. Senkova, and D.B. Miracle, "Precipitation of $\text{Al}_3(\text{Sc,Zr})$ Particle in an Al-Zn-Mg-Cu-Sc-Zr Alloy during Conventional Heat Treatment and its Effect on Tensile Properties," *Acta Materialia*, Vol. 56, 2008, pp. 3723-3738.
183. C.B. Fuller, J.L. Murray, and D.N. Seidman, "Temporal Evolution of the Nanostructure of Al(Sc,Zr) Alloys: Part 1 – Chemical Compositions of $\text{Al}_3(\text{Sc}_{1-x}\text{Zr}_x)$ Precipitates," *Acta Materialia*, Vol. 53, 2005, pp. 5401-5413.
184. M.S. Kaiser and M.K. Banerjee, "Effect of Ternary Scandium and Quaternary Zirconium and Titanium Additions on the Tensile and Precipitation Properties of Binary Cast Al-6Mg Alloys," *Jordan Journal of Mechanical and Industrial Engineering*, Vol. 2, 2008, pp. 93-99.
185. N. Roy, A.M. Samuel, and F.H. Samuel, "Porosity Formation in Al-9%Si-3%Cu Alloy Systems: Metallographic Observations," *Metallurgical and Material Transaction A*, Vol. 27, 1996, pp. 415-429.
186. G. Kumar, S. Hedge, and K.N. Prabhu, "Heat Transfer and Solidification Behaviour of Modified 357 Alloy," *Journal of Materials Processing Technology*, Vol. 182, 2007, pp. 152-156.
187. M. Drouzy, "Interpretation of Tensile Test Results Using Quality Index and Probable Elastic Limit-Applications to Cast Al-Si-Mg Alloys," *Revue de Métallurgie*, Vol. 75(1), 1978, pp. 51-59.
188. M.E. Fine, "Precipitation Hardening of Aluminum Alloys," *Metallurgical Transactions A*, 6(4) (1975), pp. 625-630.

189. Y.W. Kim and W.M. Griffith (Eds.), *Dispersion Strengthened Aluminum Alloys*, TMS, Warrendale, 1988, pp. 217-242.
190. Z. Asghar, G. Requena, and E. Boller, "Three-dimensional rigid multiphase networks providing high-temperature strength to cast AlSi₁₀Cu₅Ni₁₋₂ piston alloy," *Acta Materialia*, 2011, Vol. 59(16), pp. 6420-6432.
191. A.M. Gokhale, M.D. Dighe, and M. Horstemeyer, "Effect of Temperature on Silicon Particle Damage in A356 Alloy," *Metallurgical and Materials Transactions A*, Vol. 29A, 1998, pp. 905-907.
192. M. Brosnan and S. Shivkumar. "Elevated Temperature Tensile Properties and Fracture Behavior of A356 Castings," *AFS Transactions*, Vol. 103, 1996, pp. 727-737.
193. M.D. Dighe and A.M. Gokhale, "Relationship between microstructural extremum and fracture path in a cast Al-Si-Mg alloy," *Scripta Materialia*, Vol. 37, 1997, pp. 1435-1440.
194. E. Rincon, H.F. Lopez, M.M. Cisneros, H. Mancha, and M.A. Cisneros, "Effect of temperature on the tensile properties of an as-cast aluminum alloy A319," *Materials Science and Engineering A*, Vols. 452-453, 2007, pp. 682-687.
195. M.F. Ashby, C. Gandhi, and D.M.R. Taplin, "Fracture mechanism maps and their construction for f.c.c. metals and alloys," *Acta Metallurgica*, Vol. 27, 1979, pp. 699-729.
196. I.J. Polmer, *Light Alloys: Metallurgy of the light metals*, J. Wiley and Sons, New York (1995).
197. S. Floreen and H.W. Hayden, "Some Observations of Void Growth during Tensile Deformation of a High Strength Steel," *Scripta Metallurgica*, Vol. 4, 1970, pp. 87-94.

198. G.M. Ludtka and D.E. Laughlin, "The Influence of Microstructure and Strength on the Fracture Mode and Toughness of 7XXX Aluminium Alloy," *Metallurgical Transactions A*, Vol. 13A, 1982, pp. 411-425.
199. D.Y. Lee, J.G. Park, and D.-H. Cho, "High-temperature properties of dispersion-strengthened 7075-T6 aluminium alloy," *Journal of Materials Science Letters*, Vol. 16, 1997, pp. 158-160.
200. A.J. Tolley, V. Radmilovic, and U. Dahmen, "On the Effect of Zr on Precipitate Evolution in Al-Sc-Zr Alloys," *Congreso ConAmet/Sam* (2004).
201. M.S. Domack and D.L. Dicus, "Evaluation of Sc-Bearing Aluminum Alloy C557 for Aerospace Applications," *NASA/TM* (2002).
202. Y. Filatov, V. Yelagin, and V. Zakharov, "New Al-Mg-Sc Alloys," *Material Science and Engineering*, Vol. 280A, 2000, pp. 97-101.
203. R. Sawtell and C. Jensen, "Mechanical Properties and Microstructures of Al-Mg-Sc Alloys," *Metallurgical Transactions A*, Vol. 21A, 1990, pp. 421.
204. R. Mahmudi, P. Sepehrband, H.M. Ghasemi, "Improved properties of A319 aluminum casting alloy modified with Zr," *Materials Letters*, Vol. 60(21), 2006, pp. 2606-2610.
205. B.G. Clark, I.M. Robertson, L.M. Dougherty, D.C. Ahn, and P. Sofronis, "High-temperature dislocation-precipitate interaction in Al alloys: An in situ transmission electron microscopy deformation study," *Journal of Materials Research*, Vol. 20, 2005, pp. 1792-1801.
206. D. Hull and D.J. Bacon, *Introduction to Dislocations*, 4th Edition, Butterworth-Heinemann, Oxford, U.K. (2001), p. 222.

207. L.M. Brown and R.K. Ham, Dislocation-particle interactions, in *Strengthening Methods in Crystals*, edited by A. Kelly and R.B. Nicholson, Elsevier, New York, NY. (1971).
208. R. Lagneborg and B. Bergman, "The stress/creep rate behavior of precipitation-hardened alloys," *Metal Science*, Vol. 10(1), 1976, pp. 20.
209. E. Arzt and D.S. Wilkinson, "Threshold stresses for dislocation climb over hard particles: The effect of an attractive interaction," *Acta Metallurgica*, Vol. 34, 1986, pp. 1893.
210. N.D. Alexopoulos, "Generation of Quality Maps to Support Material Selection by Exploiting the Quality Indices Concept of Cast Aluminum Alloys," *Materials and Design*, Vol. 28, 2007, pp. 534-543.
211. N.D. Alexopoulos and Sp. G. Pantelakis, "Quality Evaluation of A357 Cast Aluminum Alloy Specimens Subjected to Different Artificial Aging Treatment," *Materials and Design*, Vol. 25, 2004, pp. 419-430.
212. N.D. Alexopoulos and Sp. G. Pantelakis, "Quality Assessment of Artificially Aged A357 Aluminum Alloy Cast Ingots by Introducing Approximate Expressions of the Quality Index QD," *Metallurgical and Materials Transactions A*, Vol. 35A, 2004, pp. 3079-3089.
213. N.D. Alexopoulos, "Definition of Quality in Cast Aluminum Alloys and Its Characterization with Appropriate Indices," *Journal of Materials Engineering and Performance*, Vol. 15(1), 2006, pp. 59-66.
214. T. Din, A.K.M.B. Rashid and J. Campbell, "High Strength Aerospace Casting Alloys: Quality Factor Assessment," *Materials Science and Technology*, Vol. 12, 1996, pp. 269-273.

215. S. Jacob, "Quality Index in Predicting of Properties of Aluminum Castings - A Review," *AFS Transactions*, Vol. 108, 2000, pp. 811-818.
216. C.H. Cáceres, "A Rationale for the Quality Index of Al-Si-Mg Casting Alloys," *International Journal of Cast Metals Research*, Vol. 10, 1998, pp. 293-299.
217. C.H. Cáceres, "A Phenomenological Approach to the Quality Index of Al-Si-Mg Casting Alloys," *International Journal of Cast Metals Research*, Vol. 12, 2000, pp. 367-375.
218. C.H. Cáceres, "Microstructure Design and Heat Treatment Selection for Casting Alloys Using the Quality Index," *Journal of Materials Engineering and Performance*, Vol. 9(2), 2000, pp. 215-221.
219. C.H. Cáceres and J. Barresi, "Selection of Temper and Mg Content to Optimize the Quality Index of Al-7Si-Mg Casting Alloys," *International Journal of Cast Metals Research*, Vol. 12, 2000, pp. 377-384.
220. C.H. Cáceres, J.H. Sokolowski, and P. Gallo, "Effect of Aging and Mg Content on the Quality Index of Two Model Al-Cu-Si-Mg Alloys," *Materials Science and Engineering A*, Vol. 271, 1999, pp. 53-61.
221. C.H. Cáceres, M. Makhlof, D. Apelian, and L. Wang, "Quality Index Chart for Different Alloys and Temperatures: A Case Study on Aluminum Die-Casting Alloys," *Journal of Light Metals*, Vol. 1, 2001, pp. 51-59.
222. C.H. Cáceres, L. Wang, D. Apelian, and M. Makhlof, "Alloy Selection for Die Castings Using the Quality Index," *AFS Transactions*, Vol. 107, 1999, pp. 239-247.
223. H.R. Ammar, C. Moreau, A.M. Samuel, F.H. Samuel, and H.W. Doty "Influences of Alloying Elements, Solution Treatment Time and Quenching Media on Quality Indices of 413-Type Al-Si Casting Alloys," *Materials Science and Engineering A*, Vol. 489(1-2), 2008, pp. 426-438.

224. H.R. Ammar, C. Moreau, A.M. Samuel, F.H. Samuel, and H.W. Doty, "Effects of Aging Parameters on the Quality of 413-Type Commercial Alloys," *Materials and Design*, Vol.30, 2009, pp. 1014-1025.
225. W.Chen, Y. Wang, J. Qiang, and C. Dong, "Bulk metallic glasses in the Zr-Al-Ni-Cu system," *Acta Materialia*, Vol. 51, 2003, pp. 1899-1907.
226. W. Yuying, L. Xiangfa, J. Binggang, and H. Cuanzhen, "Modification effect of Ni-38 wt% Si on Al-12 wt% Si alloy," *Journal of Alloys and Compounds*, Vol. 477, 2009, pp. 118-122.
227. M.A. Zamzam, A.S. El Sabbagh, and M.M. Milad, "Study of thermal effects of Al-Ni turbine blades on their lifetime," *Materials and Design*, Vol. 23, 2002, pp. 161-168.
228. D.L. Zhang, L.H. Zheng, and D.H. StJohn, "Effect of a Short Solution Treatment Time on Microstructure and Mechanical Properties of Modified Al-7wt%Si-0.3Wt%Mg Alloy," *Journal of Light Metals*, Vol. 2, 2002, pp. 27-36.
229. W.R. Osorio, L.R. Garcia, P.R. Goulart and A. Garcia, "Effects of Eutectic Modification and T4 Heat Treatment on Mechanical Properties and Corrosion Resistance of an Al-9wt%Si Casting Alloy," *Materials Chemistry and Physics*, Vol. 106, 2007, pp. 343-349.
230. M.I.Z. Cardoso, "Análisis de la solidificación de los precipitados de Cu en la aleación A319," Tesis de Maestría, Instituto Tecnológico de Saltillo, Saltillo, Coahuila, México, 2006.
231. X. Jian, T.T. Meek, and Q. Han, "Refinement of eutectic silicon phase of aluminum A356 alloy using high-intensity ultrasonic vibration," *Scripta Materialia*, Vol. 54, 2005, pp. 893-896.
232. R. Li, "Solution heat treatment of 354 and 355 cast alloys," *AFS Transactions*, Vol. 104, 1996, pp. 777-783.

233. C.H. Cáceres, "Transient environmental effects of light alloy substitutions in transport vehicles," *Materials and Design*, Vol. 30(8), 2009, pp. 2813-2822.
234. M. Easton, W.Q. Song, and T. Abbott, "A comparison of the deformation of magnesium alloys with aluminum and steel in tension, bending and buckling," *Materials Design*, Vol. 27, 2006, pp. 935-946.
235. Z. Li, A.M. Samuel, F.H. Samuel, C. Ravindran, S. Valtierra, and H.W. Doty, "Parameters controlling the performance of AA319-type alloys Part I: Tensile Properties," *Material Science and Engineering A*, Vol. A367, 2004, pp. 96-110.
236. D.H. St. John and L.M. Hogan, "The peritectic transformation," *Acta Metallurgica*, Vol. 25, 1977, pp. 77-81.
237. N.R. Andrade González, "Aging Effects in 319-Type Alloys," PhD. Thesis, McGill University (2006).
238. Derek Hull, *Fractography: Observing, Measuring and Interpreting Fracture Surface Topography*, Cambridge University Press, 4 W. 20th St., New York, NY 1001 24211, 1999.
239. C.T. Rios, R. Caram, C. Bolfarini, F.W.J. Botta, and C.S. Kiminami, "Intermetallic compounds in the Al-Si-Cu system," *Acta Microscopia*, Vol. 12, 2003, pp. 77-82.
240. P. Prasad, "Characterization of new, cast, high temperature aluminum alloys for diesel engine applications, Master's Thesis, University of Cincinnati, Cincinnati (2006).
241. K.S. Kumar, S.A. Brown and J.R. Pickens, *Acta Materialia*, Vol. 44, No. 5, 1996, pp. 1899-1915.
242. D.G. Eskin, *Journal of Materials Science*, Vol. 38, 2003, pp. 279-290.

243. W.M. Edwards, "Microstructural mechanical property modelling for the processing of Al-Si alloys," PhD. Thesis, Loughborough: Institute of Polymer Technology and Materials Engineering, Loughborough University (2002).
244. J. Gauthier and F.H. Samuel, "Tensile Properties and Fracture Behavior of Solution-Heat-Treated 319.2 Al Automotive Alloy," *AFS Transactions*, Vol. 103, 1995, pp. 849-857.
245. Z. Li, A.M. Samuel, F.H. Samuel, C. Ravindran, S. Valtierra, and H.W. Doty, "Parameters Controlling the Performance of AA319-Type Alloys, Part II. Impact Properties and Fractography," *Materials Science and Engineering A*, Vol. A367, 2004, pp. 111-122.
246. T. Gladman, "Precipitation Hardening in Metals," *Materials Science and Technology*, Vol. 15, 1999, pp. 30-36.
247. G.F. Van der Voort, "*Visual Examination and Light Microscopy*," *Metals Handbook 9th Edition*, Vol. 12, *Fractography*, American Society for Metals, Metal Park, Oh, 1987, pp. 91-165.
248. Q.C. Wang and C.H. Cáceres, "The Fracture Mode in Al-Si-Mg Casting Alloys," *Materials Science and Engineering A*, Vol. A241, 1998, pp. 72-82.
249. F.J. Tavitias-Medrano, "Artificial Aging Treatments of 319-Type Aluminum Alloys," PhD. Thesis, McGill University (2007).
250. H. Rosenbaum and D. Turnbull, "Metallographic Investigation of Precipitation of Silicon from Aluminum," *Acta Metallurgica*, Vol. 7, 1959, pp. 664-674.
251. K. Ragab, "The use of fluidized sand bed as an innovative technique for heat treating aluminum based castings," Ph.D Thesis, Université du Québec à Chicoutimi, Chicoutimi, Québec, Canada (2012).

252. Y. Zhan, J. Jiang, Z. Sun, J. Ma, Ch. Li, and Z. Hu, "Phase equilibria of the Zr-Ti-Si ternary system at 773K," *Journal of Alloys and Compounds*, Vol. 475, 2009, pp. 131-133.
253. M.A. Moustafa, F.H. Samuel, and H.W. Doty, "Effect of solution heat treatment and additives on the microstructure of Al-Si (A413.1) automotive alloys," *Journal of Materials Science*, Vol. 38, 2003, pp. 4507-4522.
254. E. Tillova and M. Chalupova, "Fatigue failure of recycled AlSi9Cu3 cast alloy," *Acta Metallurgica Slovaca Conference*, Vol. 1, No. 2, 2010, pp. 108-114.
255. M.K. Surappa, E.W. Blank, and J.C. Jaquet, "Microstructural Approach to Deformation and Fracture of Cast Al-7Si-0.3Mg," *3rd International Conference on Solidification Processing*, Sheffield, UK, 1987, pp. 424-427.
256. D. Apelian, S. Shivkumar, and G. Sigworth, "Fundamental Aspects of Heat Treatment of Cast Al-Si-Mg Alloys," *AFS Transactions*, Vol. 97, 1989, pp. 727-742.
257. F.J. Tavitias-Medrano, J.E. Gruzleski, F.H. Samuel, S.Valtierra, and H.W. Doty, "Effect of Mg and Sr-modification on the mechanical properties of 319-type aluminum cast alloys subjected to artificial aging," *Materials Science and Engineering*, Vol. 480(1-2), 2008, pp. 356-364.
258. G.A. Zaki, "On the performance of low pressure die-cast Al-Cu based automotive alloys: role of additives," Master's Thesis, Université du Québec à Chicoutimi, Chicoutimi, Quebec, Canada (2014).
259. E.A. Elsharkawi, "Effects of metallurgical parameters on the decomposition of π -AlFeMgSi phase in Al-Si-Mg alloys and its influence on the mechanical properties," PhD. Thesis, Université du Québec à Chicoutimi, Chicoutimi, Quebec, Canada (2011).

260. A.M.A. Mohamed, F.H. Samuel, and S. Alkahtani, "Influence of Mg and solution heat treatment on the occurrence of incipient melting in Al-Si-Cu-Mg cast alloys," *Materials Science and Engineering*, Vol. 543, 2012, pp. 22-24.
261. S.G. Shabestari and S. Ghodrat, "Assessment of modification and formation of intermetallic compounds in aluminum alloy using thermal analysis," *Materials Science and Engineering A*, Vol. 467, Issues 1-2, 2007, pp. 150-158.
262. M.B. Durdjevic, B. Duric, A. Mitrasinovic, and J.H. Sokolowski, "Modeling of Casting Processes Parameters for the 3xx Series of Aluminum Alloys Using the Silicon Equivalency Algorithm," *Association of Metallurgical Engineers Serbia and Montenegro*, Vol. 9, 2003, pp. 91-106.
263. L. Lu and A.K. Dahle, "Iron-Rich Intermetallic Phases and their Role in Casting Defect Formation in Hypoeutectic Al-Si Alloys," *Metallurgical and Materials Transactions A*, Vol. 36A, No. 3, 2005, pp. 819-835.
264. F.H. Samuel, A.M. Samuel, and H. Liu, "Effect of Magnesium Content on the Aging Behaviour of Water-Chilled Al-Si-Cu-Mg-Fe-Mn (380) Alloy Castings," *Journal of Materials Science*, Vol. 30, 1995, pp. 1-10.
265. F. Zeng, C. Xia, and Y. Gu, "The 430°C Isothermal Section of the Al-4Mg-Sc-Zr Quaternary System in the Al-rich Range," *Journal of Alloys and Compounds*, Vol. 363, 2004, pp.175-181.
266. P.Y. Zhu and Q.Y. Liu, "Kinetics of granulation of discontinuous phase in eutectic structures," *Materials Science and Technology*, Vol. 2, 1986, pp. 500-507.
267. C.H. Cáceres, B. Johannesson, J.A. Taylor, A. Canales-Nuñez, M. Cardoso, J. Talamantes, "The Effect of Si Content on the Size and Morphology of Fe-Rich and Cu-Rich Intermetallics in Al-Si-Cu-Mg Alloys," *Shape Casting: 2nd International*

- Symposium*, Paul N. Crepeau, Murat Tiryakioglu, John Campbell (Eds) The Minerals, Metals, and Materials Society, Warrendale, PA, 2007, pp. 1-7.
268. S.K. Chaudhury and D. Apelian, "Fluidized bed heat treatment of cast Al-Si-Cu-Mg alloys," *Metallurgical and Materials Transactions A*, Vol. 37A, 2006, pp. 2295-2311.
269. C.H. Caceres and J.A. Taylor, "Enhanced ductility in Al-Si-Cu-Mg casting alloys with high Si content," *Shape Casting: The John Campbell Symposium*, M. Tiryakioglu and P. Crepeau (Eds), TMS, California (2005), pp. 245-254.
270. R.E. Slotz and R.M. Pelloux, "The Bauschinger effect in precipitation strengthened aluminum alloys," *Metallurgical Transactions A*, Vol. 7A, 1976, pp. 1295-1306.
271. J.A. Catherall and R.F. Smart, "The effect of nickel in aluminum-silicon eutectic alloys," *Metallurgia*, Vol. 79, 1969, pp. 247-250.